Synthesis and temperature-dependent structure property relations of mullite-type tin(II) compounds

Dissertation

Zur Erlangung des Doktorgrades der Naturwissenschaften
– Dr. rer. nat. –

Fachbereich (Biologie/Chemie)
Der Universität Bremen

Vorgelegt von
M. Sc. Sarah Maria Bernadette Wittmann
Bremen 2024

Diese Arbeit wurde in der Arbeitsgruppe „Chemische Kristallographie fester Stoffe“ von Herrn Prof. Dr. Thorsten M. Gesing an der Universität Bremen im Zeitraum von August 2019 bis 2024 angefertigt.

Begutachtung des schriftlichen Teils: Abgabe 11.01.2024

1. Gutachter: Prof. Dr. Reinhard X. Fischer
2. Gutachter: Prof. Dr. Hubert Huppertz

Tag der mündlichen Prüfung: 07.03.2024

Mitglieder des Prüfungsausschusses:

1. Prof. Dr. Anne Staubitz, Fachbereich 02 Biologie und Chemie, Institut für organische und analytische Chemie, Universität Bremen
2. Prof. Dr. Tim Neudecker, Fachbereich 02 Biologie und Chemie, Institut für physikalische und theoretische Chemie, Universität Bremen
3. Jun.Prof. Dr. Ella Schmidt, Fachbereich 05 Geowissenschaften, Fachgebiet Kristallographie und Geomaterialforschung, Universität Bremen
4. Prof. Dr. Thorsten M. Gesing, Fachbereich 02 Biologie und Chemie, Institut für Anorganische Chemie und Kristallographie, Chemische Kristallographie fester Stoffe, Universität Bremen
5. M.Sc. Pascal Komorr, Fachbereich 02 Biologie und Chemie, Institut für Anorganische Chemie und Kristallographie, Universität Bremen
6. B.Sc. Nils Schmidt, Fachbereich 02 Biologie und Chemie, Masterstudent, Universität Bremen,

Danksagung

An erster Stelle gilt mein Dank meinem Doktorvater Prof. Dr. Thorsten M. Gesing für die Möglichkeit meine Promotion in seiner Gruppe anzufertigen, für seine wissenschaftlichen Ratschläge und die Diskussion während der gesamten Bearbeitungsphase. Ebenfalls möchte ich PD. Dr. M. Mangir Murshed für seine gute Betreuung und Unterstützung bei der Durchführung der gesamten Arbeit danken. Auch möchte ich bei Dr. Lars Robben, Dr. Alexander Wollbrink und Gabriele Ebert bedanken, für ihre Hilfe, Unterstützung und allzeit offenes Ohr bei allen möglichen Fragen bedanken.

Vielen Dank auch an meine beiden Gutachter, Prof. Dr. Reinhard X. Fischer und Prof. Dr. Hubert Huppertz für die Zeit, die sie sich genommen haben, meine Arbeit zu lesen und ihr Gutachten zu erstellen.

Außerdem möchte ich mich bei all denjenigen bedanken, die bei dieser Arbeit durch ihre Kollaborationen mitgewirkt haben. Vielen Dank an Ulla Gro Nielsen (SDU FKF, Odense Dänemark), Vitaliy Bilovol (UBA, Buenos Aires Argentinien), und Rainer Pöttgen, Aylin Koldemir und Lars Schumacher (alle drei von der Universität Münster).

Auch möchte ich meinen Kolleg*innen der AG Gesing für die Gespräche, das Miteinander, den wissenschaftlichen oder nicht wissenschaftlichen Austausch und so vieles mehr danken.

Für die finanzielle Unterstützung muss ich der Deutschen Forschungsgesellschaft (DFG) und der Universität Bremen während des Projekts meinen Dank ausdrücken. Ebenfalls bedanken muss ich mich für die finanzielle Unterstützung für Konferenzreisen (IUCr 2023 Melbourne, DGK 2023) bei der DFG, Universität Bremen, GDCh und der IUCr.

Besonders möchte ich an dieser Stelle auch meiner Familie und meinem Freund für die unermüdliche Stärkung und Motivierung danken, sowie für das stets offene Ohr für meine Gedanken.

Declaration

Versicherung des Eides Statt

Hiermit versichere ich, Sarah Maria Bernadette Wittmann

Matr.Nr.: 3243187

An Eides statt durch meine Unterschrift, dass ich die vorliegende Arbeit mit dem Titel „*Synthesis and temperature-dependent structrual property relations of mullite-type tin(II) compounds*“ selbstständig und ohne fremde Hilfe angefertigt und alle Stellen, die ich wörtlich dem Sinne nach aus Veröffentlichungen entnommen habe, als solche kenntlich gemacht habe, mich auch keiner anderen als der angegebenen Literatur oder sonstiger Hilfsmittel bedient habe.

Ich versichere an Eides statt, dass ich die vorgenannten Angaben nach bestem Wissen und Gewissen gemacht habe und dass die Angaben der Wahrheit entsprechen und ich nichts verschwiegen habe.

Die Strafbarkeit einer falschen eidesstattlichen Versicherung ist mit bekannt, namentlich die Strafanordnung gemäß § 156 StGB bis zu drei Jahren Freiheitsstrafe oder Geldstrafe bei vorsätzlicher Begehung der Tat bzw. gemäß § 161 Abs. 1 StGB bis zu einem Jahr Freiheitsstrafe oder Geldstrafe bei fahrlässiger Begehung.

(Sarah Maria Bernadette Wittmann) Bremen, 11.01.2024

Declaration on the contribution of the candidate to a multi-author article/manuscript which is included in the submitted doctoral thesis

The presented results in this cumulative dissertation were obtained in collaboration with several other groups. The contribution of the candidate in % of the total workload (up to 100 % for each of the following categories)

Paper Chapter 2: Mullite-type $EMBO_4$: synthesis, structural, optical, and vibrational properties of rare tin(II) borates with M = Al and Ga

Contribution of the candidate in % of the total workload (up to 100 % for each of the following categories)

Experimental concept and design: ca. 80 %

Experimental work and/or acquisition of (experimental) data: ca. 100 %

Data analysis and interpretation: ca. 75 %

Preparation of Figures and Tables: ca. 85 %

Drafting of the manuscript: ca. 70 %

Manuscript in preparation – Chapter 3: Temperature dependent characterization of $SnAlBO_4$ and $SnGaBO_4$ mullite-type ceramics

Contribution of the candidate in % of the total workload (up to 100 % for each of the following categories)

Experimental concept and design: ca. 80 %

Experimental work and/or acquisition of (experimental) data: ca. 100 %

Data analysis and interpretation: ca. 85 %

Preparation of Figures and Tables: ca. 85 %

Drafting of the manuscript: ca. 70 %

Manuscript in preparation – Chapter 4: Synthesis and characterization of mullite-type $Sn(Cr_{1-x}V_x)BO_4$ for $x = 0 – 1.0$

Contribution of the candidate in % of the total workload (up to 100 % for each of the following categories)

Experimental concept and design: ca. 80 %

Experimental work and/or acquisition of (experimental) data: ca. 100 %

Data analysis and interpretation: ca. 80 %

Preparation of Figures and Tables: ca. 90 %

Drafting of the manuscript: ca. 70 %

Manuscript in preparation – Chapter 6: Syntheses and characterization of mullite-type $Sn(M_{1-x}M'_x)BO_4$ compounds

Contribution of the candidate in % of the total workload (up to 100 % for each of the following categories)

Experimental concept and design: ca. 80 %

Experimental work and/or acquisition of (experimental) data: ca. 100 %

Data analysis and interpretation: ca. 80 %

Preparation of Figures and Tables: ca. 90 %

Drafting of the manuscript: ca. 70 %

Paper Chapter 7: On red tin (II) oxide: temperature-dependent structural, spectroscopic, and thermogravimetric properties

Contribution of the candidate in % of the total workload (up to 100 % for each of the following categories)

Experimental concept and design: ca. 80 %

Experimental work and/or acquisition of (experimental) data: ca. 100 %

Data analysis and interpretation: ca. 65 %

Preparation of Figures and Tables: ca. 65 %

Drafting of the manuscript: ca. 60 %

Paper Chapter 8: Synthesis, structural and spectroscopic investigations of dolomite-type $MSn(BO_3)_2$ with M = Mn, Fe, Co and Ni

Contribution of the candidate in % of the total workload (up to 100 % for each of the following categories)

Experimental concept and design: ca. 80 %

Experimental work and/or acquisition of (experimental) data: ca. 100 %

Data analysis and interpretation: ca. 75 %

Preparation of Figures and Tables: ca. 95 %

Drafting of the manuscript: : ca. 70 %

Detail of the declaration on own contributions to the publications

The previously published work which is presented in **chapter 2** (EMBO; M = Al, Ga) is divided in the following parts where I conducted:

- Synthesis of mullite-type phases
- Performing measurements of SEM, Raman, UV/Vis, and FTIR spectroscopy. Additionally, the data evaluation and interpretation, the structural determination and refinements
- Writing of the main manuscript (in cooperation with Prof. Dr. Thorsten M. Gesing, PD Dr. Mangir Murshed, Ulla Gro Nielsen (ssNMR, SDU Odense), Vitaliy Bilovol (Mössbauer spectroscopy, UBA Argentina), Rainer Pöttgen and Aylin Koldemir (Mössbauer spectroscopy, University of Münster))
- Generation of the figures

And parts where I did not conduct:

- Mössbauer spectroscopy measurements (Vitaliy Bilovol, University of Buenos Aires, Argentina; Rainer Pöttgen and Aylin Koldemir, University of Münster)
- Solid state NMR spectroscopy (in cooperation with Ulla Gro Nielsen, SDU Odense, Denmark)
- XRPD measurements on Stadi MP (Dr. Lars Robben, Konrad Krämer)

The previously published work which is presented in **chapter 3** (TD data of EMBO; M = Al, Ga) is divided in the following parts where I conducted:

- Synthesis of mullite-type phases

- Performing measurements of temperature dependent Raman, UV/Vis, and XRPD measurements. Additionally, the data evaluation and interpretation, the structural determination and refinements.
- Writing of the main manuscript (in cooperation with Prof. Dr. Thorsten M. Gesing, PD Dr. Mangir Murshed, Kowsik Ghosh, Rainer Pöttgen and Aylin Koldemir (Mössbauer spectroscopy, University of Münster))
- Generation of the figures

And parts where I did not conduct:

- Mössbauer spectroscopy measurements (Rainer Pöttgen and Aylin Koldemir, University of Münster)
- Low temperature XRPD measurements on Stadi MP (Dr. Lars Robben)

The previously published work which is presented in **chapter 4** (Sn($Cr_{1-x}V_x$)BO_4) is divided in the following parts where I conducted:

- Synthesis of mullite-type phases
- Performing measurements of Raman, UV/Vis, and FTIR spectroscopy. Additionally, the data evaluation and interpretation, the structural determination and refinements.
- Writing of the main manuscript (in cooperation with Prof. Dr. Thorsten M. Gesing, PD Dr. Mangir Murshed, Rainer Pöttgen and Aylin Koldemir (Mössbauer spectroscopy, University of Münster))
- Generation of the figures

And parts where I did not conduct:

- Mössbauer spectroscopy measurements (Rainer Pöttgen and Aylin Koldemir, University of Münster)

- XRPD measurements on Stadi MP (Dr. Lars Robben, Konrad Krämer)

The previously published work which is presented in **chapter 6** (solid solutions) is divided in the following parts where I conducted:

- Synthesis of mullite-type phases
- Performing measurements of temperature dependent Raman, UV/Vis, and XRPD measurements. Additionally, the data evaluation and interpretation, the structural determination and refinements.
- Writing of the main manuscript (in cooperation with Prof. Dr. Thorsten M. Gesing, PD Dr. Mangir Murshed)
- Generation of the figures

The previously published work which is presented in **chapter 7** (RSO) is divided in the following parts where I conducted:

- Synthesis of red tin(II)oxide
- Performing measurements of Raman, SEM, UV/Vis, and FTIR spectroscopy as well as their temperature-dependent measurements and thermogravimetric investigations. Additionally, the data evaluation and interpretation, the structural determination and refinements
- Writing of the main manuscript (in cooperation with Prof. Dr. Thorsten M. Gesing and PD Dr. Mangir Murshed)
- Generation of the figures

And parts where I did not conduct:

- XRPD: Room temperature and low-temperature measurements (Dr. Lars Robben)

The previously published work which is presented in **chapter 8** (dolomite-phase) is divided in the following parts where I conducted:

- Synthesis of dolomite-type phases
- Performing measurements of SEM, Raman, UV/Vis, and FTIR spectroscopy. Additionally, the data evaluation and interpretation, the structural determination and refinements
- Writing of the main manuscript (in cooperation with Prof. Dr. Thorsten M. Gesing and PD Dr. Mangir Murshed)
- Generation of the figures

And parts where I did not conduct:

- Mössbauer spectroscopy measurements (Vitaliy Bilovol, University of Buenos Aires, Argentina)
- XRPD measurements on Stadi MP (Dr. Lars Robben, Konrad Krämer)

List of content

Publications

[1] S. Wittmann, M.M. Murshed, V. Bilovol, T.M. Gesing, Synthesis, structural and spectroscopic investigations of dolomite-type $MSn(BO_3)_2$ with M = Mn, Fe, Co and Ni, (2023). DOI:10.1515/zkri-2023-0002

[2] S. Wittmann, M.M. Murshed, V. Bilovol, A. Koldemir, R. Pöttgen, U.G. Nielsen, T.M. Gesing, Mullite-type $EMBO_4$: synthesis, structural, optical, and vibrational properties of rare tin(II) borates with M = Al and Ga, Journal of the American Ceramic Society 107(2) (2023) 1302-1314. DOI:10.1111/jace.19476

[3] S. Wittmann, M.M. Murshed, T.M. Gesing, On red tin (II) oxide: temperature-dependent structural, spectroscopic, and thermogravimetric properties, Zeitschrift für anorganische und allgemeine Chemie 648(24) (2022) e202200311. DOI:10.1002/zaac.202200311

List of abbreviations

ACS	average crystallite size
ATR-FTIR	attenuated total reflectance Fourier-transformed infrared
BVS	bond valence sum
DASF	derivation of absorption spectrum fitting
DEA	Debye-Einstein-Anharmonicity
DSC	differential scanning calorimetry
EMBO	element-metal-bor-oxygen
EDX	energy dispersive X-ray
FTIR	Fourier transformed infrared
HTK	Hochtemperatur Kammer
IR	infrared
LDV	Liebau density vector
LEP	lone electron pair
MAS	magic angle spinning
MS	micro strain
NMR	nuclear magnetic resonance
RATD	relectance – absorbance – Tauc – DASF
SEM	scanning electron microscopy
TG	thermal gravimetry

TGA	thermo gravimetric analysis
UV/Vis	ultra-violet/ visible
WLE	Wang-Liebau eccentricity
wt%	weight per centage
XRPD	X-ray powder diffraction

Zusammenfassung

Mullit und mullitartige Verbindungen ziehen aufgrund ihrer vielfältigen Eigenschaften, wie z.B. kristallchemische, hohe thermische Stabilität oder geringe Wärmeausdehnung und Leitfähigkeit, ein breites Spektrum an Forschungsaufmerksamkeit auf sich. Das Hauptziel dieser Arbeit ist die Synthese und Charakterisierung der Struktur-Eigenschafts-Beziehungen von Mullit-Typ Sn(II) Oxiden in Abhängigkeit ihrer chemischen Zusammensetzung. Im Rahmen dieser Dissertation wurden Vorstufen für O8-Mullitphasen sowie die Phasen selbst, und auch das Nebenprodukt der dolomitartigen Verbindungen synthetisiert und untersucht.

Da die Untersuchung neu synthetisierter Mullit-typ-Verbindungen den Hauptteil dieser Dissertation ausmachte, befasst sich der Hauptteil mit diesem Strukturtyp. Um den Einfluss des freien Elektronenpaares (LEP) von Sn^{2+} auf die Struktur und den Unterschied zum Einfluss des LEP von Pb^{2+} zu untersuchen, werden verschiedene $SnMBO_4$ (M = Al, Ga, Cr und V) durch konventionelle Festkörpersynthesen in versiegelten Quarzrohren synthetisiert (**Kapitel 2 - 5**). Die Rietveld-Verfeinerung der Röntgenbeugungsdaten zeigt, dass alle Verbindungen in der orthorhombischen Raumgruppe *Pnam* kristallisieren, wobei die kantenverknüpften MO_6-Oktaeder eine unendliche Kette entlang der kristallographischen *c*-Achse bilden und durch trigonale-planare BO_3-Gruppen sowie quadratisch-pyramidale SnO_4-Gruppen miteinander verbunden sind. Um die Stärke der stereochemischen Aktivität des LEP zu messen, wurde aus den Strukturdaten der Wang-Liebau-Exzentrizität (WLE) Faktor berechnet, was zu einer starken Beeinflussung der Struktur führte. Weitere Untersuchungen um die strukturellen Merkmale mit z.B. ^{119}Sn Mössbauer-, Festkörper-NMR-, Raman-, IR- und UV/Vis-spektroskopische Messungen zu festigen, wurden durchgeführt. Die thermische Analyse führt bei allen vier Verbindungen zu einem Phasenübergang im Tieftemperaturbereich um 150 K, während die Hochtemperaturmessung nur zur Zersetzung führt. Für $SnCrBO_4$ wird bei tiefen Temperaturen ein magnetischer Übergang von ferromagnetisch zu antiferromagnetisch

beobachtet. In einer weiteren Studie sollte untersucht werden, wie sich das M-Kation in der oktaedrischen Kette auswirkt und wie es sich bei einer Substitution eines Kations durch ein anderes mit einer Schrittweite von 0.1 verändert (**Kapitel 6**). Basierend auf den Röntgenbeugungsdaten nehmen die Zellparameter mit zunehmender Größe des kationischen Radius zu, was zum Teil durch die magnetische Struktur der Verbindung beeinflusst wird.

Ein Ziel dieser Arbeit war es, Pb^{2+} durch Sn^{2+} in den isostrukturellen $EMBO_4$-Phasen zu ersetzen, wobei ein wichtiger Teil die Synthese verschiedener Vorstufen war (**Kapitel 7**). Rotes SnO ist eine Möglichkeit für einen Prekursor, da es reaktiver sein soll als das kommerzielle blau-schwarze SnO. Daher wurde zu Beginn der Arbeit eine Untersuchung dieser beiden Materialien im Vergleich zum farblosen SnO_2 durchgeführt, um strukturelle Unterschiede wie die unterschiedlichen Kristallstrukturen sowie die Phasenübergänge von rotem zu blau-schwarzem SnO zu SnO_2 zu erhalten [1]. Zusätzlich zu den mullitartigen Verbindungen trat während dieser Doktorarbeit das Nebenprojekt der dolomitartigen Phasen auf (**Kapitel 8**). Diese Materialien werden als Produkte bei der Synthese von SnO, M_2O_3 (M = Fe, Mn) und B_2O_3 gewonnen. Daher werden Untersuchungen bei Raumtemperatur durchgeführt, wobei der Einfluss von vier verschiedenen Metallkationen (M = Fe, Mn, Co und Ni) auf die Strukturen verstanden werden soll. Rietveld-Verfeinerungen der Röntgenbeugungsdaten bestätigen eine rhomboedrische Raumgruppe $R\bar{3}$ für alle Zusammensetzungen, bei denen die Änderung der Elementarzellparameter dem zunehmenden Kationenradius der Metallkationen folgt. Die beiden oktaedrischen Gruppen MO_6 und SnO_6 sind regelmäßig. Die Frequenzverschiebungen einiger selektiver Raman- und IR-Bänder werden durch die Änderung der Größen des kationischen Radius und der jeweiligen M-O-Bindungsabstände erklärt [2].

Reference

1. S. Wittmann, M.M. Murshed, T.M. Gesing, On red tin (II) oxide: temperature-dependent structural, spectroscopic, and thermogravimetric properties, Zeitschrift für anorganische und allgemeine Chemie 648(24) (2022) e202200311. DOI:10.1002/zaac.202200311
2. S. Wittmann, M.M. Murshed, V. Bilovol, T.M. Gesing, Synthesis, structural and spectroscopic investigations of dolomite-type $MSn(BO_3)_2$ with M = Mn, Fe, Co and Ni, (2023). DOI:10.1515/zkri-2023-0002

Summary

Mullite and mullite-type compounds draw a wide range of research attention for their diverse properties as for example crystallo-chemical, their high thermal stability or their low thermal expansion and conductivity. The main objective of this work is to synthesize and characterize the structure-property relationships of mullite-type Sn(II) oxides as a function of their chemical compositions. Within the scope of this dissertation, precursors for O8 mullite-type phases as well as the phases itself were synthesized and studied. Due to unforeseen results, an investigation of dolomite-type compounds is included in this work.

As the investigation of newly synthesized mullite-type compounds was the main part of this dissertation, the remaining part is about this structure type. To investigate the influence of the lone electron pair (LEP) of Sn^{2+} on the structure and the difference to the influence of the LEP of Pb^{2+}, different $SnMBO_4$ (M = Al, Ga, Cr, and V) are synthesized by a conventional solid-state synthesis in sealed quartz tubes (**chapter 2 - 5**). Rietveld refinement of X-ray powder diffraction data indicates that all compounds crystallize in the orthorhombic space group *Pnam*, where the edge-sharing MO_6 octahedra form an infinite chain along the crystallographic *c* axis and are interconnected by trigonal planar BO_3 groups as well as square pyramidal SnO_4 groups. To measure the strength of the stereochemical activity of the LEP, Wang-Liebau eccentricity (WLE) parameter was calculated from the structural data which lead to a highly influenced structure. Further investigations were done to consolidate the structural features with for example ^{119}Sn Mössbauer, solid state NMR, Raman, IR, and UV/Vis spectroscopic measurements. Thermal analysis leads to a phase transition in the low temperature range around 150 K for all four compounds whereas the high temperature measurements lead only to a decomposition. For $SnCrBO_4$ as well as $SnVBO_4$, a magnetic transition is obtained at low temperatures where the magnetic properties shift from ferromagnetic at room temperature to antiferromagnetic. Another study was to obtain the effect of the M-cation in the octahedral

chain and how it will change with a substitution of one by each other with a step size of 0.1 (**chapter 6**). Based on the X-ray powder diffraction data, the cell parameters increase with increasing cationic radius which is partly influenced by the magnetic structure of the compound. One goal of this work was to replace Pb^{2+} by Sn^{2+} in the isostructural $EMBO_4$ phases where an important part was the synthesis of different precursors (**chapter 7**). Red SnO is one possibility for a good precursor as it is supposed to be more reactive than the commercially available blue-black SnO. Hence, a study of these two materials compared to the colorless SnO_2 was done in the beginning of the work to obtain structural differences as the different crystal structures as well as the phase transitions from red to blue-black SnO to SnO_2 [1]. Additionally, to the mullite-type compounds, a side-project occurred during the time of this PhD work which leads to dolomite-type phases (**chapter 8**). These materials are obtained as products during the synthesis of SnO, M_2O_3 (M = Fe, Mn) and B_2O_3 where the result was $MSn(BO_3)_2$ dolomite phases. Hence, investigations of dolomite-type structures are done at room temperature where the influence of four different metal cation (M = Fe, Mn, Co, and Ni) on the structures should be understood. Rietveld refinements of the X-ray powder diffraction data confirm a rhombohedral space group $R\bar{3}$ for all compositions where the change in the unit cell parameters follow the increasing nature of the cation radius of the metal cations. Both octahedral groups MO_6 and SnO_6 are found to be quite regular. The frequency shifts of some selective Raman and IR bands are explained in terms of the change of cationic sizes and the respective M-O bond distances [2].

Reference

1. S. Wittmann, M.M. Murshed, T.M. Gesing, On red tin (II) oxide: temperature-dependent structural, spectroscopic, and thermogravimetric properties, Zeitschrift für anorganische und allgemeine Chemie 648(24) (2022) e202200311. DOI:10.1002/zaac.202200311
2. S. Wittmann, M.M. Murshed, V. Bilovol, T.M. Gesing, Synthesis, structural and spectroscopic investigations of dolomite-type $MSn(BO_3)_2$ with M = Mn, Fe, Co and Ni, (2023). DOI:10.1515/zkri-2023-0002

Chapter 1 - Introduction

For the ongoing growth of science and technology in our modern world, both fundamental research and a broad range of applications of a given material is of crucial importance. Moreover, synthesis of less toxic but sustainable materials are of pressing need to cope with the emerging environmental issues. As such, mullites and mullite-type compounds have drawn considerable research interests, which can be judged from the exponential increase of relevant publications [1, 2].

The name *mullit*e originates from the discovery of a mineral hundred years ago in the island of Mull in Scotland [3]. Samples of this mineral were found at various locations of ancient lava flows (around 65 million years ago) from the volcano Ben More [1]. These samples contained an Al_2O_3-rich acicular mineral intergrown in feldspar crystals. As shown in **figure 1.1**, these minerals have been identified earlier as sillimanites, which were wrongly described as an Al_2O_3 - SiO_2 system. The chemical composition was 3/2 (3 Al_2O_3 – 2 SiO_2) instead of 1/1 (Al_2O_3 – SiO_2). Since this finding of the chemical composition, these mineral compositions of this type are called mullite.

Mullites or mullite-type compounds, which rarely occur in nature, show, even under harsh conditions [4], high thermal stability [1, 5, 6], low thermal expansion [7], low thermal conductivity [4] and excellent creep resistance [1, 5, 6]. Hence, research of these compounds focuses on their electrical [8, 9], crystal-chemical [10, 11], mechanical [12, 13], thermal [4, 14, 15], and optical [16, 17] properties. Due to such interesting properties, these materials are used in a broad range of applications. Monolithic mullites are, for example, because of their high thermal stability [1], used in thermocouple tubes [18], crucibles [5], heat exchangers [19], advanced refractories [4], catalyst-supported devices [20] and as substrates for silicon solar cells [21, 22] as well. These ceramics can also be used as thin film coatings of metals and non-metals to avoid their oxidation [23, 24]. In addition, these mullite coatings have an excellent creep behavior [25, 26] increasing the corrosion resilience or have a suitable strength and toughness of the coated materials [27]. Mullite fibers are used, for example, in diesel emission filters [28]. Because of their advanced refractory [4] and insulating properties mullite-type compounds can be used as high-temperature insulators [29] or as electrically insulating coatings of electrodes in melting furnaces and rotary tube seals. Furthermore, studies focusing on the synthesis of these materials showed that mullite-type materials can form both at high temperatures and low pressures [1]. This explains the natural occurrence in lava and abundance in the remaining environment [1].

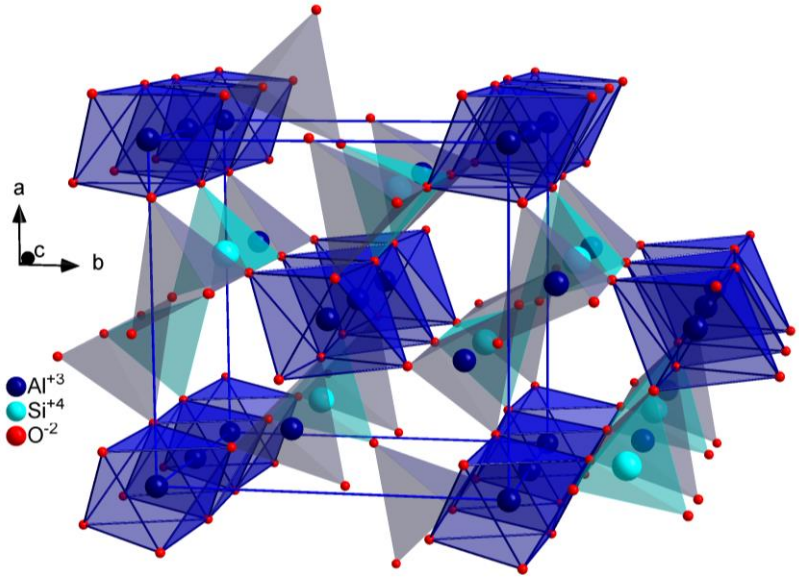

Figure 1.1: Crystal structure of sillimanite with AlO_6 octahedra chain along the crystallographic *c* axis interconnected by SiO_4 and AlO_4 tetrahedra. [30]

Mullites and mullite-type compounds possess characteristic crystal structure with common four properties:

- The highest aristotype keeps the space group *P4/mbm* [31]; the highest possible topological symmetry for a pure octahedral chain. All compounds in this family must be a subgroup of this space group. The ratio between *a*- and *b*-lattice parameter in these compounds lies close to unity [31].

- All mullite-type materials have a single Einer chain where octahedral structures share the same oxygen atom (edge-sharing oxygen atoms). The name *single Einer chain* is given because since only one single chain is interconnected by different linking groups and not another octahedral chain.
- This single Einer chain runs along the crystallographic *c*-axis [32]. The axis of the non-edge sharing atoms of this chain must point toward the edges with an adjacent octahedron. The angle ω between these two axes must be between 30° and 90°, as shown in **figure 1.2** [1, 33].
- The chain structure should resemble the orthogonal metric where the chain direction is as close as possible to an angle γ of 90(5)° (**Figure 1.2b**) [1, 33].

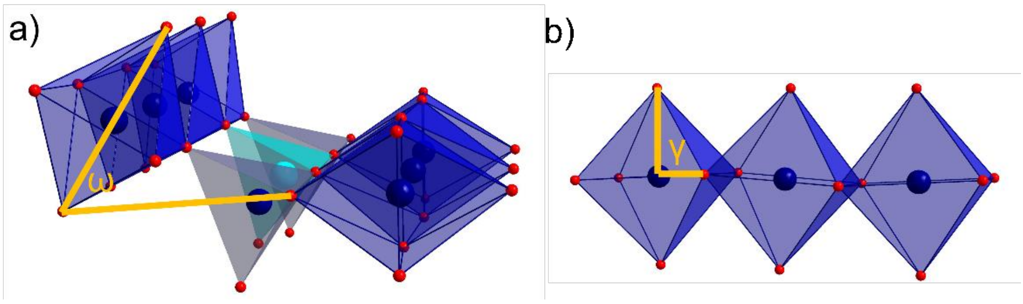

Figure 1.2: Structural features of mullites and mullite-type compounds: a) the angle ω between the two octahedral chains; b) the angle γ between one terminating and a vertex oxygen atom of the octahedra.

To combine the octahedral chain in a crystal structure, a cross-linking structure of either a geometric shape of tetrahedron, bipyramid, trigonal pyramid, distorted tetrahedron, square pyramid, trigonal planar group, or tetrahedral dimer is needed as listed in **table 1.1** and shown in **figure 1.3**.

Table 1.1: List of the different cross-linking structures with examples in different mullite-type crystal structures.

Cross-linking structure	**Example**
Tetrahedral	AlO_4 or SiO_4 in mullite or sillimanite [11] or AlO_4 and BO_4 (**figure 1.3a**) in $Al_4B_2O_9$ [34]
Bipyramid	AlO_5 (**figure 1.3b**) in A_9B_2-Boron aluminates [13] or $Al_4B_2O_9$ [34]
Trigonal pyramid	AlO_4 in Al_2SiO_5 – andalusite [35]
Distorted tetrahedron	SbO_3E in MSb_2O_4 (E = active LEP, M = Ni, Mn, Fe, Zn) [36]
Square pyramid	LO_4E in $LMBO_4$ (**figure 1.3c**) (L = Sn, Pb; E = active lone electron pair; M = Al, Ga, Cr, V, Fe, Mn) [37-51], Mn_2O_8 in $Bi_2Mn_4O_{10}$ [52, 53]
Trigonal planar	BO_3 (**figure 1.3d**) in $LMBO_4$ (L = Sn, Pb; M = Al, Ga, Cr, V, Fe, Mn) [37-51] or $Al_4B_2O_9$ [34]
Tetrahedral dimer	M_2O_7 in $Bi_2M_4O_9$ (M = Fe, Ga, Al) [14, 16, 21, 52, 54]

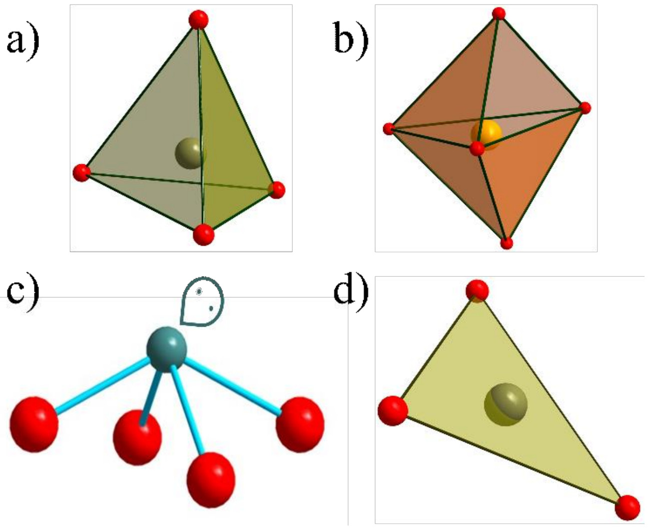

Figure 1.3: Cross-linking groups in mullites and mullite-type compounds: a) tetrahedral (BO_4), b) bipyramids (AlO_5), c) square pyramid (SnO_4E), and d) trigonal planar (BO_3).

As there are several ways to connect these chains, leading to several space groups which are subgroups of the aristotype. **Figure 1.4** depicts the Bärninghausen tree for different mullite-type phases.

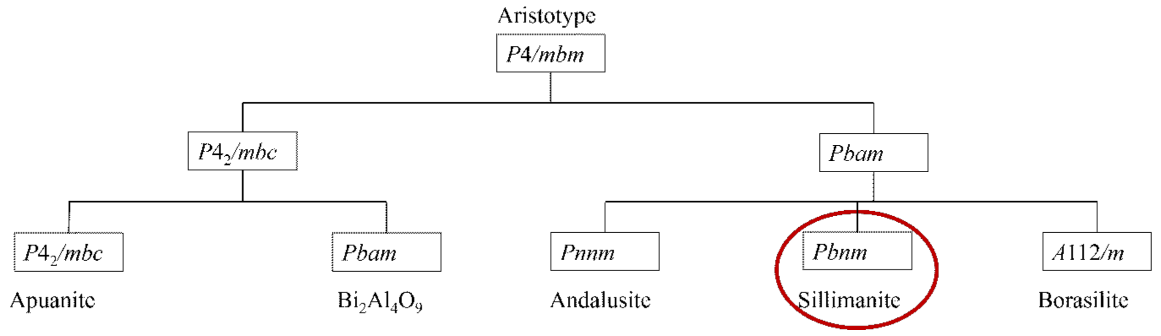

Figure 1.4: Bärninghausen tree for different mullite-type compounds.

Another shorthand way to describe the mullite-type compounds is based on the number of oxygen atoms, where three different phases (O10, O9, and O8) are known. Each phase differs in crystal structure and the physico-chemical properties as well. Well-known members of the O10 phases are $R_2Mn_4O_{10}$ (R = Bi, Y, rare earth elements) as $Bi_2Mn_4O_{10}$ or $Dy_2Mn_4O_{10}$ [53, 55] (**figure 1.5**).

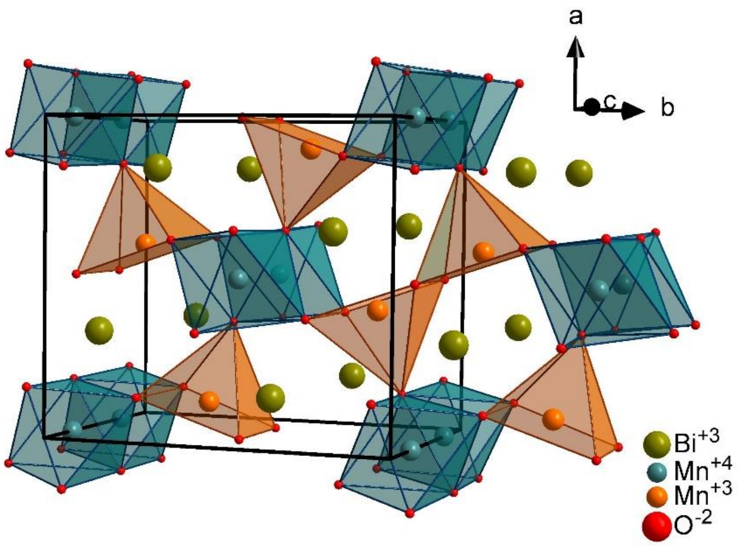

Figure 1.5: Representative crystal structure of mullite-type O10 phase $Bi_2Mn_4O_{10}$ [55] with octahedral chain (MnO_6) running along the crystallographic *c*-axis, MnO_5 square pyramids and Bi^{3+} cations in the channels.

In this structure, the octahedral MnO_6 chain is cross-linked by $[MO_5]_2$ double-square pyramidal polyhedron. They form together with two octahedra a five-membered ring, as shown in **figure 1.5** [56]. The R^{3+} cations are located in the channels of the five-membered rings, which run parallel to the chain [57]. These compounds crystallize in the space group *Pbam* which is a subgroup of the aristotype. In these O10 phases, two different oxidation states of manganese are seen, where Mn^{4+} and Mn^{3+} are located at the $Mn^{4+}O_6$ octahedral and the $Mn^{3+}O_5$ square pyramidal centroids, respectively. The structure of $Bi_2Mn_4O_{10}$ is closely related to those of $Bi_2M_4O_9$. Indeed, in the latter one, one oxygen atom is missing [9], which leads to cross-linking the octahedral chain by $[MO_4]_2$ double-tetrahedra instead of double-square pyramids. Again, a five-membered ring is built by three MO_4 tetrahedra and two octahedra [14], as shown in **figure 1.6**.

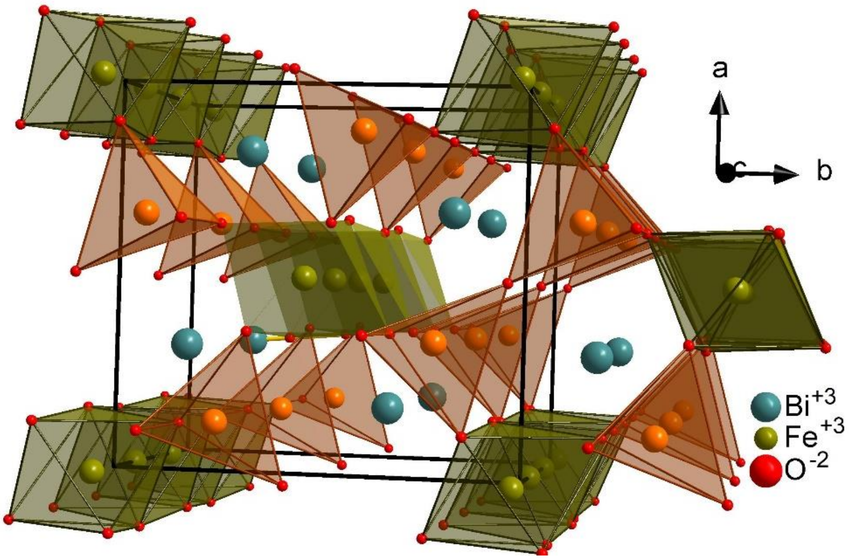

Figure 1.6: Representative crystal structure of mullite-type O9 phase of $Bi_2Fe_4O_9$ with octahedral chain (FeO_6) running along the crystallographic **c**-axis, cross-linked by the FeO_4 tetrahedra ,and the larger Bi^{3+} cation locates in the channels [58].

Another example of a O9 phase is $Al_4B_2O_9$ which crystallizes in a pseudo-tetragonal metric with $a \approx b$, leading to space group *Pbam* [34]. **Figure 1.7** shows the crystal structure of $Al_4B_2O_9$, where the AlO_6 octahedral chains are connected by BO_4 and AlO_4 tetrahedra, dimers of edge-sharing AlO_5 bipyramids and BO_3 triangles.

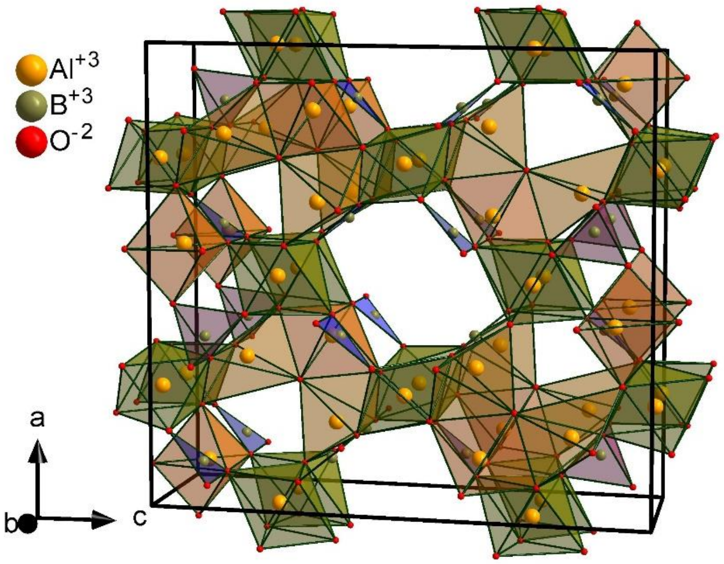

Figure 1.7: Crystal structure of $Al_4B_2O_9$ with AlO_6 octahedra along the crystallographic **c**-axis, AlO_4 and BO_4, AlO_5 bipyramids, tetrahedra as well as BO_3 trigonal planar building blocks [34].

Examples of O8 mullite-type compounds include mineral schafarzikite ($FeSb_2O_4$, **figure 1.8**) [59], minium ($PbPb_2O_4$) [60] and their chemical derivates such as Pb_2SnO_4, where the SnO_6 octahedral chains are linked by the PbO_4 tetrahedra. These mullite-types are of particular importance due the stereochemically active lone electron pairs (LEPs) of the M-cation in the linking MO_4E polyhedra (*E* refers to LEP) [36].

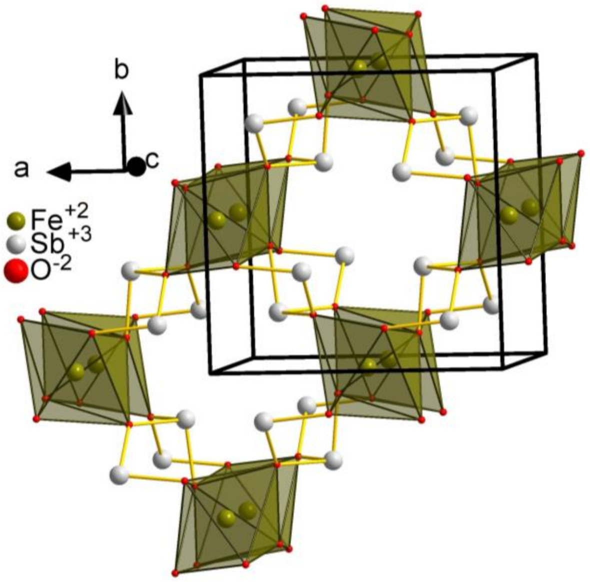

Figure 1.8: Crystal structure of $FeSb_2O_4$ mullite-type O8 phase. The octahedral FeO_6 chain is running along the crystallographic *c*-axis which is cross-linked by SbO_4E [59].

$PbMBO_4$ compounds are also O8-phases crystallize in the space group *Pnam*, where the trigonal planar BO_3 groups serve as the linking units of the edge-sharing MO_6 octahedra [38, 43, 45, 50], as shown in **figure 1.9**. The rigid nature of the BO_3 groups and the stereochemical demand of the LEP lacuna led to significantly different dihedral angles between two neighboring MO_6 octahedra [41]. Several $PbMBO_4$ compounds are known for transition metal cations in the octahedral MO_6 units (M = Cr, Mn, and Fe), showing one-dimensional magnetic behavior [47]. Both $PbCrBO_4$ and $PbFeBO_4$ show antiferromagnetic long-range spin-ordering with the antiferromagnetic MO_6 chains coupled ferromagnetically. In $PbMnBO_4$ both the intrachain and interchain couplings are ferromagnetic, which is a rare example of ferromagnetic insulator.

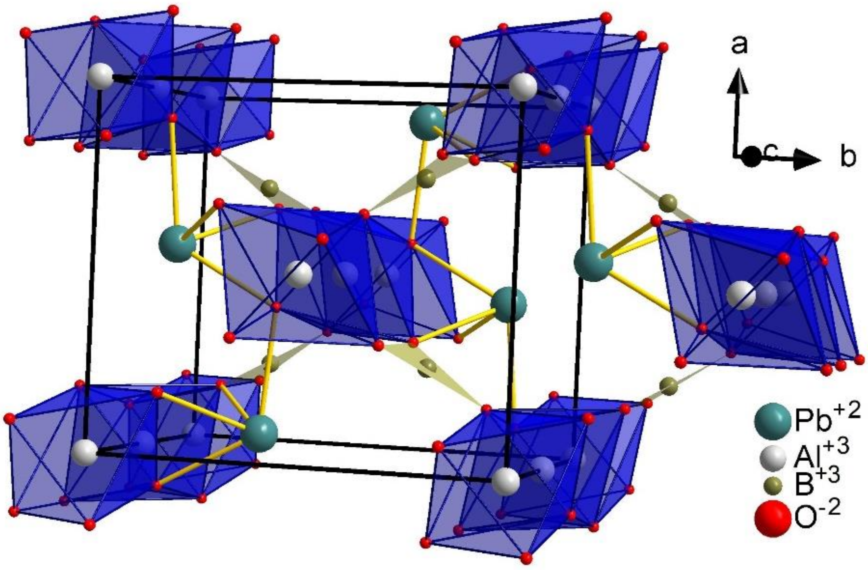

Figure 1.9: Crystal structure of mullite-type O8 phase ($PbMBO_4$ with M = Al). The octahedral AlO_6 chain is running along the crystallographic *c*-axis which is cross-linked by PbO_4E and BO_3 groups [47].

Due to the toxicity and its environmental aspects [61], Pb^{2+} should be exchanged by another cation with similar size, valence, and chemical behavior. Lead(II) has a cationic radius of 112 pm [62] and a stereochemical active $6s^2$ LEP. As such, replacement of Pb^{2+} by Sn^{2+} is possible as it has a cationic radius of 118 pm with stereochemical activity of the $5s^2$ LEP [63]. Although the stereochemical distortion in $Sn(II)O_4$ is about 3.8 times greater than that of $Pb(II)O_4$, theoretical study [37] well predicts the stability of the $SnMBO_4$ compounds. While Pb^{2+} is a stable oxidation state Sn^{2+} is susceptible to oxidize to Sn^{4+} [64]. For instance, SnO disproportionate to SnO_2 and elementary tin at 573 K [65].

The main aim of this work is to synthesize new mullite-type compounds starting from the known $PbMBO_4$ phases (M = Al, Ga, Cr, Fe, Mn) [38, 39, 49-51], where Pb^{2+} is aimed to be replaced by Sn^{2+} . After successful synthesis analysis of their structural, spectroscopic, thermal, and magnetic properties is followed. Of particular notes, this study focuses on how and at what extend the crystal-physico-chemical properties change in these O8-phases when the stereochemical activity of the $6s^2$-LEP cation is replaced by the $5s^2$-LEP cations as a measure of the Wang-Liebau eccentricity (WLE) parameter and the Liebau density vector (LDV) [52]. Crystal-chemical analysis of a given solid solution, e.g., Pb($Al_{1-x}Mn_x$)BO_4 [40, 47] can separate the polyhedral distortion between the LEP and purely geometric origin [53]. Such solid solution also helps guide how the magnetic property responses with respect to the spin-dilution /concentration of a given M-cation in the $SnM'_{1-x}M''_xBO_4$ system. Besides, the influence of different M-cations in the system draws sheer attention, in particular, when different sizes of the M-cations influence the crystal-chemistry. Whether the M-cation spin-ordering lead to nuclear phase transition could shed light on the multiferroic properties of the compounds. Indeed, the susceptibility of the oxidation state of Sn^{2+} plays important roles as the preferred redox potential lead to Sn^{4+} phases such Sn-containing dolomites [66].

In **chapter 2** – **chapter 5**, mullite-type $LMBO_4$ (L = Sn, Pb; M = Al, Ga, Cr, V) are synthesized and characterized within one published manuscript and two manuscripts in preparation. **Chapter 6** describes solid solutions with two different trivalent metal cations based on their synthesis and characteristics on their structural and spectroscopic properties. In **chapter 7**, two different types of precursors, red tin(II)oxide and MBO_3 (M = Cr, Al, Mn, Fe, Sc, In), are synthesized and characterized. **Chapter 8** is a representation of dolomite-type structures within a manuscript. A general discussion about the work which was done additionally to the before discussed one is described in **chapter 9**. **Chapter 10** concludes the PhD work with a short outlook.

Reference

1. H. Schneider, Komarneni, S., Mullite, Wiley2005.
2. Clarivate, Web of Science, 2023.
3. H. Schneider, K. MacKenzie, Proceedings of Mullite 2000 Conference, Journal of the European Ceramic Society 21(14) (2001) iii. DOI:10.1016/S0955-2219(01)00263-1
4. Y. Ren, F.Z. Dai, H. Xiang, X. Wang, L. Sun, Y. Zhou, Mechanical and thermal properties of light weight boron-mullite Al_5BO_9, Journal of the American Ceramic Society 103(10) (2020) 5939-5951. DOI:10.1111/jace.17313
5. H. Schneider, E. Eberhard, Thermal-Expansion of Mullite, Journal of the American Ceramic Society 73(7) (1990) 2073-2076. DOI:10.1111/j.1151-2916.1990.tb05270.x

6. L. Mahnicka-Goremikina, R. Svinka, V. Svinka, L. Grase, I. Juhnevica, M. Rundans, V. Goremikins, S. Tolendiuly, S. Fomenko, Thermal properties of porous Mullite ceramics modified with microsized ZrO_2 and WO_3, Materials, 2022.
7. G. Brunauer, F. Frey, H. Boysen, H. Schneider, High temperature thermal expansion of mullite: an in situ neutron diffraction study up to 1600 °C, Journal of the European Ceramic Society 21(14) (2001) 2563-2567. DOI:10.1016/S0955-2219(01)00267-9
8. S. Ohmann, P. Fielitz, L. Dörrer, G. Borchardt, T.M. Gesing, R.X. Fischer, C.H. Rüscher, J.C. Buhl, K.D. Becker, H. Schneider, Electrical conductivity of mullite-type $Bi_2Al_4O_9$ ceramics in air, Solid State Ionics 211 (2012) 46-50. DOI:10.1016/j.ssi.2012.01.030
9. H. Schneider, R.X. Fischer, T.M. Gesing, J. Schreuer, M. Mühlberg, Crystal chemistry and properties of mullite-type $Bi_2M_4O_9$: An overview, 103(4) (2012) 422-429. DOI:10.3139/146.110716
10. M. Curti, A. Kirsch, L.I. Granone, F. Tarasi, G. López-Robledo, D.W. Bahnemann, M.M. Murshed, T.M. Gesing, C.B. Mendive, Visible-Light Photocatalysis with Mullite-Type $Bi_2(Al_{1-x}Fe_x)_4O_9$: Striking the Balance between Bandgap Narrowing and Conduction Band Lowering, ACS Catalysis 8(9) (2018) 8844-8855. DOI:10.1021/acscatal.8b01210
11. S. Ďurovic, Isomorphism between Sillimanite and Mullite, Journal of the American Ceramic Society 45(4) (1962) 157-161. DOI:10.1111/j.1151-2916.1962.tb11111.x
12. M. Mangir Murshed, C.B. Mendive, M. Curti, M. Šehović, A. Friedrich, M. Fischer, T.M. Gesing, Thermal expansion of mullite-type $Bi_2Al_4O_9$: A study by X-ray diffraction, vibrational spectroscopy and density functional theory, Journal of Solid State Chemistry 229 (2015) 87-96. DOI:10.1016/j.jssc.2015.05.010
13. G.D. Gatta, N. Rotiroti, M. Fisch, T. Armbruster, Stability at high pressure, elastic behavior and pressure-induced structural evolution of "Al_5BO_9", a mullite-type ceramic material, Physics and Chemistry of Minerals 37(4) (2010) 227-236. DOI:10.1007/s00269-009-0327-x
14. A. Beran, E. Libowitzky, M. Burianek, M. Mühlberg, C. Pecharromán, H. Schneider, Infrared and Raman spectroscopy of mullite-type $Bi_2Ga_4O_9$, Crystal Research and Technology 43(11) (2008) 1230-1239. DOI:10.1002/crat.200800396
15. D.J. Lacks, B. Hildmann, H. Schneider, Effects of disorder in mullite: Molecular dynamics simulation and energy landscape analysis, Physical Review B 72(21) (2005) 214305. DOI:10.1103/PhysRevB.72.214305
16. M. Burianek, M. Mühlberg, M. Woll, M. Schmücker, T.M. Gesing, H. Schneider, Single-crystal growth and characterization of mullite-type orthorhombic $Bi_2M_4O_9$ ($M = Al^{3+}$, Ga^{3+}, Fe^{3+}), Crystal Research and Technology 44(10) (2009) 1156-1162. DOI:10.1002/crat.200900465
17. H. Saalfeld, H. Gerlach, Solid solution and optical properties of (Al, Ge)-mullites, 195(1-2) (1991) 65-73. DOI:10.1524/zkri.1991.195.1-2.65
18. A. Gahler, J.G. Heinrich, J. Günster, Direct laser sintering of Al_2O_3–SiO_2 dental ceramic components by layer-wise slurry deposition, Journal of the American Ceramic Society 89(10) (2006) 3076-3080. DOI:10.1111/j.1551-2916.2006.01217.x
19. S. Schaafhausen, E. Yazhenskikh, A. Walch, S. Heidenreich, M. Müller, Corrosion of alumina and mullite hot gas filter candles in gasification environment, Journal of the European Ceramic Society 33(15) (2013) 3301-3312. DOI:10.1016/j.jeurceramsoc.2013.05.024
20. T.F. Krenzel, J. Schreuer, T.M. Gesing, M. Burianek, M. Muhlberg, H. Schneider, Thermal expansion and elastic properties of mullite-type $Bi_2Ga_4O_9$ and $Bi_2Fe_4O_9$ single crystals, Int. J. Mater. Res. 103(4) (2012) 438-448. DOI:10.3139/146.110718
21. K.L. Da Silva, V. Sepelak, A. Duvel, A. Paesano, H. Hahn, F.J. Litterst, P. Heitjans, K.D. Becker, Mechanochemical-thermal preparation and structural studies of mullite-type

$Bi_2(Ga_xAl_{1-x})_4O_9$ solid solutions, Journal of Solid State Chemistry 184(5) (2011) 1346-1352. DOI:10.1016/j.jssc.2011.04.007

22. A. Focsa, I. Gordon, J.M. Auger, A. Slaoui, G. Beaucarne, J. Poortmans, C. Maurice, Thin film polycrystalline silicon solar cells on mullite ceramics, Renewable Energy 33(2) (2008) 267-272. DOI:10.1016/j.renene.2007.05.038
23. M. Asghari, T. Mohammadi, R.F. Alamdari, F. Agend, Thin-layer template-free polycrystalline mordenite membranes on cylindrical mullite supports, Microporous and Mesoporous Materials 114(1) (2008) 148-154. DOI:10.1016/j.micromeso.2007.12.030
24. K.N. Lee, R.A. Miller, Development and environmental durability of mullite and mullite/YSZ dual layer coatings for SiC and Si_3N_4 ceramics, Surface and Coatings Technology 86-87 (1996) 142-148. DOI:10.1016/S0257-8972(96)03074-5
25. E. Withey, C. Petorak, R. Trice, G. Dickinson, T. Taylor, Design of 7wt.% Y_2O_3–ZrO_2/mullite plasma-sprayed composite coatings for increased creep resistance, Journal of the European Ceramic Society 27(16) (2007) 4675-4683. DOI:10.1016/j.jeurceramsoc.2007.02.214
26. J. Roy, S. Das, S. Maitra, Solgel-Processed Mullite Coating—A Review, International Journal of Applied Ceramic Technology 12(S2) (2015) E71-E77. DOI:10.1111/ijac.12230
27. S. Varadarajan, A.K. Pattanaik, V.K. Sarin, Mullite interfacial coatings for SiC fibers, Surface and Coatings Technology 139(2) (2001) 153-160. DOI:10.1016/S0257-8972(01)01014-3
28. B.N. Rao, B.S. Prem Kumar, K.V. Kumar Reddy, Effect of CNG flow rate on the performance and emissions of a Mullite-coated diesel engine under dual-fuel mode, International Journal of Ambient Energy 37(6) (2016) 589-596. DOI:10.1080/01430750.2015.1023835
29. N. Bouzidi, M.A. Bouzidi, K. Bouguermouh, R.O. Nunes, N. Benabdeslem, L. Mahtout, D. Merabet, Mechanical and dielectric properties of high temperature coating insulators based on by-product of algerian kaolin, Transactions of the Indian Ceramic Society 73(4) (2014) 277-283. DOI:10.1080/0371750X.2014.926782
30. H. Yang, R.M. Hazen, L.W. Finger, C.T. Prewitt, R.T. Downs, Compressibility and crystal structure of sillimanite, Al_2SiO_5, at high pressure, Physics and Chemistry of Minerals 25(1) (1997) 39-47. DOI:10.1007/s002690050084
31. H. Schneider, R.X. Fischer, J. Schreuer, D.J. Green, Mullite: Crystal structure and related properties, Journal of the American Ceramic Society 98(10) (2015) 2948-2967. DOI:10.1111/jace.13817
32. H. Schneider, J. Schreuer, B. Hildmann, Structure and properties of mullite—A review, Journal of the European Ceramic Society 28(2) (2008) 329-344. DOI:10.1016/j.jeurceramsoc.2007.03.017
33. R.X. Fischer, A. Gaede-Kohler, J. Birkenstock, H. Schneider, Mullite and mullite-type crystal structures, Int. J. Mater. Res. 103(4) (2012) 402-407. DOI:10.3139/146.110713
34. K. Hoffmann, T.J.N. Hooper, M.M. Murshed, O. Dolotko, Z. Révay, A. Senyshyn, H. Schneider, J.V. Hanna, T.M. Gesing, R.X. Fischer, Formation, stability and crystal structure of mullite-type $A_{l6-x}B_xO_9$, Journal of Solid State Chemistry 243 (2016) 124-135. DOI:10.1016/j.jssc.2016.08.018
35. J.K. Winter, S. Ghose, Thermal-Expansion and High-Temperature Crystal-Chemistry of the Al_2SiO_5 Polymorphs, American Mineralogist 64(5-6) (1979) 573-586.
36. J.R. Gavarri, R. Chater, J. Ziółkowski, The chemical bonds in $MeSb_2O_4$ (Me = Mn, Ni, Fe, Zn) isomorphous compounds: Thermal expansion, force constants, energies, Journal of Solid State Chemistry 73(2) (1988) 305-316. DOI:10.1016/0022-4596(88)90114-4
37. M. Curti, C.B. Mendive, T. Bredow, M. Mangir Murshed, T.M. Gesing, Structural, vibrational and electronic properties of $SnMBO_4$ (M = Al, Ga): a predictive hybrid DFT study, J Phys Condens Matter 31(34) (2019) 345701. DOI:10.1088/1361-648X/ab20a1

38. M. Curti, M.M. Murshed, T. Bredow, D.W. Bahnemann, T.M. Gesing, C.B. Mendive, Elastic, phononic, magnetic and electronic properties of quasi-one-dimensional $PbFeBO_4$, Journal of Materials Science 54(21) (2019) 13579-13593. DOI:10.1007/s10853-019-03866-1
39. T.M. Gesing, e. al., Crystal structure of mullite-type $PbMn_{0.5}Al_{0.5}BO_4$ determined by combined X-ray and neutron diffraction data, Zeitschrift für Kristallographie - New Crystal Structures 227(3) (2012) 285-286. DOI:10.1524/ncrs.2012.0181
40. T.M. Gesing, C.B. Mendive, M. Curti, D. Hansmann, G. Nénert, P.E. Kalita, K.E. Lipinska, A. Huq, A.L. Cornelius, M.M. Murshed, Structural properties of mullite-type $Pb(Al_{1-x}Mn_x)BO_4$, Zeitschrift für Kristallographie - Crystalline Materials 228(10) (2013). DOI:10.1524/zkri.2013.1640
41. M. Gogolin, M.M. Murshed, M. Ende, R. Miletich, T.M. Gesing, Uniaxial negative thermal expansion in the mullite- and borax-type $PbAlBO_4$ polymorphs, Journal of Materials Science 55(1) (2019) 177-190. DOI:10.1007/s10853-019-04013-6
42. J. Head, P. Manuel, F. Orlandi, M. Jeong, M.R. Lees, R. Li, C. Greaves, Structural, magnetic, magnetocaloric, and magnetostrictive Properties of $Pb_{1-x}Sr_xMnBO_4$ (x = 0, 0.5, and 1.0), Chemistry of Materials 32(23) (2020) 10184-10199. DOI:10.1021/acs.chemmater.0c03701
43. H.-J. Koo, M.-H. Whangbo, Density functional investigation of the magnetic properties of $PbMBO_4$ (M=Cr, Mn, Fe), Solid State Communications 149(15-16) (2009) 602-604. DOI:10.1016/j.ssc.2009.01.030
44. T. Kremlika, High pressure behaviour of α-$PbAlBO_4$ single crystals under hydrostatic compression to 24 GPa, Master thesis, University of Vienna A066815 (2020) 1-75.
45. M.M. Murshed, R.X. Fischer, T.M. Gesing, The role of the Pb^{2+}lone electron pair for bond valence sum analysis in mullite-type $PbMBO_4$(M = Al, Mn and Fe) compounds, Zeitschrift für Kristallographie - Crystalline Materials 227(8) (2012) 580-584. DOI:10.1524/zkri.2012.1483
46. M.M. Murshed, C.B. Mendive, M. Curti, G. Nénert, P.E. Kalita, K. Lipinska, A.L. Cornelius, A. Huq, T.M. Gesing, Anisotropic lattice thermal expansion of $PbFeBO_4$: A study by X-ray and neutron diffraction, Raman spectroscopy and DFT calculations, Materials Research Bulletin 59 (2014) 170-178. DOI:10.1016/j.materresbull.2014.07.005
47. M.M. Murshed, A. Rusen, R.X. Fischer, T.M. Gesing, Transition-metal substitution in $PbAlBO_4$: Synthesis, structural and spectroscopic studies of manganese containing phases, Materials Research Bulletin 47(6) (2012) 1323-1330. DOI:10.1016/j.materresbull.2012.03.014
48. H. Park, J. Barbier, $PbGaBO_4$, an orthoborate with a new structure-type, Acta Crystallographica Section E Structure Reports Online 57(9) (2001) i82-i84. DOI:10.1107/s1600536801013940
49. H. Park, J. Barbier, R.P. Hammond, Crystal structure and polymorphism of $PbAlBO_4$, Solid State Sciences 5(4) (2003) 565-571. DOI:10.1016/s1293-2558(03)00056-6
50. H. Park, R. Lam, J.E. Greedan, J. Barbier, Synthesis, crystal structure, crystal chemistry, and magnetic properties of $PbMBO_4$ (M = Cr, Mn, Fe): A new structure type exhibiting one-dimensional magnetism, Chemistry of Materials 15(8) (2003) 1703-1712. DOI:10.1021/cm0217452
51. M.A. Prosnikov, A.N. Smirnov, V. Yu Davydov, K.A. Sablina, R.V. Pisarev, Lattice and magnetic dynamics of a quasi-one-dimensional chain antiferromagnet $PbFeBO_4$, Journal of Physics: Condensed Matter 29(2) (2017) 025808. DOI:10.1088/0953-8984/29/2/025808
52. M. Curti, T.M. Gesing, M.M. Murshed, T. Bredow, C.B. Mendive, Liebau density vector: a new approach to characterize lone electron pairs in mullite-type materials, Zeitschrift für Kristallographie - Crystalline Materials 228(12) (2013). DOI:10.1524/zkri.2013.1686

53. K. Ghosh, M.M. Murshed, M. Fischer, T.M. Gesing, Aluminum to germanium inversion in mullite-type $RAlGeO_5$: Characterization of a rare phenomenon for R = Y, Sm–Lu, Journal of the American Ceramic Society 105(1) (2022) 728-741. DOI:10.1111/jace.18085
54. T. Debnath, C.H. Rüscher, P. Fielitz, S. Ohmann, G. Borchardt, Series of compositions $Bi_2(M'_xM_{1-x})_4O_9$ (M', M=Al, Ga, Fe; 0≤x≤1) with mullite-type crystal structure: Synthesis, characterization and $^{18}O/^{16}O$ exchange experiment, Journal of Solid State Chemistry 183(11) (2010) 2582-2588. DOI:10.1016/j.jssc.2010.07.019
55. K. Ghosh, M.M. Murshed, T.M. Gesing, Synthesis and characterization of $(Bi_{1-x}R_x)_2Mn_4O_{10}$: structural, spectroscopic and thermogravimetric analyses for R = Nd, Sm and Eu, Journal of Materials Science 54(21) (2019) 13651-13659. DOI:10.1007/s10853-019-03852-7
56. J.A. Alonso, M.T. Casais, M.J. Martínez-Lope, J.L. Martínez, M.T. Fernández-Díaz, A structural study from neutron diffraction data and magnetic properties of (R = La, rare earth), Journal of Physics: Condensed Matter 9(40) (1997) 8515. DOI:10.1088/0953-8984/9/40/017
57. J.A. Alonso, M.J. Martínez-Lope, M.T. Casais, J.L. Martínez, V. Pomjakushin, Synthesis, structural, and magnetic characterization of $YCrMnO_5$, European Journal of Inorganic Chemistry 2005(13) (2005) 2600-2606. DOI:10.1002/ejic.200401057
58. A. Friedrich, J. Biehler, W. Morgenroth, L. Wiehl, B. Winkler, M. Hanfland, M. Tolkiehn, M. Burianek, M. Mühlberg, High-pressure phase transition of $Bi_2Fe_4O_9$, Journal of Physics: Condensed Matter 24(14) (2012) 145401. DOI:10.1088/0953-8984/24/14/145401
59. M.J. Whitaker, R.D. Bayliss, F.J. Berry, C. Greaves, The synthesis, structure, magnetic and electrical properties of $FeSb_{2-x}Pb_xO_4$, Journal of Materials Chemistry 21(38) (2011) 14523-14529. DOI:10.1039/C1JM12645H
60. A. Byström, A. Westgren, Crystal Structure of Pb_3O_4 and $SnPb_2O_4$, Arkiv for Kemi Mineralogi Och Geologi B16 (1943) 1-7.
61. C. Bellinger David, J. Burger, J. Cade Tom, A. Cory-Slechta Deborah, M. Finkelstein, H. Hu, M. Kosnett, J. Landrigan Philip, B. Lanphear, A. Pokras Mark, T. Redig Patrick, A. Rideout Bruce, E. Silbergeld, R. Wright, R. Smith Donald, Health Risks from Lead-Based Ammunition in the Environment, Environmental Health Perspectives 121(6) (2013) a178-a179. DOI:10.1289/ehp.1306945
62. R.D. Shannon, Revised effective ionic radii and systematic studies of interatomic distances, Acta Crystallographica A32 (1976) 751.
63. T. Wang, K.C. Pitike, Y. Yuan, S.M. Nakhmanson, V. Gopalan, B. Jalan, Chemistry, growth kinetics, and epitaxial stabilization of Sn^{2+} in Sn-doped $SrTiO_3$ using $(CH_3)_6Sn_2$ tin precursor, APL Materials 4(12) (2016). DOI:10.1063/1.4972995
64. J.D. Donaldson, The chemistry of bivalent tin, Inorganic Chemsitry 8 (1967).
65. M.T. G. Murken, Uber das bei der Disproportionierung von SnO entstehende Zinnoxid, Zeitschrift für anorganische und allgemeine Chemie 397 (1973) 117-126. DOI:10.1002/zaac.19733970204
66. S. Wittmann, M.M. Murshed, V. Bilovol, T.M. Gesing, Synthesis, structural and spectroscopic investigations of dolomite-type $MSn(BO_3)_2$ with M = Mn, Fe, Co and Ni, (2023). DOI:10.1515/zkri-2023-0002

Chapter 2 – Syntheses of $SnMBO_4$ (M = Al, Ga)

As the primary focus of this study is the synthesis and characterization of mullite-type compounds, the next chapters deal mostly with this structure type. In the beginning, the focus was on the so-called endmembers with their chemical composition $SnMBO_4$ and $PbMBO_4$ where the last-mentioned are known in the literature with M = Al, Ga, Cr, Mn, and Fe [1-3]. As mentioned in **chapter 1**, the replacement of Pb^{2+} by the environmental healthier and less toxic Sn^{2+} is of importance of the study prima facie. For a given synthesis of the mullite-type O8-phase, two important parameters must be considered. First, the size of the metal cation must fit to the MO_6 octahedral coordination. Five structures of the lead containing compounds, where the cationic radii in the octahedra lie between 53.5 pm and 64.5 pm for Al^{3+} and Mn^{3+}/Fe^{3+} (if the high spin configuration is considered), respectively [4] exist which should be tried in the beginning to synthesize $SnMBO_4$. Additionally, based on the table of Shannon [4] only five other trivalent metal cationic radii are within the range, namely, As^{3+} (58.0 pm), Co^{3+} (61 pm for high spin and 54.5 pm for low spin configuration), Cu^{3+} (54.0 pm for low spin configuration), and V^{3+} (64.0 pm) which could be tried as well. Indeed, As_2O_3 and V_2O_3 are known to keep the optimum radius, whereas Cu(III) rarely exists [5]. The oxidation state +3 is not the most stable form for cobalt [6]. If the range of the metal radius is increased to 80 pm, 13 other metals can be used such as silver, gold, indium, iridium, molybdenum, niobium, palladium, rhodium, ruthenium, antimony, scandium, tantalum, and titanium. As the replacement of lead by tin is cost effective, more expensive iridium [7] and rhodium [8] are excluded as well as silver(III) [9]. The second aspect is the redox potential (**figure 2.1**) of the cation, which should be lower than that of tin.

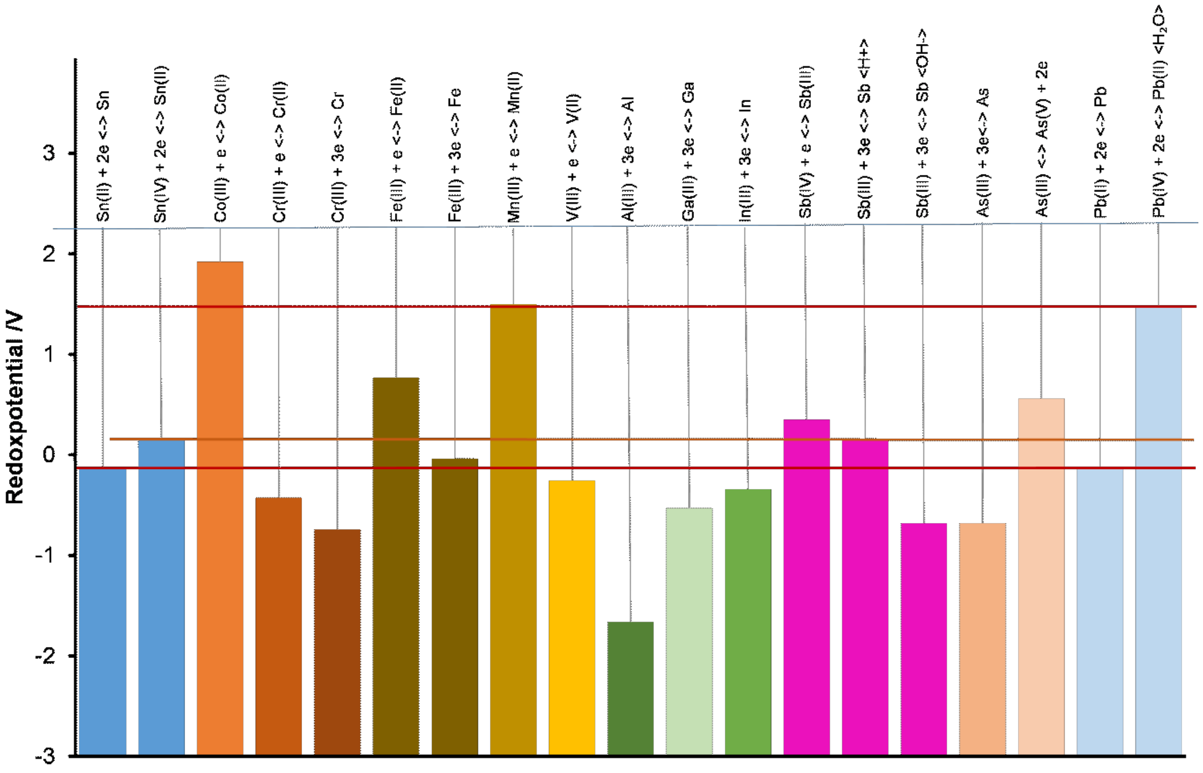

Figure 2.1: Redox potentials of necessary metal ions for this work where the potentials which do not oxidize Sn^{2+} to Sn^{4+} are below the orange line and therefore, more likely to result in a mullite-type compound [6, 10-12].

As the redox potential for Co^{3+} is larger compared to tin, the synthesis results in dolomite-type phases as described in **chapter 8**. For Fe^{3+} and Mn^{3+}, the oxidation of Sn^{2+} to Sn^{4+} followed by the reduction of iron and manganese to respective lower oxidation state. As such, both are excluded for the synthesis of mullite-type $SnMnBO_4$ and $SnFeBO_4$ compounds. Therefore, replacement of lead in $PbMBO_4$ are likely to work with Sn^{2+} for aluminum, gallium, and chromium. Scandium, indium, vanadium, arsenic, and antimony should also be tested. Detailed of the synthesis is described in this chapter (published work).

Mullite-type EMBO$_4$: Synthesis, structural, optical and vibrational properties of rare tin(II) borates with M = Al and Ga

Sarah Wittmann, M. Mangir Murshed, Vitaliy Bilovol, Aylin Koldemir, Rainer Pöttgen, Ulla Gro Nielsen, Thorsten M. Gesing

Reprinted with kind permission from Wiley and upon approval of the co-authors.

Published in: J. Am. Ceram. Soc. 107 (2024) 1302-1314.

https://doi.org/10.1111/jace.19476

ORCID:

SW:	0000-0003-1404-3434
MMM:	0000-0002-9063-372X
VB:	0000-0002-3363-1840
AK:	0009-0004-3819-3853
RP:	0000-0003-0962-279X
UGN:	0000-0002-2336-3061
TMG:	0000-0002-4119-2219

Received: 14 April 2023 | Revised: 1 August 2023 | Accepted: 7 September 2023

DOI: 10.1111/jace.19476

Journal of the American Ceramic Society

RESEARCH ARTICLE

Mullite-type $EMBO_4$: synthesis, structural, optical, and vibrational properties of rare tin(II) borates with M = Al and Ga

Sarah Wittmann[1] | **Mohammad Mangir Murshed**[1,2] | **Vitaliy Bilovol**[3] | **Aylin Koldemir**[4] | **Rainer Pöttgen**[4] | **Ulla Gro Nielsen**[5] | **Thorsten Michael Gesing**[1,2]

[1]Institute of Inorganic Chemistry and Crystallography, University of Bremen, Bremen, Germany

[2]MAPEX Center for Materials and Processes, University of Bremen, Bremen, Germany

[3]Laboratorio de Sólidos Amorfos-INTECIN, University of Buenos Aires, Buenos Aires, Argentina

[4]Institute für Anorganische und Analytische Chemie, Universität Münster, Münster, Germany

[5]Department of Physics, Chemistry and Pharmacy, University of Southern Danmark, Odense, Denmark

Correspondence
Mohammad Mangir Murshed, University of Bremen, Institute of Inorganic Chemistry and Crystallography, Leobener Straße 7, D-28359 Bremen, Germany.
Email: murshed@uni-bremen.de

Present address
Vitaliy Bilovol, Academic Centre for Materials and Nanotechnology, AGH University of Science and Technology, Al. Mickiewicza 30, Krakow 30-059, Poland

Funding information
Deutsche Forschungsgemeinschaft, DFG, Grant/Award Number: GE1981/14-1

Abstract

Metal tin-(II)-borates are rarely studied mainly due to the susceptibility of either oxidation into tin(IV) or disproportionation into elemental tin(0) and tin(IV). We report mullite-type $SnAlBO_4$ and $SnGaBO_4$ ceramics produced by conventional solid-state synthesis in sealed quartz tubes at low pressure of 10^{-7} MPa. Both compounds are isostructural to $PbAlBO_4$ as confirmed by Rietveld refinements of powder X-ray data. The crystal structures are highly influenced by the stereochemical activity of the $5s^2$ lone electron pair of the Sn^{2+} cation measured by the Wang–Liebau eccentricity parameter. To further consolidate the structural features ^{119}Sn Mössbauer, solid state NMR, Raman, IR and UV/vis spectroscopic measurements are performed. The ^{119}Sn Mössbauer isomer shifts and the quadrupole splitting values confirm the SnO_4 coordination and Sn(II) valence states. Solid state ^{11}B, ^{27}Al and ^{119}Sn NMR spectra provided insights into the local crystal-chemical environment. The vibrational properties are discussed from group theoretical analysis to mode assignments. $SnAlBO_4$ and $SnGaBO_4$, respectively, possess an electronic band gap of 3.73(9) and 3.21(4) eV calculated from the diffuse reflectance UV/Vis spectra.

KEYWORDS
crystal structure, metal tin-(II)-borate, Mössbauer spectroscopy, Raman spectroscopy, solid-state NMR spectroscopy

---

1 | INTRODUCTION

Mullite-type compounds have received long wide research attention due to their diverse crystal-chemical,[1,2,3] thermal,[4,5,6,7] mechanical,[8,9,10] electrical,[11,12,13] and optical[14,15,16] properties. A general and convenient way to describe the mullite-type composition is based on the relative number of oxygen atoms in the chemical formula (normalized to even number). For instance, $R_2Mn_4O_{10}$ (R = Y, Bi, and rare-earth element)[17] are called as O10 phase, $Bi_2M_4O_9$ (M = Fe, Al, Ga etc.) as O9 phase,[9,18] $E_2M_2B_2O_8$ (e.g., $PbAlBO_4$[19]), and $M_2E_4O_8$ (e.g., $FeSb_2O_4$[20]) as O8 phases.[21,22] The O8-phase family members are particularly interesting due to the crystal-chemical influence of the lone-electron pairs (LEPs) of the E-cations.[23,24,25,26] To better compare their physical properties with those of other members of the mullite-type family, the crystal structure of a representative O8 member $EAlBO_4$ is described in Figure 1 using the space group *Pnam*, where the chains of edge-sharing MO_6 octahedra run parallel to the crystallographic *c*-axis.[27,28,29] These chains are bridged by planar BO_3 groups and connected by distorted, for instance, PbO_4 square pyramids.[26] The O–M–O bridging angles in the MO_6 octahedral chain leads to a M–M distance of about 297 pm[26] which is the crucial structural feature to understand the magnetic properties of the O8-phases.[30] The rigidity of the trigonal planar BO_3 groups[19,29] and the stereochemically active $6s^2$ LEPs of the Pb^{2+} cations play important roles[24] for the thermo-mechanical properties.[9] Gogolin et al.[19] demonstrated an interplay between the topology-induced negative cross-compliance and the anisotropic Grüneisen parameter, play pivotal roles for the axial negative linear compressibility and axial negative thermal expansion of $PbAlBO_4$. The similar chemical nature of the cations Sn^{2+} and Pb^{2+} indicates the feasibility of the synthesis of isostructural compounds $SnMBO_4$. As a measure of the stereochemical activity, the Wang–Liebau eccentricity |Φ| (WLE)[31] parameter in the $Sn(II)O_x$ polyhedra is about 3.8(1) times greater than that of $Pb(II)O_x$, predicting the stability of the O8 compounds with Sn^{2+} cations. Density functional theory (DFT) calculations[24] suggested that both $SnAlBO_4$ and $SnGaBO_4$ are stable with respect to decomposition into their corresponding binary oxides. However, solid state synthesis of these two O8-phases may not be straightforward since Sn^{2+} is susceptible to oxidation and hence acts as a reducing agent.[24,32,33] As such, most of the known tin minerals contain Sn^{4+} instead of Sn^{2+}. In the present study, we report the synthesis of borate ceramics $SnAlBO_4$ and $SnGaBO_4$, their structural and spectroscopic characterizations using X-ray powder diffraction (XRPD), ultraviolet to visible range (UV/Vis), Raman, IR, Mössbauer, and solid-state NMR spectroscopies.

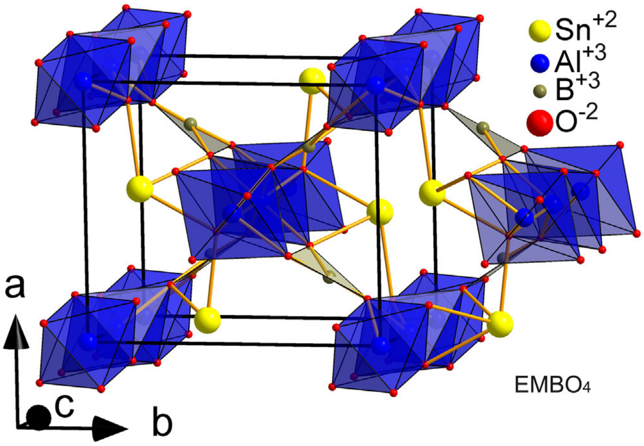

FIGURE 1 Crystal structure of $SnAlBO_4$, showing the constituent AlO_6, SnO_4, and BO_3 coordination.

2 | EXPERIMENTAL

2.1 | Synthesis

A 4:1 mixture of SnO to Sn, stoichiometric amount of M_2O_3 (M = Al, Ga) along with an excess (80%) of B_2O_3 were dried at 473 K overnight, mixed and put into a quartz tube which was also preheated at 1073 K for about 15 h. The mixture was further heated at 473 K for 2 h to reduce absorbed moisture. The internal pressure of the quartz tube was then reduced to 10^{-7} MPa which is higher ($\sim 5 \times 10^{-8}$ MPa)[24] than the theoretical prediction for the phase formation. During the dynamic vacuum process, the tube was sealed. The sealed samples were placed into an oven and heated at 1023 K for 3 days with a cooling and heating rate of 200 K/h to obtain the polycrystalline powders. It is noted that repeated trials guide to the successful synthesis using an excess (80 wt-%) of B_2O_3 which, nevertheless, could lead to the formation of additional amorphous phases identified by solid-state NMR spectroscopy (see later). Moreover, the use of a mixture of SnO and Sn helped suppress the oxidation of Sn^{2+} to Sn^{4+}.[28]

2.2 | X-ray diffraction

XRPD measurements were carried out on a Stoe Stadi MP diffractometer (Stoe & Cie. GmbH, Darmstadt, Germany) using a Debye–Scherrer geometry. Each sample was put into a borosilicate glass capillary of 0.5 mm outer diameter and 0.01 mm wall thickness. Homogeneous X-ray irradiation on the powders was achieved through sample spinning. Ge(111) monochromatized MoKα_1 radiation and a Mythen-1K detector were used. Data were collected at ambient conditions between 3.000° and 85.195° 2θ with a step size of 0.005° and a total data collection time of 477.0 s/step. The fundamental parameter approach, where the fundamental parameters were fitted against a LaB_6 standard material, was applied for the Rietveld refinement using the "Diffrac^{Plus} Topas 6" software (Bruker AXS GmbH, Karlsruhe, Germany). The starting atomic coordinates were taken from the single crystal data of $PbAlBO_4$,[28] where Pb^{2+} was replaced by Sn^{2+} in the asymmetric unit. During the Rietveld refinements, the background, zero-point of the counter, unit-cell parameters, atomic coordinates, isotropic displacement parameters (B), L_{Vol}(IB) as apparent average crystallite size (ACS), and ε_0 as micro-strain (MS) parameters were optimized for the description of the reflection profiles.

2.3 | Spectroscopy

2.3.1 | Fourier transform infrared

Fourier transform infrared (FTIR) data were collected on a Bruker VERTEX 80v spectrometer using the standard KBr method (2 mg sample in 200 mg KBr) in the mid-infrared range between 370 and 4000 cm^{-1}. All IR spectra are plotted in absorption units (a.u.) according to $-\ln(I/I_O)$, where I and I_O refer to transmitted intensity of the sample with KBr and pure KBr discs, respectively. The peaks were fitted using the LabSpec 5 suite (Horiba Jobin Yvon).

2.3.2 | Raman spectroscopy

Raman spectra were recorded on a LabRam ARAMIS (Horiba Jobin Yvon) micro-Raman spectrometer equipped with a laser working at 532 nm and less than 20 mW. The use of a 50× objective (Olympus) with a numerical aperture of 0.75 provides a focus spot of about 0.5 μm diameter when closing the confocal hole to 200 μm. Raman spectra were collected in the range of 85–1500 cm^{-1} with a spectral resolution of approximately 1.2 cm^{-1} using a grating of 1800 grooves/mm and a thermo-electrically cooled CCD detector (Synapse, 1024×256 pixels). The obtained spectra were analyzed with the LabSpec 5 suite (Horiba Jobin Yvon). During the fitting, the position, the line-width, and the line-shape (Gaussian/Lorentzian) are optimized.

2.3.3 | Ultraviolet to visible range spectroscopy

UV/Vis diffuse reflectance spectra were obtained on a Shimadzu UV/Vis spectrophotometer UV-2600 equipped with an ISR-2600 plus two-detector integrating sphere. Barium sulfate powder was used for background reflectance as 100%. Reflectance data were collected in the wavelength range between 190 and 800 nm in steps of 1 nm. The reflectance data was transformed into absorption using the Kubelka–Munk[34] approach. Direct and indirect band gaps were calculated using the Tauc[35,36,37] method and compared with the value obtained from the absorption spectrum fitting (DASF) method[38]. This leads to a full analysis of the band gap transition type and energy combined in the so-called RATD (reflectance–absorbance–Tauc–DASF) analysis.[39,40]

2.3.4 | ^{119}Sn Mössbauer spectroscopy

For ^{119}Sn Mössbauer spectroscopic investigations, a $Ca^{119m}SnO_3$ source with γ-radiation at 23.875 keV was used. A thin palladium foil (thickness 0.05 mm) was placed between the sample and the detector to reduce K X-rays emitted by the source. The measurements were conducted in the usual transmission geometry. The source and the metal tin-(II)-borates were kept at room temperature. The samples were mixed with α-quartz and enclosed in thin-walled PMMA containers. To obtain suitable integral fits for the ^{119}Sn spectra the WinNormos of Igor6 program package[41] was used and graphical editing was done with the program CorelDRAW2017.[42]

2.3.5 | Solid-state NMR spectroscopy

Single pulse ^{11}B and ^{119}Sn NMR spectra were recorded on a 600 MHz Agilent spectrometer (Agilent Technologies, Inc., CA, USA) using a 3.2 mm triple resonance magic angle spinning (MAS) NMR probe with spinning speeds of 15 kHz (^{11}B) and 12–17 kHz (^{119}Sn) kHz. A ^{27}Al single pulse NMR spectrum was recorded on a 950 MHz Avance spectrometer (Avance III 950 HD) using a 2.5 mm triple resonance magic angle spinning (MAS) NMR probe with spinning speeds of 30 kHz. The ^{11}B and ^{27}Al NMR spectra were recorded with a short, hard pulse (< 10°), whereas the ^{119}Sn spectrum was recorded with a 45° pulse. The relaxation delay was optimized on each sample. For instance, a 90° (180°) pulse of 3.6 (7.1) μs was used with a relaxation delay of 0.2 s. As such, ca. 2, 1, and 300–500 s relaxation delay were used, respectively, for the ^{11}B, ^{27}Al, and ^{119}Sn NMR spectra. SnO_2 ($\delta_{iso}(^{119}Sn) = -603$ ppm), $B(OH)_3$($\delta_{iso}(^{11}B) = 19.6$ ppm), and a 1 M aqueous solution of aluminum chloride ($\delta_{iso}(^{27}Al) = 19.6$ ppm) were used as external reference for ^{119}Sn, ^{11}B, and ^{27}Al MAS NMR, respectively. The spectra were analyzed with ssNake.[43]

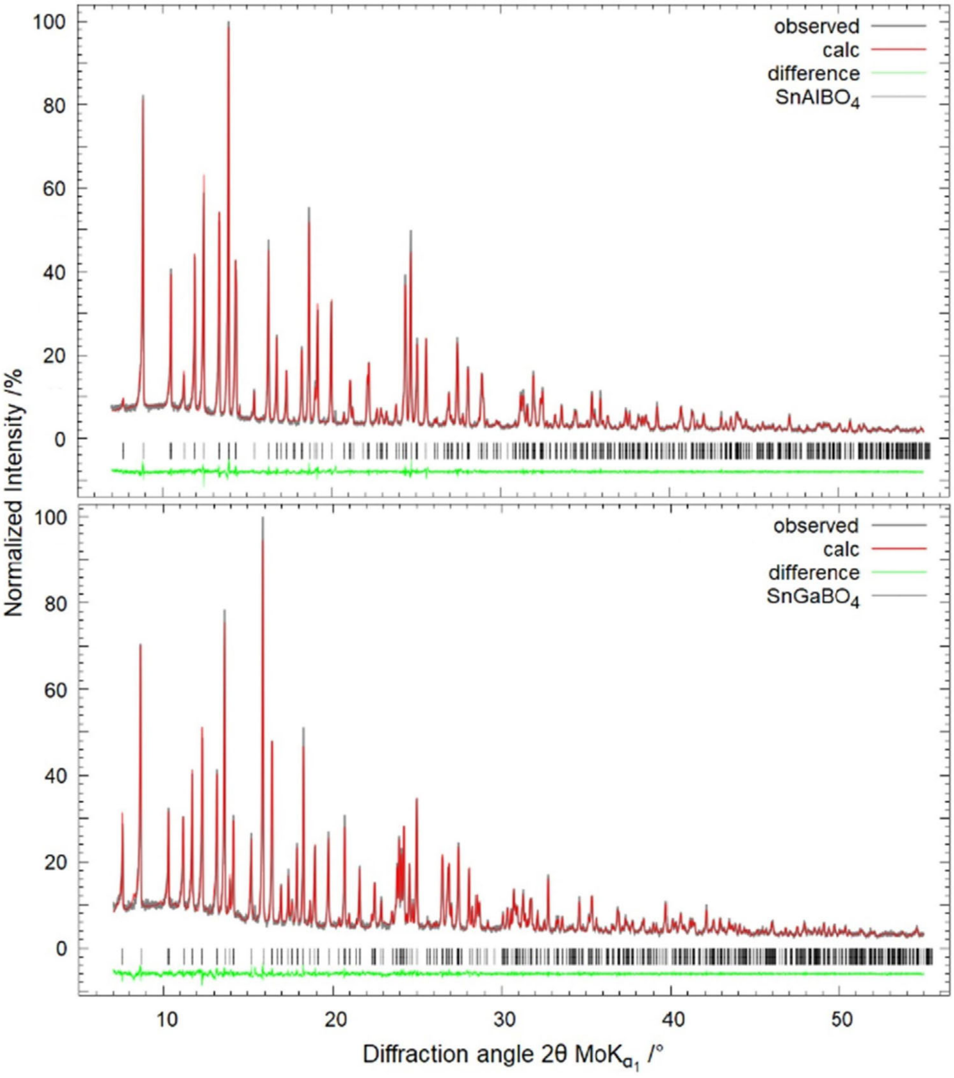

FIGURE 2 Rietveld refinement plot of $SnAlBO_4$ and $SnGaBO_4$ with calculated (red) and observed (grey) patterns, difference curve (green), Bragg peaks of $SnGaBO_4$ (black), showing the crystalline sample purity of $SnAlBO_4$ and $SnGaBO_4$.

3 | RESULTS AND DISCUSSION

3.1 | Structure

The formation of $SnAlBO_4$ and $SnGaBO_4$ crystallized in the space group *Pnam* is confirmed by XRPD data Rietveld refinements, as shown in Figure 2. The crystal structure, metric parameters, ACS, and MS are listed in Tables 1 and 2. All lattice parameters are slightly larger for $SnGaBO_4$ than those of $SnAlBO_4$ as the ionic radius of Al^{3+} (53.5 pm) is substantially smaller than that of Ga^{3+} (62.0 pm).[44] Indeed, the larger cell volume of $SnGaBO_4$ (336.4(1) $\times 10^6$ pm^3) can be compared to 317.3(1) $\times 10^6$ pm^3 of $SnAlBO_4$. The *a*- and *b*-lattice parameters are only about 1% larger, whereas the *c*-lattice parameter is about 1% smaller than theoretically predicted.[24] It is interesting to note that the *a*-lattice parameters are ~ 4% larger for $SnMBO_4$ than for $PbMBO_4$. In contrast, the *b*-lattice parameters are ~ 4% smaller for $SnMBO_4$ than those of $PbMBO_4$. The respective *c*-lattice parameters for both $SnMBO_4$ and $PbMBO_4$ remain nearly identical to each other, leading to a volume increase of ~ 1% for the Pb-containing compounds.[25,26] A correlation between the *a*- and *b*-lattice parameters is a common structural effect for the orthorhombic members of the mullite-type family,[17] where the increase in the *b*-lattice parameter occurs with a concomitant contraction of the *a*-lattice parameter.[24] Such a correlative change between *a*- and *b*-lattice parameters can be explained in terms of the strength and orientation of the stereochemically activity of the $5s^2$ and $6s^2$ LEPs (E in geometry) of Sn^{2+} and Pb^{2+}, respectively.

TABLE 1 X-ray powder data (Rietveld refined parameters) of $SnAlBO_4$ and $SnGaBO_4$ along with average crystallite size (ACS) and microstrain (MS).

Empirical formula	$SnAlBO_4$	$SnGaBO_4$
Formula weight (g/mol)	220.499	263.240
Temperature (K)	296(2)	296(2)
Instrument, radiation	Stoe MP, Mo $K_{\alpha1}$	
Geometry	Debye-Scherrer, glass capillary	
Crystal system	orthorhombic	
Space group	*Pnam*	*Pnam*
a (pm)	720.8(1)	728.1(1)
b (pm)	774.6(1)	791.2(1)
c (pm)	568.3(1)	583.9(2)
V (10^6 pm^3)	317.3(1)	336.4(1)
ACS (nm)	477.31(4)	403.03(5)
MS (%)	0.229(2)	0.178(2)
D_{calc} (g/cm^3)	4.613(1)	5.199(4)
R_{wp} (%)	10.2	8.3
χ^2 (%)	4.8	2.7
Goodness-of-fit (GOF) on F^2	1.39	1.40

TABLE 2 Crystal structure parameters of $SnAlBO_4$ and $SnGaBO_4$.

$SnAlBO_4$					
Atom	***Pnam***	***x***	***y***	***z***	***B*** **(10^4 pm)^2**
Sn1	4*c*	0.0932(18)	0.3626(18)	¼	0.25(2)
Al1	4*a*	0	0	0	0.25(11)
B1	4*c*	0.2080(4)	0.7910(3)	¼	3.00(7)
O11	4*c*	0.4030(16)	0.3870(13)	¼	0.3(2)
O12	4*c*	0.1638(15)	0.9079(14)	¼	0.3(3)
O2	8*d*	0.3284(11)	0.6913(11)	0.0412(15)	0.3(2)
$SnGaBO_4$					
Atom	***Pnam***	***x***	***y***	***z***	***B*** **(10^4 pm)^2**
Sn1	4*c*	0.0954(18)	0.36080(19)	¼	0.7(3)
Ga1	4*a*	0	0	0	0.50(4)
O12	4*c*	0.138	0.8000(9)	¼	0.40(5)
O11	4*c*	0.384041(14)	0.3730	¼	0.30(2)
B1	4*c*	0.204(17)	0.9120(2)	¼	0.43.00(4)
O2	8*d*	0.3499(15)	0.69217(9)	0.05(10)	0.27(17)

The interatomic bond distances and angles are given in Table 3. The SnO_4E pyramid in $SnAlBO_4$ is highly distorted ($|\Phi| = 1.87(2) \times 10^{-5}$) due to significant difference of the Sn–O distances between (217.7(5) pm and 233.4(7) pm). On the other hand, the WLE of the SnO_4E pyramid in $SnGaBO_4$ is higher ($|\Phi| = 2.30(3) \times 10^{-5}$) for bond distances of 215.5(3) pm and 234.9(3) pm. Indeed, the larger GaO_6 octahedra leave less space (Figure 1) for the SnO_4 pyramid for a greater spatial extension of the LEPs, leading to a higher distortion in SnO_4E. For comparison, the WLE of the PbO_4E pyramid in $PbAlBO_4$ and $PbGaBO_4$ are found to be $|\Phi| = 1.93(2) \times 10^{-5}$ and $1.83(2) \times 10^{-5}$, respectively.[45] Gogolin et al.,[19] however, obtained a slightly higher distortion ($|\Phi| = 2.02 \times 10^{-5}$) in $PbAlBO_4$. The AlO_6 octahedra possess three different Al–O distances (2 × 185.2(3), 2 × 190.9(2), and 2 × 198.1(2) pm), resulting in an average Al–O bond distance of 191.4(2) pm which is comparable to those in sillimanite,[46] mullite-type $PbMBO_4$,[26] and the corresponding calculated values.[24] Similarly, the Ga–O bond distances in the GaO_6 octahedra are also comparable to those of the respective Ga-containing phases. The B–O bond lengths in the BO_3 coordination hardly change irrespective of the chemical composition (Table 3), indicating the usual rigidity of the planar BO_3 group. Bond valence calculations for boron show that the cations keep their oxidation state close to the respective formal value (Table 3) and other O8-compounds. The tin cations in both phases are slightly over-bonded, which is not surprising due to the interplay between the MO_6 octahedral distortion and the LEP-effect in SnO_4E coordination.

3.2 | Infrared and Raman spectroscopy

Correlative internal vibrational modes between free ion symmetry (for an isolated species), site symmetry, and factor group symmetry for each MO_x group in the host unit cell are listed in Table S3. In interpreting the vibrational spectral features of a given crystalline solid, the site symmetry (Wyckoff site) approach eventually resembles an isolated (free) molecule. On the other hand, the factor group approach considers the collective atomic motions available in the sampling volume of the crystals. As such, a low-resolution spectrum may be assigned using the site symmetries. However, the high-resolution fine features, as shown in the non-polarized Raman and IR spectra stack plots in Figure 3, require factor group symmetry analysis. Both the mullite-type compounds belong to the factor group symmetry of D_{2h} (Table S1),and the internal modes are split from those of the site symmetry group into different regions for the subgroups. Factor analysis results in 84 zone center vibrational modes, as listed in Table S1. Of them, 36 are Raman active ($11A_g + 7B_{1g} + 11B_{2g} + 7B_{3g}$), 35 are IR active ($13B_{1u} + 9B_{2u} + 13B_{3u}$), 3 ($B_{1u} + B_{2u} + B_{3u}$) belong to acoustic mode, and 10 A_u modes are optically inactive (silent modes).

The Raman spectra of $SnMBO_4$ are shown in Figure 3 and the deconvoluted peak maxima listed in Table S2. The technical limitations and low intensity of some bands

TABLE 3 Comparative bond distances [pm], and bond valence sum (BVS) [v.u.], Wang–Liebau eccentricity parameter (WLE) [$|\Phi| \times 10^{-5}$] of the constituent elements in $SnMBO_4$ and $PbMBO_4$ compounds.

Compound	Sn–O	M–O	B–O	BVS (Sn, Pb)	BVS (Al, Ga)	BVS (B)	WLE (SnO_4, PbO_4)	Ref.
$SnAlBO_4$	218(5) ×2 233(3) ×1 222(2) ×1	191(5) ×2 198(4) ×2 185(4) ×2	133(8) ×1 141(3) ×2	2.07(1)	2.84(3)	2.90(2)	1.87(2)	This study
$SnAlBO_4$	222 ×2 228 ×1 231 ×1	185 ×2 191 ×2 196 ×2	137 ×1 138 ×2	1.91(1)	2.87(1)	2.95(4)	2.88(1)	24
$SnGaBO_4$	216(3) ×2 219(4) ×1 234(3) ×1	196(3) ×2 193(2) ×2 194(2) ×2	150(1) ×2 139(1) ×1	2.15(3)	3.37(3)	2.97(2)	2.30(3)	This study
$SnGaBO_4$	225 ×2 229 ×1 230 ×1	192 ×2 199 ×2 203 ×2	167 ×1 138 ×2	1.83(4)	3.05(3)	2.25(5)	2.58(1)	24
$PbAlBO_4$	233 ×2 230 ×1 235 ×1	182 ×2 192 ×2 199 ×2	137 ×1 138 ×2	2.25	3.04	2.97		26
$PbAlBO_4$							1.93(2)	45
$PbAlBO_4$							2.02	19
$PbGaBO_4$				1.83 (6)	3.04 (8)	2.92 (21)		25
$PbGaBO_4$							1.83(2)	45
$PbGaBO_4$	235 ×2 232 ×1 237 ×1	189 ×2 201 ×2 207 ×2	137 ×1 139 ×2					25
$PbMnBO_4$	243 ×2 235 ×1 241 ×1	189 ×2 199 ×2 223 ×2	136 ×1 140 ×2	1.79	3.06	3.00		23
$PbFeBO_4$	237 ×2 232 ×1 237 ×1	192 ×2 204 ×2 210 ×2	139 ×1 138 ×2	2.08	3.02	2.93		23
$PbCrBO_4$	239 ×2 229 ×1 231 ×1	194 ×2 199 ×2 203 ×2	137 ×1 140 ×2	2.15	2.98	2.88		23

reduce the number of modes to be observed.[24] Based on calculated phonon density of states (PDOSs) of $SnAlBO_4$ and $SnGaBO_4$ it has been shown that the vibrational contribution can be divided into three distinct ranges,[24] which is also observed in the experimental IR and Raman spectra of $PbAl_{1-x}Mn_xBO_4$[45] and $PbFeBO_4$:[47] (I) low-frequency range between 40 and 300 cm^{-1}, (II) mid-range from 300 to 600 cm^{-1}, and (III) high-frequency range above 700 cm^{-1}, respectively, for the SnO_4, MO_6, and BO_3 groups. The Raman and IR fit component peak maxima are listed in Table S2, the Raman fit of $SnAlBO_4$ is shown in Figure 4, for $SnGaBO_4$ in Figure S1. The characteristic Raman shifts around 121 (B_{1g}), 476 (E_g), 635 (A_{1g}), and 776 cm^{-1} (B_{2g}) for SnO_2,[48,49] and 115 cm^{-1} (B_{1g}), and 211 cm^{-1} (A_{1g}) for SnO[50] are not observed in either $SnAlBO_4$ nor $SnGaBO_4$.[51] An isolated planar BO_3 group confirms the D_{3h} symmetry (Table S3) characterized by nonplanar nondegenerate (A''_2, ν_2), antisymmetric degenerate (E', ν_3), and deformational degenerate (E', ν_4) vibrational modes. The band at 976(1) cm^{-1} can be assigned to the B–O symmetric stretching (A_g) of the BO_3 group of $SnAlBO_4$, which is shifted down to 962(1) cm^{-1} for $SnGaBO_4$. An additional band resolved at 950(1) cm^{-1} can be assigned to the B_{2g} mode (BO_3) for the Ga-containing sample. A Davydov splitting[52] of the ν_3 mode either to sharp components or to a broadening of the spectral intensity can be seen between 1200 and 1400 cm^{-1} both in the Raman (B_{1g}, B_{3g}) and FTIR (A_u, B_{2u}) spectra. The sharp intense Raman band at 1225(1) cm^{-1} for $SnAlBO_4$ shifts to 1209(1) cm^{-1} for $SnGaBO_4$.

The IR spectra of $SnMBO_4$ are shown in Figure 3. Although the factor group analysis allows for 38 IR modes,

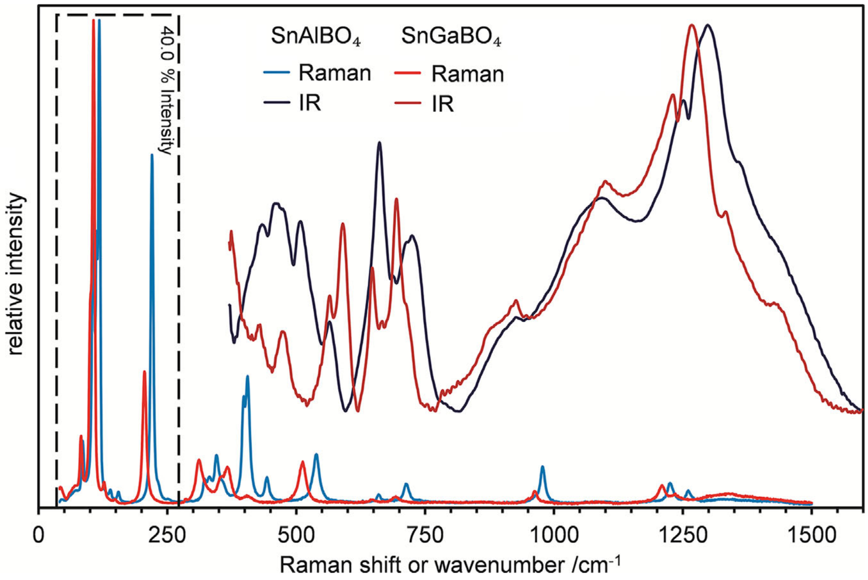

FIGURE 3 Raman and IR spectra of $SnAlBO_4$ and $SnGaBO_4$.

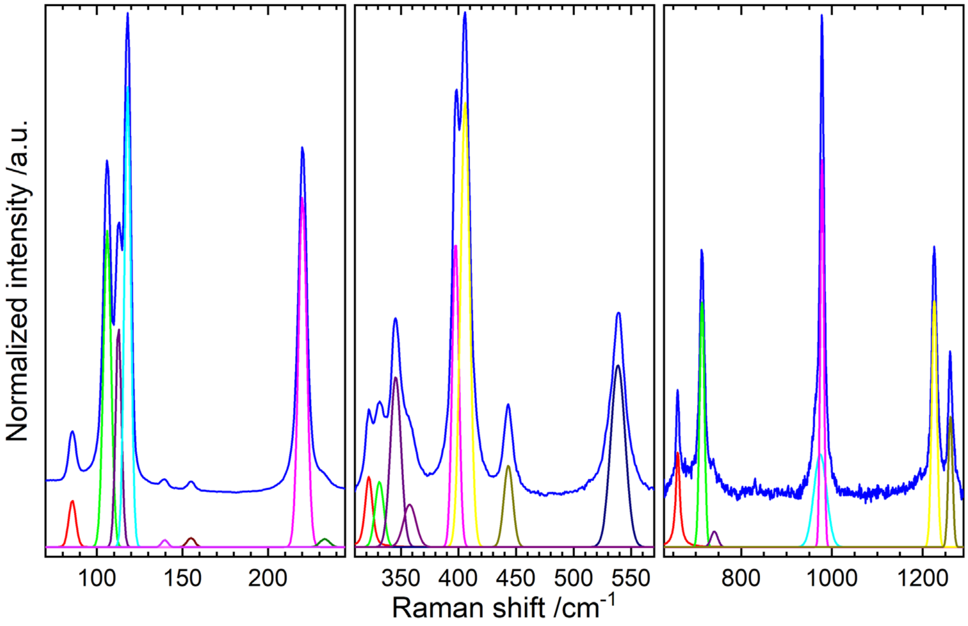

FIGURE 4 Representative fitted Raman spectra of $SnAlBO_4$ segmented into three regions for better clarity with observed data (blue) and fitted peaks (colored).

each spectrum requires only 25–32 bands within the measured region (Table S1) due to strong overlapping between the absorbed regions. Curti et al.[24] demonstrated that the Raman spectral intensity around 1000 cm^{-1} is exclusively contributed by the vibrations of O11, O12, and O2, which must be absent in the respective IR spectra due to lack of a dipole moment for a purely symmetric BO_3 group. However, the presence of IR bands at 922 and 957 cm^{-1} for $SnAlBO_4$ and at 933 cm^{-1} for $SnGaBO_4$ (Figure 3) confirms that the free ion D_{3h} symmetry of BO_3 reduces to factor group C_s symmetry driven by the local distortion. Indeed, we observed a slight deviation (10(3) pm) between two types of B–O bond lengths in the O3-scalene triangle, where the B-atom locates slightly (2(1) pm) above the O3 plane. The substitution of tin in hulsite ($(Fe^{2+},Mg)_2(Fe^{3+},Sn)BO_5$)[53] lowers the BO_3 symmetry, leading to appearance of a ν_1 mode at 940 cm^{-1}. The bands at 813.0(5), 881.9(2), 921.8(7), and 957.2(3) cm^{-1} can be assigned to the C_s symmetry. Moreover, the splitting of each of the ν_1 and ν_3 modes in the IR spectra can be explained by the ^{10}B and ^{11}B isotopic ratio and the integrated intensities at 1231(8) and 1248(1) cm^{-1} result in 87(3)% and 13(3)% of ^{11}B and ^{10}B, respectively, which remains close to the natural abundance of boron

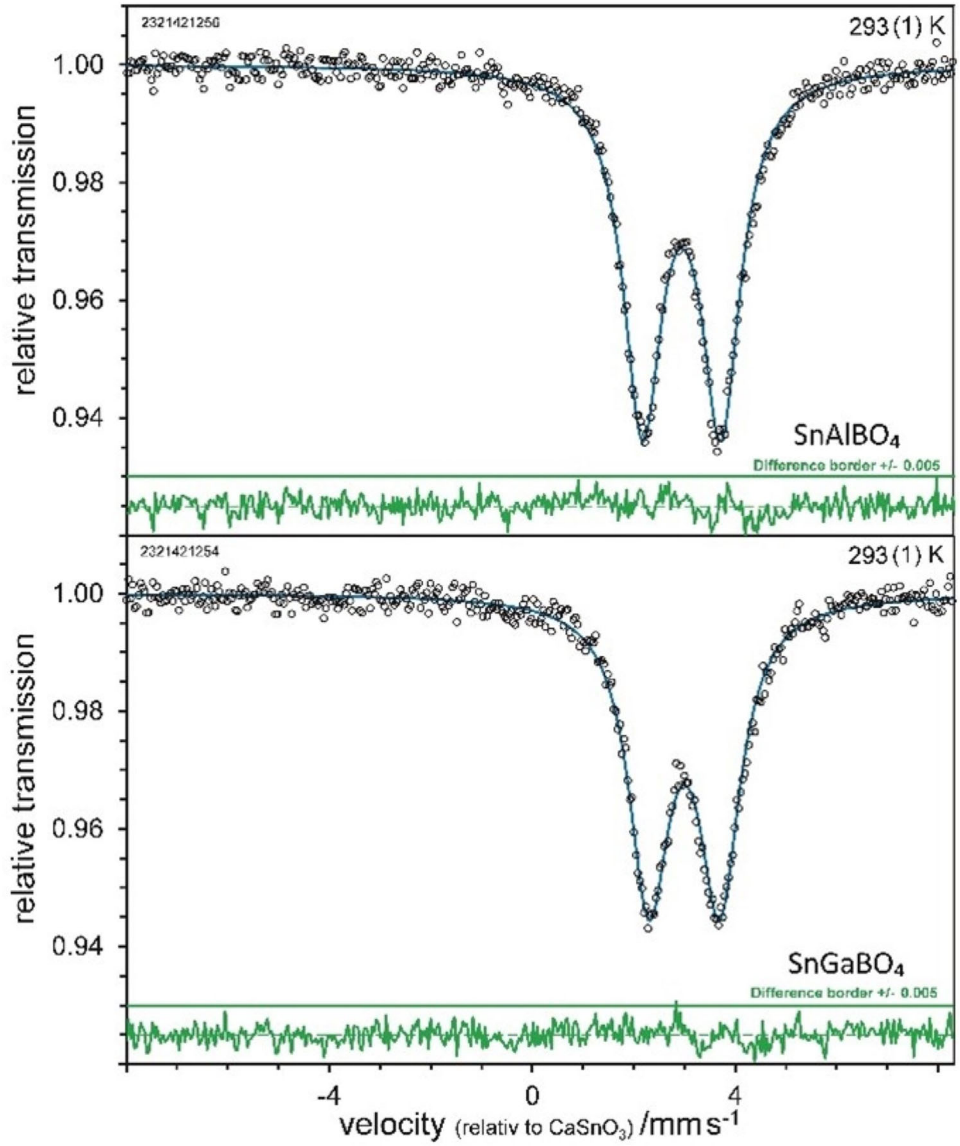

FIGURE 5 Experimental (open circles) and simulated (blue lines) ^{119}Sn Mössbauer spectra with their difference curves.

(^{10}B: 18%–19%; ^{11}B: 81%–82%[54]). The bands at 729(2), 740(1), and 760(2) cm^{-1} correspond to the ν_2 modes of the BO$_3$ group. An unambiguous assignment of the ν_4 modes of the BO$_3$ group is difficult, as they overlap with the range of the M–O asymmetric stretching modes for the MO$_6$ octahedra. Thus, the M–O stretching and O–M–O bending modes (300–650 cm^{-1}) of the MO$_6$ cannot be separated.

In both the Raman and IR spectra, the global redshift is associated with the quasi-harmonic nature of the larger unit cell of SnGaBO$_4$ compared to SnAlBO$_4$ (Figure 3). The nonlinear shift for a given band can be explained in terms of the corresponding local MO$_x$ geometry and force constant. For instance, the Sn–O bond distance in the aluminum-containing compound lies between 217.7(5) and 233.4(7) pm, whereas it is between 215.5(3) and 234.9(3) pm for the Ga-containing phase. Although Sn^{2+} locates with a higher asymmetry in SnO$_4$, the low-frequency Raman bands in SnAlBO$_4$ are clearly separable, while the corresponding bands partly merge for SnGaBO$_4$.

3.3 | Mössbauer spectroscopy

^{119}Sn Mössbauer spectroscopy is a sensitive method to obtain information on the valence and the local environment of tin nuclei. The important parameter manifesting the tin valence is the isomer shift. During the different systematic, ^{119}Sn Mössbauer spectroscopic studies of ionic, covalent, intermetallic, and tin coordination compounds, different scales have been used that depend on

TABLE 4 Fitting parameters of ^{119}Sn Mössbauer spectroscopic measurements of $SnAlBO_4$ and $SnGaBO_4$ at room temperature.

Parameter	$SnAlBO_4$	$SnGaBO_4$
δ (mm/s)	2.94(1)	3.00(1)
ΔE_Q (mm/s)	1.54(1)	1.40(1)
Γ (mm/s)	0.92(1)	0.97(1)
n_s	1.22(1)	1.24(1)
n_p	0.79(2)	0.76(1)
(n_x+n_y)	0.26(1)	0.27(2)
n_z	0.52(1)	0.49(2)

Note: δ, isomer shift; ΔE_Q, electric quadrupole splitting; Γ, experimental line width.

the Mössbauer source applied for the experiments. The early work by Lees and Flinn[55] used ^{119m}Sn in Mg_2Sn. However, nowadays $Ca^{119m}SnO_3$ is the common source material for ^{119}Sn Mössbauer spectroscopic experiments. The isomer shift values are referenced to this source also earlier used by Lippens.[56] Suitable reference materials for tetravalent and divalent tin in oxidic matrices are SnO_2 (the electronic situation is very close to the source material) at 0 mm s^{-1}/divalent SnO at 2.7 mm s^{-1}.[56] The isomer shifts lie far apart, allowing for a clear distinction between tin valences. The room temperature ^{119}Sn Mössbauer spectra of the $SnAlBO_4$ and $SnGaBO_4$ samples are presented in Figure 5 along with transmission integral fits, and the fitting parameters are summarized in Table 4. In agreement with the crystal structure, we could well reproduce both spectra with single signals at isomer shifts of δ = 2.93(1) mm s^{-1} ($SnAlBO_4$) and δ = 3.00(1) mm s^{-1} ($SnGaBO_4$), which are slightly higher than that observed for SnO, indicating slightly increased *s*-electron density at the tin nuclei. The lone-pair character at Sn^{2+} is evident by pronounced quadrupole splitting of 1.55(1) and 1.40(1) mm s^{-1} for $SnAlBO_4$ and $SnGaBO_4$, respectively. The experimental line width parameters (Table 4) are in the usual range. So far, only few data are available on ^{119}Sn Mössbauer spectroscopic studies on tin borates. An interesting Sn(II) borate is β-SnB_4O_7;[57] which, however, exhibits a much higher isomer shift value of 4.09(1) mm s^{-1} and thus distinctly higher *s*-electron density at the tin nuclei as compared to the quaternary borates discussed here. Samples prepared at different batches exhibit, however, a slightly different Sn^{2+} doublet at 3.01(1) and 3.03(3) mm/s for $SnAlBO_4$ and $SnGaBO_4$, respectively. A low-intense signal observed at −0.1(3) mm/s is assigned to the tiny impurity of SnO_2 along with $SnGaBO_4$, as depicted in Figure S3. The difference of the ^{119}Sn Mössbauer spectral values between these two phases is markedly appeared in the quadrupole splitting parameters. The lower value of 1.40(1) mm s^{-1} points to a less active LEP character in $SnGaBO_4$. For a better quantification, we compare the effective 5*s* and 5*p* electron population of Sn(II) in both compounds, which can be determined from the following relationship:[58]

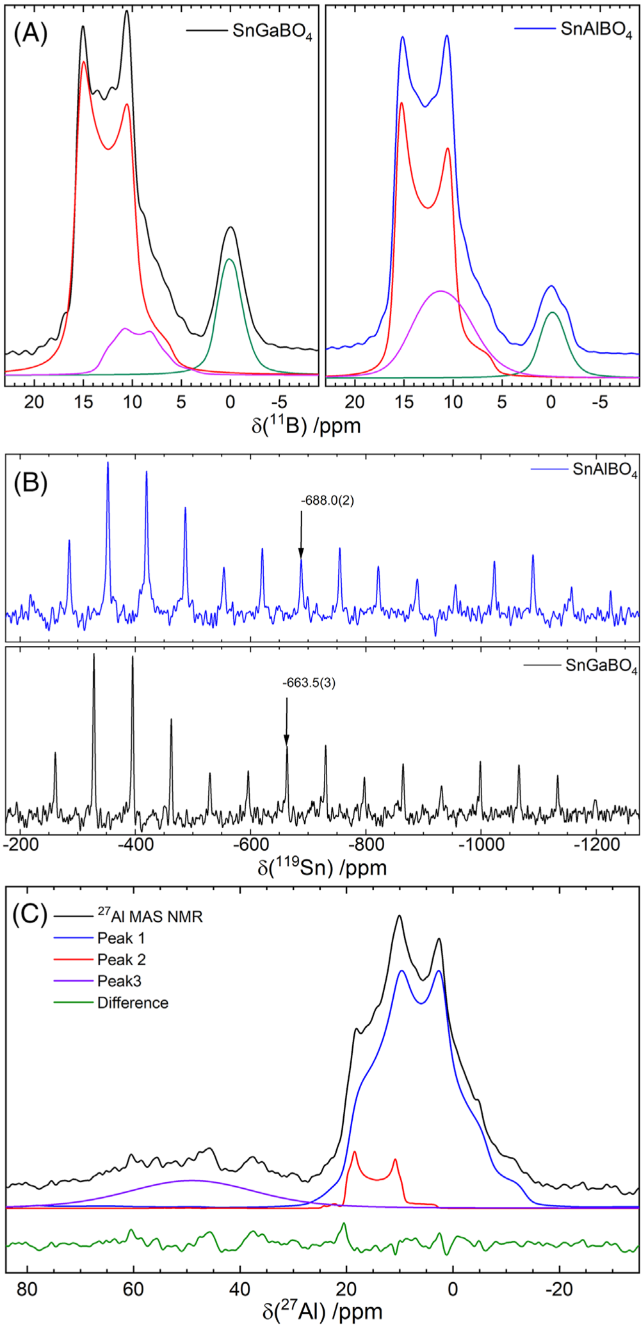

FIGURE 6 ^{11}B MAS NMR spectra (A) and ^{119}Sn MAS NMR (B) of $SnAlBO_4$ and $SnGaBO_4$, and ^{27}Al MAS NMR spectrum of $SnAlBO_4$, along with simulated spectra using the values reported in Tables 5 and 6 as well as the text. MAS, magic angle spinning.

$$\delta = \left(3.10n_s - 0.2{n_s}^2 - 0.17n_sn_p - 0.38\right)\ \ \text{mm s}^{-1}, \quad (1)$$

where n_s and n_p are the numbers of the *s* and *p* electrons. Furthermore, the quadrupole splitting parameter is

TABLE 5 Fitted isotropic chemical shift (δ), quadrupole coupling constant (C_Q), anisotropy parameter (η), integral, Lorentzian (L), and Gaussian (G) broadening obtained from ^{11}B MAS NMR spectra (Table 6c).

	δ (ppm)	C_Q (MHz)	H	Integral (%)	L (Hz)	G (Hz)
$SnAlBO_4$	1.6(2)	1.6(1)	0.5(2)	10(1)	248.9(2)	149.2(1)
	15.1(3)	2.4(3)	0.3(1)	28(1)	266.3(3)	677.7(2)
	17.3(1)	2.6(3)	0.1(2)	62(1)	123.5(2)	123.0(3)
$SnGaBO_4$	1.8(1)	1.6(6)	0.5(2)	7(2)	231.7(2)	10.57(1)
	13.6(2)	2.4(4)	0.4(1)	11(3)	166.0(1)	0
	17.1(1)	2.6(1)	0.1(1)	82(1)	212.7(4)	119.0(2)

related to the populations n_x, n_y, and n_z of the p orbitals[59] according to the expression:

$$\Delta E_Q = 4.0\left(n_z - 0.5\left(n_x + n_y\right)\right) \text{ mm s}^{-1} \quad (2)$$

$$n_p = n_z + n_x + n_y \quad (3)$$

and considering that $n_s + n_p = 2$ for the Sn^{2+}. The resulting values are listed in Table 4. The calculated populations indicate that the 5s^2 LEPs keep a mixed (s–p) character instead of pure s-character. This is consistent with the Wang–Liebau hypothesis for Sn^{2+} phases[60] and an increased bonding power. This is also supported by the isomer shift values, which are lower than that of a free Sn^{2+} cation (5s^2).[56] Plotting the ^{119}Sn Mössbauer spectroscopic data of many ionically and covalently bonded Sn(II) compounds[55,58] shows a clear correlation between the isomer shift and the quadrupole splitting parameters, where the data of both $SnAlBO_4$ and $SnGaBO_4$ well fit within a broad locus of the linear trend, as shown in Figure S2.

3.4 | Solid-state NMR spectroscopy

To further probe the local environments of boron, tin, and aluminum ^{11}B, ^{119}Sn, and ^{27}Al solid-state NMR spectra were recorded. The ^{11}B MAS NMR spectra are shown in Figure 6. Each spectrum can be analyzed using three different ^{11}B sites, as summarized in Table 5. The chemical shifts at $\delta(^{11}B) = 15.1(3)$ ppm and 13.6(2) ppm observed for $SnAlBO_4$ and $SnGaBO_4$, respectively, are assigned to B_2O_3. The amount of anhydrous boric acid is estimated as 28(2)% and 11(1)% in $SnAlBO_4$ and $SnGaBO_4$, respectively, which is ascribed to the use of an 80(1)% stoichiometric excess. The intense signals at 17.3(1) and 17.1(1) ppm are assigned to the planar BO_3 groups in $SnAlBO_4$ and $SnGaBO_4$, respectively, both of which lie close to the corresponding shifts at about 17(1) ppm in $Al_2B_4O_9$.[61] The chemical shifts of 1.6(2) ppm (10%) and 1.8(1) ppm (7%), which have a weaker quadrupolar interaction, for $SnAlBO_4$ and $SnGaBO_4$, respectively, are assigned to BO_4[61]—most likely present in the amorphous phases, which was also evident as an apparent amorphous hump in the XRPD diffraction patterns.

TABLE 6 Fitted chemical shift (δ), quadrupole coupling constant (C_Q), anisotropy parameter (η), and integral in percentage obtained from ^{27}Al MAS NMR spectra.

δ (ppm)	C_Q (MHz)	η	Integral
20.6(1)	11.5(2)	0.5(2)	78(2)%
22.1(1)	8.8(1)	0.2(6)	7(1)%
51.5(1)	5.1(2)	0.2(1)	15(1)%

The ^{119}Sn MAS NMR spectra exhibit resonances at $\delta(^{119}Sn) = -688.0(2)$ and $-663.5(3)$ ppm for $SnAlBO_4$ and $SnGaBO_4$, respectively, indicating to the single environment for tin (Figure 6). The chemical shift values are comparable to those reported for blue-black SnO[62] and $SnBr_2$[63] with similar Sn(II)-coordination. The higher chemical shift value implies that the Sn-site is more shielded in $SnAlBO_4$ than in $SnGaBO_4$. These results support both the XRPD and the Mössbauer spectroscopic findings. Sn in both compounds is influenced by a significant chemical shift anisotropy, $\delta_\sigma = -704(3)$ ppm and $-716(3)$ ppm for $SnAlBO_4$ and $SnGaBO_4$, respectively, which is characteristic for Sn^{2+}. Moreover, for both compounds the asymmetry parameter is around 0.15, indicating close to the axial symmetry.

Simulation of the ^{27}Al MAS NMR spectrum (Figure 6) requires four ^{27}Al sites with large second-order quadrupole line shape, as summarized in Table 6. The broad feature from 78(3) to 24(2) ppm spans chemical shifts range for AlO_4[61,64] and AlO_5,[61] respectively. These signals are assigned the amorphous phases in the sample. The minor component (7(1)%) observed at 22.1(1) ppm is small polymeric aluminum borates with AlO_6 octahedra, where the coherence length lies below the XRPD detection limit. The intense signal centered at 20.6(1) ppm for $SnAlBO_4$ belongs to Al in the octahedral coordination.[65] Comparing the ^{27}Al chemical shifts in mullite,[61] sillimanite,[66] and other mullite-type compounds,[67] aluminum in $SnAlBO_4$ is found to be highly shielded due most probably to spatial requirements of the LEPs.

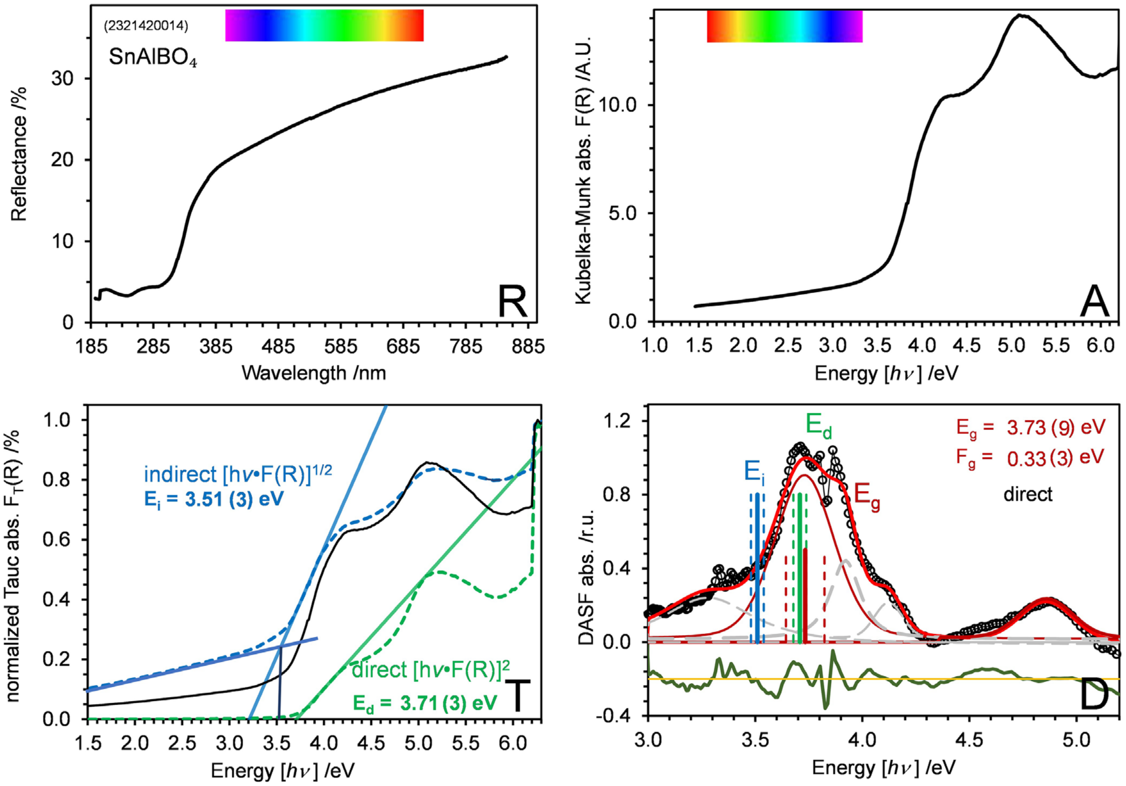

FIGURE 7 UV/Vis spectrum of $SnAlBO_4$ (top left), Kubelka–Munk graph (top right), normalized Tauc plot (bottom left), and normalized DASF plot (bottom right). DASF, absorption spectrum fitting.

3.5 | UV/Vis spectroscopy

For the UV/Vis data, the nature of transition can establish using the RATD analysis method,[39] as shown in Figure 7 for $SnAlBO_4$ and Figure S4 for $SnGaBO_4$. Both samples result in a direct band gap. The required transition energy of $SnAlBO_4$ is obtained at 3.73(9) eV which lies close to the calculated value of 3.66(4) eV.[24] On the other hand, $SnGaBO_4$ exhibits a transition energy of 3.21(4) eV which significantly differs from the calculated one of 4.54(6) eV.[24] The obtained band gap values categorize the samples to be wide band gap semiconductors (3–4 eV). Indeed, the beige color of the samples can be explained as noticeable absorbance.

4 | CONCLUSION

Despite the challenges in solid-state synthesis of Sn(II) oxides due to the high-temperature susceptibility of the oxidation of Sn^{2+} into Sn^{4+}, $SnAlBO_4$ and $SnGaBO_4$ as two new members of mullite-type O8-phases were successfully produced. Comparative crystal chemical aspects are discussed between isostructural compounds $PbMBO_4$ and $SnMBO_4$ in terms of the stereochemical activity of $6s^2$ and $5s^2$ LEPs of Pb^{2+} and Sn^{2+} cation, respectively. Indeed, the crystal structural features are less influenced by the respective LEPs between $SnAlBO_4$ and $SnGaBO_4$ than that of Al^{3+} and Ga^{3+} cationic radii. Nevertheless, the influence of the LEP is stronger in the aluminum than in the gallium phase. The bulk and local structural features are complemented by Raman, IR, Mössbauer, and solid-state NMR spectroscopies. The electronic band gaps obtained from the UV/Vis diffuse reflectance suggest that both $SnAlBO_4$ and $SnGaBO_4$ are high band gap semiconductors.

ACKNOWLEDGMENTS

We gratefully thank the German science foundation (Deutsche Forschungsgemeinschaft, DFG) under grant number GE1981/14-1 for the financial support.

Open access funding enabled and organized by Projekt DEAL.

ORCID

Sarah Wittmann https://orcid.org/0000-0003-1404-3434
Mohammad Mangir Murshed https://orcid.org/0000-0002-9063-372X
Vitaliy Bilovol https://orcid.org/0000-0002-3363-1840
Aylin Koldemir https://orcid.org/0009-0004-3819-3853

Rainer Pöttgen https://orcid.org/0000-0003-0962-279X
Ulla Gro Nielsen https://orcid.org/0000-0002-2336-3061
Thorsten Michael Gesing https://orcid.org/0000-0002-4119-2219

REFERENCES

1. Curti M, Kirsch A, Granone LI, Tarasi F, López-Robledo G, Bahnemann DW, et al. Visible-light photocatalysis with mullite-type $Bi_2(Al_{1-x}Fe_x)_4O_9$: striking the balance between bandgap narrowing and conduction band lowering. ACS Catal. 2018;8(9):8844–55.
2. Ďurovic S. Isomorphism between sillimanite and mullite. J Am Ceram Soc. 1962;45(4):157–61.
3. Fischer RX, Schneider H. Crystal chemistry of borates and borosilicates with mullite-type structures: a review. Eur J Mineral. 2008;20(5):917–33.
4. Beran A, Libowitzky E, Burianek M, Mühlberg M, Pecharromán C, Schneider H. Infrared and Raman spectroscopy of mullite-type $Bi_2Ga_4O_9$. Cryst Res Technol. 2008;43(11):1230–39.
5. Schneider H, Eberhard E. Thermal expansion of Mullite. J Am Ceram Soc. 1990;73(7):2073–76.
6. Lacks DJ, Hildmann B, Schneider H. Effects of disorder in mullite: molecular dynamics simulation and energy landscape analysis. Phys Rev B. 2005;72(21):214305.
7. Ren Y, Dai F-Z, Xiang H, Wang X, Sun L, Zhou Y. Mechanical and thermal properties of light weight boron–mullite Al_5BO_9. J Am Ceram Soc. 2020;103(10):5939–51.
8. Schneider H, Komarneni S. Mullite. Weinheim: Wiley;2005.
9. Mangir Murshed M, Mendive CB, Curti M, Šehović M, Friedrich A, Fischer M, et al. Thermal expansion of mullite-type $Bi_2Al_4O_9$: a study by X-ray diffraction, vibrational spectroscopy and density functional theory. J Solid State Chem. 2015;229:87–96.
10. Gatta GD, Rotiroti N, Fisch M, Armbruster T. Stability at high pressure, elastic behavior and pressure-induced structural evolution of "Al_5BO_9", a mullite-type ceramic material. Phys Chem Miner. 2010;37(4):227–36.
11. Fielitz P, Borchardt G, Burianek M, Ottinger J, Muhlberg M, Gesing TM, et al. Oxygen-18 tracer diffusion in nominally undoped and Sr-doped single crystals of mullite-type $Bi_2Ga_4O_9$. Solid State Ionics. 2012;221:40–42.
12. Ohmann S, Fielitz P, Dörrer L, Borchardt G, Gesing TM, Fischer RX, et al. Electrical conductivity of mullite-type $Bi_2Al_4O_9$ ceramics in air. Solid State Ionics. 2012;211:46–50.
13. Schneider H, Fischer RX, Gesing TM, Schreuer J, Mühlberg M. Crystal chemistry and properties of mullite-type $Bi_2M_4O_9$: an overview. Int J Mater Res. 2012;103(4):422–29.
14. Burianek M, Muhlberg M, Woll M, Schmucker M, Gesing TM, Schneider H. Single-crystal growth and characterization of mullite-type orthorhombic $Bi_2M_4O_9$ ($M = Al^{3+}, Ga^{3+}, Fe^{3+}$). Cryst Res Technol. 2009;44(10):1156–62.
15. Debnath T, Rüscher CH, Fielitz P, Ohmann S, Borchardt G. Series of compositions $Bi_2(M'_xM_{1-x})_4O_9$ (M', M = Al, Ga, Fe; $0 \le x \le 1$) with mullite-type crystal structure: synthesis, characterization and $^{18}O/^{16}O$ exchange experiment. J Solid State Chem. 2010;183(11):2582–88.
16. Saalfeld H, Gerlach H. Solid solution and optical properties of (Al, Ge)-mullites. Z Krist—Cryst Mater. 1991;195(1–2):65–73.
17. Kirsch A, Murshed MM, Litterst FJ, Gesing TM. Structural, spectroscopic, and thermoanalytic studies on $Bi_2Fe_4O_9$: tunable properties driven by nano- and poly-crystalline states. J Phys Chem C. 2019;123(5):3161–71.
18. Cai D, Du D, Yu S, Cheng J. Oriented growth of $Bi_2Fe_4O_9$ crystal and its photocatalytic activity. Proc Eng. 2012;27:577–82.
19. Gogolin M, Murshed MM, Ende M, Miletich R, Gesing TM. Uniaxial negative thermal expansion in the mullite- and borax-type $PbAlBO_4$ polymorphs. J Mater Sci. 2019;55(1):177–90.
20. Ghosh K, Murshed MM, Gesing TM. Synthesis and characterization of $(Bi_{1-x}R_x)_2Mn_4O_{10}$: structural, spectroscopic and thermogravimetric analyses for R = Nd, Sm and Eu. J Mater Sci. 2019;54(21):13651–59.
21. Kirsch A, Murshed MM, Schowalter M, Rosenauer A, Gesing TM. Nanoparticle precursor into polycrystalline $Bi_2Fe_4O_9$: an evolutionary investigation of structural, morphological, optical, and vibrational properties. J Phys Chem C. 2016;120(33):18831–40.
22. Gesing TM, Fischer RX, Burianek M, Mühlberg M, Debnath T, Rüscher CH, et al. Synthesis and properties of mullite-type $(Bi_{1-x}Sr_x)_2(M^1{}_{1-y}M^2{}_y)_4O_{9-x}$ (M = Al, Ga, Fe). J Eur Ceram Soc. 2011;31(16):3055–62.
23. Park H, Lam R, Greedan JE, Barbier J. Synthesis, crystal structure, crystal chemistry, and magnetic properties of $PbMBO_4$ (M = Cr, Mn, Fe): a new structure type exhibiting one-dimensional magnetism. Chem Mater. 2003;15(8):1703–12.
24. Curti M, Mendive CB, Bredow T, Mangir Murshed M, Gesing TM. Structural, vibrational and electronic properties of $SnMBO_4$ (M = Al, Ga): a predictive hybrid DFT study. J Phys Condens Matter. 2019;31(34):345701.
25. Park H, Barbier J. $PbGaBO_4$, an orthoborate with a new structure-type. Acta Crystallogr E. 2001;57(9):i82–i84.
26. Park H, Barbier J, Hammond RP. Crystal structure and polymorphism of $PbAlBO_4$. Solid State Sci. 2003;5(4):565–71.
27. Murshed MM, Nénert G, Gesing TM. Crystal structure of mullite-type $PbMn_{0.5}Al_{0.5}BO_4$ determined by combined X-ray and neutron diffraction data. Z Krist—New Cryst Struct. 2012;227(3):285–86.
28. Murshed MM, Rusen A, Fischer RX, Gesing TM. Transition-metal substitution in $PbAlBO_4$: synthesis, structural and spectroscopic studies of manganese containing phases. Mater Res Bull. 2012;47(6):1323–30.
29. Murshed MM, Mendive CB, Curti M, Nénert G, Kalita PE, Lipinska K, et al. Anisotropic lattice thermal expansion of $PbFeBO_4$: a study by X-ray and neutron diffraction, Raman spectroscopy and DFT calculations. Mater Res Bull. 2014;59:170–78.
30. Head J, Manuel P, Orlandi F, Jeong M, Lees MR, Li R, et al. Structural, magnetic, magnetocaloric, and magnetostrictive properties of $Pb_{1-x}Sr_xMnBO_4$ (x = 0, 0.5, and 1.0). Chem Mater. 2020;32(23):10184–99.
31. Curti M, Gesing TM, Murshed MM, Bredow T, Mendive CB. Liebau density vector: a new approach to characterize lone electron pairs in mullite-type materials. Z Krist—Cryst Mater. 2013;228(12):629–34.
32. Drago RS. Thermodynamic evaluation of the inert pair effect. J Phys Chem. 1958;62(3):353–57.
33. Donaldson JD. The chemistry of bivalent tin. Inorg Chem. 1967;8:287–356.
34. Kubelka P, Munk F. Ein Beitrag zur Optik des Farbanstriches. Z Tech Phys. 1931;12:593–601.

35. Tauc J, Grigorovici R, Vancu A. Optical properties and electronic structure of amorphous germanium. Phys Status Solidi B. 1966;15(2):627–37.
36. Tauc J, Menth A. States in the gap. J Non-Cryst Solids. 1972;8–10:569–85.
37. Tauc J. Optical properties and electronic structure of amorphous Ge and Si. Mater Res Bull. 1968;3(1):37–46.
38. Souri D, Tahan ZE. A new method for the determination of optical band gap and the nature of optical transitions in semiconductors. Appl Phys B. 2015;119(2):273–79.
39. Gesing TM, Murshed MM, Schuh S, Thüringer O, Krämer K, Neudecker T, et al. Nano-crystalline precursor formation, stability, and transformation to mullite-type visible-light photocatalysts. J Mater Sci. 2022;57:19280–99.
40. Ghosh K, Murshed MM, Fischer M, Gesing TM. Aluminum to germanium inversion in mullite-type $RAlGeO_5$: characterization of a rare phenomenon for R = Y, Sm–Lu. J Am Ceram Soc. 2022;105(1):728–41.
41. Brand RA. WinNORMOS for IGOR6. In: University D, editor. 2017.
42. Corporation C. CorelDRAW Graphic Suite, Ottowa, Canada. 2017.
43. van Meerten SGJ, Franssen WMJ, Kentgens APM. ssNake: a cross-platform open-source NMR data processing and fitting application. J Magn Reson. 2019;301:56–66.
44. Shannon RD. Revised effective ionic radii and systematic studies of interatomic distances. Acta Crystallogr. 1976;A32:751.
45. Murshed MM, Fischer RX, Gesing TM. The role of the Pb^{2+}lone electron pair for bond valence sum analysis in mullite-type $PbMBO_4$(M = Al, Mn and Fe) compounds. Z Krist—Cryst Mater. 2012;227(8):580–84.
46. Yang H, Hazen RM, Finger LW, Prewitt CT, Downs RT. Compressibility and crystal structure of sillimanite, Al_2SiO_5, at high pressure. Phys Chem Miner. 1997;25(1):39–47.
47. Prosnikov MA, Smirnov AN, Yu Davydov V, Sablina KA, Pisarev RV. Lattice and magnetic dynamics of a quasi-one-dimensional chain antiferromagnet $PbFeBO_4$. J Phys: Condens Matter. 2017;29(2):025808.
48. Chen ZW, Lai JKL, Shek CH. Insights into microstructural evolution from nanocrystalline SnO_2 thin films prepared by pulsed laser deposition. Phys Rev B. 2004;70(16):165314.
49. Peercy PS, Morosin B. Pressure and temperature dependences of the Raman-active phonons in SnO_2. Phys Rev B. 1973;7(6):2779–86.
50. Becker M, Polity A, Klar PJ, Meyer BK. Synthesis of tin oxides SnO_{2-x} in the entire composition range ($x = 0$ to 1) by ion-beam sputter-deposition. Phys Status Solidi. 2015;9(5):326–30.
51. Kuzume A OM, Tang Y, Yamada Y, Haruta N, Yamamoto K. Ultrahigh sensitive Raman spectroscopy for subnanoscience: direct observation of tin oxide clusters. Sci Adv. 2019;5:eaax6455.
52. Basel BS, Hetzer C, Zirzlmeier J, Thiel D, Guldi R, Hampel F, et al. Davydov splitting and singlet fission in excitonically coupled pentacene dimers. Chem Sci. 2019;10(13):3854–63.
53. Suknev VS, Diman EN. Characteristic features of the infrared absorption spectra of tin-containing ludwigites and hulsites. J Appl Spectrosc. 1975;22(2):194–96.
54. Bentley PG, Hamer AN. Boron-10 abundance in nature. Nature. 1958;182(4643):1156.
55. Lees JK, Flinn PA. Mössbauer effect in tin compounds: interpretation of isomer shifts and determination of the nuclear radius change in ^{119}Sn. J Chem Phys. 1968;48(2):882–89.
56. Lippens PE. Interpretation of the ^{119}Sn Mössbauer isomer shifts in complex tin chalcogenides. Phys Rev B. 1999;60(7):4576–86.
57. Knyrim JS, Schappacher FM, Pöttgen R, Schmedt auf der Günne J, Johrendt D, Huppertz H. Pressure-induced crystallization and characterization of the tin borate β-SnB_4O_7. Chem Mater. 2007;19(2):254–62.
58. Kuzmann E, Kégl T, Kollár L, Vértes A, Garg VK. Mössbauer characterization of tin triflate $Sn(OTf)_2$. J Radioanal Nucl Chem. 1997;220(1):103–4.
59. Solis JL, Frantti J, Lantto V, Häggström L, Wikner M. Characterization of phase structures in semiconducting $SnWO_4$ powders by Mössbauer and Raman spectroscopies. Phys Rev B. 1998;57(21):13491–500.
60. Wang X, Liebau F. Influence of lone-pair electrons of cations on bond-valence parameters. Z Krist. 1996;211(7):437–39.
61. Hoffmann K, Hooper TJN, Murshed MM, Dolotko O, Révay Z, Senyshyn A, et al. Formation, stability and crystal structure of mullite-type $A_{16-x}B_xO_9$. J Solid State Chem. 2016;243:124–35.
62. Cossement C, Darville J, Gilles J-M, Nagy JB, Fernandez C, Amoureux J-P. Chemical shift anisotropy and indirect coupling in SnO_2 and SnO. Magn Reson Chem. 1992;30(3):263–70.
63. Abrahams I, Demetriou DZ. Inert pair effects in tin and lead dihalides: crystal structure of tin(II) bromide. J Solid State Chem. 2000;149(1):28–32.
64. Gesing TM, Mendive CB, Curti M, Hansmann D, Nénert G, Kalita PE, et al. Structural properties of mullite-type $Pb(Al_{1-x}Mn_x)BO_4$. Z Krist—Cryst Mater. 2013;228(10):532–43.
65. Haouas M, Taulelle F, Martineau C. Recent advances in application of ^{27}Al NMR spectroscopy to materials science. Prog Nucl Magn Reson Spectrosc. 2016;94–95:11–36.
66. Massiot D, Fayon F, Capron M, King I, Le Calvé S, Alonso B, et al. Modelling one- and two-dimensional solid-state NMR spectra. Magn Reson Chem. 2002;40(1):70–76.
67. Gesing TM, Schowalter M, Weidenthaler C, Murshed MM, Nénert G, Mendive CB, et al. Strontium doping in mullite-type bismuth aluminate: a vacancy investigation using neutrons, photons and electrons. J Mater Chem. 2012;22(36):18814–23.

SUPPORTING INFORMATION

Additional supporting information can be found online in the Supporting Information section at the end of this article.

How to cite this article: Wittmann S, Murshed MM, Bilovol V, Koldemir A, Pöttgen R, Nielsen UG, et al. Mullite-type $EMBO_4$: synthesis, structural, optical, and vibrational properties of rare tin(II) borates with M = Al and Ga. J Am Ceram Soc. 2024;107:1302–1314. https://doi.org/10.1111/jace.19476

Supporting Information

Mullite-type $EMBO_4$: Synthesis, structural, optical and vibrational properties of rare tin(II) borates with M = Al and Ga

Sarah Wittmann[1], M. Mangir Murshed[1,2*], Vitaliy Bilovol[3,+], Aylin Koldemir[4], Rainer Pöttgen[4], Ulla Gro Nielsen[5], Thorsten M. Gesing[1,2]

[1]University of Bremen, Institute of Inorganic Chemistry and Crystallography, Leobener Straße 7, D-28359 Bremen, Germany

[2]University of Bremen, MAPEX Center for Materials and Processes, Bibliothekstraße 1, D-28359 Bremen, Germany

[3]University of Buenos Aires, Laboratorio de Sólidos Amorfos – INTECIN, Av. Paseo Colón 850- C1063ACV – Buenos Aires, Argentina

[4]Universität Münster, Institut für Anorganische und Analytische Chemie, Corrensstraße 30, D-48149 Münster, Germany

[5]University of Southern Danmark, Department of Physics, Chemistry and Pharmacy, Campusvej 55, DK-5230 Odense, Denmark

*Corresponding author: murshed@uni-bremen.de, phone: +49 (0)421 218 63144

[+]Current address: Academic Centre for Materials and Nanotechnology, AGH University of Science and Technology, Al. Mickiewicza 30, 30-059 Krakow, Poland

Table S1: Irreducible representations for the nonequivalent atomic sites for the *Pnam* space group of $SnMBO_4$ with four formula units per unit cell.

Atom	**Wyckoff**	**Irreducible representation**
Sn	*4c*	$A_u + 2A_g + B_{1g} + 2B_{2g} + B_{3g} + 2B_{1u} + B_{2u} + 2B_{3u}$
M	*4a*	$3A_u + 3B_{1u} + 3B_{2u} + 3B_{3u}$
B	*4c*	$A_u + 2A_g + B_{1g} + 2B_{2g} + B_{3g} + 2B_{1u} + B_{2u} + 2B_{3u}$
O11	*4c*	$A_u + 2A_g + B_{1g} + 2B_{2g} + B_{3g} + 2B_{1u} + B_{2u} + 2B_{3u}$
O12	*4c*	$A_u + 2A_g + B_{1g} + 2B_{2g} + B_{3g} + 2B_{1u} + B_{2u} + 2B_{3u}$
O2	*8d*	$3A_u + 3A_g + 3B_{1g} + 3B_{2g} + 3B_{3g} + 3B_{1u} + 3B_{2u} + 3B_{3u}$

Γ_{Raman}: $11A_g + 7B_{1g} + 11B_{2g} + 7B_{3g}$

Γ_{IR}: $13B_{1u} + 9B_{2u} + 13B_{3u}$

$\Gamma_{acoustic}$: $B_{1u} + B_{2u} + B_{3u}$

Γ_{silent}: $10A_u$

Table S2: Fitted Raman and FTIR peak maxima (cm^{-1}).

Raman **Fo**		**IR**	
$SnAlBO_4$	**$SnGaBO_4$**	**$SnAlBO_4$**	**$SnGaBO_4$**
65.9(4)	-	-	-
73.0(1)	81.8(6)	-	-
85.6(9)	82.4(5)	-	-
-	91.2(4)	-	-
-	100.6(5)	-	-
106.0(3)	106.8(2)	-	-
112.7(1)	-	-	-
117.9(5)	-	-	-
122.6(9)	127.0(4)	-	-
139.2(8)	138.5(7)	-	-
154.8(6)	-	-	-
220.2(2)	205.6(1)	-	-
232.9(1)	-	-	-
235.0(8)	-	-	-
321.9(8)	312.5(5)	-	-

331.8(7)	-	-	-
344.9(5)	353.7(9)	347.1(6)	-
348.1(5)	367.7(6)	-	369.5(4)
397.5(3)	-	-	372.2(1)
405.8(3)	406.1(4)	-	406.9(8)
-	-	421.7(1)	420.3(6)
443.2(7)	-	432.4(7)	430.0(1)
-	-	470.9(1)	475.0(3)
-	-	-	495.4(1)
538.6(1)	511.8(9)	511.7(4)	509.2(6)
-	-	-	536.4(7)
-	-	567.6(8)	563.7(1)
-	-	625.0(6)	591.2(7)
659.9(4)	647.4(4)	660.9(7)	648.7(8)
-	-	-	656.2(8)
-	693.0(5)	691.9(8)	695.8(7)
-	-	701.8(1)	-
713.6(5)	-	722.7(5)	-
-	-	-	789.3(1)
-	-	-	794.1(7)
-	-	-	807.0(2)
-	-	813.0(5)	813.6(9)
-	-	881.9(2)	881.4(2)
-	-	921.8(7)	932.9(6)
-	950(1)	957.2(3)	-
978(1)	963(1)	-	-
-	-	1042(2)	1013(9)
-	-	1118(3)	1094(4)
-	-	-	1168(4)
1225(4)	1209(3)	1208(1)	1212(3)
-	1235(1)	1231(8)	1226(6)
1261(2)	-	1248(1)	1272(1)
-	-	1299(5)	-

-	1326(3)	1308(2)	1335(2)
-	-	1374(5)	1384(3)
-	-	-	1391(1)
-	-	-	1396(8)
-	-	1435(2)	1437(1)
-	-	1511(8)	1470(8)

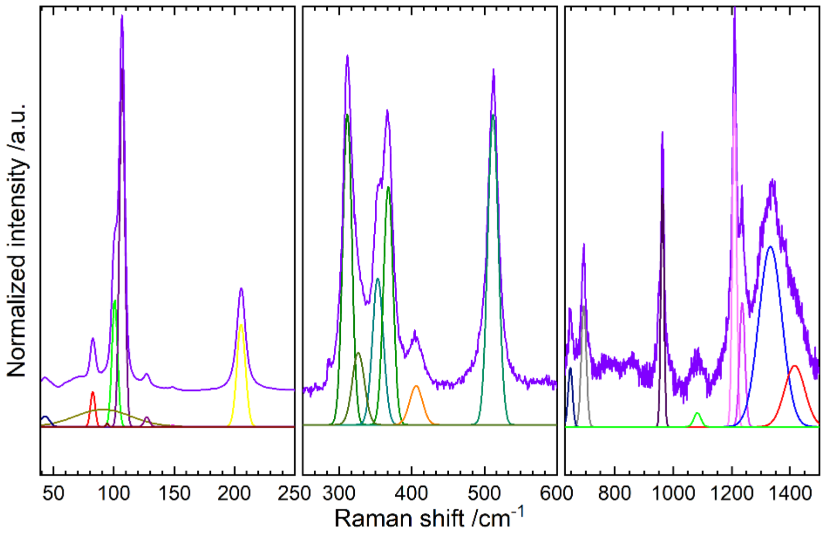

Figure S1: Fitted Raman spectra of $SnGaBO_4$ segmented into three regions for better clarity with observed data (blue) and fitted peaks (colored).

Table S3: Correlative internal vibrational modes between the free ion symmetry (FIS), the site symmetry (SS), and the factor group symmetry (FGS) for the of the MO$_x$ groups in SnMBO$_4$.

MO$_6$		
FIS (O_h)	SS (C_i)	FGS (D_{2h})

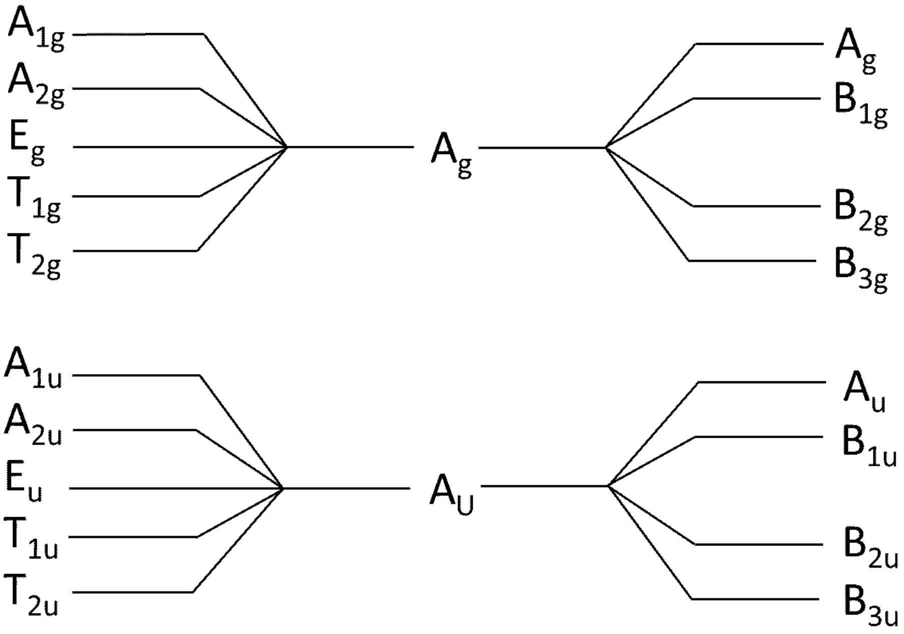

SnO$_4$		
FIS (T_d)	SS (C_s)	FGS (D_{2h})

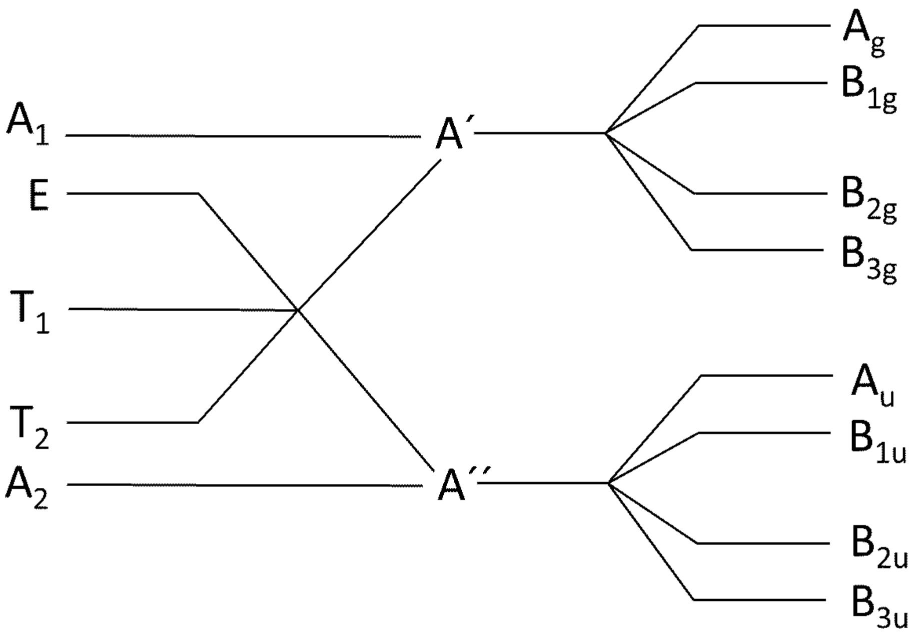

BO$_3$		
FIS (D_{3h})	SS (C_s)	FGS (D_{2h})

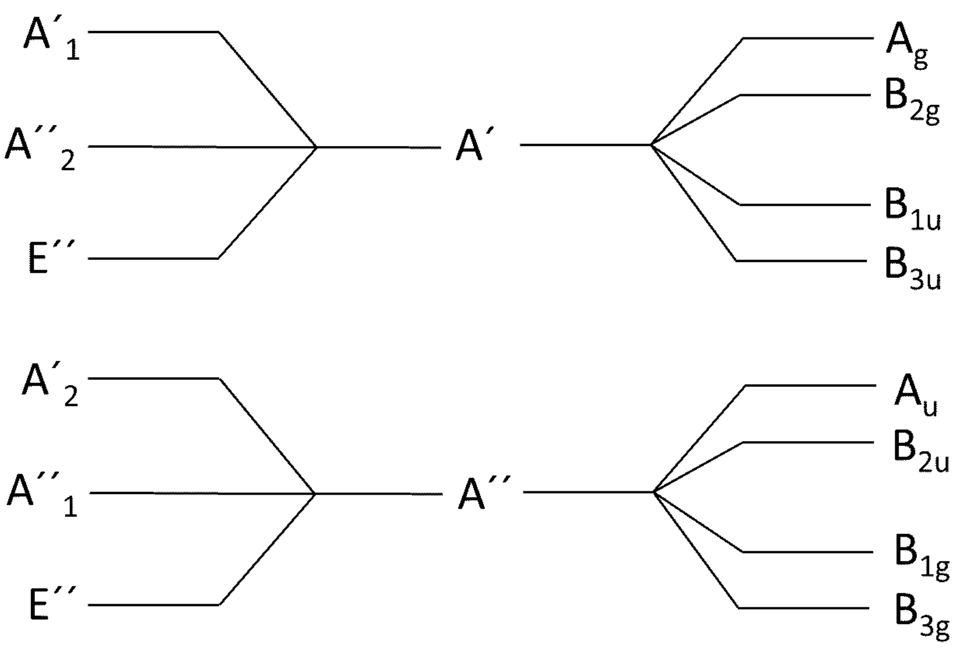

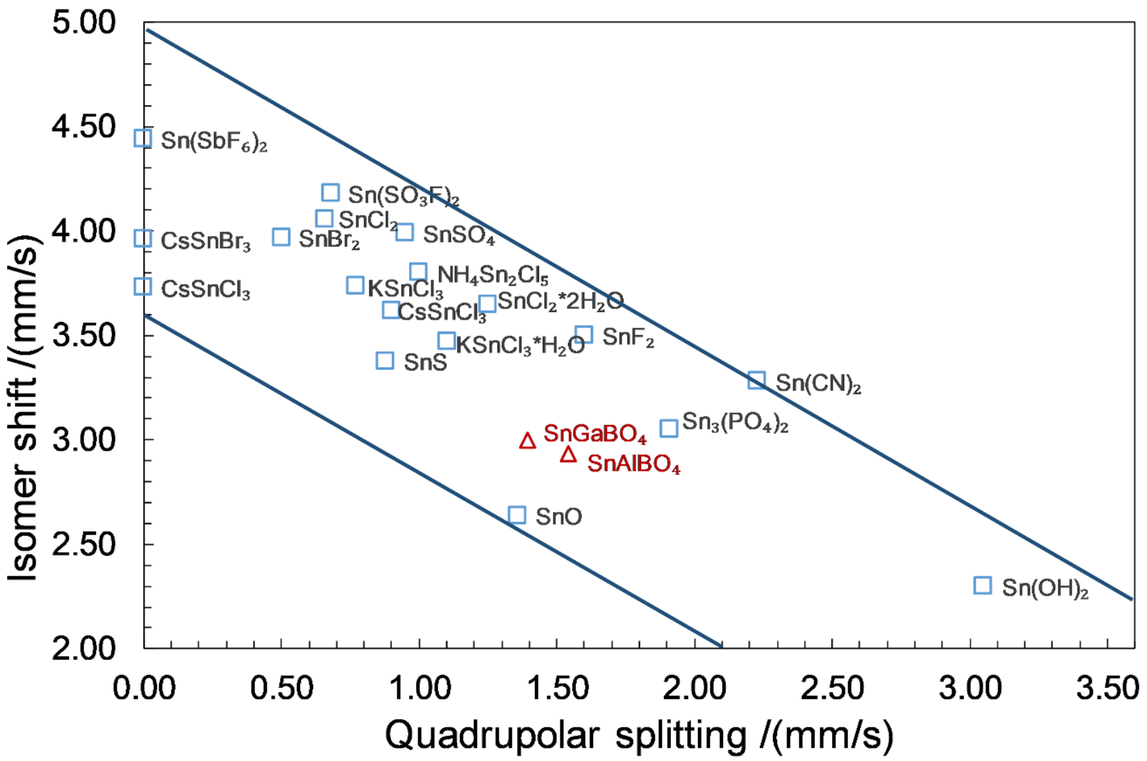

Figure S2: Quadrupolar splitting versus isomer shift of some Sn(II)-containing compounds observed by ^{119}Sn Mössbauer spectroscopy. Data (open square) are taken from the reference ([1] & refs.cited therein). Updated version of Figure 2 from Ref. 1.

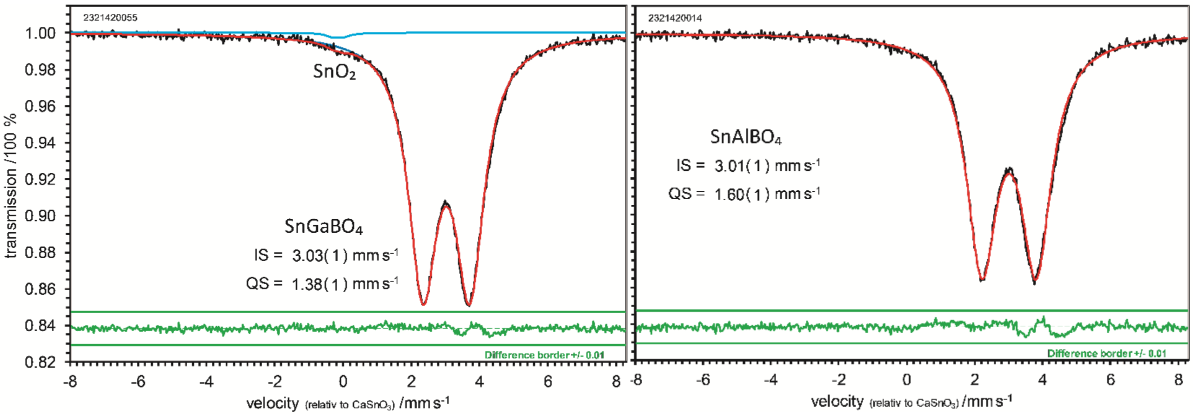

Figure S3: ^{119}Sn Mössbauer spectra of $SnGaBO_4$ (left) with SnO_2 as minor by-product and $SnAlBO_4$ (right).

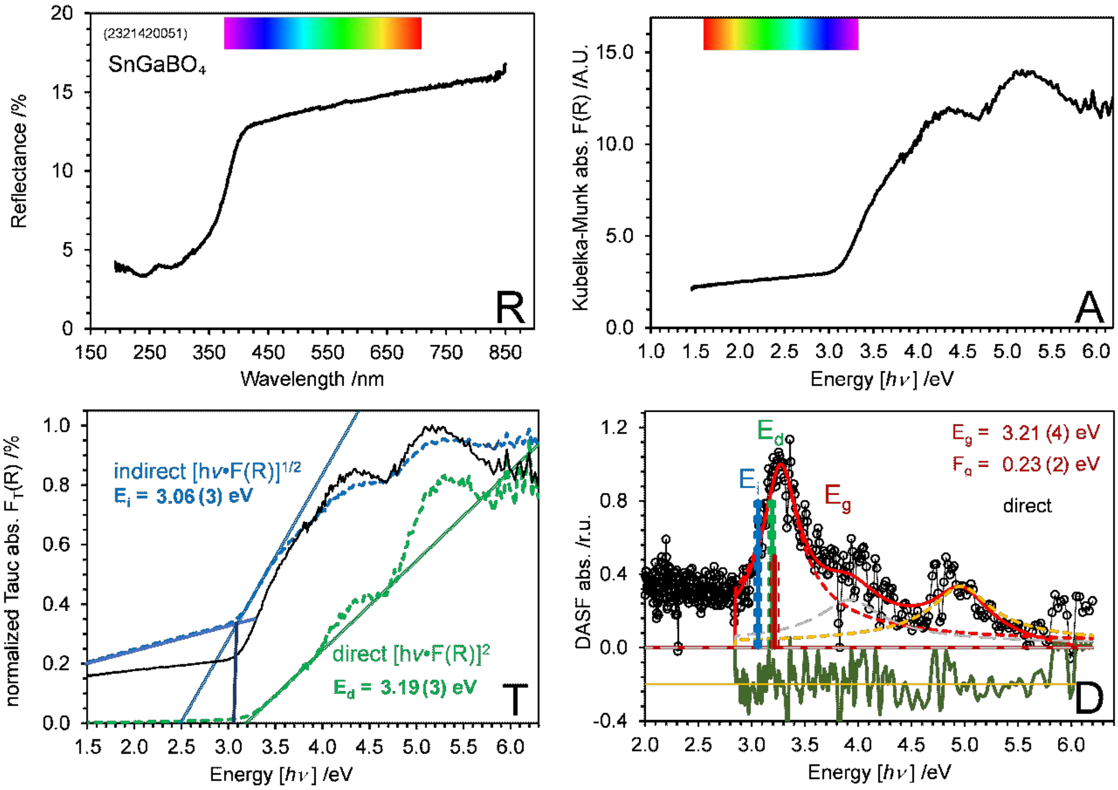

Figure S4: UV/Vis reflectance spectrum of $SnGaBO_4$ (R), Kubelka-Munk graph (A), normalized Tauc plot (T), normalized DASF plot (D).

Reference

1. Kuzmann E, Kégl T, Kollár L, Vértes A, Garg VK. Mössbauer characterization of tin triflate $Sn(OTf)_2$. Journal of Radioanalytical and Nuclear Chemistry. 1997;220(1):103-4.

Reference

1. M. Gogolin, M.M. Murshed, M. Ende, R. Miletich, T.M. Gesing, Uniaxial negative thermal expansion in the mullite- and borax-type $PbAlBO_4$ polymorphs, Journal of Materials Science 55(1) (2019) 177-190. DOI:10.1007/s10853-019-04013-6
2. H.-J. Koo, M.-H. Whangbo, Density functional investigation of the magnetic properties of $PbMBO_4$ (M=Cr, Mn, Fe), Solid State Communications 149(15-16) (2009) 602-604. DOI:10.1016/j.ssc.2009.01.030
3. T. Kremlika, High pressure behaviour of α-$PbAlBO_4$ single crystals under hydrostatic compression to 24 GPa, Master thesis, University of Vienna A066815 (2020) 1-75.
4. R.D. Shannon, Revised effective ionic radii and systematic studies of interatomic distances, Acta Crystallographica A32 (1976) 751.
5. I.M. DiMucci, J.T. Lukens, S. Chatterjee, K.M. Carsch, C.J. Titus, S.J. Lee, D. Nordlund, T.A. Betley, S.N. MacMillan, K.M. Lancaster, The Myth of d8 Copper(III), Journal of the American Chemical Society 141(46) (2019) 18508-18520. DOI:10.1021/jacs.9b09016
6. N. Wiberg, Lehrbuch der Anorganischen Chemie, De Gruyter2008.
7. E.K. Ohriner, Processing of Iridium and Iridium Alloys, Platinum Metals Review 52(3) (2008) 186-197. DOI:10.1595/147106708X333827
8. E. Benguerel, G.P. Demopoulos, G.B. Harris, Speciation and separation of rhodium (III) from chloride solutions: a critical review, Hydrometallurgy 40(1) (1996) 135-152. DOI:10.1016/0304-386X(94)00086-I
9. D. Tudela, Silver(II) Oxide or Silver(I,III) Oxide?, Journal of Chemical Education 85(6) (2008) 863. DOI:10.1021/ed085p863
10. S.M. Shaheen, D.S. Alessi, F.M.G. Tack, Y.S. Ok, K.H. Kim, J.P. Gustafsson, D.L. Sparks, J. Rinklebe, Redox chemistry of vanadium in soils and sediments: Interactions with colloidal materials, mobilization, speciation, and relevant environmental implications- A review, Adv Colloid Interface Sci 265 (2019) 1-13. DOI:10.1016/j.cis.2019.01.002
11. J.B. Allen, L.R. Faulkner, Electrochemical methods: fundamentals and applications, second edition ed., Wiley2000.
12. P. Vanýsek, Electrochemical series.

Chapter 3 - Temperature dependent characterization of $SnAlBO_4$ and $SnGaBO_4$ mullite-type ceramics

As discussed in the **chapter 2**, the successful syntheses of mullite-type $SnMBO_4$ ceramics with M = Al, Ga is possible, and the characterization was done at room temperature. Stability at high temperatures for oxides is an important research topic, where mullite and mullite-types are some of the most studied ceramics. They are known for their thermal stability, low thermal and electrical conductivity and low thermal expansion as explained in **chapter 1**. [1] As stated in literature, the thermal expansion of mullites is strongest along the crystallographic **b**-axis, where the highest thermal expansion coefficient (TEC) is explained as the elongation of the relatively longer M-O bonds along the **b**-direction [2]. Mullite-type $PbMnBO_4$ compound exhibits an interesting thermal behavior, where the TEC changes from negative to positive along the crystallographic **a**-axis [3] in increasing temperature. Hence, the thermal investigations of $SnMBO_4$ (M = Al, Ga) mullite-type compounds are discussed in this chapter (manuscript in preparation).

Temperature dependent characterization of $SnAlBO_4$ and $SnGaBO_4$ mullite-type ceramics

Sarah Wittmann[1], M. Mangir Murshed[1,2*], Kowsik Ghosh[1†], Aylin Koldemir[3], Rainer Pöttgen[3], Thorsten M. Gesing[1,2]

(Manuscript in preparation)

[1]University of Bremen, Institute of Inorganic Chemistry and Crystallography, Leobener Straße 7, D-28359 Bremen, Germany

[2]University of Bremen, MAPEX Center for Materials and Processes, Bibliothekstraße 1, D-28359 Bremen, Germany

[3]Universität Münster, Institute für Anorganische und Analytische Chemie, Corrensstrasse 30, D-48149 Münster, Germany

ORCID:

SW:	0000-0003-1404-3434
MMM:	0000-0002-9063-372X
KG:	0000-0003-2622-7046
AK:	0009-0004-3819-3853
RP:	0000-0003-0962-279X
TMG:	0000-0002-4119-2219

*Corresponding author: murshed@uni-bremen.de, phone: +49 (0)421 218 63144

†Present address: Department of Chemistry and Biochemistry, University of Delaware, Newark, Delaware, USA.

Abstract

Temperature-dependent structural investigations of $SnMBO_4$ (M = Al, Ga) mullite-type structures are carried out using in situ X-ray diffraction. Between 10 K and 850 K, the samples show low thermal expansion coefficients with a maximum of $10 \cdot 10^{-6}$ K^{-1} at 800 K without any anomaly. Temperature-dependent Raman spectroscopy helps understand the local feature, complementing the X-ray results. However, low temperature ^{119}Sn Mössbauer spectroscopy points to change of symmetry.

Keywords: mullite-type, LEP, $SnMBO_4$, WLE, symmetry loss, Mössbauer spectroscopy

1. Introduction

Mullite-type compounds can be categorized based on the relative number of oxygen atoms in the chemical formular. For instance, $Bi_2Mn_4O_{10}$ [1] is known as O10 phase, $Bi_2Fe_4O_9$ [2] as O9 phase, and $E_2M_2O_8$ (e.g., $PbAlBO_4$) as O8 phase. Of them, the $PbMBO_4$ (M = Al, Ga, Mn, Fe, Cr) O8-phases have drawn considerable interest due to their broad range of crystal-chemical [3], thermal [4] and optical [2, 5] properties. In the unconventional *Pnam* setting, the edge-sharing MO_6 octahedral chain run parallel to the crystallographic **c**-axis [6, 7]. While in mullite octahedral chain is bridged by the MO_4 tetrahedral units, in O8-phase it is alternatively bridged by planar BO_3 groups and distorted PbO_4 square pyramids [8]. The interplay between the crystal-chemistry of the MO_6 octahedral chain, the rigidity of the trigonal planar BO_3 groups and the stereochemically active $6s^2$ lone electron pair (LEP) of Pb^{2+} plays important role to the associated thermo-mechanical properties [9]. In search of high-temperature oxides, mullite and mullite-type ceramics are some of the most widely studied systems for their thermal stability, low thermal expansion, low thermal and electrical conductivity and excellent creep resistance [10]. In some cases, the thermo-mechanical behavior is the key factor in determining the functionality of many mullite materials [10]. Generally, the thermal expansion of mullites is strongest parallel to the crystallographic **b**-axis followed by **c**- and **a**-axis [11]. The highest thermal expansion coefficient (TEC) was explained in terms of the elongation of the relatively longer M-O bond along the **b**-direction [11]. The mullite-type $PbAlBO_4$ [6], however, showed negative TEC in the **a**-discretion, leading to an overall positive thermal expansion for the cell volume. Gogolin *et al.* [6] demonstrated that an interplay between the negative cross-compliance and the anisotropic Grüneisen parameter plays pivotal roles for axial negative linear compressibility and negative thermal expansion. Such thermal expansion anisotropy is not surprising in compounds with BO_3 planar group. The thermal expansion of borates was reported to be maximal in the direction perpendicular to the preferred orientation of the isolated planar

BO_3 groups [12]. In a series of borates, Bubnova and Filatov [13] demonstrated that a given BO_3-containing crystal structure shows the maximum and the minimum thermal expansion in the direction perpendicular and parallel to the preferred orientation of the BO_3 planes, respectively, leading to substantial thermal expansion anisotropy. Such anisotropy can be mitigated for the spatially distributed BO_4 tetrahedra in 3D-space, leading to isotropic thermal expansion.

Based on theoretical calculations [14] we were able to synthesize two O8-phases $SnAlBO_4$ and $SnGaBO_4$ followed by their detail structural and spectroscopic characterizations [15]. The compounds are substantial replacement of the isostructural lead-containing materials with health hazards and environmental issues. The stereochemical activity, as a measure of the Wang-Liebau eccentricity (WLE) [16] parameter, of $Sn(II)O_x$ is about 3.8(1) times greater than that of $Pb(II)O_x$. Therefore, it would of great interest to understand how the SnO_4 units in $SnMBO_4$ compounds respond, to the external stimulus, for instance for axial TECs, compared to that of PbO_4 in $PbMBO_4$. Because thermal orientation of LEPs [17] and thermal response to $5s^2$ LEPs of Sn^{2+} may result in different stability of these O8 compounds. From this standpoint, this report bears particular importance of producing phase-pure $SnMBO_4$ samples followed by a detailed characterization using temperature-dependent X-ray powder diffraction (XRPD), Raman, and Mössbauer spectroscopy.

2. Experimental

2.1. Synthesis

Stoichiometric amounts of SnO, elementary tin, M_2O_3 (M = Al, Ga) and B_2O_3 were dried at 473 K overnight, mixed and put into a quartz tube which was also preheated at 1073 K for about 15 hours. The mixture was further heated at 473 K for 2 hours to reduce the absorbed moisture.

The internal pressure of the quartz tube was then reduced to 10^{-7} MPa. During the dynamic vacuum process the tube was sealed. The sealed samples were placed into an oven and heated at 1023 K for 3 days with a cooling and heating rate of 200 K /h to obtain a polycrystalline powder.

2.2. X-ray diffraction

X-ray powder diffraction (XRPD)

High-temperature data were collected on a PANalytical MPD powder diffractometer in Bragg-Brentano geometry equipped with a secondary Ni filter, CuKα radiation and an X'Celetator multi-strip detector using an Anton Paar HTK1200N heating chamber. A flat corundum sample holder was used, where a small evaporation channel served as additional space to compensate the thermal expansion of the sample. Measurements were carried out between 300 K and 835 K with a consecutive slice of 10 K. Each pattern was recorded from 10° to 85° 2θ with a step size of 0.0167° and a scan time of 0.95 s/step for $SnAlBO_4$ and 0.45 s/step for $SnGaBO_4$. Low-temperature data were collected on a STOE Stadi-MP diffractometer configured in Bragg-Brentano geometry. They were recorded with a Dectris Mythen 1 K detector while limiting the angular coverage of the detector to 6.25° 2θ to avoid aberration effects. $MoK_{\alpha 1}$ X-ray radiation was used with a Ge(111) monochromator. With a step width of 0.005° from 5° to 50° 2θ a total of 3007 data points were collected for 55 s/step using 428 channels of the detector. The samples were mixed into thick pastes with thermally conductive paint (Kemo Electronic L100 Conducting Silver) and fixed on a copper sample holder for better thermal equilibration. The temperature was controlled utilizing an Oxford Cryosystems PheniX cryostat and powder patterns were recorded at 13 K, 18 K, and between 23 K and 293 K using 10 K increments. For both instruments, the reflection profile was modeled using the fundamental parameter approach [18], as implemented in TOPAS 6 (Bruker AXS GmbH, Karlsruhe, Germany). The crystal data of isostructural $PbAlBO_4$ [19] was used for Rietveld refinements. The difference between the two different measurement routines at room temperature was adjusted by a fact or 0.8 pm for the metric parameters.

2.3. Spectroscopy

Raman spectroscopy

Raman spectra were recorded on a LabRam ARAMIS (Horiba Jobin Yvon) Micro-Raman Spectrometer equipped with a laser working at 532 nm. The use of a 50× objective (Olympus) with a numerical aperture of 0.55 provides a focus spot of about 2 µm diameter. Data were collected between 90 cm^{-1} and 800 cm^{-1} with a spectral resolution of approximately 1.2 cm^{-1} using a grating of 1800 grooves /mm and a thermoelectrically cooled CCD detector (Synapse, 1024×256 pixels). The spectral position and the linearity of the spectrometer were calibrated against the Raman mode at 520.7±0.1 cm^{-1} of a Si wafer and emission lines of a neon lamp, respectively. Temperature-dependent data sets were collected between 80 K and 300 K using a Linkam THMS350 stage, and between 300 K and 880 K using a Linkam TS1500V stage with 10 K temperature increments. Peak maximum, linewidths, and profile shapes (Gaussian/Lorentzian) were obtained using the LAMP software package. [20]

Mössbauer spectroscopy

For ^{119}Sn Mössbauer spectroscopic investigations a $Ca^{119m}SnO_3$ source with γ-radiation at 23.875 keV was used. A thin palladium foil (thickness 0.05 mm) was placed between the sample and the detector to reduce K X-rays emitted by the source. The measurements were conducted in usual transmission geometry. The source and the metal tin-(II)-borates were kept at room temperature and at 78 K. The samples were mixed with α-quartz and enclosed in thin walled PMMA containers. To obtain suitable integral fits for the ^{119}Sn spectra the WinNormos of Igor6 program package [21] was used and graphical editing was done with the program CorelDRAW2017 [22].

Thermal analysis

Simultaneous thermogravimetry and differential scanning calorimetry (TG-DSC) were carried out under a dry synthetic air atmosphere (80 vol-% N2 and 20 vol-% O2) and N_2 air with a heating rate of 10 K/min from 303 K to 1473 K on a Mettler Toledo TGA/DSC 3^+ STARe System. 10.6(1) mg sample was measured relative to a corundum crucible with 10 mg Al_2O_3 as the reference. A drift correction to the collected data was applied using an empty corundum crucible measurement. DSC analyses were carried out under a N_2 atmosphere with a cooling rate of 10 K/min from 293 K to 123 K on a Mettler Toledo 3^+ STARe System. 10.2(1) mg and 10.3(2) mg sample of $SnAlBO_4$ and $SnGaBO_4$, respectively, were measured to an alumina crucible with an empty crucible as reference.

3. Results and discussion

Results of the thermogravimetry (TG) and differential scanning calorimetry (DSC) are shown in **figure 1**. Both samples exhibit almost an insignificant weight-loss along with weak endothermic process, which might be due to loss of left-over humidity even after the preheating. For $SnAlBO_4$, the endothermic signal begins to arise up to the decomposition temperature of 1070 K whereas the endothermic effect of $SnGaBO_4$ is observed in two processes (**figure S1)**. A slight mass gain of ~1 % can be seen between 790 K and 970 K followed by another mass gain of 5 % at about 1070 K where the decomposition takes place. The decomposition process might follow one of the two reaction schemes:

$$2\ SnAlBO_4 + O_2 \rightarrow 2\ SnO_2 + Al_2O_3 + B_2O_3 \qquad (1)$$

$$SnAlBO_4 + \tfrac{1}{2}\ O_2 \rightarrow SnO_2 + AlBO_3 \qquad (2)$$

With only the TG/DSC data, both decomposition reactions are possible, which can be better described when decomposed samples are analyzed. X-ray powder data Rietveld refinement on the sample heated up to 1273 K suggests the decomposition is more likely follows **scheme 1**. It's worth mentioning that another mullite-type $Al_4B_2O_9$ was reported to be decomposed at around 1308 K [23].

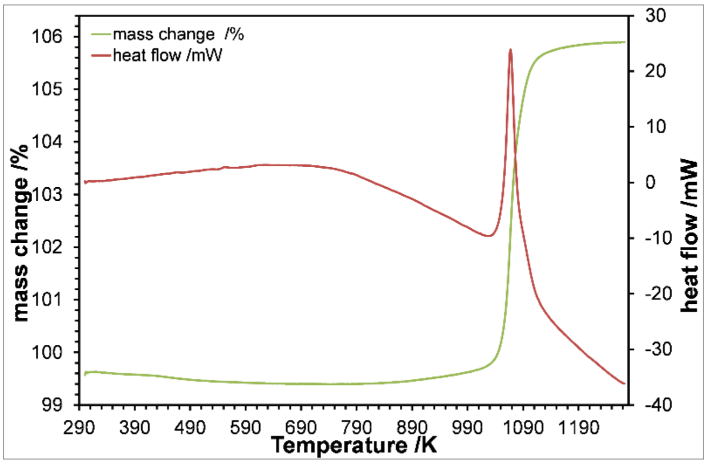

Figure 1: Temperature-dependent mass change (green) and heat flow (red) for $SnAlBO_4$.

Figure 2 depicts the DSC investigations carried out at low-temperature, where both samples show respective point of inflection (change of slope) for the heat-flow at around 150 K (**figure 2** and **figure S2**). Further investigations between 183 K and 123 K were carried out to confirm the observation. The change of the slope in the smaller temperature range is more pronounced. The exothermic signal is likely to be associated with phase transition, which deserves detailed investigations.

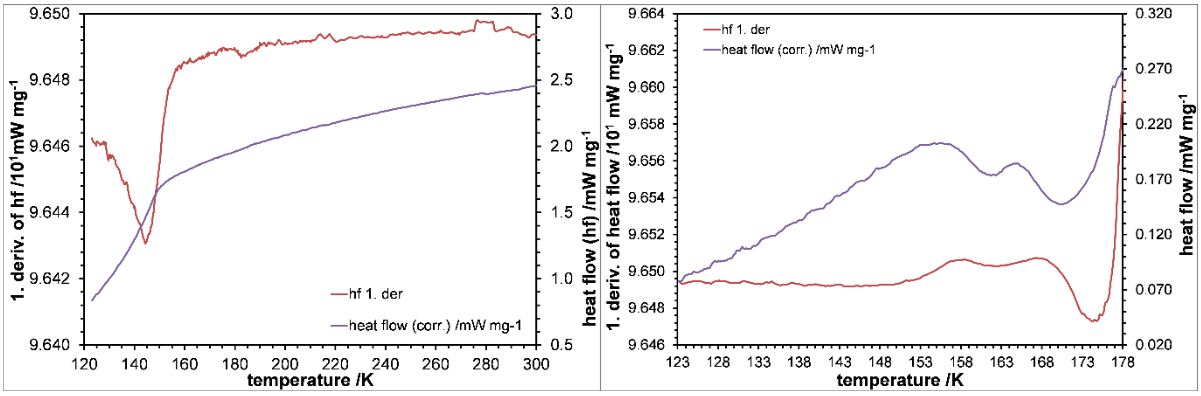

Figure 2: DSC plots of $SnAlBO_4$ with the heat flow (violet) and its first derivative (red).

The thermal events followed by TD-XRPD up to 840 K (**figure 3**), however, shows only the parent phases between 13 K and 850 K (**figure S3**). Comparing the diffraction patterns, the Bragg reflections are shifted to higher Q-values for the larger unit cell of $SnGaBO_4$.

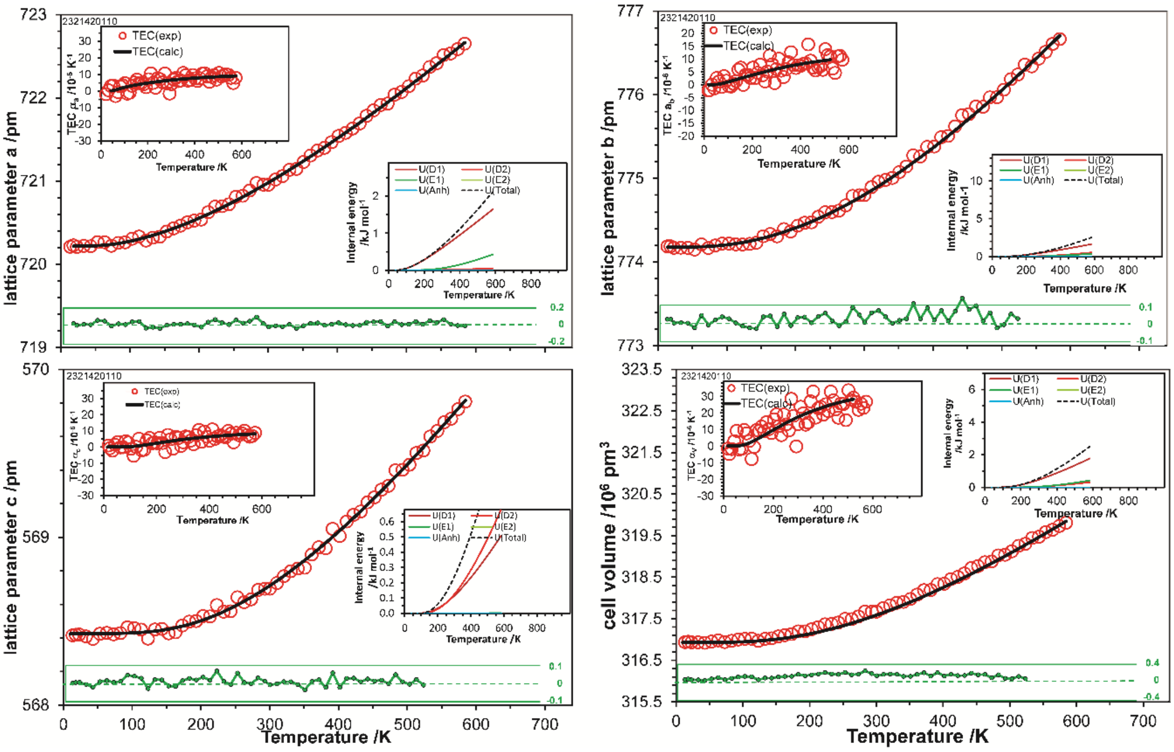

Figure 3: Debye-Einstein-Anharmonicity (DEA) fits of the metric parameters of $SnAlBO_4$. The respective thermal expansion coefficients (TECs) and the Debye energy terms are seen as insets.

For $SnAlBO_4$, the lattice parameters and the cell volume increase of about 3-4 pm and 5 $\cdot 10^6$ pm^3, respectively, with increasing temperature where the trend is $\Delta a = \Delta b > \Delta c$. While the TECs hardly change between 13 K and 100 K, the positive thermal expansion is almost linear from 300 K to 840 K. Similar trend is observed for $SnGaBO_4$, where the cell volume increases about 6 $\cdot 10^6$ pm^3, and the lattice parameter a and b about 5 pm, and c about 2 pm between 13 K and 840 K.

The lattice thermal expansion was modeled using the Debye-Einstein-Anharmonicity (DEA) [24-26] approach. Each model line shows excellent agreement with the respective observed data, as shown in **figure 4** for $SnAlBO_4$ and **figure S4** for $SnGaBO_4$. The model-fit parameters are given in **table 1**. Based on the calculated phonon density of states (PDOS) [14], a single Debye spectrum along with a single Einstein oscillator approach is enough to fit the temperature-dependent lattice parameters. The Debye temperature of the $SnGaBO_4$ phase is found to be lower than that of $SnAlBO_4$, supporting the early findings [14]. The experimental bulk modulus of $SnAlBO_4$ at 316.93(5) 10^{-6} pm^3 is compared to the calculated ones (at 312.5(5) 10^{-6} pm^3) which are in the same range and therefore, predict the same trend. Another observation is if the volume of one compound increases the crystal structure gets more unstable. Therefore, the higher temperatures are leading to a decomposition of the mullite-type phase. The same trend is expected for $SnGaBO_4$. The average Grüneisen parameter lies close to unity (1.02 at 80 K and 1.01 at 850 K), which seems to be temperature independent.

Table 1: Debye-Einstein-Anharmonicity (DEA) fit parameters of $SnAlBO_4$ and $SnGaBO_4$.

$SnAlBO_4$	***Cell volume***	***Lattice parameters***		
Fit-parameter	***V***	***a***	***b***	***c***
V_0 /10^{-6} pm^3	316.93(5)	720.2(2)	774.2(2)	568.4(1)
k_{D1} /10^{-12} GPa	5.73(1)	4.20(1)	5.65(1)	4.44(1)
θ_{D1} /K	739(3)	498(3)	825(4)	1269(3)
k_E /10^{-12} GPa	4.79(1)	2.83(1)	3.06(1)	0.95(2)
θ_E /K	1586(2)	1414(4)	1681(4)	1333(4)
$SnGaBO_4$	***Cell volume***	***Lattice parameters***		
Fit-parameter	***V***	***a***	***b***	***c***
V_0 /10^{-6} pm^3	335.01(2)	726.50(8)	790.02(9)	583.66(6)
k_{D1} /10^{-12} GPa	7.61(1)	4.40(1)	5.03(1)	4.32(1)
θ_{D1} /K	546(4)	1092(4)	1551(5)	972(3)
k_E /10^{-12} GPa	3.53(1)	3.25(1)	3.33(1)	0.52(3)
θ_E /K	2513(2)	131(5)	197(7)	1258(4)

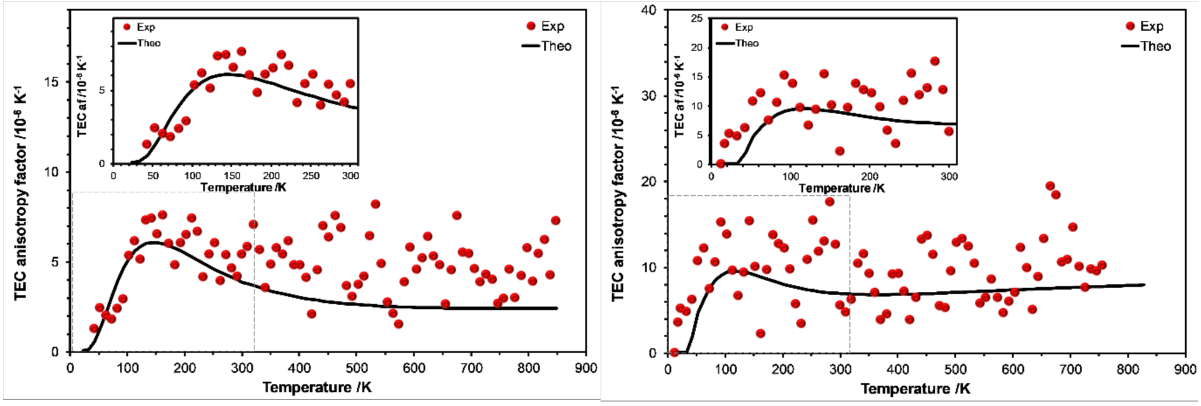

Figure 4: Temperature-dependent thermal expansion coefficient (TEC) anisotropy parameter of $SnAlBO_4$ and $SnGaBO_4$.

Temperature-dependent Raman spectroscopy

Details of the vibrational features of $SnAlBO_4$ and $SnGaBO_4$ at ambient conditions have been recently reported [15]. Temperature-dependent Raman spectra are shown in **figure 5** and **figure S6** for $SnAlBO_4$ and $SnGaBO_4$, respectively. Each M-O stretching of the respective BO_3, SnO_4, AlO_6 polyhedron shows clear red-shift due to quasi-harmonic behaviors associated with the thermal expansion of the lattices. As the measuring conditions were unpolarized, almost all the bands, as previously observed [15] were clearly seen.

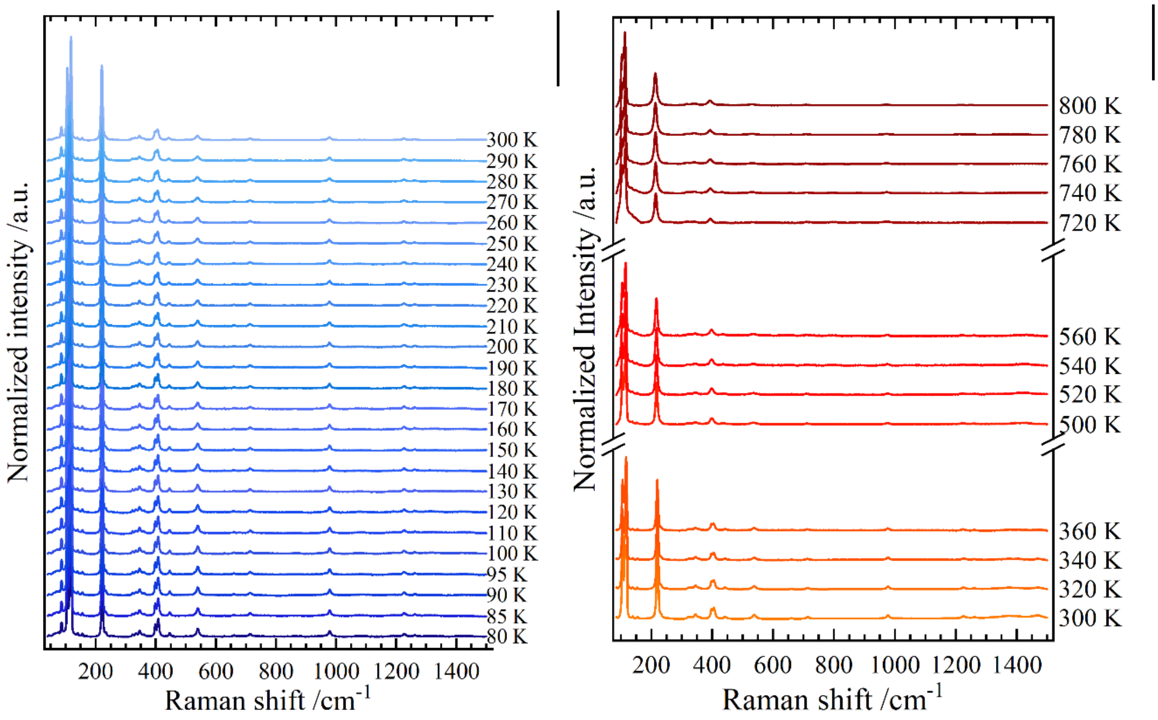

Figure 5: Low-temperature (left) and high-temperature (right) Raman spectra of $SnAlBO_4$.

For anharmonic analyses, we selected six frequencies (in cm^{-1}) ω_i, where $i = 106, 156, 345, 447, 715,$ *and* 979 at room temperature of SnAlBO$_4$, respectively assigned to B–O, Al–O, and Sn–O stretching of the corresponding polyhedra. Such selection helps in understanding the change of the frequencies and line-widths due to both quasi-harmonic (lattice) and isochoric (intrinsic) contributions. Mode Grüneisen parameter has been calculated from the temperature-independent data. ($\gamma_i = \partial ln\omega_i)/\partial lnV$). Considering the Klemens approach [27] the 3-phonon (for a cubic decay) and 4-phonon (for quartic decay) interactions are analyzed [19, 28, 29] and the associated damping factors are given in **table 2** for SnAlBO$_4$ and in **table S1** for SnGaBO$_4$. This simplified semi-quantitative model convincingly describes our experimental observation for the anharmonic phonon contribution to the frequency shift. **Figure 6** shows the contributions from the anharmonic phonon decay processes to frequency shift for SnAlBO$_4$. The respective figures for SnGaBO$_4$ are shown in **Figure S4**. The 3-phonon and 4-phonon contributions are separately given for the entire temperature range between 80 K and 800 K.

Table 2: Selective Raman frequencies of SnAlBO$_4$ at 0 K, their corresponding mode Grüneisen parameter together with the fitting parameters

ω_{i0} /cm^{-1}	$(\gamma_i)_T$	A /cm^{-1}	B /cm^{-1}
106.4	1.87	-0.06(1)	-0.002(2)
156.4	2.43	-0.14(3)	-0.005(1)
345.4	1.04	-0.01(3)	-0.004(3)
446.5	2.25	-0.26(1)	-0.012(5)
714.9	0.51	-0.09(1)	-0.004(7)
979.3	0.51	-0.12(3)	-0.057(2)

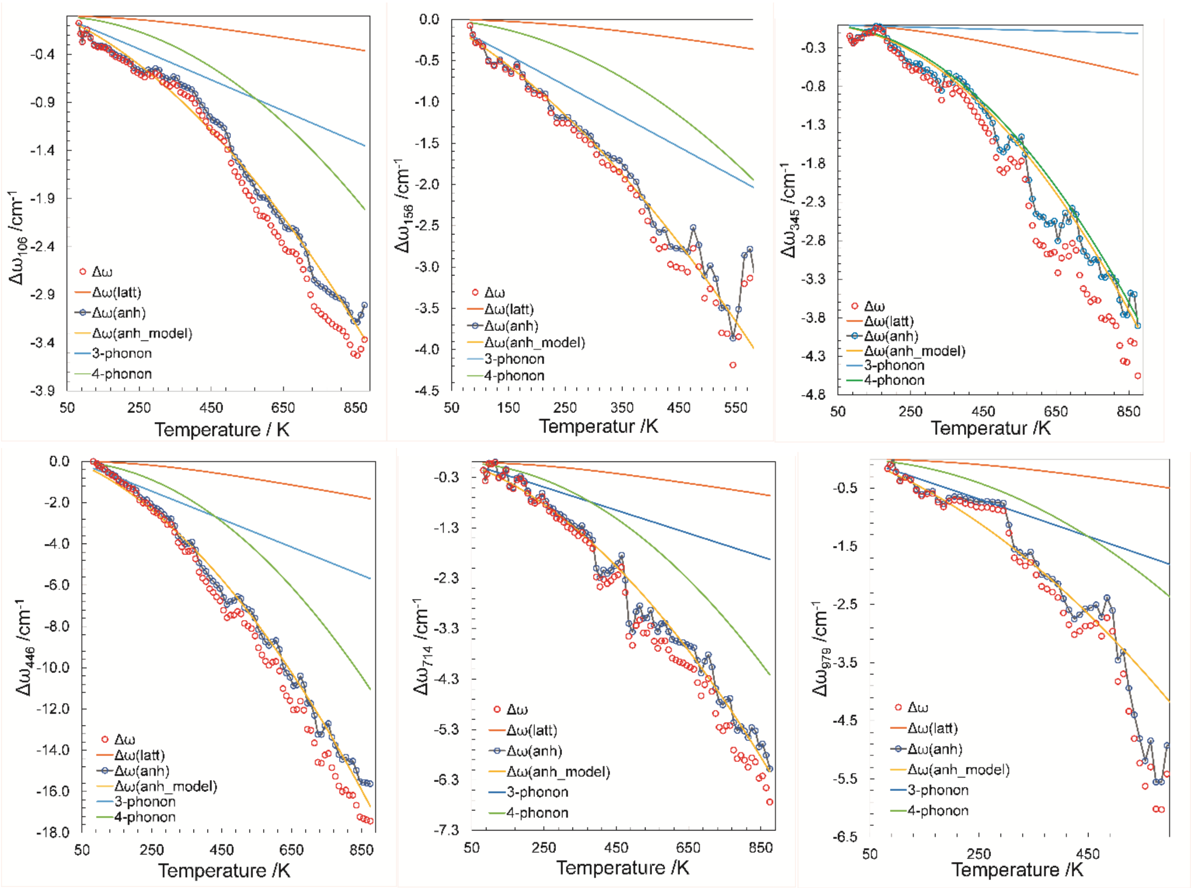

Figure 6: Temperature dependent change of phonon frequencies of some representative Raman bands of $SnAlBO_4$. The red circles, the blue circles combined with the grey solid line, and the orange solid line refer to observed frequency shift, frequency shift due to volume and anharmonic contributions, respectively. The solid lines in blue and green represent the model calculation based on the phonon-phonon interactions.

Low-temperature Mössbauer spectroscopy

The room temperature ^{119}Sn Mössbauer spectroscopy data were fitted with a single doublet at 2.93 (1) mm/s and 3.00 (1) mm/s for $SnAlBO_4$ and $SnGaBO_4$, respectively, as shown in **figure 7**. The isomer shift values unanimously support the oxidation state of tin (Sn(II) for both phases. Lowering the temperature down to 78(1) K clearly show two doublets still in the range of Sn(II) isomer shift values.

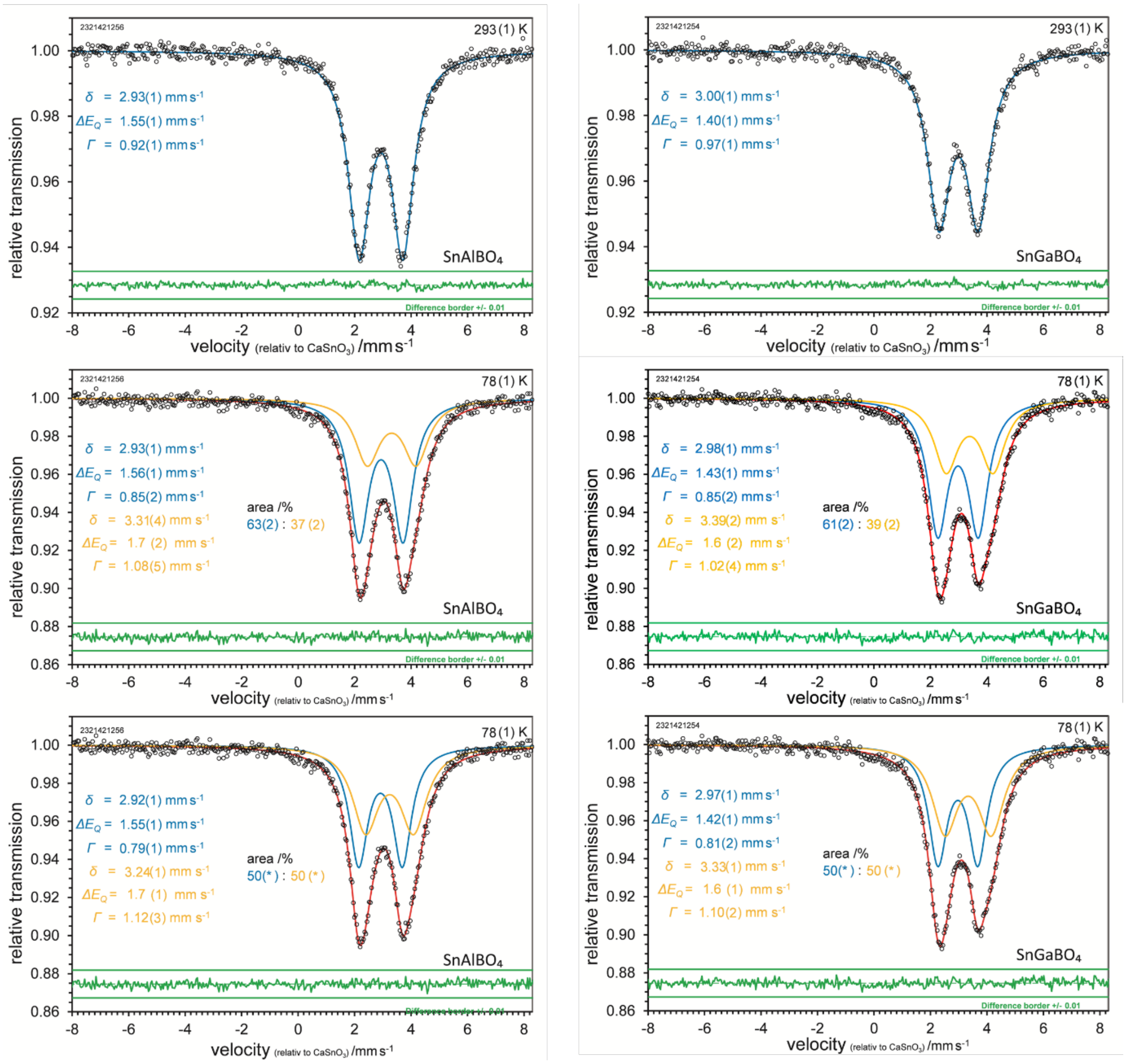

Figure 7: Experimental (open circles) and simulated (blue lines) ^{119}Sn Mössbauer spectra with their difference curves at room temperature and 78 K which is fitted either without any restrictions of the occupancy or a 50:50 setting.

The doublets can be fitted using two different models (**figure 7**), namely, 2/3:1/3 ratio and 1/2:1/2 ratio. Difference curve suggests that the former one shows slightly a better fit than the later one. Detailed of the fitting parameters are given in **table 3**. As published earlier [15], the room temperature calculated populations indicate that the 5s^2 LEPs keep a mixed (*s*-*p*) character. For both fittings at 78 K, the calculated population give a similar mixture of (*s*-*p*) character. This result is also supported by the isomer shift values of the measurements which are lower than for a free Sn(II) cation.

Table 3: Fitting parameters of ^{119}Sn Mössbauer spectroscopic measurements of SnAlBO$_4$ and SnGaBO$_4$ at room temperature [15] and at 78 K with two different fittings. δ = isomer shift, ΔE_Q = electric quadrupole splitting, Γ = experimental line width.

Parameter	**SnAlBO$_4$ (293 K) [15]**	**SnAlBO$_4$ (78 K;63:37)**		**SnAlBO$_4$ (78 K;50:50)**	
δ /(mm/s)	2.93(1)	2.93(1)	3.31(4)	2.92(1)	3.24(1)
ΔE_Q /(mm/s)	1.55(1)	1.56(1)	1.70(2)	1.55(1)	1.70(1)
Γ /(mm/s)	0.92(1)	0.85(2)	1.08(5)	0.79(1)	1.12(3)
n_s	1.22(1)	1.22(1)	1.36(1)	1.21(1)	1.33(1)
n_p	0.79(2)	0.79(2)	0.64(1)	0.79(2)	0.67(1)
(n_x+n_y)	0.26(1)	0.26(1)	0.15(2)	0.26(1)	0.61(1)
n_z	0.52(1)	0.52(3)	0.50(1)	0.52(1)	0.73(1)
Parameter	**SnGaBO$_4$ (293 K) [15]**	**SnGaBO$_4$ (78 K;61:39)**		**SnGaBO$_4$ (78 K;50:50)**	
δ /(mm/s)	3.00(1)	2.98(1)	3.39(2)	2.97(1)	3.33(1)
ΔE_Q /(mm/s)	1.40(1)	1.43(1)	1.60(2)	1.42(1)	1.60(1)
Γ /(mm/s)	0.97(1)	0.85(2)	1.02(4)	0.81(2)	1.10(2)
n_s	1.25(1)	1.23(3)	1.48(1)	1.23(1)	1.36(4)
n_p	0.76(1)	0.77(2)	0.52(1)	0.77(1)	0.64(2)
(n_x+n_y)	0.27(2)	0.82(5)	0.84(1)	0.79(1)	0.64(1)
n_z	0.49(2)	0.75(1)	0.61(3)	0.75(1)	0.48(1)

The reason for the two doublet is mainly a change in the symmetry of the Sn(II) of SnMBO$_4$ mullite-type phase. For the first signal with the lower isomer shift value, the (*s*-*p*) character is similar to the room temperature measurement. The second signal with the higher isomer shift value, the character shifted a bit to the (*s*) character. Hence, the influence of the s-orbital might be higher for the second one. Compared to the before mentioned DSC measurements, a likely phase transition of the mullite-type materials takes place which should be structural. Hence, the orthorhombic crystal structure is lowering the symmetry to a monoclinic one which influences the Mössbauer spectra.

4. Conclusion

While both the temperature-dependent XRPD and Raman spectroscopy, in particular at low temperatures, could not resolve possible phase transition, temperature-dependent ^{119}Sn Mössbauer data leave hints of phase transition below 80 K for both $SnAlBO_4$ and $SnGaBO_4$ phases. Modeling of lattice thermal expansion using DEA approach shows that the Ga-containing sample possesses slightly lower Deby temperature than that of the $SnAlBO_4$, which can be explained from the respective bulk modulus as the thermodynamic Grüneisen parameters are found to be temperature independent. The observation of two doublets at low temperatures in ^{119}Sn Mössbauer spectroscopy leads to a change in symmetry. This change is not noticeable in the other characterization methods before, hence Mössbauer spectroscopy is very sensitive to the environment of Sn^{2+}. This observation could not be done in the in-house XRPD measurements and therefore, one future work is to investigate this phenomenon with for example synchrotron measurements.

Acknowledgement

We gratefully thank the German science foundation (Deutsche Forschungsgemeinschaft, DFG) under grant number GE1981/14-1 for the financial support. The University of Bremen is cordially acknowledged for technical and administrative supports.

Reference

1. K. Ghosh, M.M. Murshed, T.M. Gesing, Synthesis and characterization of $(Bi_{1-x}R_x)_2Mn_4O_{10}$: structural, spectroscopic and thermogravimetric analyses for R = Nd, Sm and Eu, Journal of Materials Science 54(21) (2019) 13651-13659. DOI:10.1007/s10853-019-03852-7
2. M. Burianek, M. Mühlberg, M. Woll, M. Schmücker, T.M. Gesing, H. Schneider, Single-crystal growth and characterization of mullite-type orthorhombic $Bi_2M_4O_9$ (M = Al^{3+}, Ga^{3+}, Fe^{3+}), Crystal Research and Technology 44(10) (2009) 1156-1162. DOI:10.1002/crat.200900465
3. M. Curti, A. Kirsch, L.I. Granone, F. Tarasi, G. López-Robledo, D.W. Bahnemann, M.M. Murshed, T.M. Gesing, C.B. Mendive, Visible-Light Photocatalysis with Mullite-Type

$Bi_2(Al_{1-x}Fe_x)_4O_9$: Striking the Balance between Bandgap Narrowing and Conduction Band Lowering, ACS Catalysis 8(9) (2018) 8844-8855. DOI:10.1021/acscatal.8b01210

4. A. Beran, E. Libowitzky, M. Burianek, M. Mühlberg, C. Pecharromán, H. Schneider, Infrared and Raman spectroscopy of mullite-type $Bi_2Ga_4O_9$, Crystal Research and Technology 43(11) (2008) 1230-1239. DOI:10.1002/crat.200800396
5. T. Debnath, C.H. Rüscher, P. Fielitz, S. Ohmann, G. Borchardt, Series of compositions $Bi_2(M'_xM_{1-x})_4O_9$ (M', M=Al, Ga, Fe; $0 \leq x \leq 1$) with mullite-type crystal structure: Synthesis, characterization and $^{18}O/^{16}O$ exchange experiment, Journal of Solid State Chemistry 183(11) (2010) 2582-2588. DOI:10.1016/j.jssc.2010.07.019
6. M. Gogolin, M.M. Murshed, M. Ende, R. Miletich, T.M. Gesing, Uniaxial negative thermal expansion in the mullite- and borax-type $PbAlBO_4$ polymorphs, Journal of Materials Science 55(1) (2019) 177-190. DOI:10.1007/s10853-019-04013-6
7. M. Curti, M.M. Murshed, T. Bredow, D.W. Bahnemann, T.M. Gesing, C.B. Mendive, Elastic, phononic, magnetic and electronic properties of quasi-one-dimensional $PbFeBO_4$, Journal of Materials Science 54(21) (2019) 13579-13593. DOI:10.1007/s10853-019-03866-1
8. T.M. Gesing, C.B. Mendive, M. Curti, D. Hansmann, G. Nénert, P.E. Kalita, K.E. Lipinska, A. Huq, A.L. Cornelius, M.M. Murshed, Structural properties of mullite-type $Pb(Al_{1-x}Mn_x)BO_4$, Zeitschrift für Kristallographie - Crystalline Materials 228(10) (2013). DOI:10.1524/zkri.2013.1640
9. J. Head, P. Manuel, F. Orlandi, M. Jeong, M.R. Lees, R. Li, C. Greaves, Structural, magnetic, magnetocaloric, and magnetostrictive Properties of $Pb_{1-x}Sr_xMnBO_4$ (x = 0, 0.5, and 1.0), Chemistry of Materials 32(23) (2020) 10184-10199. DOI:10.1021/acs.chemmater.0c03701
10. H. Schneider, Komarneni, S., Mullite, Wiley2005.
11. H. Schneider, E. Eberhard, Thermal expansion of Mullite, Journal of the American Ceramic Society 73(7) (1990) 2073-2076. DOI:10.1111/j.1151-2916.1990.tb05270.x
12. K.M. Kosyl, W. Paszkowicz, A.N. Shekhovtsov, M.B. Kosmyna, J. Antonowicz, A. Olczak, A.N. Fitch, Variation of cation distribution with temperature and its consequences on thermal expansion for $Ca_3Eu_2(BO_3)_4$, Acta Crystallogr B Struct Sci Cryst Eng Mater 76(Pt 4) (2020) 554-562. DOI:10.1107/S2052520620006757
13. R.S. Bubnova, S.K. Filatov, High-temperature borate crystal chemistry, Zeitschrift für Kristallographie - Crystalline Materials 228(9) (2013). DOI:10.1524/zkri.2013.1646
14. M. Curti, C.B. Mendive, T. Bredow, M. Mangir Murshed, T.M. Gesing, Structural, vibrational and electronic properties of $SnMBO_4$ (M = Al, Ga): a predictive hybrid DFT study, J Phys Condens Matter 31(34) (2019) 345701. DOI:10.1088/1361-648X/ab20a1
15. S. Wittmann, M.M. Murshed, V. Bilovol, A. Koldemir, R. Pöttgen, U.G. Nielsen, T.M. Gesing, Mullite-type $EMBO_4$: synthesis, structural, optical, and vibrational properties of rare tin(II) borates with M = Al and Ga, Journal of the American Ceramic Society 107(2) (2023) 1302-1314. DOI:10.1111/jace.19476
16. M. Curti, T.M. Gesing, M.M. Murshed, T. Bredow, C.B. Mendive, Liebau density vector: a new approach to characterize lone electron pairs in mullite-type materials, Zeitschrift für Kristallographie - Crystalline Materials 228(12) (2013). DOI:10.1524/zkri.2013.1686
17. M. Mangir Murshed, C.B. Mendive, M. Curti, M. Šehović, A. Friedrich, M. Fischer, T.M. Gesing, Thermal expansion of mullite-type $Bi_2Al_4O_9$: A study by X-ray diffraction, vibrational spectroscopy and density functional theory, Journal of Solid State Chemistry 229 (2015) 87-96. DOI:10.1016/j.jssc.2015.05.010
18. R.W. Cheary, A. Coelho, A fundamental parameters approach to X-ray line-profile fitting, Journal of Applied Crystallography 25(2) (1992) 109-121. DOI:10.1107/S0021889891010804
19. M.M. Murshed, A. Rusen, R.X. Fischer, T.M. Gesing, Transition-metal substitution in

$PbAlBO_4$: Synthesis, structural and spectroscopic studies of manganese containing phases, Materials Research Bulletin 47(6) (2012) 1323-1330. DOI:10.1016/j.materresbull.2012.03.014

20. D. Richard, M. Ferrand, G.J. Kearley, Analysis and visualisation of neutron-scattering data, Journal of Neutron Research 4 (1996) 33-39. DOI:10.1080/10238169608200065
21. R.A. Brand, Normos Programs (SITE-DIST), in: D. University (Ed.) 1991.
22. C. Corporation, CorelDRAW Graphic Suite 2017, Ottowa Canada, 2017.
23. P.J.M. Gielisse, W.R. Foster, The System Al_2O_3–B_2O_3, Nature 195(4836) (1962) 69-70. DOI:10.1038/195069a0
24. H.R. Glyde, Relation of vacancy formation and migration energies to the Debye temperature in solids, J. Phys. Chem. Solids 28(10) (1967) 2061-2065. DOI:10.1016/0022-3697(67)90182-5
25. P. Mishra, Variation of Debye temperature with size of nanoparticles, AIP Conference Proceedings 2220 (2020). DOI:10.1063/5.0002346
26. M. Wolpmann, L. Robben, T.M. Gesing, Halide-sodalites: thermal expansion, decomposition and the Lindemann criterion, Z. Kristallor.-Cryst. Mater. 237(1-3) (2022) 39-50. DOI:10.1515/zkri-2022-0004
27. P.G. Klemens, Anharmonic Decay of Optical Phonons, Physical Review 148(2) (1966) 845-848. DOI:10.1103/PhysRev.148.845
28. M.M. Murshed, T.M. Gesing, Anisotropic thermal expansion and anharmonic phonon behavior of mullite-type $Bi_2Ga_4O_9$, Materials Research Bulletin 48(9) (2013) 3284-3291. DOI:10.1016/j.materresbull.2013.05.007
29. M.M. Murshed, C.B. Mendive, M. Curti, G. Nénert, P.E. Kalita, K. Lipinska, A.L. Cornelius, A. Huq, T.M. Gesing, Anisotropic lattice thermal expansion of $PbFeBO_4$: A study by X-ray and neutron diffraction, Raman spectroscopy and DFT calculations, Materials Research Bulletin 59 (2014) 170-178. DOI:10.1016/j.materresbull.2014.07.005

Supporting information

Temperature dependent characterization of $SnAlBO_4$ and $SnGaBO_4$ mullite-type ceramics

Sarah Wittmann[1], M. Mangir Murshed[1,2*], Kowsik Ghosh[1†], Aylin Koldemir[3], Rainer Pöttgen[3], Thorsten M. Gesing[1,2]

[1]University of Bremen, Institute of Inorganic Chemistry and Crystallography, Leobener Straße 7, D-28359 Bremen, Germany

[2]University of Bremen, MAPEX Center for Materials and Processes, Bibliothekstraße 1, D-28359 Bremen, Germany

[3]Universität Münster, Institute für Anorganische und Analytische Chemie, Corrensstrasse 30, D-48149 Münster, Germany

ORCID:

SW:	0000-0003-1404-3434
MMM:	0000-0002-9063-372X
KG:	0000-0003-2622-7046
AK:	0009-0004-3819-3853
RP:	0000-0003-0962-279X
TMG:	0000-0002-4119-2219

*Corresponding author: murshed@uni-bremen.de, phone: +49 (0)421 218 63144

†Present address: Department of Chemistry and Biochemistry, University of Delaware, Newark, Delaware, USA.

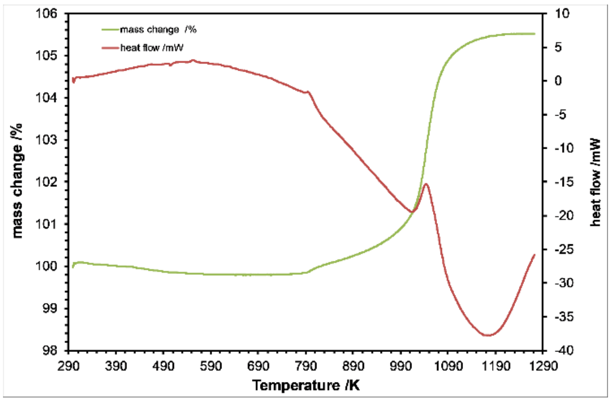

Figure S1: Temperature-dependent mass change (green) and heat flow (red) $SnGaBO_4$.

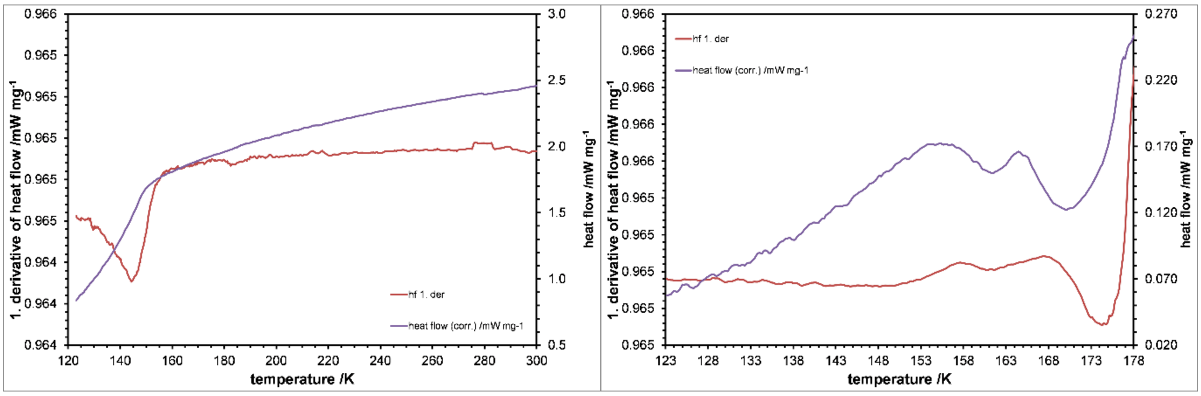

Figure S2: DSC plots of $SnGaBO_4$ with the heat flow (violet) and its first derivative (red).

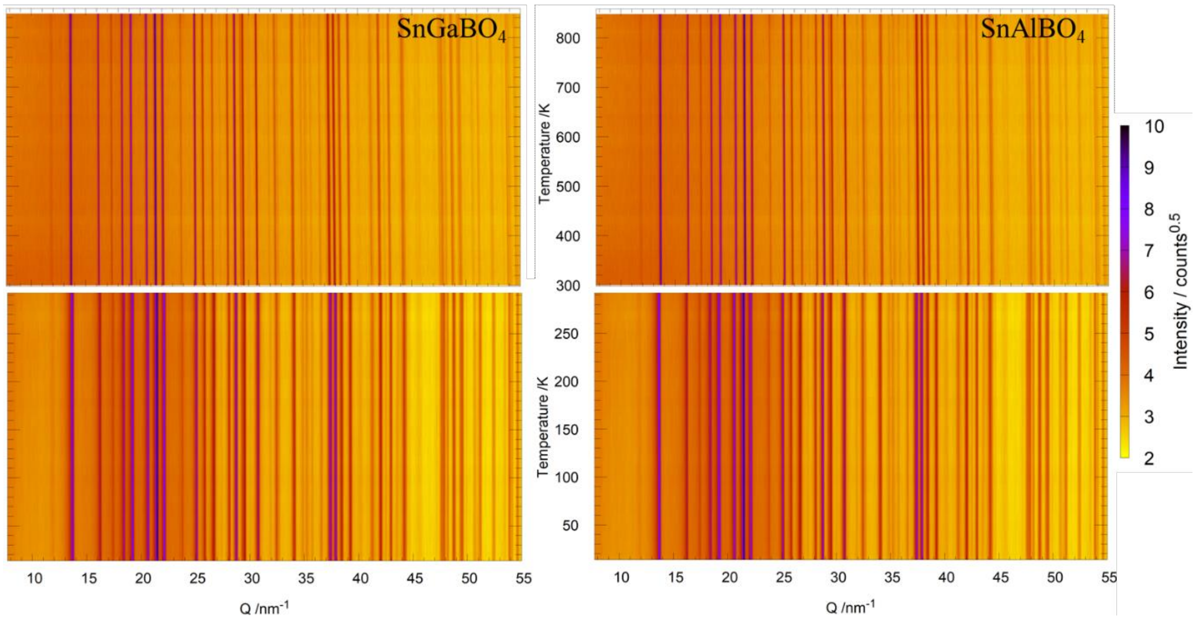

Figure S3: 2D plot of temperature-dependent X-ray powder diffraction pattern of $SnGaBO_4$ (left) and $SnAlBO_4$ (right).

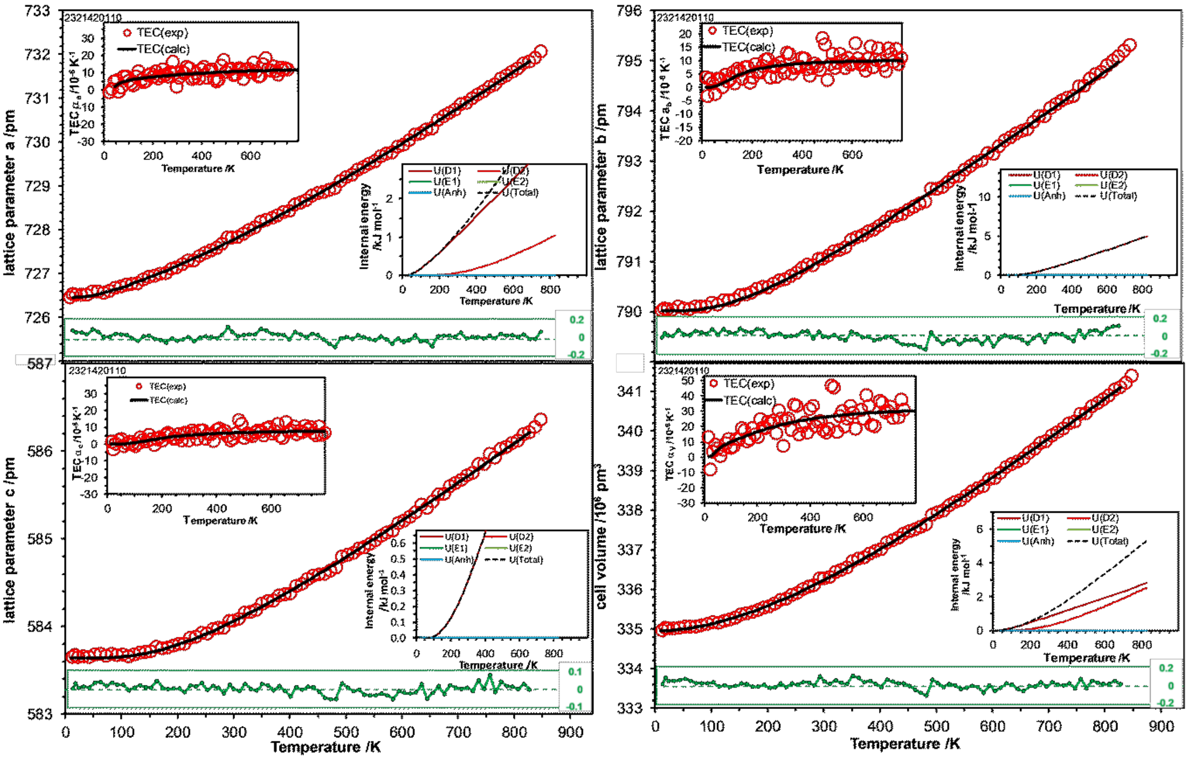

Figure S4: Debye-Einstein-Anharmonicity (DEA) fits of the metric parameters of SnGaBO₄. The respective thermal expansion coefficients (TECs) and the Debye energy terms are seen as insets.

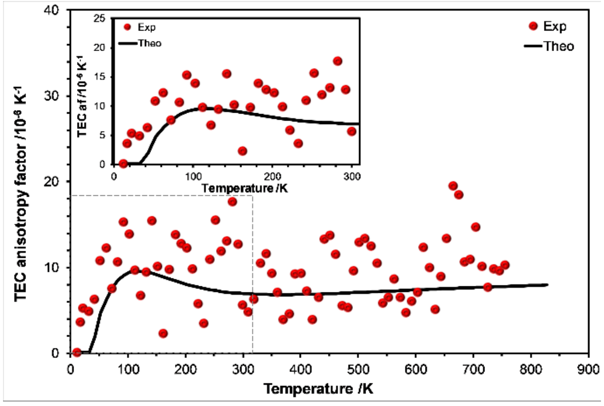

Figure S5: Temperature-dependent thermal expansion coefficient (TEC) anisotropy parameter of SnGaBO₄.

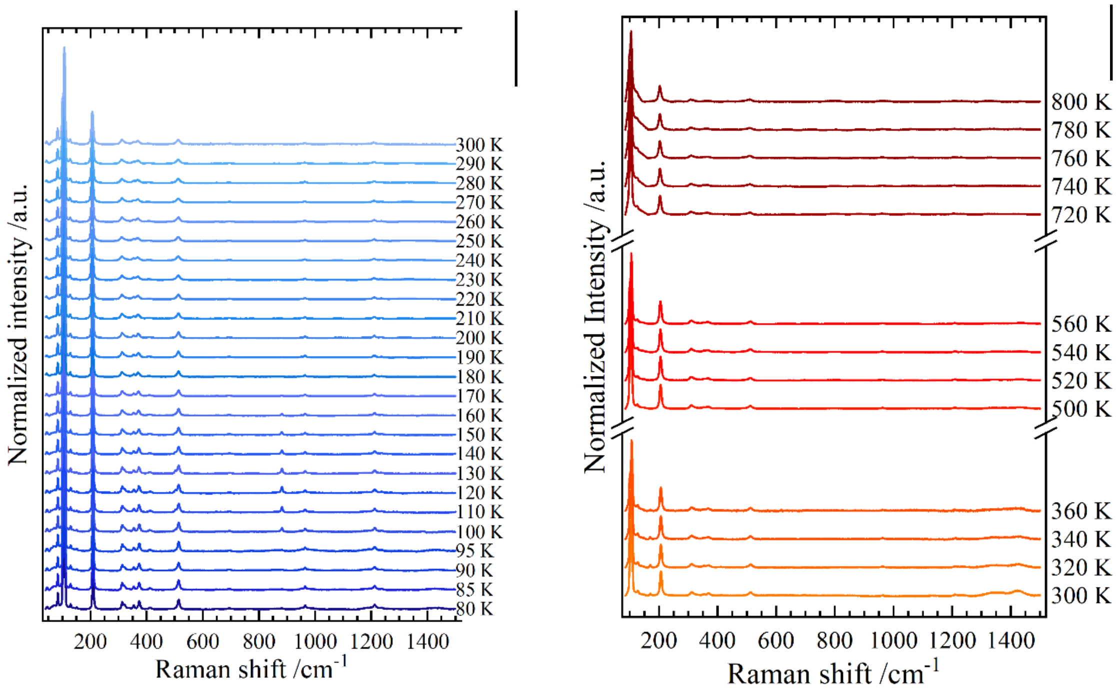

Figure S6: Low-temperature (left) and high-temperature (right) Raman spectra of $SnGaBO_4$.

Table S1: Selective Raman frequencies of $SnGaBO_4$ at 0 K, their corresponding mode Grüneisen parameter together with the fitting parameters

ω_{i0} /cm^{-1}	$(\gamma_i)_T$	A /cm^{-1}	B /cm^{-1}
126.5	0.71	-0.23(1)	-0.005(2)
151.6	1.08	-0.37(1)	0
321.6	0.36	-0.31(3)	-0.001(5)
373.7	0.52	-0.30(1)	-0.005(1)
960.0	0.09	-0.13(5)	-0.001(1)
1213	0.12	-0.32(5)	-0.001(4)

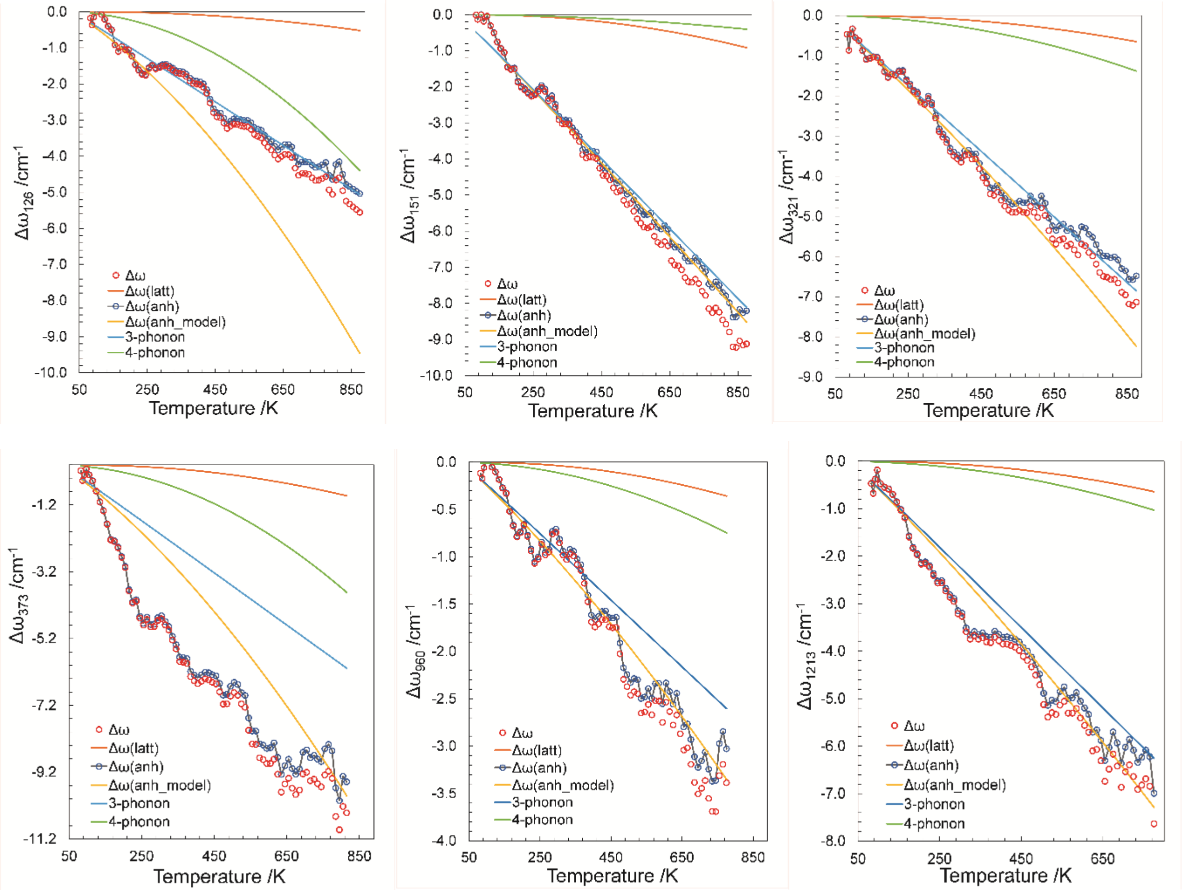

Figure S8: Temperature dependent change of phonon frequencies of some representative Raman bands of $SnGaBO_4$. The red circles, the blue circles combined with the grey solid line, and the orange solid line refer to observed frequency shift, frequency shift due to volume and anharmonic contributions, respectively. The solid lines in blue and green represent the model calculation based on the phonon-phonon interactions.

Reference

1. M. Burianek, M. Mühlberg, M. Woll, M. Schmücker, T.M. Gesing, H. Schneider, Single-crystal growth and characterization of mullite-type orthorhombic $Bi_2M_4O_9$ (M = Al^{3+}, Ga^{3+}, Fe^{3+}), Crystal Research and Technology 44(10) (2009) 1156-1162. DOI:10.1002/crat.200900465
2. M. Curti, A. Kirsch, L.I. Granone, F. Tarasi, G. López-Robledo, D.W. Bahnemann, M.M. Murshed, T.M. Gesing, C.B. Mendive, Visible-Light Photocatalysis with Mullite-Type $Bi_2(Al_{1-x}Fe_x)_4O_9$: Striking the Balance between Bandgap Narrowing and Conduction Band Lowering, ACS Catalysis 8(9) (2018) 8844-8855. DOI:10.1021/acscatal.8b01210
3. T.M. Gesing, C.B. Mendive, M. Curti, D. Hansmann, G. Nénert, P.E. Kalita, K.E. Lipinska, A. Huq, A.L. Cornelius, M.M. Murshed, Structural properties of mullite-type $Pb(Al_{1-x}Mn_x)BO_4$, Zeitschrift für Kristallographie - Crystalline Materials 228(10) (2013). DOI:10.1524/zkri.2013.1640

Chapter 4 - Synthesis and characterization of mullite-type $Sn(Cr_{1-x}V_x)BO_4$ for x = 0 – 1.0

Based on redox potentials as discussed in **chapter 2,** other trivalent metal cations such as V^{3+} and Cr^{3+} are predicted to be incorporated in the mullite-type $SnMBO_4$ ceramics. Earlier $PbCrBO_4$ was reported with detailed magnetic characterizations [1-3]. However, due to the toxicity of lead, the replacement by tin is of crucial importance. Sn(II) possesses stereochemically active LEP. Hence, the influence of the LEP in both $SnVBO_4$ and $SnCrBO_4$ phases can be compared with those of early reported $SnAlBO_4$ and $SnGaBO_4$ phases. Moreover, the vibrational and magnetic properties of these phases can be compared with those of the $PbCrBO_4$, $PbMnBO_4$, and $PbFeBO_4$ compounds [2-12]. The manuscript *in-preparation* covers the overall investigations of the solid solution $Sn(Cr_{1-x}V_x)BO_4$ for x = 0 -1.0.

Synthesis and characterization of mullite-type $Sn(Cr_{1-x}V_x)BO_4$ for $x = 0- 1.0$.

Sarah Wittmann[1], M. Mangir Murshed[1,2*], Aylin Koldemir[3], Rainer Pöttgen[3], Thorsten M. Gesing[1,2]

[1]University of Bremen, Institute of Inorganic Chemistry and Crystallography, Leobener Straße 7, D-28359 Bremen, Germany

[2]University of Bremen, MAPEX Center for Materials and Processes, Bibliothekstraße 1, D-28359 Bremen, Germany

[3]University of Münster, Institute of Inorganic and Analytical Chemistry, Corrensstrasse 30, D-48149 Münster, Germany

*Corresponding author: murshed@uni-bremen.de, phone: +49 (0)421 218 63144

ORCID:

SW:	0000-0003-1404-3434
MMM:	0000-0002-9063-372X
AK:	0009-0004-3819-3853
RP:	0000-0003-0962-279X
TMG:	0000-0002-4119-2219

Abstract

The susceptibility of either oxidation into tin(IV), or disproportionation into tin(IV) and elemental tin(0) limits the study of metal tin-(II)-borates. We report mullite-type $SnCrBO_4$ and $SnVBO_4$ ceramics synthesized in sealed quartz tubes by conventional solid-state method. X-ray powder diffraction data Rietveld refinement confirmed that both compounds are isostructural to $PbMBO_4$ phases for M = Al, Ga, Cr, Mn and Fe. The end-members show a complete miscibility within the $Sn(Cr_{1-x}V_x)BO_4$ solid solution. Both the microstructural (average crystallite size, macrostrain, degree of crystallinity) and crystal structural (metric, bond length, polyhedral volume, polyhedral distortion) parameters are observed with respect to the compositional x-value. The stereochemical activity of the $5s^2$ lone electron pairs (LEPs) of Sn^{2+} cation has been measured using Wang-Liebau eccentricity (WLE) parameter. The structural features are complemented by ^{119}Sn Mössbauer, Raman, FTIR and UV/Vis spectroscopy. The ^{119}Sn Mössbauer isomer shifts and the quadrupole splitting values confirm the SnO_4 coordination and Sn(II) valence states. The vibrational properties are observed using Raman and FTIR spectroscopy and discussed from group theoretical analysis to mode assignments. The electronic band gap has been calculated from the UV/Vis diffuse reflectance spectra, which increases with successive decrease of the cationic radius from V to Cr. Temperature-dependent inverse DC magnetic susceptibility suggests that both $SnCrBO_4$ are antiferromagnetic with Neel temperature of 20 K, respectively. The structural, spectroscopic, and magnetic properties are monitored with respect to compositional x-value.

Keywords: metal tin-(II)-borate, crystal structure, vibrational property, magnetic property, electronic property

1. Introduction

The mullite-type $PbMBO_4$, so called O8-phases have drawn considerable attention due to its interesting thermal [1-3], mechanical [4, 5], electrical [6, 7], crystal-chemical [8-10] and optical [11-13] properties. Although the susceptible oxidation of Sn^{2+} to Sn^{4+} [14] posed challenge for the solid state synthesis recent reports on $SnAlBO_4$ and $SnGaBO_4$ ceramics added two members of the O8-family [14]. Indeed, such an attempt successfully replace the environmental and health hazard Pb-containing O8-phases.

The crystal structure of $SnMBO_4$ [14] (M = Al and Ga) was described using the space group setting *Pnam* for a better comparison of the crystal-chemical properties with those of the mullite and other mullite-type ceramics. The edge-sharing MO_6 octahedra run along the crystallographic **c**-axis, which are bridged by the trigonal planar BO_3 and distorted pyramid SnO_4 [15-17]. The Sn-atom locates in the 1D channels where the $5s^2$ lone electron pairs (LEPs) of Sn^{2+} [18] are stereochemically active. Since two edges (O11-O2) of the MO_6 octahedra and two vertices of BO_3 are linked to the distorted SnO_4 square pyramid, the stereochemical activity of Sn^{2+} heavily influences all the associated coordination , thus the overall crystal structure [18]. Moreover, since the asymmetric angels (M-O11-M and M-O12-M) serve for the M-M bond lengths which are of crucial importance for the magnetic couplings [19], the degree of stereochemical activity of the Sn^{2+} cation can be understood, playing pivotal roles for the magnetic properties of the phases. According to Goodenough–Kanamori–Anderson rules [20-22], the nearest-neighbour M–M spin exchange interaction changes from antiferromagnetic (AFM) to ferromagnetic (FM) when the M–O–M angle changes from 180° to 90°. DFT study suggests three main exchange interactions can better describe the magnetic property of some isostructural $PbMBO_4$ compounds [23]. Neutron powder diffraction [17] demonstrated that both $PbCrBO_4$ and $PbFeBO_4$ follow long-range AFM orderings in the **c**-axis, where the MO_6-chains are ferromagnetically coupled. However, both the MO_6 intra-chain and inter-chain couplings are observed for $PbMnBO_4$ at a Curie temperature of 31 K. Replacing the non-magnetic M-cations in $SnMBO_4$ [14] with magnetic V^{3+} and Cr^{3+} would not only introduce two members in O8-family but also offer interesting magnetic properties. The present study reports the synthesis of $SnVBO_4$ and $SnCrBO_4$ compounds followed by their structural, spectroscopic, and magnetic characterizations. Their solid solution $Sn(Cr_{1-x}V_x)BO_4$ for x = 0 – 1.0 with a chemical slice of x = 0.1 would provide a miscibility between the end-members, leading to follow the evolution of a given property with respect to compositional x-value.

2. Experimental

2.1. Synthesis

For the synthesis of a given composition of $Sn(Cr_{1-x}V_x)BO_4$, stoichiometric mixture of SnO, Sn, M_2O_3 (M = V, Cr) and an excess (80 Wt%) of B_2O_3 were mixed and put into a quartz tube which was already preheated at 1073 K for at least 12 h. The mixture in the quartz tube (still open) was further heated at 473 K for two hours to reduce the absorbed moisture. The internal pressure of the quartz tube was then reduced to 10^{-7} MPa. During the dynamic vacuum process, the tube was sealed. The sealed samples were then placed into an oven and heated at 1023 K for three days with a heating and cooling rate of 200 K/h to obtain a micro-crystalline powder sample. Of notes, a higher temperature (1123 K) and longer (five days) reaction time was required to get a phase pure polycrystalline end-member $SnCrBO_4$.

2.2. X-ray diffraction

X-ray powder diffraction (XRPD)

X-ray powder diffraction (XRPD) data were measured on a Stoe Stadi MP diffractometer (Stoe & Cie. GmbH, Darmstadt, Germany) using Debye-Scherrer geometry. The samples were put into a borosilicate glass capillary of 0.5 mm outer diameter and 0.01 mm wall thickness.

Homogeneous X-ray irradiation on the powders was achieved through sample spinning. The Ge(111) monochromatized MoKα_1 radiation and a Mythen-1K detector were used. Data were collected at ambient conditions between 3.000° and 85.195° 2θ with a 2θ step size of 0.005° and a data collection time of 477.0 s/step. A substraction of the background contribution was necessary due to a high background of the sample container and air scattering. The XRPD measurements of the solid solutions of $Sn(Cr_{1-x}V_x)BO_4$ were carried out on a Bruker D8 discover diffractometer using Bragg-Brentano geometry with a $CuK_{\alpha 1}$ and $CuK_{\alpha 2}$ radiation. The data were collected at ambient conditions in the 2θ range from 5 to 85° with a step size of 0.0167 and a data collection time of 0.30 s/step.

The fundamental parameter approach, where the fundamental parameters were fitted against a LaB_6 standard material, was applied for the Rietveld refinement using the "Diffrac^{Plus} Topas 6" software (Bruker AXS GmbH, Karlsruhe, Germany). The starting atomic coordinates were taken from the single crystal data of $PbAlBO_4$ [24], where the Pb^{2+} was replaced by Sn^{2+} in the asymmetric unit cell. During the Rietveld refinement the background, unit-cell parameters, atomic coordinates, isotropic displacement parameters (B) , average crystallite size (ACS) and micro-strain (MS) parameters were optimized for the description of the reflection profile of the phases.

2.3. Spectroscopy

Raman

Raman spectra were recorded on a LabRam ARAMIS (Horiba Jobin Yvon) Micro_Raman Spectrometer equipped with laser working at 532 nm and less than 20 mW. The use of a 50× objective (Olympus) with a numerical aperture of 0.55 provides focus spot of about 2 μm diameter when closing the confocal hole to 200 μm. Data were collected in the range of 50 cm^{-1} to 1500 cm^{-1} with a spectral resolution of approximately 1.2 cm^{-1} using a grating of 1800 grooves /mm and a thermoelectrically-cooled CCD detector (Synapse, 1024×256 pixels).

Fourier-transformed infrared (FTIR)

FTIR data were measured on a Bruker VERTEX 80v spectrometer using the standard KBr method (2 mg sample in 200 mg KBr) in the mid-infrared range between 370 cm^{-1} and 4000 cm^{-1}. All observed IR spectra are plotted in arbitrary units (a.u.) according to $-\ln (I/I_O)$, where I and I_O refer to transmitted intensity of the sample with KBr and pure KBr disc, respectively. The peaks were fitted using the LabSpec 5 suite (Horiba Jobin Yvon).

UV/Vis diffuse reflectance

UV/Vis diffuse reflectance spectra were obtained on a Shimadzu UV/Vis spectrophotometer UV-2600 equipped with an ISR-2600 plus two-detector integrating sphere. Barium sulfate powder was used for background reflectance as 100 %. Reflectance data were over the photonic wavelength range between 190 nm and 800 nm with a step of 1 nm. The optical bandgap was calculated using the derivation of the absorption spectrum fitting (DASF) method [25] that includes the combined reflectance, absorbance and Tauc calculation, resulting in the so-called RATD (reflectance-absorbance-Tauc-DASF) analysis [26].

Mössbauer

For the ^{119}Sn Mössbauer spectroscopic investigations a Ca^{119m}SnO$_3$ source with γ-radiation at 23.875 keV was used. A thin palladium foil (thickness 0.05 mm) was placed between the sample and the detector to reduce the K X-rays emitted by the source. The measurements were conducted in usual transmission geometry. The source and the metal tin-(II)-borates were kept at room temperature. The samples were mixed with α-quartz and enclosed in thin-walled PMMA containers. To obtain suitable integral fits for the ^{119}Sn spectra the WinNormos of Igor6 program package [27] was used and graphical editing was done with the program CorelDRAW2017 [28].

2.4. Magnetic susceptibility

Temperature-dependent DC magnetic susceptibility measurements were carried out with a Magnetic Property Measurement System MPMS-XL7 (Quantum Design, San Diego, USA) using the field-cooling process at a magnetic field of 0.01 T. The polycrystalline samples were sealed in a gel capsule and attached to a nonmagnetic sample holder. Data were collected between 300 K and 2 K with an incremental cooling rate of 2 K/min. The magnetic signal was well above the standard deviations, where the order of the instrumental noise was estimated to be $\sim 10^{-11}\mathrm{Am}^2$.

3. Results and discussion

Synthesis

Polycrystalline samples of green $SnCrBO_4$ and dark-grey $SnVBO_4$ were synthesized using the sealed quartz tube method to avoid the oxidation of Sn^{2+} to Sn^{4+}. The degree of crystallinity was obtained to be 91(4) % and 99(1) % for $SnCrBO_4$ and $SnVBO_4$, respectively. The phase purity was proven by Rietveld refinement. The Cr-containing mullite-type phase was obtained along with a secondary phase of Cr_2O_3 (5(3) %), and the V-containing phase with 3(2) % Sn. Each member of the solid solution $Sn(Cr_{1-x}V_x)BO_4$, was synthesized at lower temperature of 1073 K compared to $SnCrBO_4$. Almost phase pure members were obtained for a given x-value along with slight impurities of SnO_2 or elementary tin.

Crystal structure

XRPD data Rietveld refinements confirm that both $SnVBO_4$ and $SnCrBO_4$ compounds crystallize in the mullite-type structure in the space group P*nam*. The Rietveld plots are shown in **figure 1** and **figure S1** (Supplementary Information), respectively for $SnCrBO_4$ and $SnVBO_4$. The comparative metric parameters are given in **table 1**, and details of the crystal structural information are available in **table 2** and for the solid solutions in **figure S2 – S10** and in **table S1**.

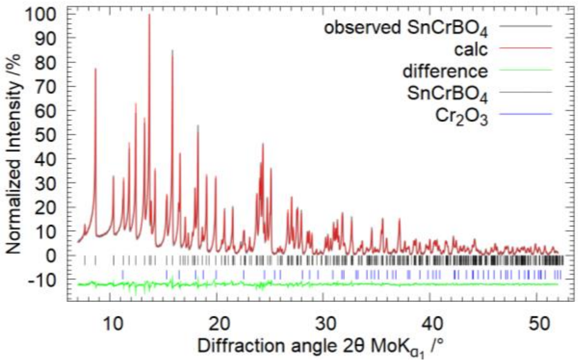

Figure 1: Representative Rietveld plot of $SnCrBO_4$ with observed, calculated and difference curves. The vertical bars show the respective Bragg-peaks of $SnCrBO_4$ and Cr_2O_3.

Table 1: X-ray powder data of Rietveld refinements of $SnCrBO_4$ and $SnVBO_4$ along with the average crystallite size (ACS) and the microstrain (MS).

Empirical formula	$SnCrBO_4$	$SnVBO_4$
Formula weight /(g/mol)	245.51(1)	244.46(1)
Temperature /K	298(2)	298(1)
Instrument, radiation	Stoe MP, Mo $K_{\alpha 1}$	
Geometry	Debye-Scherrer, glass capillary	
Crystal system	orthorhombic	
Space group	*Pnam*	*Pnam*
a /pm	721.71(5)	728.54(2)
b /pm	785.20(1)	791.13(3)
c /pm	587.48(4)	586.11(2)
V /10^6 pm^3	332.92(4)	337.82(2)
ACS /nm	316(7)	340(2)
MS /%	0.153(1)	0.290(3)
D_{calc} (g/cm^3)	4.89(4)	4.67(3)
R_{wp} /%	3.45	4.41
Goodness-of-fit (GOF) on F^2	1.86	1.97

Table 2: Crystal structural parameters of $SnCrBO_4$ and $SnVBO_4$ in the orthorhombic setting of the space group Pnam.

$SnCrBO_4$

Atom	Site	*x*	*y*	*z*	B /10^4 pm^2
Sn1	4*c*	0.0890(2)	0.3626(3)	¼	0.31(5)
Cr1	4*a*	0	0	0	0.25(12)
B1	4*c*	0.2853(4)	0.7739(4)	¼	0.83(8)
O11	4*c*	0.3969(4)	0.3664(5)	¼	0.25(3)
O12	4*c*	0.1624(4)	0.9104(4)	¼	0.31(5)
O2	8*d*	0.3389(3)	0.7027(3)	0.0449(3)	0.38(3)

$SnVBO_4$

Atom	Site	*x*	*y*	*z*	B /10^4 pm^2
Sn1	4*c*	0.0925(3)	0.3607(3)	¼	0.44(4)
V1	4*a*	0	0	0	0.25(7)
B1	4*c*	0.3640(6)	0.7810(6)	¼	0.30(11)
O11	4*c*	0.4058(9)	0.3645(8)	¼	0.90(2)
O12	4*c*	0.1594(10)	0.8890(2)	¼	3.00(4)
O2	8*d*	0.3375(7)	0.6994(3)	0.0473(9)	0.60(2)

While the *c*- lattice parameter differs only 1 pm between $SnVBO_4$ and $SnCrBO_4$, the *a*- and *b*-lattice parameters of $SnVBO_4$ are found to be larger than those of $SnCrBO_4$. Indeed, the larger V^{3+} cation [29] ensures larger VO_6 octahedral volume than that of CrO_6. As such, the solid solution $SnV_xCr_{1-x}BO_4$ follows the Vegard's rule [30] in changing the lattice parameters with increasing compositional x-value, as shown in **figure 2**. The slight departure elsewhere from the Vegard's line can be understood in terms of the amount of a given minor phase which slightly shifts the chemical composition (x).

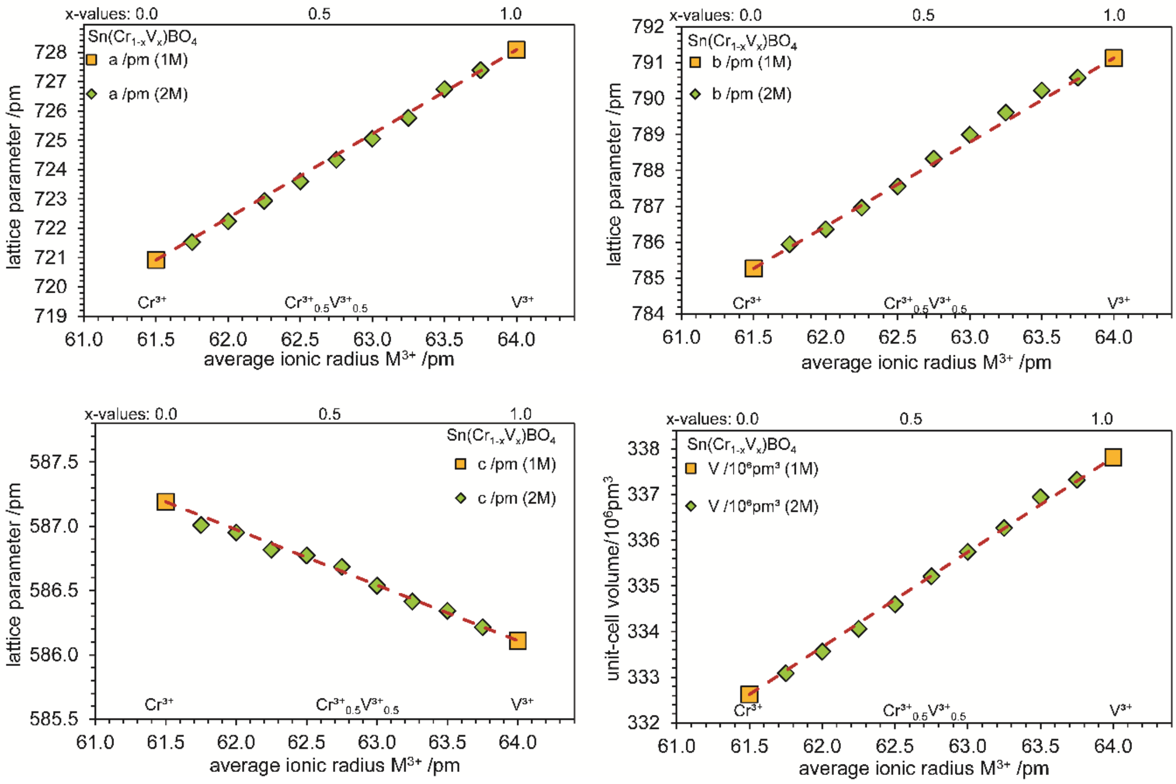

Figure 2: Trend of the metric parameters of the solid solutions of Sn$(Cr_{1-x}V_x)B$O4: a (top left), b (top right), and c (bottom left) lattice parameter, and the cell volume (bottom right).

The interatomic bond distances for the end members are given in **table 3** where the average Sn -O bond length is similar compared to the already published results of $SnAlBO_4$ and $SnGaBO_4$ [14]. Of notes, the rigidity of the B – O bond length is noticeable with a range of 133 pm to 150 pm. The octahedral structure of the MO6 octahedra has three different bond length which are slightly larger for $SnVBO_4$ than for $SnCrBO_4$ which was expected based on the lager cationic radius of V^{3+} than Cr^{3+}.

Table 3: Selective bond distances, bond-valence sum (BVS), and Wang-Liebau eccentricity parameter of SnO_4 of the constituent elements in $SnMBO_4$.

Compound	**Sn-O /pm**	**M-O /pm**	**B-O /pm**	**BVS /v.u. (Sn)**	**BVS /v.u. (M)**	**BVS /v.u. (B)**	**WLE /10^{-5}**	**Ref.**
$SnCrBO_4$	222(3) ×1 227(2) ×1 221(3) ×2	195(3) ×2 199(3) ×2 201(3) ×2	139(8) ×1 138(4) ×2	2.07(2)	2.98(1)	2.90(2)	3.20(2)	This study
$SnVBO_4$	224(3) ×1 228(2) ×1 222(1) ×2	194(2) ×2 199(2) ×2 207(5) ×2	142(5) ×1 137(3) ×2	2.00(2)	2.99(5)	2.63(9)	2.91(1)	This study
$SnAlBO_4$	218(5) ×2 233(3) ×1 222(2) ×1	191(5) ×2 198(4) ×2 185(4) ×2	133(8) ×1 141(3) ×2	2.07(1)	2.84(3)	2.90(2)	1.87(2)	[14]
$SnAlBO_4$	222 ×2 228 ×1 231 ×1	185 ×2 191 ×2 196 ×2	137 ×1 138 ×2	1.91(1)	2.87(1)	2.95(4)	2.88(1)	[31]
$SnGaBO_4$	216(3) ×2 219(4) ×1 234(3) ×1	196(3) ×2 193(2) ×2 194(2) ×2	150(1) ×2 139(1) ×1	2.15(3)	3.37(3)	2.97(2)	2.30(3)	[14]
$SnGaBO_4$	225 ×2 229 ×1 230 ×1	192 ×2 199 ×2 203 ×2	167 ×1 138 ×2	1.83(4)	3.05(3)	2.25(5)	2.58(1)	[31]

As the comparable Sn – O bonds of $SnCrBO_4$ and $SnVBO_4$ differ only by 1 – 2 pm, the trend of the solid solution is nearly linear with small deviations around the error shown in **figure 3**. Tin in the square pyramidal coordination is found to be slightly over-bonded in $SnCrBO_4$ and chromium slightly under-bonded. For the solid solution, the BVS of Sn^{2+} is between 1.94 v.u. and 2.02 v.u which is again slightly under – or over – bonded. The slightly over-bonding nature of Sn(II) is not surprising due to the interplay between the MO_6 octahedral distortion and the LEP-effect in SnO_4E [31].

For the Cr – O bond distances, a comparison to the isostructural $PbCrBO_4$ can be done with comparable values (**table S2**). In the mullite-type structure, the MO_6 octahedra have three different M – O bonds where one is between M^{3+} and O^{2-} to one site of the octahedra (M – O11), the second to the tip of the octahedra (M – O12), and the third to the other site of the octahedra (M – O2). In $Sn(Cr_{1-x}V_x)BO_4$, the smallest bond distance is M – O11 which has a value between 194 pm and 196 pm which has a linear trend over the whole solid solution. A slightly larger value is obtained for the bond distance of M – O2, which is again linear and only in a small range of 1 pm for all compositional x-values. The last bond distance of the octahedra shows an increase from x = 0 to x = 1.0. This observation leads to a possible more distorted octahedra for a higher V^{3+} value in the composition which might be influenced by the larger cationic radius of V^{3+} compared to Cr^{3+}. This trend explains the increase in lattice parameters *a* and *b* with increasing V^{3+} content whereas lattice parameter *c* is nearly constant. The BVS of M^{3+} in these structures is more of less constant at a value of 3.02(3).

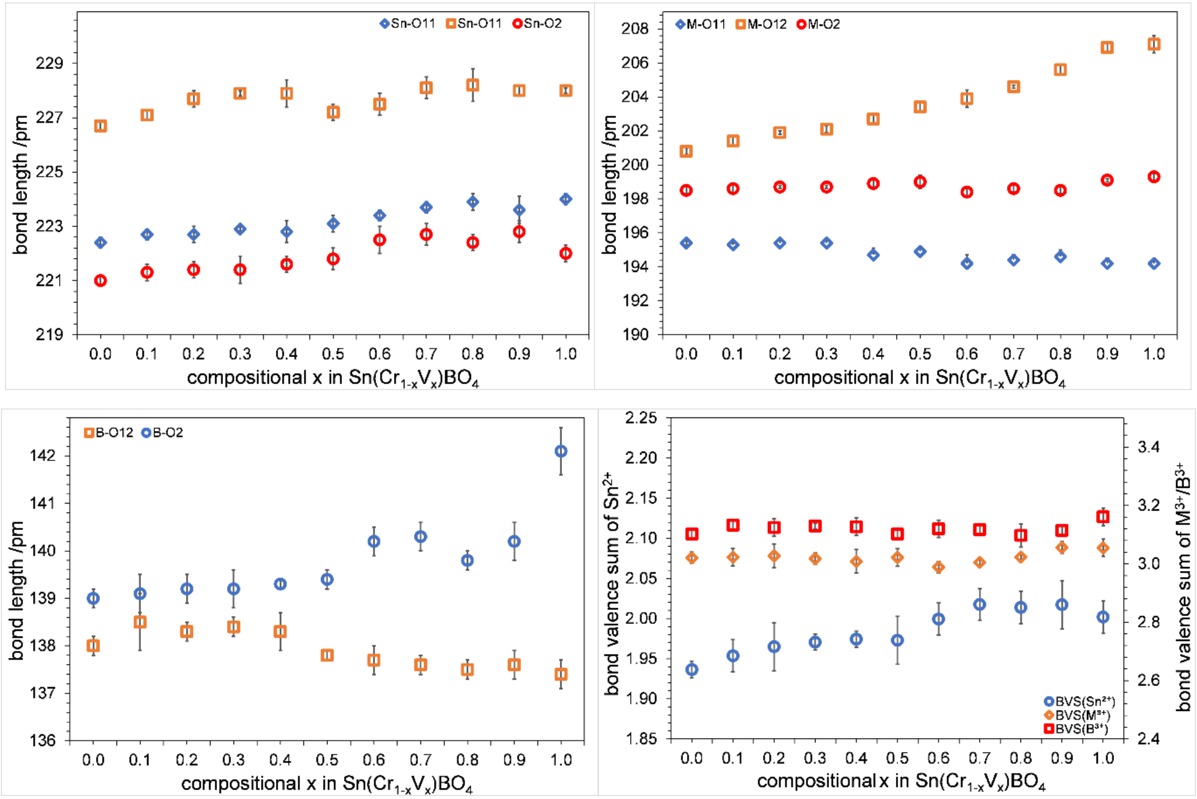

Figure 3: Trend of the Sn – O (top left), M – O (top right) and B – O (bottom left) bond length as well as the BVS of the cations (bottom right) of the solid solution $Sn(Cr_{1-x}V_x)BO_4$.

Irrespective to the change of the chemical composition (x), the B-O bond distances in the trigonal planar BO_3 groups remain close to 137 pm due to usual B-O rigidity (covalency), keeping the BVS close to formal value (3 v.u.).

The WLE parameter of the SnO_4E pyramid in $SnVBO_4$ ($|\Phi| = 2.99(1) \cdot 10^{-5}$) stems from the asymmetric Sn-O bond lengths (222(1) pm and 228(2) pm), which is found to be higher for $SnCrBO_4$ ($|\Phi| = 3.20(2) \cdot 10^{-5}$) for the bond distances of 221(3) pm to 227(3) pm. The trend of the solid solution is decreasing from $SnCrBO_4$ to $SnVBO_4$ which was expected as it fits to the values of the two end members.

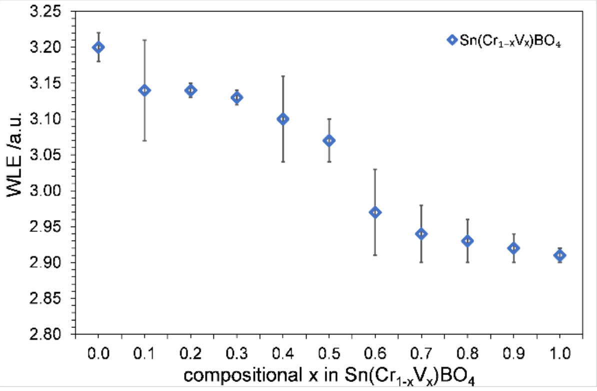

Figure 4: Wang-Liebau eccentricity (WLE) parameter of $Sn(Cr_{1-x}V_x)BO_4$ with x = 0 – 1.0.

Magnetic property

Temperature-dependent field-cooled (FC) and zero field-cooled (ZFC) DC magnetic susceptibility measurements are done which are shown in **figure 5**. At temperatures below 20 K, a significant enhancement of the susceptibility was observed. The isostructural $PbCrBO_4$ and $PbFeBO_4$ show a weakly ferromagnetic coupling along the crystallographic **c**-axis and therefore along the octahedral MO_6 chain whereas the long-range ordering along the *c* axis is antiferromagnetic. Hence, these two effects are expected for the $SnCrBO_4$ mullite-type phase as well which is seen in **figure 5**.

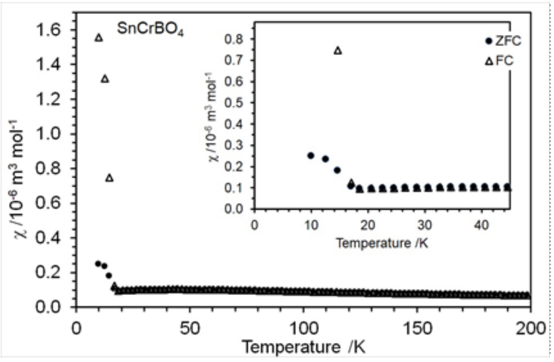

Figure 5: Zero-field (open circle) and field cooled (filled circle) DC magnetic susceptibility of SnCrBO$_4$.

Vibrational property

For mullite-type SnMBO$_4$ structures, factor group analysis results in 84 vibrational modes. Of them, 36 are Raman active ($11A_g + 7B_{1g} + 11B_{2g} + 7B_{3g}$), 35 are IR active ($13B_{1u} + 9B_{2u} + 13B_{3u}$), three ($B_{1u} + B_{2u} + B_{3u}$) belong to acoustic mode and 10 A_u modes are optically inactive (silent modes). Both mullite-type end members belong to factor group symmetry of D_{2h}. **Figure 6** shows the stacked plot of Raman and IR spectra of these two samples, and **figure 7** depicts the deconvoluted peak maxima of SnCrBO$_4$ which are listed for both end members in **table 4**.

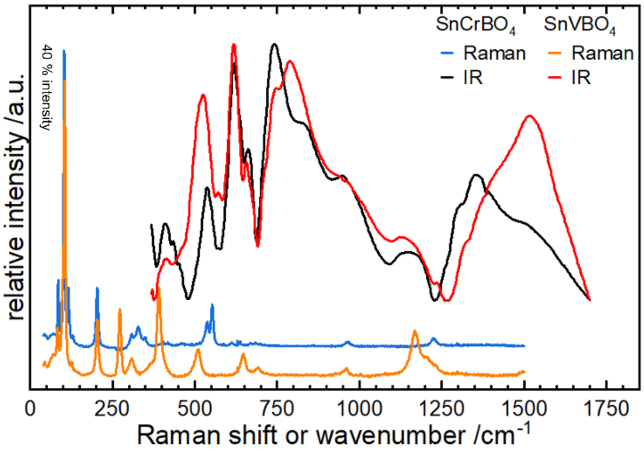

Figure 6: Stacked IR and Raman plot of SnCrBO$_4$ and SnVBO$_4$.

Based on the calculated phonon density of states (PDOSs) [31] and compared with the earlier studies on $SnMBO_4$ [14] and $PbAl_{1-x}Mn_xBO_4$ [32], the vibrational features can be categorized into three distinct ranges: (I) low frequency range between 35 and 300 cm^{-1}, (II) mid-range from 300 to 600 cm^{-1} and (III) high frequency range above 700 cm^{-1}. Either SnO with its typical Raman shifts around 115 cm^{-1} (B_{1g}) and 211 cm^{-1} (A_{1g}) nor SnO_2 with its known frequencies around 121 cm^{-1} (B_{1g}), 476 cm^{-1} (E_g), 635 cm^{-1} (A_{1g}) and 776 cm^{-1} (B_{2g}) are observed [33-35]. Planar BO_3 groups possesses D_{3h} symmetry which can be characterized by nonplanar nondegenerate (ν_2), antisymmetric degenerate (ν_3) and deformational degenerate (ν_4) vibrations with its corresponding observed frequencies at 1168 – 1226 cm^{-1}. The modes at 958.5(5) and 965.8(1) cm^{-1} can be assigned to the B-O symmetric stretching mode (ν_1) for $SnVBO_4$ and $SnCrBO_4$, respectively. Bands between 32.4 and 272.1 cm^{-1} belong to the different vibrations of SnO_4 pyramids whereas the bands between 308.8 and 553.0 cm^{-1} can be assigned to the MO_6 octahedra.

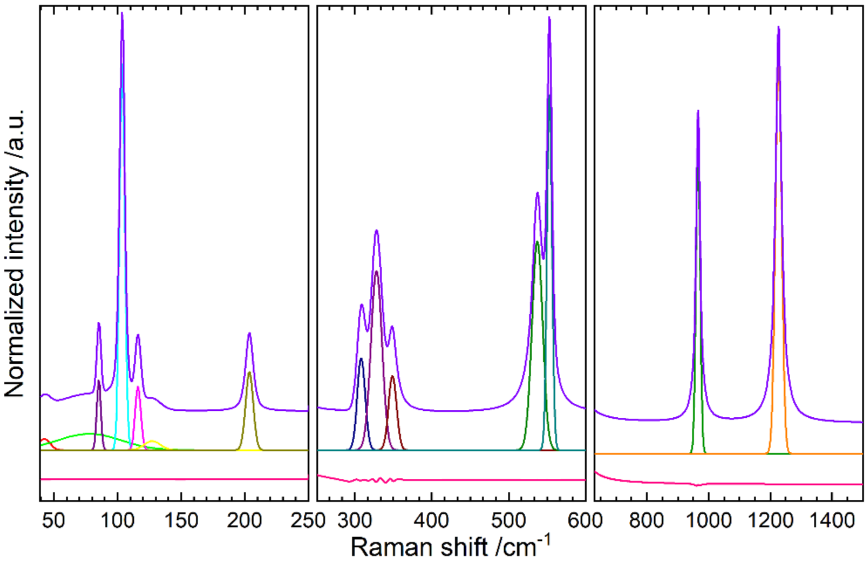

Figure 7: Representative fitted Raman spectra of $SnCrBO_4$ segmented into three regions for better clarity with observed data (blue), fitted peaks (colored) and the difference curve (pink, lowest).

The stacked plot of the Raman spectra of the whole solid solution is shown in **figure S12** in the SI. If some of the peaks are compared one observation can be done that the Raman shift around 85 cm^{-1} is increasing with increasing V^{3+} content whereas the Raman shifts of the other peaks are decreasing which is shown in **figure 8**. The trend of all Raman shift comparison is linear.

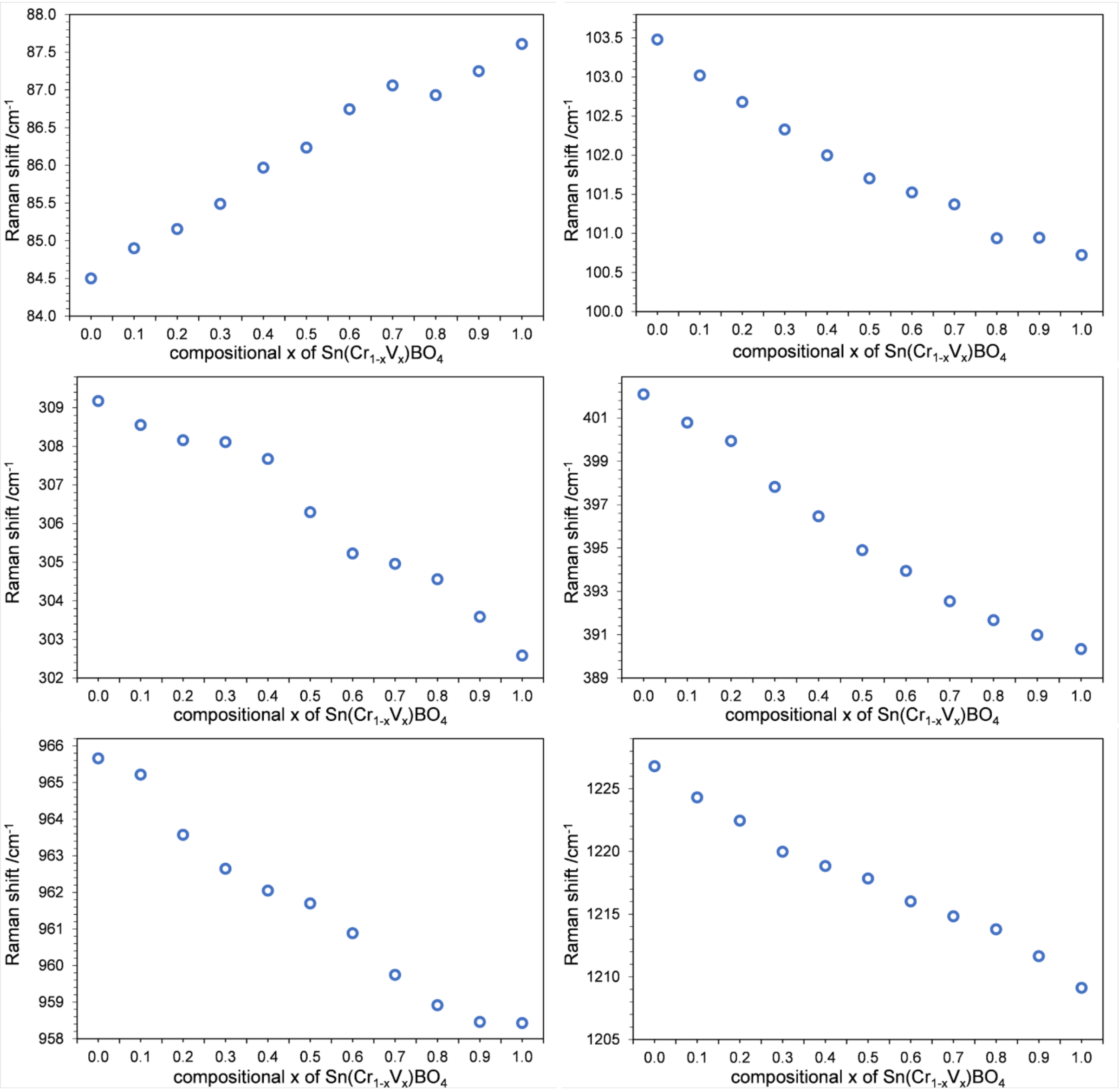

Figure 8: Comparison of Raman shifts of the solid solution $Sn(Cr_{1-x}V_x)BO_4$ with compositional x = 0 – 1.0.

Whereas factor group allows 38 IR active modes each spectrum requires only 24 to 25 band within the measured region (**table 4**) due to overlapping between the absorbed regions. The signals at 940.6(2) cm^{-1} and 930.6(2) cm^{-1} for $SnCrBO_4$ and $SnVBO_4$, respectively, show the band for the free ion D_{3h} symmetry of BO_3 which is reduced to factor group C_s symmetry driven by the local distortion [14].

Table 4: Deconvoluted peak maxima [cm^{-1}] obtained from the of $SnMBO_4$ compounds.

Raman		**IR**	
$SnCrBO_4$	**$SnVBO_4$**	**$SnCrBO_4$**	**$SnVBO_4$**
-	32.4(1)	-	-
42.4(4)	-	-	-
43.1(1)	43.2(6)	-	-
77.8(4)	68.2(1)	-	-
85.3(1)	83.1(1)	-	-
-	98.3(2)	-	-
103.7(1)	105.1(1)	-	-
116.1(3)	-	-	-
127.3(1)	126.1(1)	-	-
203.7(1)	203.8(1)	-	-
-	272.1(1)	-	-
308.6(1)	308.0(1)	-	-
328.0(3)	-	-	-
348.6(1)	-	367.2(3)	-
-	390.6(1)	391.8(1)	-
-	-	-	402.4(2)
-	-	411.2(2)	410.1(3)
-	-	437.2(1)	442.1(2)
-	-	454.3(3)	450.0(2)
537.1(1)	508.3(4)	538.5(1)	521.9(3)
553.0(4)	-	562.8(2)	576.3(1)
-	-	599.2(2)	-

-	-	621.4(1)	618.8(2)
-	646.7(1)	-	655.3(2)
-	-	665.1(1)	669.9(2)
-	692.1(1)	717.0(1)	707.0(1)
-	-	734.7(1)	735.3(2)
-	-	777.3(4)	781.7(1)
-	-	838.8(3)	837.6(1)
965.8(1)	958.5(5)	940.6(2)	930.6(2)
-	-	1016(5)	1010(4)
-	-	1135(4)	1093(2)
-	1168(3)	1185(4)	1161(2)
1226(4)	1208(1)	1218(8)	1219(1)
-	-	1241(3)	1237(2)
-	-	1298(1)	1315(1)
-	-	1352(7)	1367(1)
-	-	1398(3)	-
-	-	1436(1)	1441(5)
-	-	1522(7)	1527(4)
-	-	1606(5)	1612(3)

Modes between 300 cm^{-1} - 650 cm^{-1} can be associated with the M-O stretching and O-M-O bending modes. The modes observed above 650 cm^{-1} are assigned to BO_3 groups. In both the FTIR and Raman spectra, the global red-shift observed for the larger unit cell of $SnVBO_4$ can be explained purely from quasi-harmonic effect. Sn^{2+} located with higher symmetry for SnO_4E is assigned to the low-frequency Raman bands in $SnCrBO_4$ which are clearly separated.

UV/Vis diffuse reflectance

The RATD analysis [26] on the UV/Vis diffuse reflectance data helps assign the nature of transition (direct or indirect), as shown in **figure 9**. For both samples, the nature of transition is indirect. $SnCrBO_4$ and $SnVBO_4$ require the band-gap transition energy of 3.15(9) eV and 3.22(9) eV, respectively. As such, their bandgaps lie in the range of semiconductors. The complemental color of the sample is absorbed which is in the case of green $SnCrBO_4$ violet to blue light, in the case of greyish $SnVBO_4$ the whole visible range is absorbed.

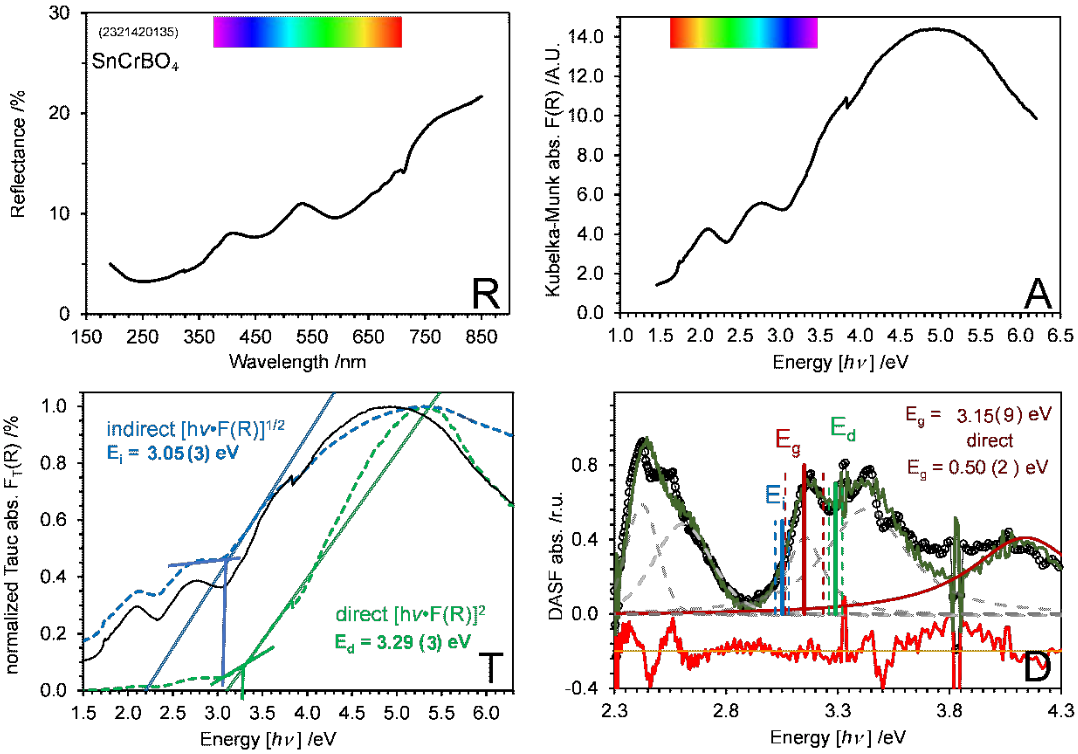

Figure 9: UV/Vis spectrum of $SnCrBO_4$ (top left), Kubelka-Munk graph (top right), normalized Tauc plot (bottom left) and normalized DASF plot (bottom right).

^{119}Sn Mössbauer

The ^{119}Sn Mössbauer spectra at room temperature of $SnCrBO_4$ are shown in **figure 10** and the fitted parameters are summarized in **table 5**. The spectra exhibit isomer shifts at 2.98(1) mm/s and 2.93(2) mm/s, respectively for $SnVBO_4$ and $SnCrBO_4$ compounds, which are comparable to recently reported isostructural $SnAlBO_4$ and $SnGaBO_4$ [14], however, slightly higher than that of SnO. The quadrupole splitting of 1.50(1) and 1.30(3) mm s^{-1}, respectively, demonstrates the LEP-character around the Sn^{2+} cations. The line width parameters (**table 5**) remain in the usual range. An additional signal at 0.00(1) mm/s can be assigned to SnO_2 which could not be seen in XRPD. The trace impurity could be due to the oxidation of SnO during the synthesis. The effective *5s* and *5p* electron population of Sn(II) was calculated [14] where the number of the *s*-electron (n_s) is 1.20(6) mm/s and the *p*-electron (n_p) is 0.78(3) mm/s for $SnVBO_4$. The respective values are comparable to those of $SnCrBO_4$ (**table 5**), indicating to a mixed (*s*-*p*) character instead of pure *s*-character [14] of the out shell electrons.

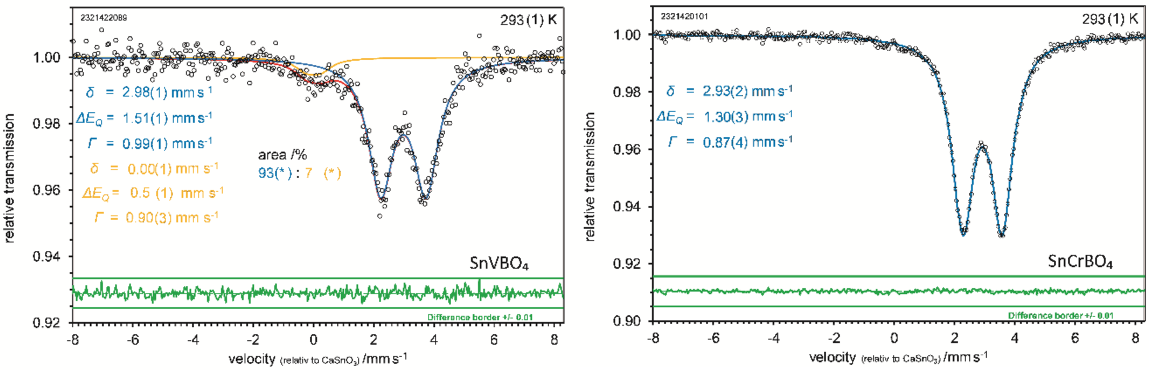

Figure 10: ^{119}Sn Mössbauer spectra of $SnVBO_4$ *(left)* and $SnCrBO_4$ *(right)*. The open circle and the solid line refer to observed and fit data.

Table 5: Fitted isomer shift (δ), electric quadrupole splitting (ΔE_Q) and line width (Γ) obtained from the ^{119}Sn Mössbauer spectra of $SnVBO_4$ and $SnCrBO_4$.

Parameter	**$SnVBO_4$**	**$SnCrBO_4$**
δ /(mm/s)	2.98(1)	2.93(2)
ΔE_Q /(mm/s)	1.50(1)	1.30(3)
Γ /(mm/s)	0.99(3)	0.87(4)
n_s	1.20(6)	1.21(5)
n_p	0.78(3)	0.79(3)
(n_x+n_y)	0.27(2)	0.28(2)
n_z	0.47(2)	0.48(2)

4. Conclusion

The successively synthesis added two new members of the mullite-type O8 family ($SnCrBO_4$ and $SnVBO_4$), where a complete miscibility is possible within the $Sn(Cr_{1-x}V_x)BO_4$ solid solution.

Crystal structural features are less influenced by the respective LEP than that of the cationic radius which was already observed in the before published $SnMBO_4$ phases. Nevertheless, the influence of the LEP is stronger for $SnCrBO_4$ compared to $SnVBO_4$ which is less strong compared to $SnAlBO_4$. The bulk and local structural features are complemented by Raman, IR, Mössbauer spectroscopy. The electronic band gaps obtained from the UV/Vis diffuse reflectance suggest that both newly synthesized compounds are high band gap semiconductors. To continue this study, thermal investigations of these structures should be done to see the influence of the stereochemically active LEP as well as the different size of the cationic radii of the trivalent metal cations.

Acknowledgement

We gratefully thank the German science foundation (Deutsche Forschungsgemeinschaft, DFG) under grant number GE1981/14-1 for the financial support of this project as well as the funding of our new IR spectrometer under grant number INST144/521-1FUGG. The University of Bremen is cordially acknowledged for technical and administrative supports. We acknowledge Kowsik Ghosh for his preliminary research on the topic of mullite-type $SnMBO_4$ phases.

Reference

1. A. Beran, E. Libowitzky, M. Burianek, M. Mühlberg, C. Pecharromán, H. Schneider, Infrared and Raman spectroscopy of mullite-type $Bi_2Ga_4O_9$, Crystal Research and Technology 43(11) (2008) 1230-1239. DOI:10.1002/crat.200800396

2. H. Schneider, E. Eberhard, Thermal-Expansion of Mullite, Journal of the American Ceramic Society 73(7) (1990) 2073-2076. DOI:10.1111/j.1151-2916.1990.tb05270.x
3. D.J. Lacks, B. Hildmann, H. Schneider, Effects of disorder in mullite: Molecular dynamics simulation and energy landscape analysis, Physical Review B 72(21) (2005) 214305. DOI:10.1103/PhysRevB.72.214305
4. H. Schneider, Komarneni, S., Mullite, Wiley2005.
5. G.D. Gatta, N. Rotiroti, M. Fisch, T. Armbruster, Stability at high pressure, elastic behavior and pressure-induced structural evolution of “Al_5BO_9”, a mullite-type ceramic material, Physics and Chemistry of Minerals 37(4) (2010) 227-236. DOI:10.1007/s00269-009-0327-x
6. S. Ohmann, P. Fielitz, L. Dörrer, G. Borchardt, T.M. Gesing, R.X. Fischer, C.H. Rüscher, J.C. Buhl, K.D. Becker, H. Schneider, Electrical conductivity of mullite-type $Bi_2Al_4O_9$ ceramics in air, Solid State Ionics 211 (2012) 46-50. DOI:10.1016/j.ssi.2012.01.030
7. H. Schneider, R.X. Fischer, T.M. Gesing, J. Schreuer, M. Mühlberg, Crystal chemistry and properties of mullite-type $Bi_2M_4O_9$: An overview, 103(4) (2012) 422-429. DOI:10.3139/146.110716
8. M. Curti, A. Kirsch, L.I. Granone, F. Tarasi, G. López-Robledo, D.W. Bahnemann, M.M. Murshed, T.M. Gesing, C.B. Mendive, Visible-Light Photocatalysis with Mullite-Type $Bi_2(Al_{1-x}Fe_x)_4O_9$: Striking the Balance between Bandgap Narrowing and Conduction Band Lowering, ACS Catalysis 8(9) (2018) 8844-8855. DOI:10.1021/acscatal.8b01210
9. S. Ďurovic, Isomorphism between Sillimanite and Mullite, Journal of the American Ceramic Society 45(4) (1962) 157-161. DOI:10.1111/j.1151-2916.1962.tb11111.x
10. R.X. Fischer, H. Schneider, Crystal chemistry of borates and borosilicates with mullite-type structures: a review, European Journal of Mineralogy 20(5) (2008) 917-933. DOI:10.1127/0935-1221/2008/0020-1831
11. M. Burianek, M. Mühlberg, M. Woll, M. Schmücker, T.M. Gesing, H. Schneider, Single-crystal growth and characterization of mullite-type orthorhombic $Bi_2M_4O_9$ ($M = Al^{3+}$, Ga^{3+}, Fe^{3+}), Crystal Research and Technology 44(10) (2009) 1156-1162. DOI:10.1002/crat.200900465
12. T. Debnath, C.H. Rüscher, P. Fielitz, S. Ohmann, G. Borchardt, Series of compositions $Bi_2(M'_xM_{1-x})_4O_9$ (M', M=Al, Ga, Fe; $0 \leq x \leq 1$) with mullite-type crystal structure: Synthesis, characterization and $^{18}O/^{16}O$ exchange experiment, Journal of Solid State Chemistry 183(11) (2010) 2582-2588. DOI:10.1016/j.jssc.2010.07.019
13. H. Saalfeld, H. Gerlach, Solid solution and optical properties of (Al, Ge)-mullites, 195(1-2) (1991) 65-73. DOI:10.1524/zkri.1991.195.1-2.65
14. S. Wittmann, M.M. Murshed, V. Bilovol, A. Koldemir, R. Pöttgen, U.G. Nielsen, T.M. Gesing, Mullite-type $EMBO_4$: synthesis, structural, optical, and vibrational properties of rare tin(II) borates with M = Al and Ga, Journal of the American Ceramic Society 107(2) (2023) 1302-1314. DOI:10.1111/jace.19476
15. T.M. Gesing, e. al., Crystal structure of mullite-type $PbMn_{0.5}Al_{0.5}BO_4$ determined by combined X-ray and neutron diffraction data, Zeitschrift für Kristallographie - New Crystal Structures 227(3) (2012) 285-286. DOI:10.1524/ncrs.2012.0181
16. T. Kremlika, High pressure behaviour of α-$PbAlBO_4$ single crystals under hydrostatic compression to 24 GPa, Master thesis, University of Vienna A066815 (2020) 1-75.
17. H. Park, J. Barbier, R.P. Hammond, Crystal structure and polymorphism of $PbAlBO_4$, Solid State Sciences 5(4) (2003) 565-571. DOI:10.1016/s1293-2558(03)00056-6
18. M. Gogolin, M.M. Murshed, M. Ende, R. Miletich, T.M. Gesing, Uniaxial negative thermal expansion in the mullite- and borax-type $PbAlBO_4$ polymorphs, Journal of Materials Science 55(1) (2019) 177-190. DOI:10.1007/s10853-019-04013-6
19. M. Curti, M.M. Murshed, T. Bredow, D.W. Bahnemann, T.M. Gesing, C.B. Mendive, Elastic, phononic, magnetic and electronic properties of quasi-one-dimensional $PbFeBO_4$,

Journal of Materials Science 54(21) (2019) 13579-13593. DOI:10.1007/s10853-019-03866-1
20. J.B. Goodenough, Theory of the Role of Covalence in the Perovskite-Type Manganites [La, *M*(II)]MnO_3, Physical Review 100(2) (1955) 564-573. DOI:10.1103/PhysRev.100.564
21. J. Kanamori, Superexchange interaction and symmetry properties of electron orbitals, Journal of Physics and Chemistry of Solids 10(2) (1959) 87-98. DOI:10.1016/0022-3697(59)90061-7
22. P.W. Anderson, New Approach to the Theory of Superexchange Interactions, Physical Review 115(1) (1959) 2-13. DOI:10.1103/PhysRev.115.2
23. H.-J. Koo, M.-H. Whangbo, Density functional investigation of the magnetic properties of $PbMBO_4$ (M=Cr, Mn, Fe), Solid State Communications 149(15-16) (2009) 602-604. DOI:10.1016/j.ssc.2009.01.030
24. M.M. Murshed, A. Rusen, R.X. Fischer, T.M. Gesing, Transition-metal substitution in $PbAlBO_4$: Synthesis, structural and spectroscopic studies of manganese containing phases, Materials Research Bulletin 47(6) (2012) 1323-1330. DOI:10.1016/j.materresbull.2012.03.014
25. D. Souri, Z.E. Tahan, A new method for the determination of optical band gap and the nature of optical transitions in semiconductors, Applied Physics B 119(2) (2015) 273-279. DOI:10.1007/s00340-015-6053-9
26. T.M. Gesing, M.M. Murshed, S. Schuh, O. Thüringer, K. Krämer, T. Neudecker, C.B. Mendive, L. Robben, Nano-crystalline precursor formation, stability, and transformation to mullite-type visible-light photocatalysts, Journal of Material Science 57 (2022) 19280-19299. DOI:10.1007/s10853-022-07854-w
27. R.A. Brand, Normos Programs (SITE-DIST), in: D. University (Ed.) 1991.
28. C. Corporation, CorelDRAW Graphic Suite 2017, Ottowa Canada, 2017.
29. R.D. Shannon, Revised effective ionic radii and systematic studies of interatomic distances, Acta Crystallographica A32 (1976) 751.
30. A.R. Denton, N.W. Ashcroft, Vegard's law, Physical Review A 43(6) (1991) 3161-3164. DOI:10.1103/PhysRevA.43.3161
31. M. Curti, C.B. Mendive, T. Bredow, M. Mangir Murshed, T.M. Gesing, Structural, vibrational and electronic properties of $SnMBO_4$ (M = Al, Ga): a predictive hybrid DFT study, J Phys Condens Matter 31(34) (2019) 345701. DOI:10.1088/1361-648X/ab20a1
32. T.M. Gesing, C.B. Mendive, M. Curti, D. Hansmann, G. Nénert, P.E. Kalita, K.E. Lipinska, A. Huq, A.L. Cornelius, M.M. Murshed, Structural properties of mullite-type $Pb(Al_{1-x}Mn_x)BO_4$, Zeitschrift für Kristallographie - Crystalline Materials 228(10) (2013). DOI:10.1524/zkri.2013.1640
33. M. Becker, A. Polity, P.J. Klar, B.K. Meyer†, Synthesis of tin oxides SnO_{2-x} in the entire composition range (x = 0 to 1) by ion-beam sputter-deposition, physica status solidi (RRL) - Rapid Research Letters 9(5) (2015) 326-330. DOI:10.1002/pssr.201510058
34. Z.W. Chen, J.K.L. Lai, C.H. Shek, Insights into microstructural evolution from nanocrystalline SnO_2 thin films prepared by pulsed laser deposition, Physical Review B 70(16) (2004) 165314. DOI:10.1103/PhysRevB.70.165314
35. P.S. Peercy, B. Morosin, Pressure and Temperature Dependences of the Raman-Active Phonons in SnO_2, Physical Review B 7(6) (1973) 2779-2786. DOI:10.1103/PhysRevB.7.2779

Supporting information

Synthesis and characterization of mullite-type $Sn(Cr_{1-x}V_x)BO_4$ for x = 0- 1.0.

Sarah Wittmann[1], M. Mangir Murshed[1,2*], Aylin Koldemir[3], Rainer Pöttgen[3], Thorsten M. Gesing[1,2]

[1]University of Bremen, Institute of Inorganic Chemistry and Crystallography, Leobener Straße 7, D-28359 Bremen, Germany

[2]University of Bremen, MAPEX Center for Materials and Processes, Bibliothekstraße 1, D-28359 Bremen, Germany

[3]University of Münster, Institute of Inorganic and Analytical Chemistry, Corrensstrasse 30, D-48149 Münster, Germany

*Corresponding author: murshed@uni-bremen.de, phone: +49 (0)421 218 63144

ORCID:

SW:	0000-0003-1404-3434
MMM:	0000-0002-9063-372X
AK:	0009-0004-3819-3853
RP:	0000-0003-0962-279X
TMG:	0000-0002-4119-2219

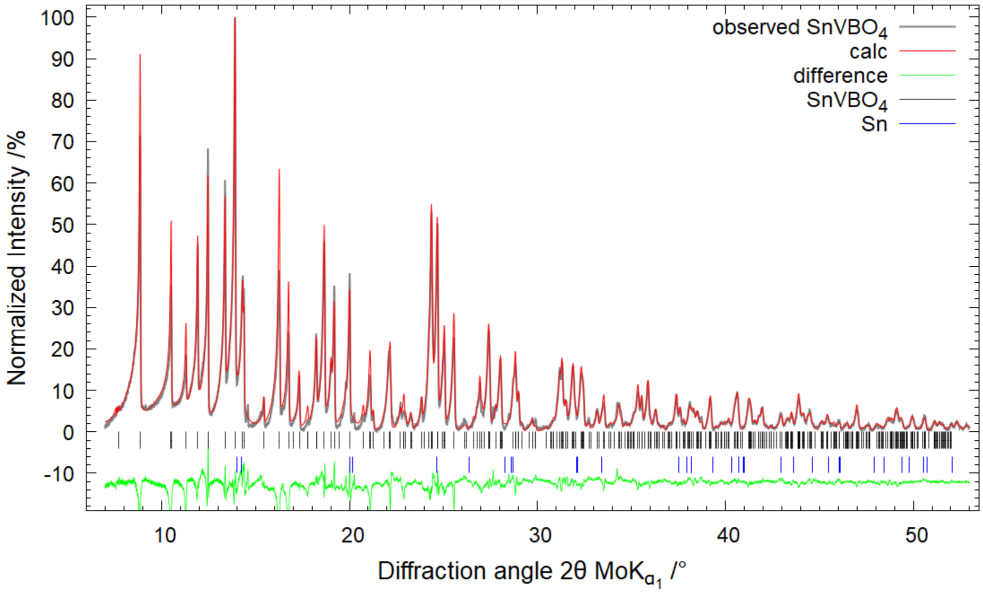

Figure S1: Rietveld Plot of $SnVBO_4$ with observed, calculated and difference curves and the hkl tics of $SnVBO_4$ and Sn.

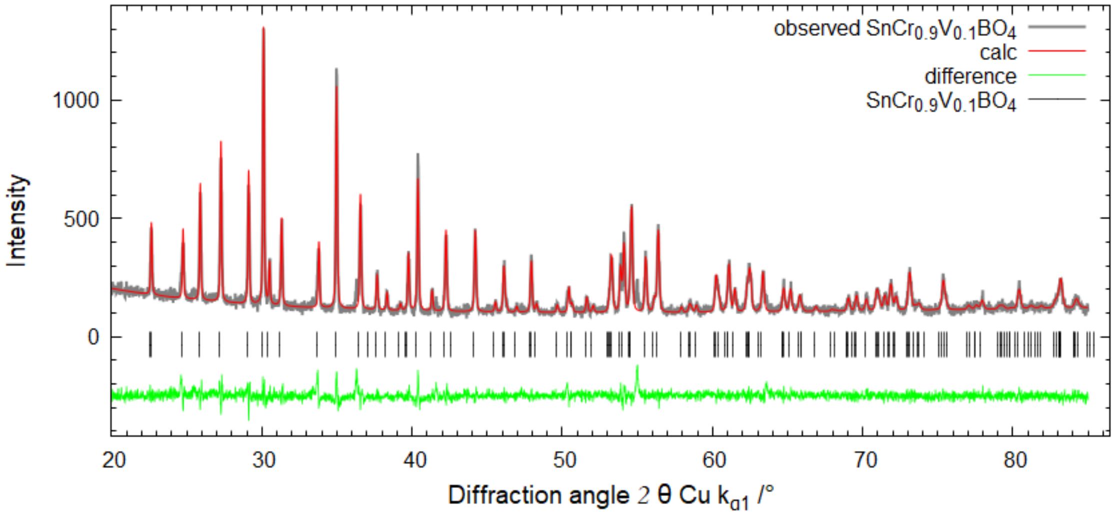

Figure S11: Rietveld Plot of $Sn(Cr_{0.9}V_{0.1})BO_4$ with observed, calculated and difference curves and the hkl tics of $Sn(Cr_{0.9}V_{0.1})BO_4$.

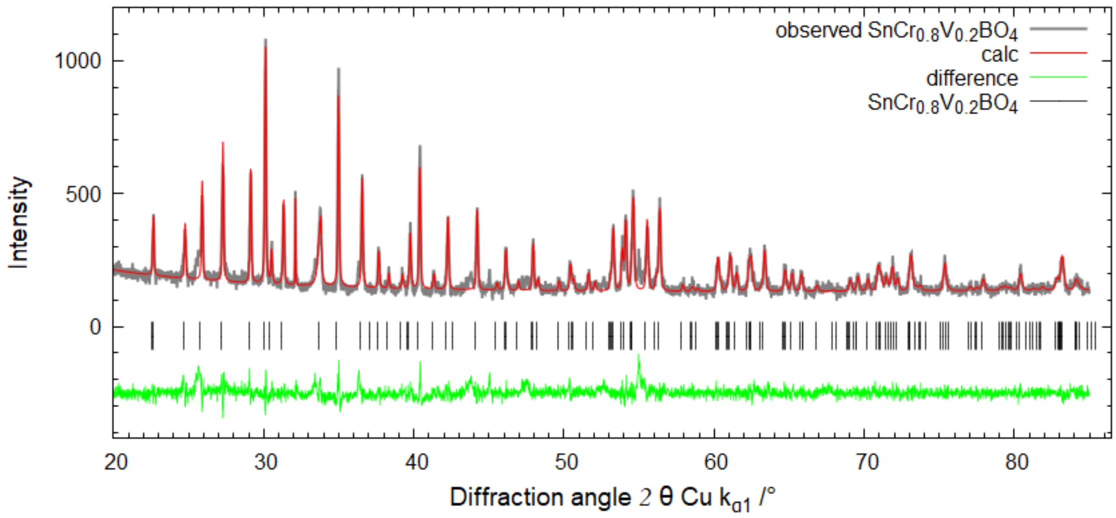

Figure S12: Rietveld Plot of Sn($Cr_{0.8}V_{0.2}$)BO_4 with observed, calculated and difference curves and the hkl tics of Sn($Cr_{0.8}V_{0.2}$)BO_4.

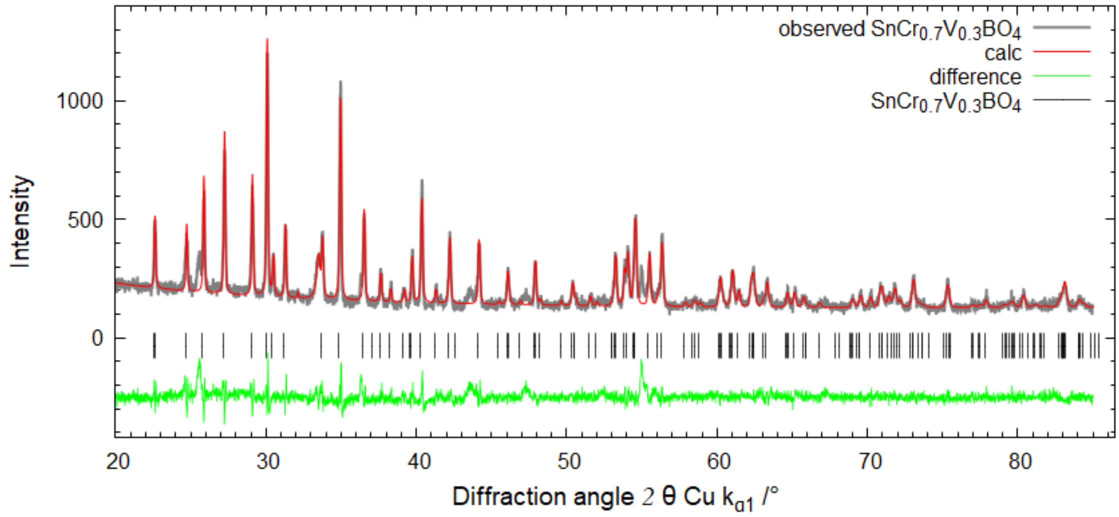

Figure S13: Rietveld Plot of Sn($Cr_{0.7}V_{0.3}$)BO_4 with observed, calculated and difference curves and the hkl tics of Sn($Cr_{0.7}V_{0.3}$)BO_4.

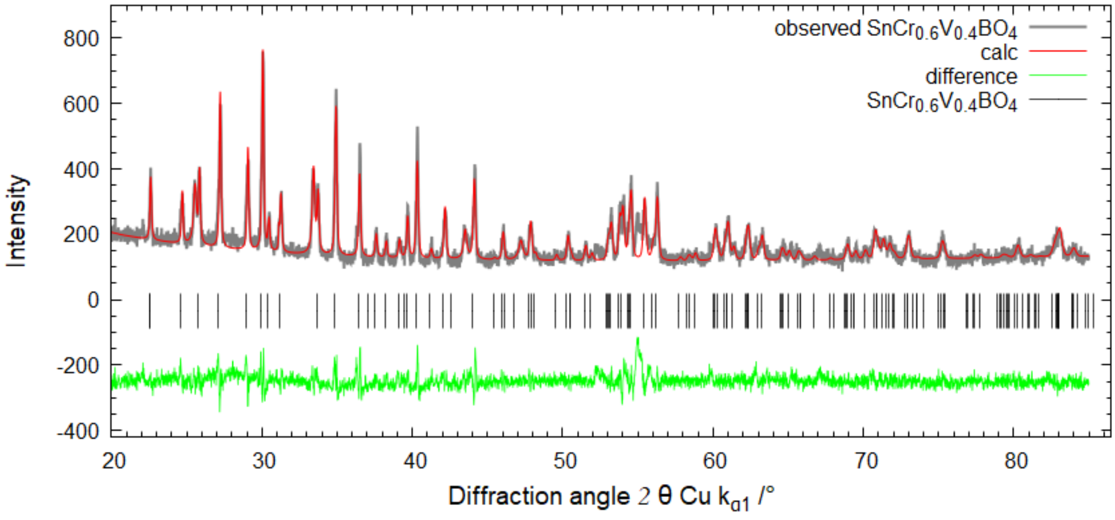

Figure S14: Rietveld Plot of Sn($Cr_{0.6}V_{0.4}$)BO_4 with observed, calculated and difference curves and the hkl tics of Sn($Cr_{0.6}V_{0.4}$)BO_4.

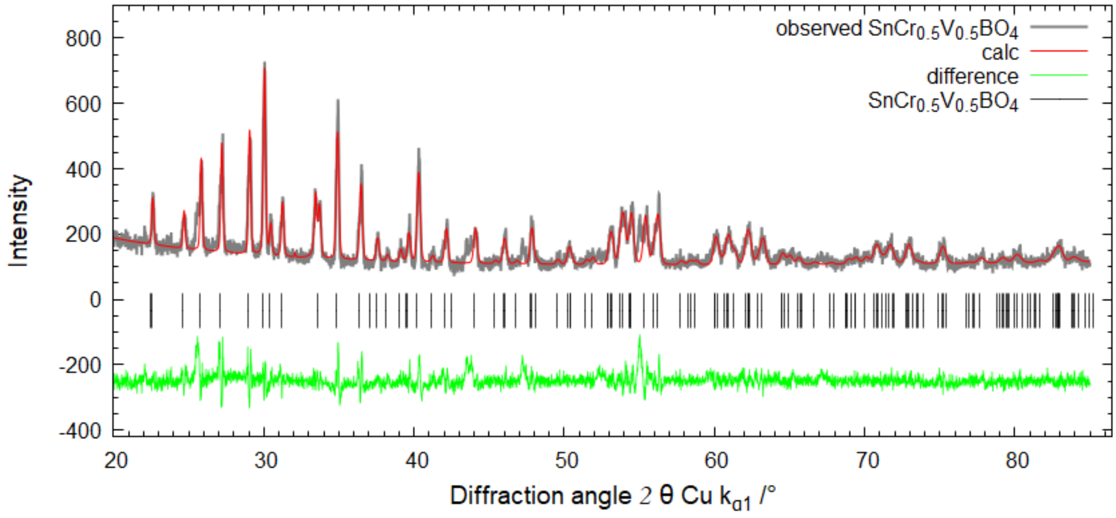

Figure S15: Rietveld Plot of Sn($Cr_{0.5}V_{0.5}$)BO_4 with observed, calculated and difference curves and the hkl tics of Sn($Cr_{0.5}V_{0.5}$)BO_4.

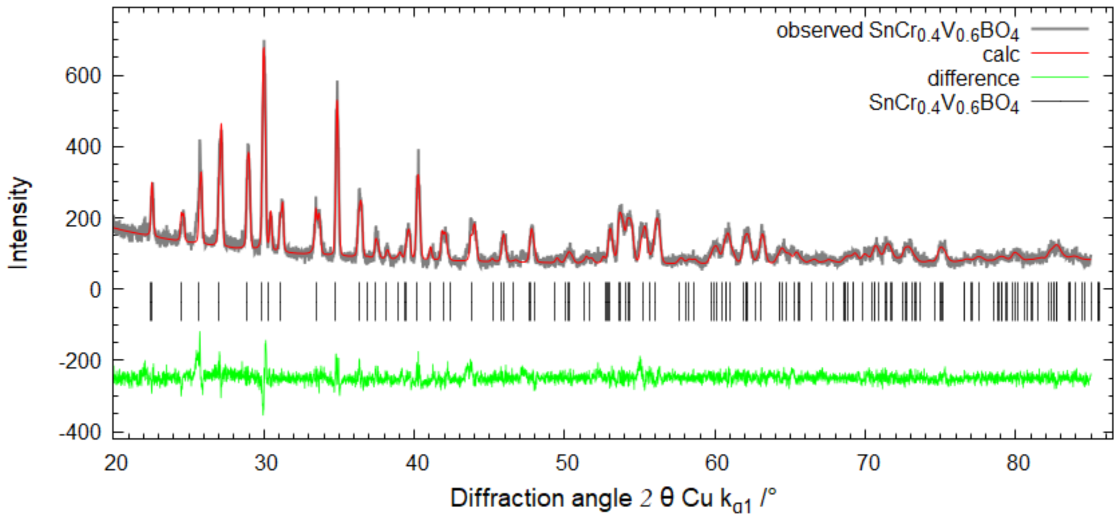

Figure S16: Rietveld Plot of Sn($Cr_{0.4}V_{0.6}$)BO_4 with observed, calculated and difference curves and the hkl tics of Sn($Cr_{0.4}V_{0.6}$)BO_4.

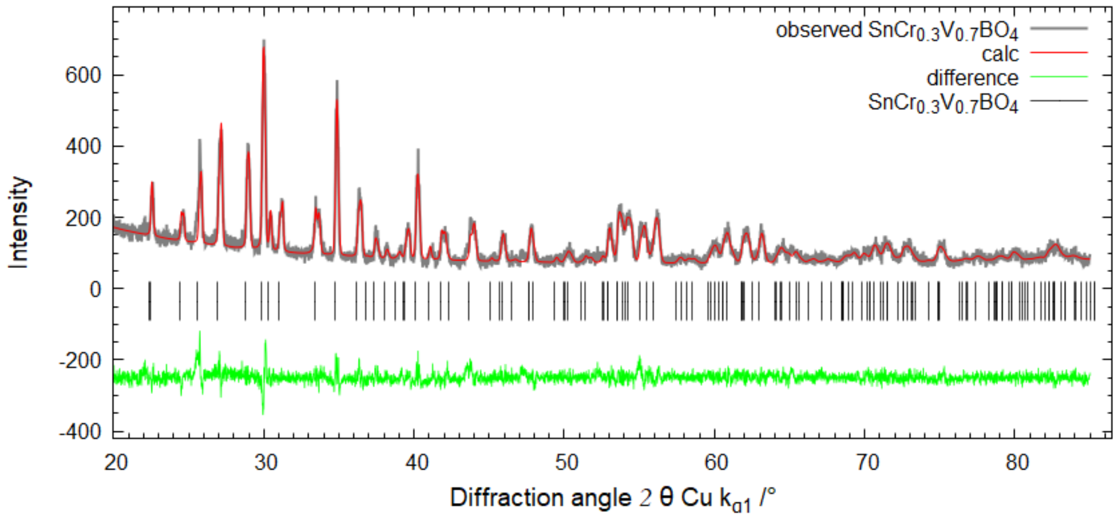

Figure S17: Rietveld Plot of Sn($Cr_{0.3}V_{0.7}$)BO_4 with observed, calculated and difference curves and the hkl tics of Sn($Cr_{0.3}V_{0.7}$)BO_4.

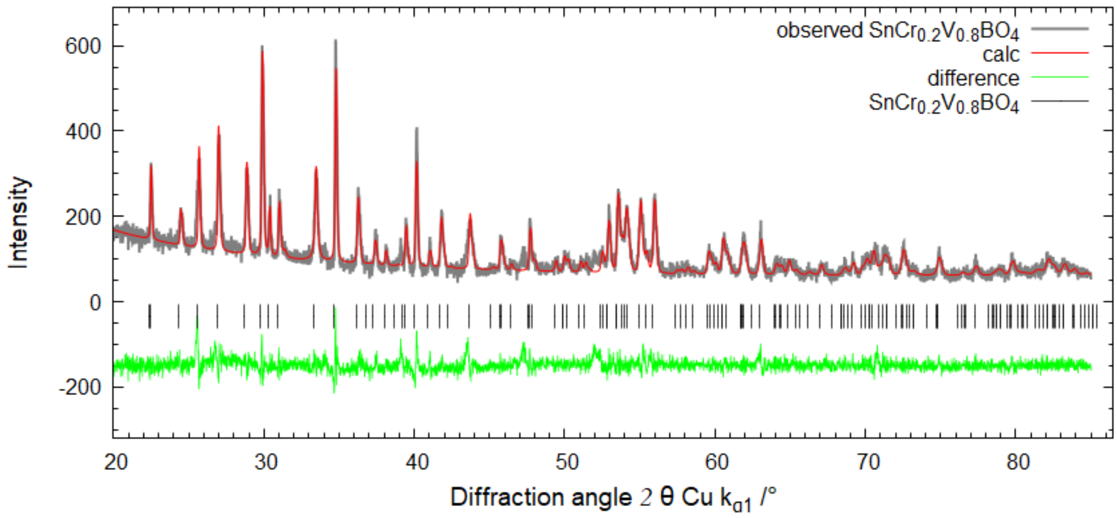

Figure S18: Rietveld Plot of $Sn(Cr_{0.2}V_{0.8})BO_4$ with observed, calculated and difference curves and the hkl tics of $Sn(Cr_{0.2}V_{0.8})BO_4$.

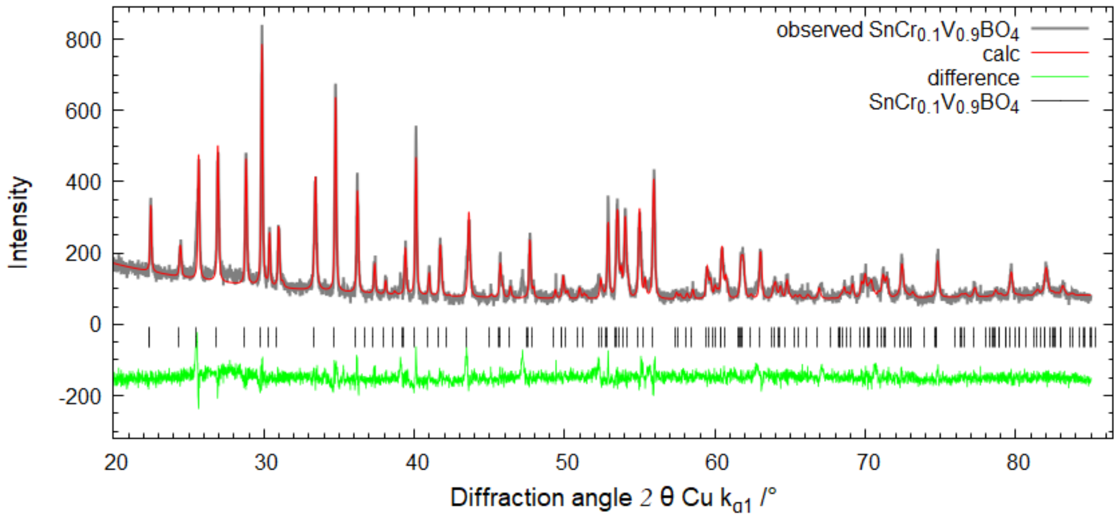

Figure S19: Rietveld Plot of $Sn(Cr_{0.1}V_{0.9})BO_4$ with observed, calculated and difference curves and the hkl tics of $Sn(Cr_{0.1}V_{0.9})BO_4$.

Table S6: Crystal structural parameters of $SnCrBO_4$ and $SnVBO_4$ in the orthorhombic setting of the space group *Pnam*.

$Sn(Cr_{0.9}V_{0.1})BO_4$						
Atom	Site	*x*	*y*	*z*	*Occ*	*B* /10^4 pm^2
Sn1	4*c*	0.0863(2)	0.3641(3)	¼	1	0.31(5)
Cr1	4*a*	0	0	0	0.9	0.25(12)
V1	4*a*	0	0	0	0.1	0.25(12)
B1	4*c*	0.2647(4)	0.7557(4)	¼	1	0.83(8)
O11	4*c*	0.3969(4)	0.3664(5)	¼	1	0.25(3)
O12	4*c*	0.1657(4)	0.8721(4)	¼	1	0.31(5)
O2	8*d*	0.3492(3)	0.7221(3)	0.0450(3)	1	0.38(3)
$Sn(Cr_{0.8}V_{0.2})BO_4$						
Atom	Site	*x*	*y*	*z*	*Occ*	*B* /10^4 pm^2
Sn1	4*c*	0.0863(3)	0.3642(3)	¼	1	0.44(4)
Cr1	4*a*	0	0	0	0.8	0.25(7)
V1	4*a*	0	0	0	0.2	0.25(7)
B1	4*c*	0.2647(6)	0.7557(6)	¼	1	0.30(11)
O11	4*c*	0.4357(3)	0.3645(8)	¼	1	0.90(2)
O12	4*c*	0.1657(4)	0.8721(2)	¼	1	3.00(4)
O2	8*d*	0.3492(7)	0.7221(3)	0.0450(9)	1	0.60(2)
$Sn(Cr_{0.7}V_{0.3})BO_4$						
Atom	Site	*x*	*y*	*z*	*Occ*	*B* /10^4 pm^2
Sn1	4*c*	0.0863(2)	0.3642(3)	¼	1	0.26(5)
Cr1	4*a*	0	0	0	0.7	0.25(12)
V1	4*a*	0	0	0	0.3	0.25(12)
B1	4*c*	0.2647(4)	0.7557(4)	¼	1	0.81(8)
O11	4*c*	0.4357(4)	0.3664(5)	¼	1	0.25(3)
O12	4*c*	0.1657(4)	0.8721(4)	¼	1	0.98(5)
O2	8*d*	0.3389(3)	0.7027(3)	0.0449(3)	1	0.25(3)
$Sn(Cr_{0.6}V_{0.4})BO_4$						
Atom	Site	*x*	*y*	*z*		*B* /10^4 pm^2
Sn1	4*c*	0.0863(1)	0.3642(3)	¼	1	0.44(4)
Cr1	4*a*	0	0	0	0.6	0.25(2)

V1	4*a*	0	0	0	0.4	0.25(2)
B1	4*c*	0.3640(6)	0.7810(2)	¼	1	0.30(11)
O11	4*c*	0.4058(9)	0.3645(4)	¼	1	0.90(2)
O12	4*c*	0.1657(2)	0.8790(2)	¼	1	2.00(3)
O2	8*d*	0.3475(7)	0.6994(3)	0.0473(9)	1	0.60(2)

$Sn(Cr_{0.5}V_{0.5})BO_4$

Atom	Site	*x*	*y*	*z*	*Occ*	*B* /10^4 pm^2
Sn1	4*c*	0.0860(2)	0.3638(3)	¼	1	0.31(5)
Cr1	4*a*	0	0	0	0.5	0.25(12)
V1	4*a*	0	0	0	0.5	0.25(12)
B1	4*c*	0.2653(4)	0.7639(4)	¼	1	0.83(8)
O11	4*c*	0.4375(4)	0.4375(5)	¼	1	0.25(3)
O12	4*c*	0.1654(4)	0.8804(4)	¼	1	0.31(5)
O2	8*d*	0.3389(3)	0.7227(3)	0.0449(3)	1	0.38(3)

$Sn(Cr_{0.4}V_{0.6})BO_4$

Atom	Site	*x*	*y*	*z*	*Occ*	*B* /10^4 pm^2
Sn1	4*c*	0.0825(4)	0.3647(3)	¼	1	0.47(4)
Cr1	4*a*	0	0	0	0.4	0.25(7)
V1	4*a*	0	0	0	0.6	0.25(7)
B1	4*c*	0.3640(6)	0.7810(6)	¼	1	0.54(11)
O11	4*c*	0.4058(9)	0.3645(3)	¼	1	0.32(2)
O12	4*c*	0.1594(5)	0.8890(2)	¼	1	2.00(4)
O2	8*d*	0.3475(7)	0.7294(4)	0.0453(3)	1	0.40(2)

$Sn(Cr_{0.3}V_{0.7})BO_4$

Atom	Site	*x*	*y*	*z*	*Occ*	*B* /10^4 pm^2
Sn1	4*c*	0.0890(2)	0.3626(3)	¼	1	0.31(5)
Cr1	4*a*	0	0	0	0.3	0.25(3)
V1	4*a*	0	0	0	0.7	0.25(3)
B1	4*c*	0.2853(4)	0.7739(4)	¼	1	0.83(8)
O11	4*c*	0.3969(4)	0.3664(5)	¼	1	0.25(3)
O12	4*c*	0.1624(4)	0.9104(4)	¼	1	0.31(5)
O2	8*d*	0.3389(3)	0.7027(3)	0.0449(3)	1	0.38(3)

Sn(Cr$_{0.2}$V$_{0.8}$)BO$_4$

Atom	Site	x	y	z		B /10^4 pm^2
Sn1	4c	0.0905(3)	0.3647(3)	¼	1	0.44(4)
Cr1	4a	0	0	0	0.2	0.25(7)
V1	4a	0	0	0	0.8	0.25(7)
B1	4c	0.3649(3)	0.7270(4)	¼	1	0.30(11)
O11	4c	0.4358(2)	0.3645(3)	¼	1	0.90(2)
O12	4c	0.1594(5)	0.8720(2)	¼	1	1.80(4)
O2	8d	0.3375(7)	0.6994(3)	0.0473(9)	1	0.60(2)

Sn(Cr$_{0.1}$V$_{0.9}$)BO$_4$

Atom	Site	x	y	z		B /10^4 pm^2
Sn1	4c	0.0865(3)	0.3657(3)	¼	1	0.54(4)
Cr1	4a	0	0	0	0.1	0.25(2)
V1	4a	0	0	0	0.9	0.25(2)
B1	4c	0.2640(6)	0.7245(6)	¼	1	0.30(11)
O11	4c	0.4358(3)	0.3545(4)	¼	1	0.90(2)
O12	4c	0.1694(3)	0.8790(2)	¼	1	2.34(4)
O2	8d	0.3375(7)	0.6994(3)	0.0473(9)	1	0.60(2)

Table S7: Selective bond distances [pm], bond-valence sum (BVS) [v.u.], and Wang-Liebau eccentricity parameter [$|\Phi|\cdot10^{-5}$] of the constituent elements in PbMBO$_4$ compounds.

Compound	**Sn-O**	**M-O**	**B-O**	**BVS (Sn, Pb)**	**BVS (M)**	**BVS (B)**	**WLE (SnO$_4$, PbO$_4$)**	**Ref.**
PbAlBO$_4$	233 ×2 230 ×1 235 ×1	182 ×2 192 ×2 199 ×2	137 ×1 138 ×2	2.25	3.04	2.97		[1]
PbAlBO$_4$							1.93(2)	[2]
PbGaBO$_4$							1.83(2)	[2]
PbGaBO$_4$	235 ×2 232 ×1 237 ×1	189 ×2 201 ×2 207 ×2	137 ×1 139 ×2	1.83 (6)	3.04 (8)	2.92 (21)		[3]
PbMnBO$_4$	243 ×2 235 ×1 241 ×1	189 ×2 199 ×2 223 ×2	136 ×1 140 ×2	1.79	3.06	3.00		[4]
PbFeBO$_4$	237 ×2 232 ×1 237 ×1	192 ×2 204 ×2 210 ×2	139 ×1 138 ×2	2.08	3.02	2.93		[4]
PbCrBO$_4$	239 ×2 229 ×1 231 ×1	194 ×2 199 ×2 203 ×2	137 ×1 140 ×2	2.15	2.98	2.88		[4]

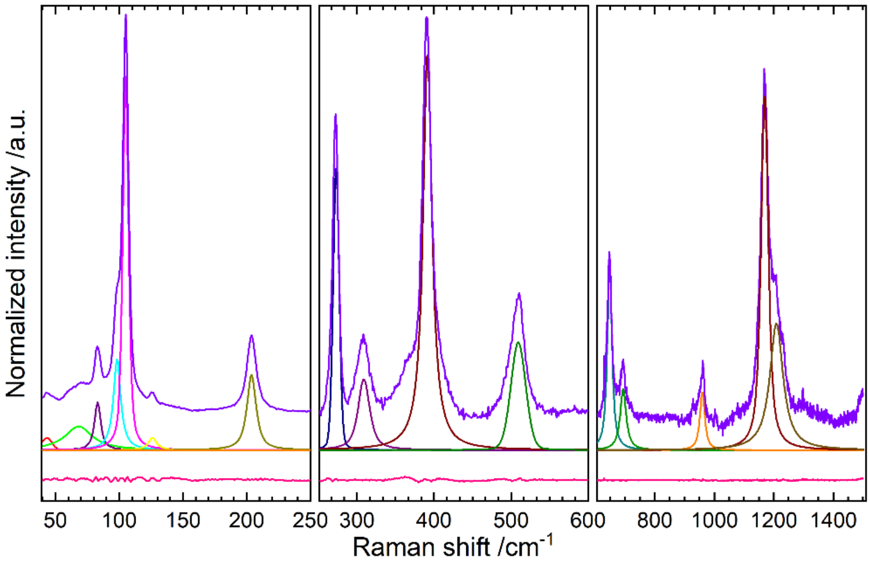

Figure S20: Fitted Raman spectra of $SnVBO_4$ segmented into three regions for better clarity with observed data (blue), fitted peaks (colored) and the difference curve (pink, lowest).

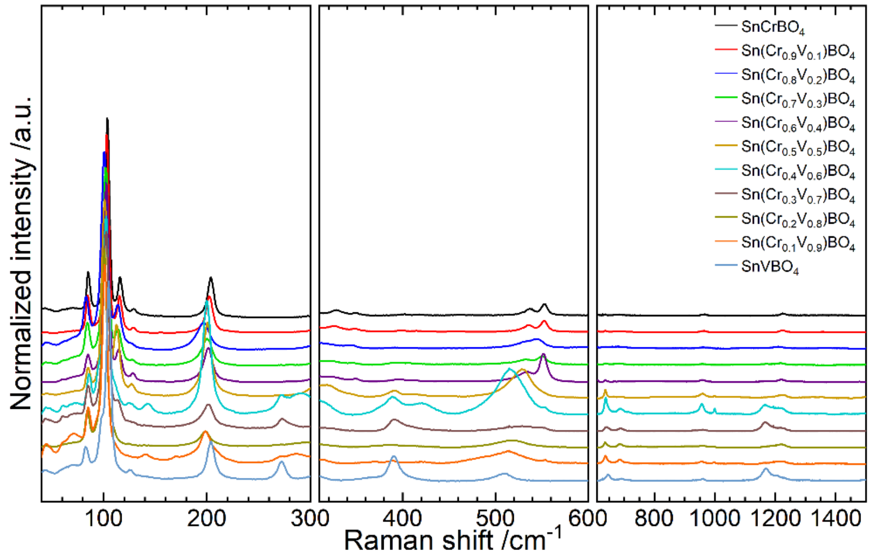

Figure S21: Stacked Raman spectra of $Sn(Cr_{1-x}V_x)BO_4$.

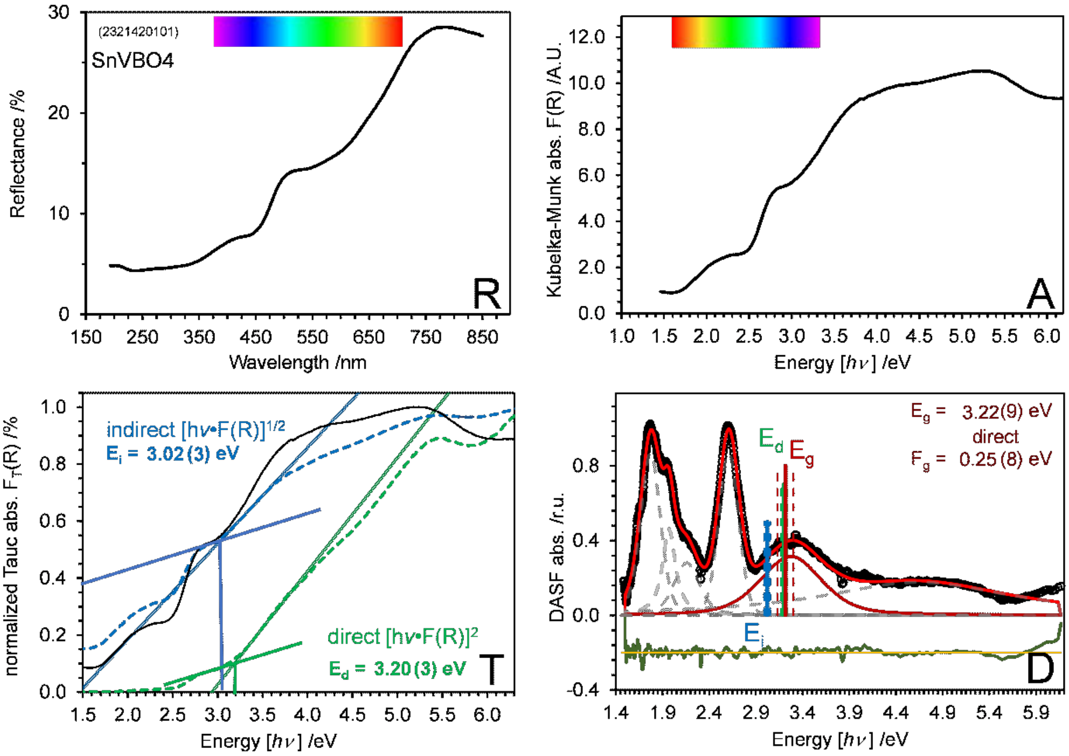

Figure S22: UV/Vis spectrum of SnVBO4 (top left), Kubelka-Munk graph (top right), normalized Tauc plot (bottom left) and normalized DASF plot (bottom right).

Reference

1. H. Park, J. Barbier, R.P. Hammond, Crystal structure and polymorphism of PbAlBO4, Solid State Sciences 5(4) (2003) 565-571. DOI:10.1016/s1293-2558(03)00056-6
2. M.M. Murshed, R.X. Fischer, T.M. Gesing, The role of the Pb^{2+}lone electron pair for bond valence sum analysis in mullite-type PbMBO4(M = Al, Mn and Fe) compounds, Zeitschrift für Kristallographie - Crystalline Materials 227(8) (2012) 580-584. DOI:10.1524/zkri.2012.1483
3. H. Park, J. Barbier, PbGaBO4, an orthoborate with a new structure-type, Acta Crystallographica Section E Structure Reports Online 57(9) (2001) i82-i84. DOI:10.1107/s1600536801013940
4. H. Park, R. Lam, J.E. Greedan, J. Barbier, Synthesis, crystal structure, crystal chemistry, and magnetic properties of PbMBO4 (M = Cr, Mn, Fe): A new structure type exhibiting one-dimensional magnetism, Chemistry of Materials 15(8) (2003) 1703-1712. DOI:10.1021/cm0217452

Reference

1. H. Xiang, Y. Tang, S. Zhang, Z. He, Intra-chain superexchange couplings in quasi-1D 3d transition-metal magnetic compounds, Journal of Physics: Condensed Matter 28(27) (2016) 276003. DOI:10.1088/0953-8984/28/27/276003
2. H.-J. Koo, M.-H. Whangbo, Density functional investigation of the magnetic properties of $PbMBO_4$ (M=Cr, Mn, Fe), Solid State Communications 149(15-16) (2009) 602-604. DOI:10.1016/j.ssc.2009.01.030
3. H. Park, R. Lam, J.E. Greedan, J. Barbier, Synthesis, crystal structure, crystal chemistry, and magnetic properties of $PbMBO_4$ (M = Cr, Mn, Fe): A new structure type exhibiting one-dimensional magnetism, Chemistry of Materials 15(8) (2003) 1703-1712. DOI:10.1021/cm0217452
4. M. Curti, M.M. Murshed, T. Bredow, D.W. Bahnemann, T.M. Gesing, C.B. Mendive, Elastic, phononic, magnetic and electronic properties of quasi-one-dimensional $PbFeBO_4$, Journal of Materials Science 54(21) (2019) 13579-13593. DOI:10.1007/s10853-019-03866-1
5. S.N. Martynov, Ground state of the orbitally ordered $PbMnBO_4$ ferromagnet, JETP Letters 115(11) (2022) 679-684. DOI:10.1134/S0021364022600860
6. M.M. Murshed, R.X. Fischer, T.M. Gesing, The role of the Pb^{2+}lone electron pair for bond valence sum analysis in mullite-type $PbMBO_4$(M = Al, Mn and Fe) compounds, Zeitschrift für Kristallographie - Crystalline Materials 227(8) (2012) 580-584. DOI:10.1524/zkri.2012.1483
7. A. Pankrats, M. Kolkov, S. Martynov, S. Popkov, A. Krasikov, A. Balaev, M. Gorev, Peculiarities of a magnetic transition in a quasi-one-dimensional ferromagnet $PbMnBO_4$, Journal of Magnetism and Magnetic Materials 471 (2019) 416-422. DOI:10.1016/j.jmmm.2018.09.098
8. A. Pankrats, K. Sablina, M. Eremin, A. Balaev, M. Kolkov, V. Tugarinov, A. Bovina, Ferromagnetism and strong magnetic anisotropy of the $PbMnBO_4$ orthoborate single crystals, Journal of Magnetism and Magnetic Materials 414 (2016) 82-89. DOI:10.1016/j.jmmm.2016.04.042
9. A.I. Pankrats, K.A. Sablina, D.A. Velikanov, O.A. Bayukov, A.M. Vorotynov, A.D. Balaev, M.S. Molokeev, M.I. Kolkov, Magnetic and dielectric properties of $PbFeBO_4$ and $PbMnBO_4$ single crystals, Solid State Phenomena 215 (2014) 372-377. DOI:10.4028/www.scientific.net/SSP.215.372
10. M.A. Prosnikov, One- and two-magnon excitations in the antiferromagnet $PbFeBO_4$, Physical Review B 103(9) (2021) 094443. DOI:10.1103/PhysRevB.103.094443
11. M.A. Prosnikov, M.E. Bal, M.I. Kolkov, A.I. Pankrats, R.V. Pisarev, P.C.M. Christianen, Subterahertz and terahertz spin and lattice dynamics of the insulating ferromagnet $PbMnBO_4$, Physical Review Research 4(1) (2022) 013004. DOI:10.1103/PhysRevResearch.4.013004
12. M.A. Prosnikov, A.N. Smirnov, V. Yu Davydov, K.A. Sablina, R.V. Pisarev, Lattice and magnetic dynamics of a quasi-one-dimensional chain antiferromagnet $PbFeBO_4$, Journal of Physics: Condensed Matter 29(2) (2017) 025808. DOI:10.1088/0953-8984/29/2/025808

Chapter 5 – Temperature-dependent investigations of $SnMBO_4$ (M = V, Cr)

In the previous **chapter 4**, details of the crystal structural and vibrational properties of $SnVBO_4$ and $SnCrBO_4$ are discussed based on the respective data collected at ambient conditions. Herein, temperature-dependent properties of these two phases are focused. As mentioned in the introduction as well as **chapter 3** higher temperatures for oxides are an important research topic where mullites and their synthetic ones are quite well studied [1]. The thermal expansion of mullites and mullite-type compounds is strongest along the crystallographic **b**-axis, where the highest TEC is explained as the elongation of the relatively longer M-O bonds along the **b**-direction [2]. An interesting thermal behavior was noticed for $PbMnBO_4$, where the TEC changes from negative to positive along the crystallographic **a**-axis in increasing temperature [3] which might be influenced by the magnetic properties of Mn^{3+}. Hence, the thermal investigations of $SnMBO_4$ (M = V, Cr) mullite-type compounds with magnetic properties are discussed in this chapter.

Results of thermogravimetric observations combined with differential scanning calorimetry (TG/DSC) from 300 K to 1298 K are shown in **figure 5.1** for $SnVBO_4$ and $SnCrBO_4$. Between 750 K and 870 K a small endothermic signal is seen for $SnVBO_4$ followed by the decomposition at 960(2) K. Afterward, X-ray powder data Rietveld analysis confirmed that the $SnVBO_4$ decomposed into SnO_2, V_2O_3/V_2O_5 and B_2O_3. The first mass gain might indicate that the decomposition starts which might follow the same reaction scheme as mentioned in **chapter 3** for $SnAlBO_4$:

$$2\ SnVBO_4 + O_2 \rightarrow 2\ SnO_2 + V_2O_3 + B_2O_3 \qquad (1)$$

The reaction which was shown in **reaction scheme (1)** is followed by the oxidation of V_2O_3 to V_2O_5 [4]. This could also be seen due to a color change of the sample where the initial sample was greyish, the heated sample was orange which indicates V_2O_5.

The thermal analysis for $SnCrBO_4$ shows at lower temperatures up to 750 K a slight mass loss, which might be due to removal of left-over humidity of the sample. $SnCrBO_4$, however, shows the first endothermic signal between 790 K and 870 K, which decomposed at 1074(1) K to SnO_2, Cr_2O_3 and B_2O_3. The first endothermic signal might be that the decomposition starts where **reaction scheme (2)** is possible to happen:

$$2\ SnCrBO_4 + O_2 \rightarrow 2\ SnO_2 + 2\ CrBO_3 \qquad (2)$$

This decomposition could not be obtained during the high temperature XRPD measurements which might be that the transition is not stable and quite fast. The larger endothermic signal at 1074(1) K exhibits the decomposition to the oxides which was described for $SnVBO_4$ in **reaction scheme (1).**

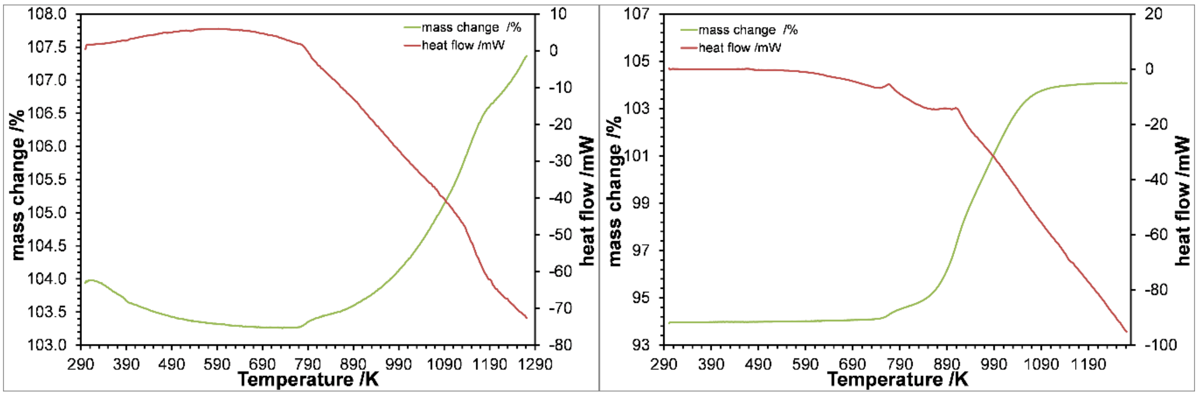

Figure 5.1: Temperature dependent mass change (green) and heat flow (red) for $SnCrBO_4$ (left) and $SnVBO_4$ (right).

The differential scanning calorimetric results at lower temperatures between 123 K and 443 K is shown in **figure 5.2**. A change (hump) in the heat flow is observed at 140 K and 147 K for $SnCrBO_4$ and $SnVBO_4$, respectively. Both these endothermic changes are most likely associated with respective magnetic phase transition [5].

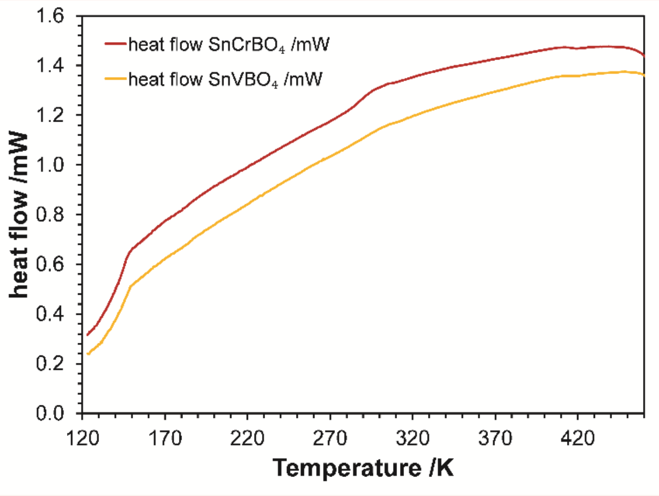

Figure 5.2: Differential scanning calorimetry of $SnCrBO_4$ (red) and $SnVBO_4$ (orange) with its heat flow.

The 2D temperature-dependent Rietveld plots are shown in **figure A5.1** . For both mullite-type phases the TD-XRPD measurements show only the parental phases between 13 K and 850 K. Comparing these findings to the in **chapter 3** discussed compounds, the only observation was the parental phase. The Bragg reflections of the larger unit cells are shifted to higher Q-values (**figure A5.1**). **Figure 5.3** and **figure A5.2** show temperature-dependent evolutions of metric parameters of $SnCrBO_4$ and $SnVBO_4$, respectively along with the model fits. The lattice parameters and the cell volumes of $SnVBO_4$ and $SnCrBO_4$ are increasing during the whole temperature range of about 1-4 pm and 3-4 · 10^6 pm^3. As mentioned in **chapter 3**, the trend of the lattice parameter for $SnMBO_4$ (M = Al, Ga) is $\Delta\, a = \Delta\, b > \Delta\, c$ which is similar to $SnVBO_4$ whereas the trend for $SnCrBO_4$ is $\Delta\, b < \Delta\, a < \Delta\, c$. The shift of the trend might be influence by different magnetic properties of Cr^{3+} compared to the two non-magnetic Al^{3+} and Ga^{3+} as well as the magnetic V^{3+}. The magnetic effect of $SnCrBO_4$ can also be seen in the TD XRPD evolutions of the metric parameters in **figure 5.3**. Especially, lattice parameter b and c show a negative thermal expansion from 13 K to around 100 K.

The Debye-Einstein-Anharmonicity (DEA) model [6, 7] well describes the metric parameters above 145 K for both phases, leading to the fit parameters, as listed in **table 5.1**. As such, the axial negative thermal expansion coefficients for the *a*- and *b*-lattice parameters and positive thermal expansion coefficient for *c*-lattice parameter exhibit clear point of inflections at around 145 K, supporting the endothermic humps at low-temperatures (**Figure 5.1 & 5.2**). For all metric parameters of $SnVBO_4$, the cell volume and lattice parameter *a* for $SnCrBO_4$, a single Debye spectrum with a single Einstein oscillator approach is enough to fit the temperature-dependent parameters. For lattice parameter *b* and *c* of $SnCrBO_4$, another Debye term should be used to also describe the magnetic effect along these two directions.

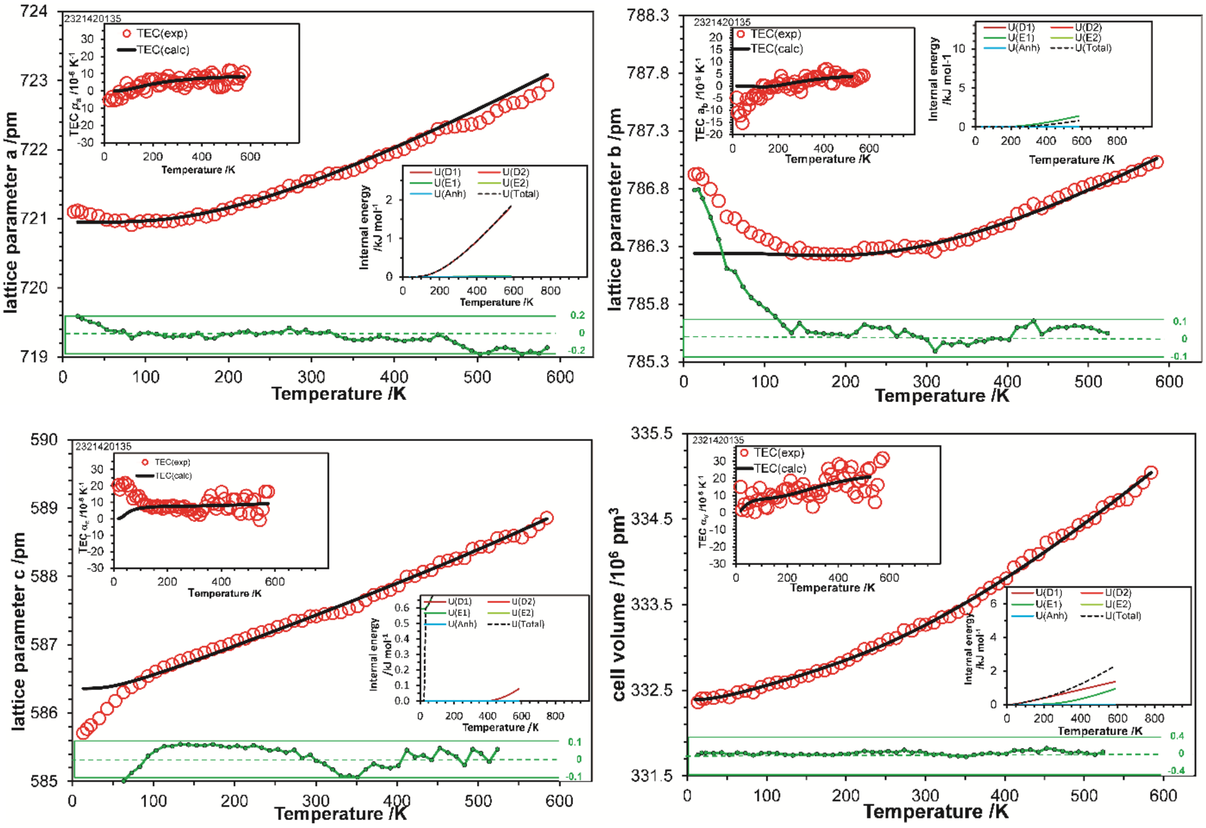

Figure 5.3: Debye-Einstein-Anharmonicity (DEA) fits of the metric parameters of $SnCrBO_4$. The respective thermal expansion coefficients (TECs) are seen as insets.

The Debye temperature of $SnCrBO_4$ phase is found to be lower than of $SnVBO_4$, which are both lower compared to $SnAlBO_4$ (739 K) and $SnGaBO_4$ (546 K). This lowering might be due to the magnetic trivalent metal cations of the newly characterized structures. The observation that the stability of the compound decreases with increasing cell volume can also be done for these two compounds. Hence, the higher the temperature the more unstable the compound which is leading to a decomposition of the mullite-type phase.

Table 5.1: Debye-Einstein-Anharmonicity (DEA) fit parameters of $SnCrBO_4$.

	Cell volume	lattice parameters		
Fit-parameter	***V***	***a***	***b***	***c***
M_0 /10^{-6} pm^3	332.39(9)	720.95(5)	786.77(6)	585.28(4)
k_{D1} /10^{-12} GPa	2.54(1)	5.92(1)	8.18(1)	11.05(1)
θ_{D1} /K	238(10)	910(70)	647(9)	3536(9)
k_{D2} /10^{-12} GPa			6.41(1)	12.10(1)
θ_{D2} /K			47(1)	28(9)
k_E /10^{-12} GPa	5.27(1)	0.18(1)	1.51(1)	9.72(2)
θ_E /K	1196(8)	1512(9)	41(1)	219(9)

While the calculated thermal expansion coefficient (TEC) which is shown in **figure 5.4** is nearly linear between 300 K and 600 K, the TECs hardly change between 13 K and 200 K. In the case of $SnCrBO_4$, an increase of the TEC of about 70 $\cdot 10^{-6}$ K^{-1} is followed by a sudden decrease to an oscillation around 15 $\cdot 10^{-6}$ K^{-1}. This is influenced by the change of magnetic property in the structure which is explained later. For the TEC of $SnVBO_4$, the influence of the magnetic structure is not as impregnant as for $SnCrBO_4$ and therefore, the TEC is in a range between 2 $\cdot 10^{-6}$ K^{-1} and 20 $\cdot 10^{-6}$ K^{-1} which means that it is quite linear and nearly no change can be observed.

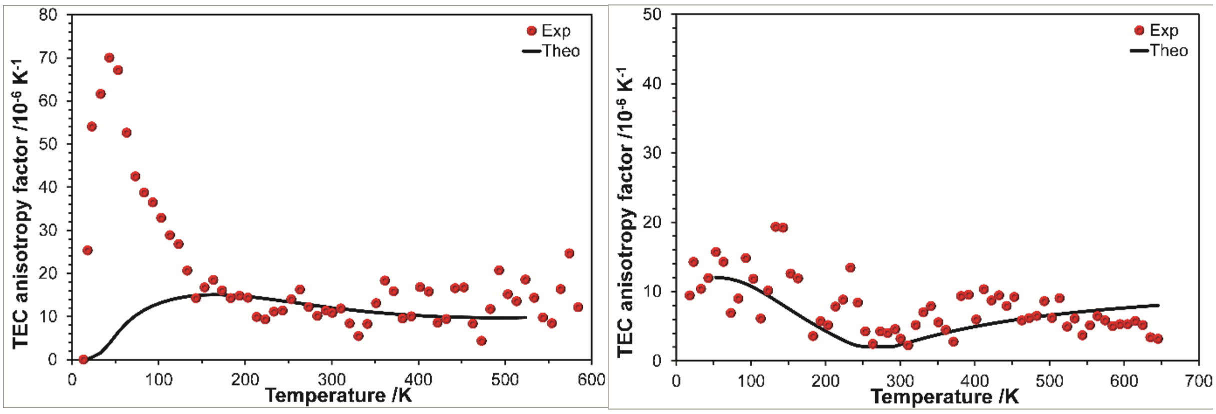

Figure 4: Temperature-dependent thermal expansion coefficient (TEC) anisotropy parameter of $SnCrBO_4$ (left) and $SnVBO_4$ (right).

Details of vibrational feature of $SnCrBO_4$ and $SnVBO_4$ at ambient conditions have been described in the prepared manuscript of **chapter 4**. The temperature-dependent Raman spectra are shown in **figure 5.5** for low temperature measurements and in **figure 5.6** for the high temperature measurements. Each M-O stretching mode of the respective polyhedral as BO_3, SnO_4, and AlO_6 shows a clear red-shift with the thermal expansion of the lattice due to quasi-harmonic behaviors. The measuring conditions were unpolarized and therefore, almost all bands, as previously observed (**chapter 4**) were clearly seen.

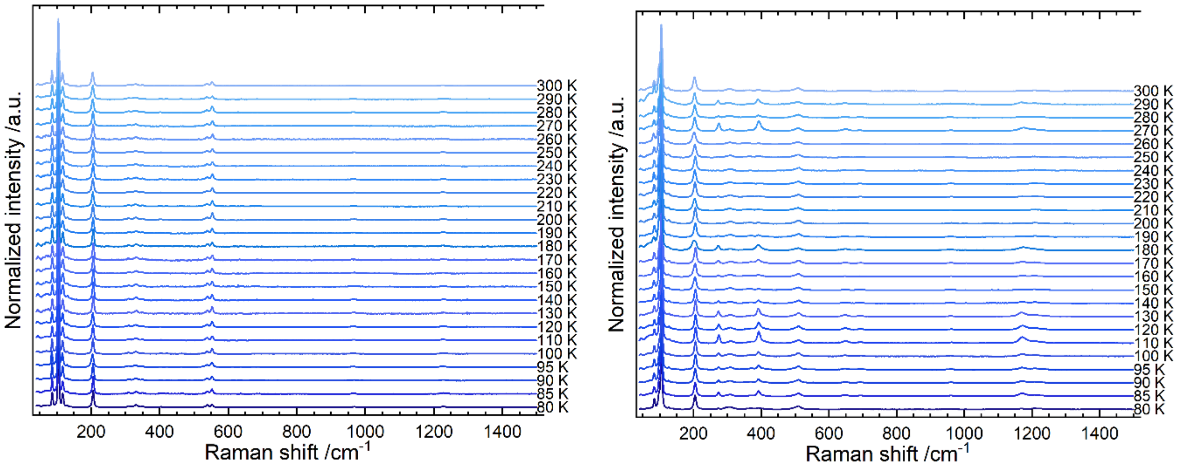

Figure 5.5: Low-temperature Raman spectra of $SnCrBO_4$ (left) and $SnVBO_4$ (right).

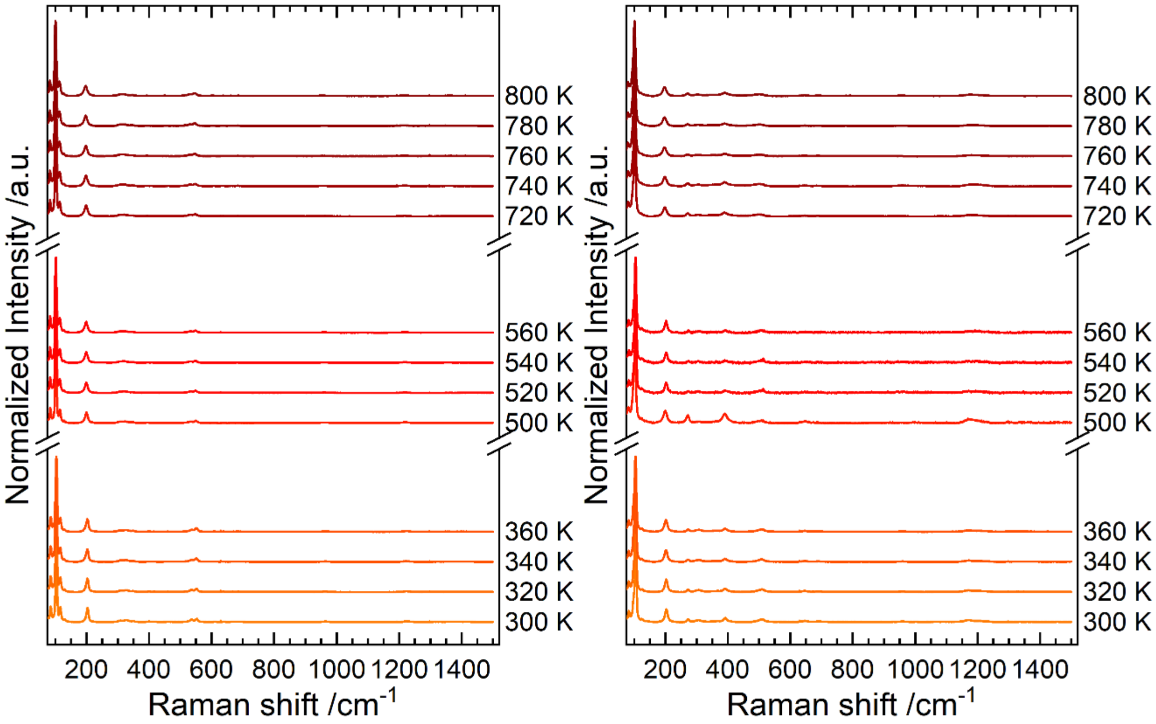

Figure 5.6: High-temperature Raman spectra of $SnCrBO_4$ (left) and $SnVBO_4$ (right).

Both mullite-type compounds show global blue shift (hardening) of the Raman bands below 145 K due to magneto volume effects, as shown in **figure 5.7** for some representative optical modes of $SnCrBO_4$. On the other hand, above 145 K the red-shifts are associated with usual positive thermal expansion (quasi-harmonic) and high-temperature phonon anharmonicity (phonon-phonon interactions). The usual line-shape broadening of the signals can be explained in terms of phonon scattering and anharmonic decay. Compared to the DSC measurements of before, the three humps can also be seen in the Raman spectra shown in **figure 5.7** at ω_i = 85 cm^{-1}.

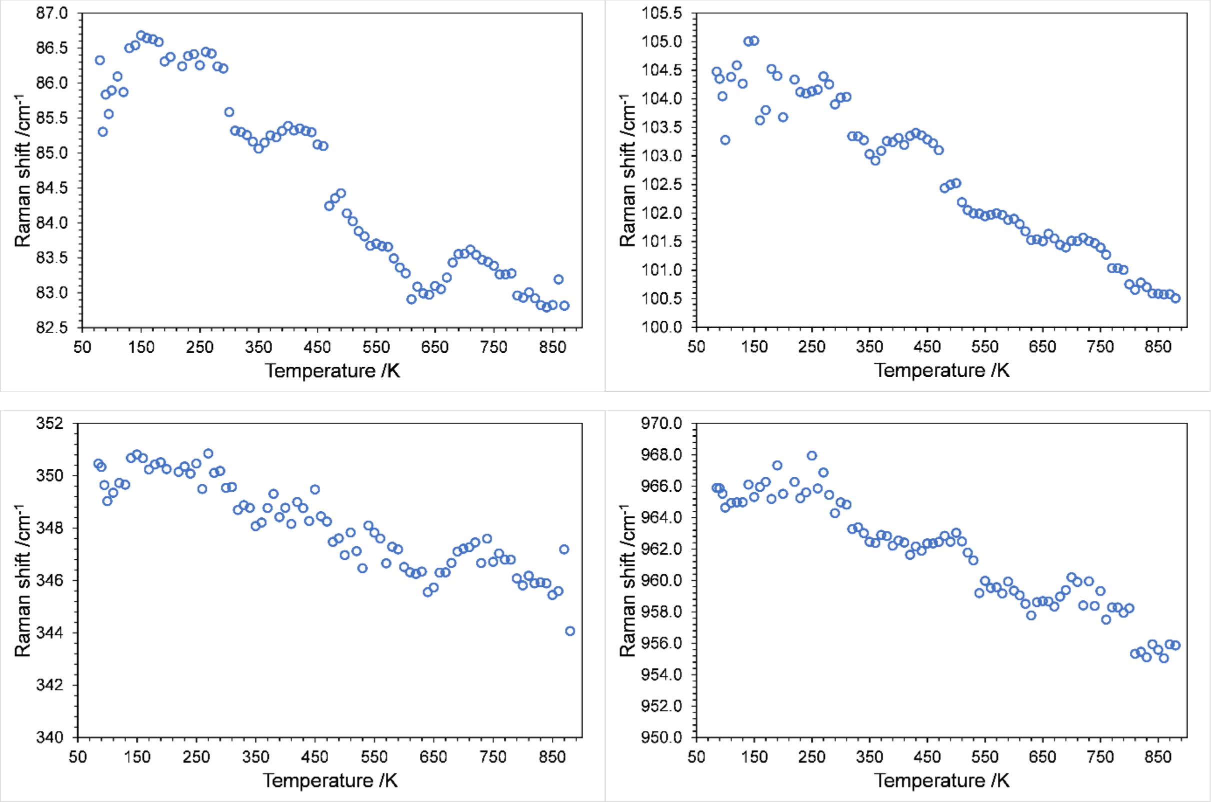

Figure 5.7: Respective Raman frequencies of $SnCrBO_4$ at ω_i, where i = 85 cm^{-1}, 105 cm^{-1}, 350 cm^{-1}, and 955 cm^{-1}.

For detailed anharmonic analysis, we selected six frequencies (in cm^{-1}) ω_i, where *i = 83, 204, 321, 364, 693 and 1173* of $SnCrBO_4$ at room temperature, respectively assigned to B-O, M-O and Sn-O stretching of the corresponding polyhedra which is explained more detailed in the paper about temperature dependent properties of $SnAlBO_4$ and $SnGaBO_4$ (**chapter 3**). The trend of these frequencies of $SnCrBO_4$ is shown in **figure 5.8** where it is obtained that the bands are shifting towards smaller frequencies. The bands with their trend of $SnVBO_4$ is shown in the appendix (**figure A5.3**).

Table 5.2: Selective Raman frequencies of $SnVBO_4$ and $SnCrBO_4$ at 0 K, their corresponding mode Grüneisen parameter together with the fitting parameters

$SnVBO_4$				$SnCrBO_4$			
ω_{i0} /cm^{-1}	$(\gamma_i)_T$	A /cm^{-1}	B /cm^{-1}	ω_{i0} /cm^{-1}	$(\gamma_i)_T$	A /cm^{-1}	B /cm^{-1}
83.97	0.39	-0.18(4)	-0.004(2)	83.97	0.20	-0.18(8)	-0.001(1)
204.36	0.51	-0.26(5)	-0.003(4)	204.36	0.46	-0.09(1)	-0.008(5)
364.34	1.18	-0.07(2)	-0.011(1)	321.15	0.36	-0.32(1)	-0.001(1)
510.96	0.58	-0.24(5)	-0.006(2)	364.34	1.42	-0.81(1)	-0.007(1)
959.81	1.07	-0.50(1)	-0.015(1)	692.88	1.75	-0.68(1)	-0.028(3)
1172	0.61	-0.42(2)	-0.001(1)	1173	1.03	-0.40(1)	-0.001(1)

The selection of the bands helps in understanding the change of the frequencies and line-widths due to the quasi-harmonic (lattice) and isochoric (intrinsic) contributions. With the following equation, the Mode Grüneisen parameter has been calculated: $\gamma_i = \partial ln\omega_i / \partial lnV$ [8]. If the Klemens approach [9] is considered, the 3-phonon and 4-phonon interactions are analyzed [10] which is shown in **figure 5.8** for $SnCrBO_4$ and in **figure A5.3** for $SnVBO_4$ and the parameters are shown in **table 5.2**. This model is simplified and shows the contributions from the anharmonic phonon decay which processes to the frequency shift of the respective compound.

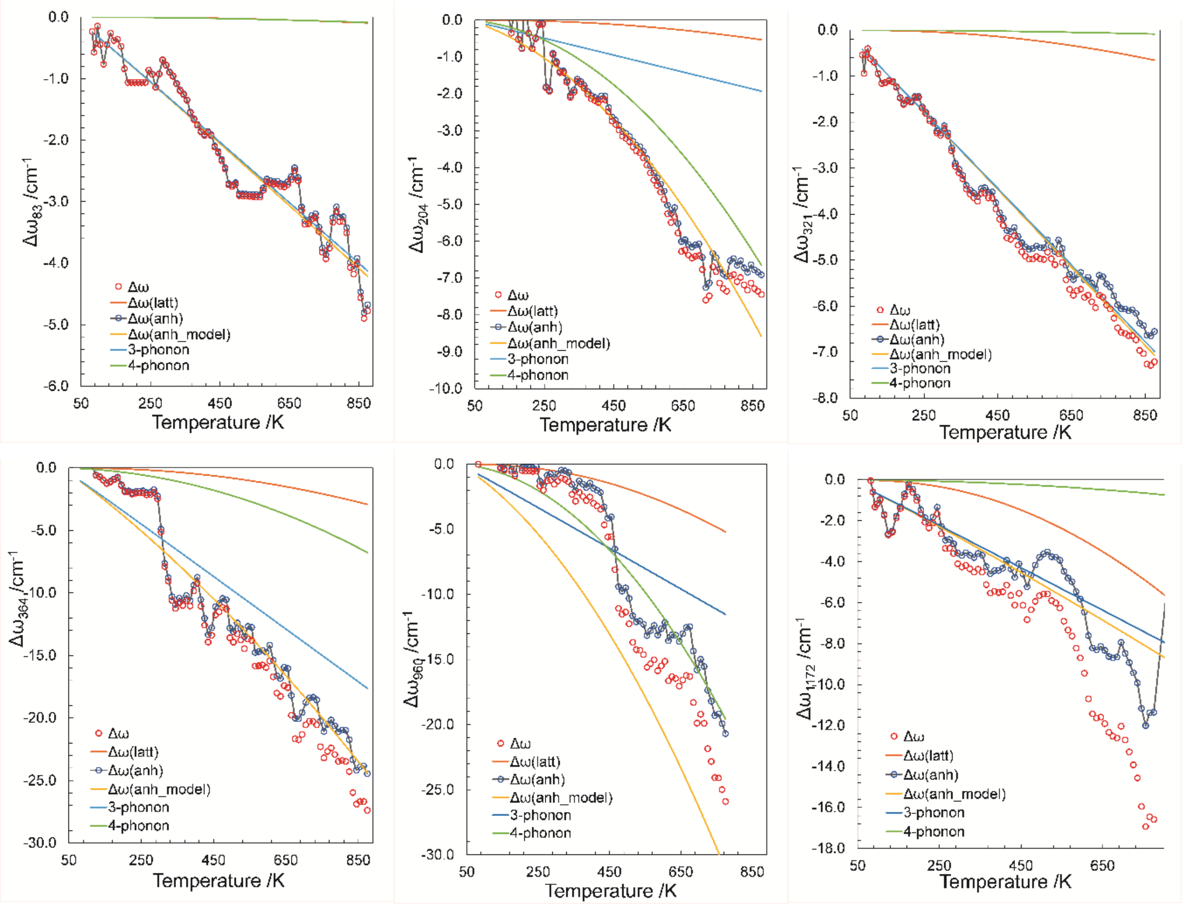

Figure 5.8: Temperature dependent change of phonon frequencies of some representative Raman bands of $SnCrBO_4$. The red circles, the blue circles combined with the grey solid line, and the orange solid line refer to observed frequency shift, frequency shift due to volume and anharmonic contributions, respectively. The solid lines in blue and green represent the model calculation based on the phonon-phonon interactions.

The ^{119}Sn Mössbauer spectra at room temperature and at 78 K of $SnCrBO_4$ are shown in **figure 5.9** and the fitted values are summarized in **table 5.3**. At 293 K, the spectrum consists of one doublet with an isomeric shift at 2.93(2) mm/s which is described in more detail in **chapter 4**. This peak is associated with a Sn^{2+} cation, showing quadrupole splitting of 1.30(3) mm/s and an absorber linewidth at 0.87(4) mm/s. The isomeric shift of $SnCrBO_4$ is close to that of $SnAlBO_4$ [11]. The lower quadrupolar splitting value indicates lower local distortion around Sn^{2+} cation in SnO_4 polyhedra. The effective *5s* and *5p* electron population of Sn(II) was calculated [11] where the number of *s* electron (n_s) is 1.21(5) and of the *p* electron (n_p) is 0.79(3). These values indicate a mixed (*s*-*p*) character instead of a pure *s*-character of the cation.

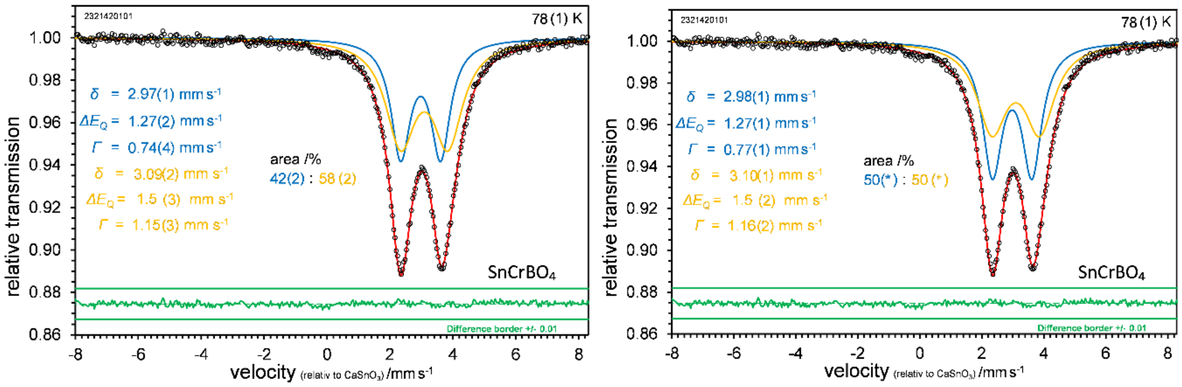

Figure 5.9: Mössbauer spectra of $SnCrBO_4$ at 78 K with two different fittings where one is fitted 50:50 and the other one 42:58 for the ratio of the two doublets. The spectra show both the observed (filled cycles) and fit data (solid line).

At 78 K, an additional doublet is observed, and two different models were tested for fitting the doublets. The first model results in chemical shifts at 2.96 mm/s and 3.10 mm/s with 1:1 ratio. The second model suggests slightly a different shift at 2.97 mm/s and 3.09 mm/s with 2:3 ratio. This second doublet apparently supports for either a displacive/isostructural phase transition or magnetostriction at low temperature, leading to slightly a different Sn^{2+} environment, which could not be observed within the XRPD resolution. In both cases the second doublet shows slightly a higher quadrupole splitting, pointing to slightly a higher *s*-electron density at the tin nuclei.

Table 5.3: Fitting parameters of ^{119}Sn Mössbauer spectroscopic measurements of $SnCrBO_4$ at room temperature and 78 K (with two different fittings). δ = isomer shift; ΔE_Q = electric quadrupole splitting; Γ = experimental line width.

Parameter	**SnCrBO₄ (293 K)**	**SnCrBO₄ (78 K;2:3)**		**SnCrBO₄ (78 K; 1:1)**	
δ /(mm/s)	2.93(2)	2.97(1)	3.09(2)	2.98(1)	3.10(1)
ΔE_Q /(mm/s)	1.30(3)	1.27(2)	1.50(3)	1.27(1)	1.50(2)
Γ /(mm/s)	0.87(4)	0.74(4)	1.15(3)	0.77(1)	1.16(2)
n_s	1.21(5)	1.23(1)	1.27(1)	1.23(3)	1.28(1)
n_p	0.79(3)	0.77(2)	0.73(2)	0.77(2)	0.72(2)
(n_x+n_y)	0.28(2)	0.28(2)	0.24(2)	0.28(2)	0.24(2)
n_z	0.48(2)	0.49(1)	0.49(3)	0.49(1)	0.49(2)

The second doublet for the $SnCrBO_4$ ^{119}Sn Mössbauer spectroscopy measurement is mainly based on the change of the symmetry of Sn(II) of the mullite-type phase. Compared to the before mentioned DSC measurements, a likely phase transition of the mullite-type materials takes place where the orthorhombic crystal structure lowers its symmetry to a possible monoclinic one. For the $SnVBO_4$ mullite-type compound only one signal is obtainable which is shown in the appendix in **figure A5.4**. As the DSC shows the same effects as for $SnCrBO_4$, the isomeric shift of the second doublet might be overlapping with the first one. Hence, the second doublet is not observable in the spectrum. As also obtained in **chapter 4**, an additional signal of SnO_2 as impurity is obtained in the spectrum. Anyways, the doublet indicates a Sn(II) with a mixed (*s*-*p*) character (**table A5.3**). Hence, for all four described and during this work newly synthesized mullite-type compounds, the influence of *s*- and *p*- orbital is similar with a slightly different isomeric shift of the signal.

While a likely phase transition is only obtained in ^{119}Sn Mössbauer measurements as well as DSC measurements, temperature dependent XRPD and Raman spectroscopy could not predict one. Modeling of the lattice thermal expansion using the DEA approach shows that the two magnetic mullite-type compounds $SnVBO_4$ and $SnCrBO_4$ have the lowest Debye temperature which might be influenced by the magnetic properties. Hence, one future work should be the magnetic investigations of these two samples. For $SnCrBO_4$, a magnetic trend was obtained in TD-XRPD and Raman measurements which could be explained with a magnetic susceptibility measurement. As these two methods could not prove the observation of the more sensitive Mössbauer spectroscopy, a higher resolution is necessary to solve this problem, for example with a measurement at a synchrotron facility.

Reference

1. M. Burianek, M. Mühlberg, M. Woll, M. Schmücker, T.M. Gesing, H. Schneider, Single-crystal growth and characterization of mullite-type orthorhombic $Bi_2M_4O_9$ (M = Al^{3+}, Ga^{3+}, Fe^{3+}), Crystal Research and Technology 44(10) (2009) 1156-1162. DOI:10.1002/crat.200900465
2. M. Curti, A. Kirsch, L.I. Granone, F. Tarasi, G. López-Robledo, D.W. Bahnemann, M.M. Murshed, T.M. Gesing, C.B. Mendive, Visible-Light Photocatalysis with Mullite-Type $Bi_2(Al_{1-x}Fe_x)_4O_9$: Striking the Balance between Bandgap Narrowing and Conduction Band Lowering, ACS Catalysis 8(9) (2018) 8844-8855. DOI:10.1021/acscatal.8b01210
3. T.M. Gesing, C.B. Mendive, M. Curti, D. Hansmann, G. Nénert, P.E. Kalita, K.E. Lipinska, A. Huq, A.L. Cornelius, M.M. Murshed, Structural properties of mullite-type $Pb(Al_{1-x}Mn_x)BO_4$, Zeitschrift für Kristallographie - Crystalline Materials 228(10) (2013). DOI:10.1524/zkri.2013.1640
4. P. Hu, P. Hu, T.D. Vu, M. Li, S. Wang, Y. Ke, X. Zeng, L. Mai, Y. Long, Vanadium Oxide: Phase Diagrams, Structures, Synthesis, and Applications, Chemical Reviews 123(8) (2023) 4353-4415. DOI:10.1021/acs.chemrev.2c00546
5. H. Park, J. Barbier, R.P. Hammond, Crystal structure and polymorphism of $PbAlBO_4$, Solid State Sciences 5(4) (2003) 565-571. DOI:10.1016/s1293-2558(03)00056-6
6. P. Mishra, Variation of Debye temperature with size of nanoparticles, AIP Conference Proceedings 2220 (2020). DOI:10.1063/5.0002346
7. M. Wolpmann, L. Robben, T.M. Gesing, Halide-sodalites: thermal expansion, decomposition and the Lindemann criterion, Z. Kristallor.-Cryst. Mater. 237(1-3) (2022) 39-50. DOI:10.1515/zkri-2022-0004
8. M.M. Murshed, T.M. Gesing, Anisotropic thermal expansion and anharmonic phonon behavior of mullite-type $Bi_2Ga_4O_9$, Materials Research Bulletin 48(9) (2013) 3284-3291. DOI:10.1016/j.materresbull.2013.05.007
9. P.G. Klemens, Anharmonic Decay of Optical Phonons, Physical Review 148(2) (1966) 845-848. DOI:10.1103/PhysRev.148.845
10. M.M. Murshed, C.B. Mendive, M. Curti, G. Nénert, P.E. Kalita, K. Lipinska, A.L. Cornelius, A. Huq, T.M. Gesing, Anisotropic lattice thermal expansion of $PbFeBO_4$: A study by X-ray and neutron diffraction, Raman spectroscopy and DFT calculations, Materials Research Bulletin 59 (2014) 170-178. DOI:10.1016/j.materresbull.2014.07.005
11. S. Wittmann, M.M. Murshed, V. Bilovol, A. Koldemir, R. Pöttgen, U.G. Nielsen, T.M. Gesing, Mullite-type $EMBO_4$: synthesis, structural, optical, and vibrational properties of rare tin(II) borates with M = Al and Ga, Journal of the American Ceramic Society 107(2) (2023) 1302-1314. DOI:10.1111/jace.19476

Chapter 6 – Syntheses and characterization of mullite-type $Sn(M_{1-x}M'_{x})BO_4$ compounds

The successful syntheses of some parental phases ($SnAlBO_4$, $SnGaBO_4$, $SnVBO_4$ and $SnCrBO_4$) leads to check the miscibility between two trivalent cations in the mullite-type structure within the solution $SnM'_{1-x}M''_{x}BO_4$. This chapter (manuscript in preparation) particularly emphasizes on how co-sharing a given Wyckoff of the mullite-type systems by two different sized cations influence the crystal-physico-chemical properties.

Synthesis and characterization of mullite-type $Sn(M_{1-x}M'_{x})BO_4$ (M = Al, Ga, Cr; M' = Al, Ga, Cr)

Sarah Wittmann[1], M. Mangir Murshed[1,2*], Thorsten M. Gesing[1,2]

(Manuscript in preparation)

[1]University of Bremen, Institute of Inorganic Chemistry and Crystallography, Leobener Straße 7, D-28359 Bremen, Germany

[2]University of Bremen, MAPEX Center for Materials and Processes, Bibliothekstraße 1, D-28359 Bremen, Germany

ORCID:

SW:	0000-0003-1404-3434
MMM:	0000-0002-9063-372X
TMG:	0000-0002-4119-2219

*Corresponding author: murshed@uni-bremen.de, phone: +49 (0)421 218 63144

Abstract

We report solid solutions between the endmembers of the mullite-type compounds of $SnAlBO_4$, $SnGaBO_4$, and $SnCrBO_4$. The samples $Sn(Al_{1-x}Ga_x)BO_4$, $Sn(Al_{1-x}Cr_x)BO_4$, and $Sn(Ga_{1-x}Cr_x)BO_4$ are produced by conventional solid-state syntheses using sealed-quartz tubes at low pressures of 10^{-7} MPa. Each member of the solid solutions is characterized by X-ray powder diffraction followed by Rietveld refinement. The influence of the stereochemical activity of the $5s^2$ lone electron pair of the Sn^{2+} cation has been measured by the Wang-Liebau eccentricity parameter. The metric parameters mostly follow the Vegard's rule in changing the chemical composition. The complementary vibrational properties are discussed from group theoretical analysis to mode assignments. Characteristic mode frequencies are studied with respect to the compositional x-values. For the Cr(III) containing sample, the decomposition temperature increases with increasing Cr^{3+} content, whereas the $Sn(Al_{1-x}Ga_x)BO_4$ decreases with increasing averaged cationic radii of the trivalent metal cation.

Keywords: metal tin-(II)-borate, crystal structure, trivalent metal cation, Raman spectroscopy, thermal investigation

1. Introduction

$SnMBO_4$ (M = Al, Ga, and Cr) are members of mullite-type O8 phases, where the MO_6 octahedral chain runs along the crystallographic **c**-axis [1]. These chains are interconnected by trigonal planar BO_3 and distorted pyramidal SnO_4 groups. The Sn^{2+} keeps stereochemically active lone electron pairs (LEPs) which influence the local distortion which eventually distributed to the octahedral chains. Each of the $SnMBO_4$ phases (M = Al, Ga, Cr) crystallizes in the space group *Pnam* [2-5]. Two asymmetric O-M-O bridging angels in the MO_6 chains serve for the M-M bond length [3, 6]. As the different size of the trivalent M-cation (M = Al, Ga, Cr) influences the MO_6 octahedra as well as the crystallite size, an investigation of substation of different cations is important to understand the different structural properties. Herein, we report three solid solutions $Sn(Al_{1-x}Ga_x)BO_4$, $Sn(Al_{1-x}Cr_x)BO_4$, and $Sn(Ga_{1-x}Cr_x)BO_4$ and particularly emphasizes on how co-sharing a given M-Wyckoff site with different cations influence the crystal-physico-chemical properties. Since the size of the M-cation directly influences the MO_6 octahedra, leading to axial metric parameters study of these solid solutions not only check the crystal-chemical miscibility but also help tune the average crystallite size, microstrain and thermal stability. While syntheses of $SnMBO_4$ compounds are recently reported not to be straightforward due to oxidation of Sn^{2+} to Sn^{4+} [7], synthesis of these solid solutions with different M-cationic radii would demonstrate how the associated challenges are resolved followed by structural, spectroscopic, and thermogravimetric characterizations. The present study describes the synthesis of the three different solid solutions and their characterization including XRPD with Rietveld refinements, Raman spectroscopy and thermal analysis.

2. Experimental

2.1 Synthesis

A stoichiometric mixture of SnO where 20 % were replaced by elementary tin, M_2O_3 and M'_2O_3 (M and M' build one of the solid solutions $Al_{1-x}Ga_x$, $Al_{1-x}Cr_x$ or $Ga_{1-x}Cr_x$) as well as 80 % excess of B_2O_3 were mixed and put in a preheated quartz tube which was further heated to 473 K for at least two hours to reduce the absorbed moisture. During a dynamic vacuum process where the pressure was reduced to 10^{-7} MPa, the quartz tube was sealed. The sealed samples were placed in an oven, heated at 1023 K for three days with a cooling and heating rate of 200 K /h to obtain a polycrystalline powder and grinded again.

2.2 X-ray diffraction

XRPD measurements were carried out on a Bruker D8 Advance diffractometer (Bruker AXS GmbH, Karlsruhe Germany) using Bragg-Brentano geometry with a $CuK_{\alpha 1}$ radiation and a Johansson Monochromator. The data were collected at ambient conditions in the 2θ range from 10 to 90° with a step size of 0.0145 and a data collection time of 1.25 s/step. The fundamental parameter approach, where the fundamental parameters were fitted against a LaB_6 standard material, was applied for the Rietveld refinement using the "Diffrac^{Plus} Topas 6" software (Bruker AXS GmbH, Karlsruhe, Germany). The starting atomic coordinates were taken from the single crystal data of $PbAlBO_4$ [8], where Pb^{2+} was replaced by Sn^{2+} in the asymmetric unit.

2.3 Spectroscopy

Raman spectroscopy

Raman spectra were recorded on a LabRam ARAMIS (Horiba Jobin Yvon) Micro Raman spectrometer which was equipped with a laser working at 532 nm and less than 20 mW. A 50× objective (Olympus) with a numerical aperture of 0.55 provides a spot focus of about 2 µm diameter. The spectra were collected in the range of 40 cm^{-1} to 1500 cm^{-1} with a spectral resolution of about 1.2 cm^{-1} using a grating of 1800 grooves/mm and a thermoelectrically-cooled CCD detector (Synapse, 1024×256 pixels). Peak positions, peak widths and profile shapes were deconvoluted into Gaussian and Lorentzian components using the LAMP software package.

2.4 Thermogravimetric analysis

Simultaneous thermal analyses of TG-DSC were carried out under a dry synthetic air atmosphere (80 vol-% N2 and 20 vol-% O2) and N_2 air with a heating rate of 10 K/min from 303 K to 1273 K on a Mettler Toledo TGA/DSC 3^+ STARe System. About 10(1) mg sample was measured relative to a corundum crucible with 10 mg Al_2O_3 as the reference. A drift correction to the data was applied using an empty corundum crucible measurement.

3. Results and discussion

Synthesis

The endmembers of the solid solutions (x = 0, or x =1) were recently reported [7]. While synthesis of the other members (0 < x < 1) of the $Sn(Ga_{1-x}Cr_x)BO_4$ series results in phase pure products as much as 2(1) % impurity, mainly of either SnO_2 or/and SiO_2, are found along with the $Sn(Al_{1-x}Cr_x)BO_4$ and $Sn(Al_{1-x}Ga_x)BO_4$ samples for any given x-value. The cationic radii most probably plays the important roles for phase pure outcomes as the ionic radius between Ga^{3+} (62 pm) and Cr^{3+} (61.5 pm) [9] lies close to each other, while that of Al^{3+}(53.5 pm) significantly differ, leading to microstrain within the ..O-Al-O-Ga-O.. or ..O-Al-O-Cr-O.. The crystal structure of each phase has been confirmed by XRPD analysis and respective Rietveld plots are shown in **figure S1 – S27** (Supplementary Information).

Based on previous results [7], the metric parameters of the three different end – members $SnAlBO_4$, $SnGaBO_4$, and $SnCrBO_4$ are increasing for lattice parameter *a* and *b* as well as for the cell volume with increasing cationic radius. Only lattice parameter *c* is slightly larger for $SnCrBO_4$ compared to $SnGaBO_4$. If the solid solutions are compared separately, all of them follow Vegard's rule [10] which is a linear trend with increasing cationic radius of the trivalent metal cation (**figure 1**).

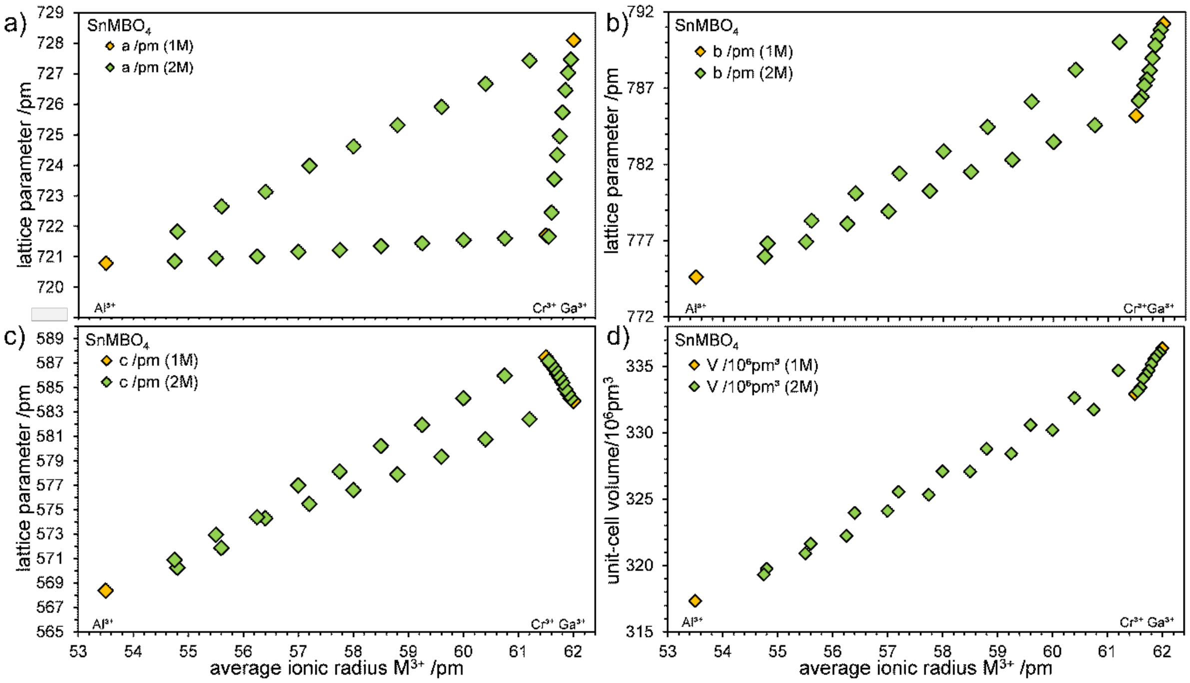

Figure 1: Metric parameters of the solid solutions $Sn(Al_{1-x}Ga_x)BO_4$, $Sn(Al_{1-x}Cr_x)BO_4$, and $Sn(Ga_{1-x}Cr_x)BO_4$ with a) lattice parameter a, b) lattice parameter b, c) lattice parameter c, and d) cell volume.

As mentioned before, the BO_3 groups of the structure have a quite strong rigidity and therefore, the bond length are expected to be stable for the solid solutions. For the three endmembers, bond lengths of B-O are obtained between 133 pm and 150 pm [7]0. If the bond lengths of the three different solid solutions are compared, the same trend is observed where the values are between 131 pm and 143 pm (**figure 2 and figure S28**). Hence, the influence of the BO_3 group during the substitution of one trivalent metal cation to the other one is not to be mentioned.

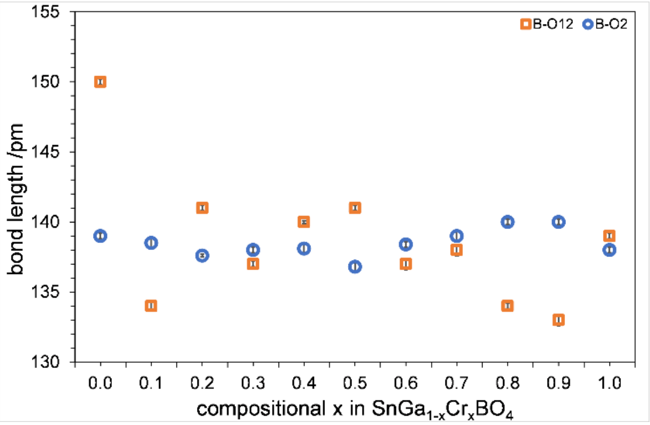

Figure 2: Representative plot of the B – O bond length of the BO_3 groups of $Sn(Ga_{1-x}Cr_x)BO_4$.

The MO_6 octahedra can be divided into three different bond groups which are M-O11 and M-O12 as equatorial oxygen atoms and M-O2 for the apex oxygen atom (**figure 3 and figure S29**). The M-O11 bond length is obtained to be the shortest one for all three solid solutions. Both other M-O bonds in the crystal structure of these mullite-type compounds change slightly but no obvious trend is obtainable. The lattice parameter *a* increases with increasing cationic radius which is noticeable in the bond length to the apex oxygen atom (M-O2) which increases as well with increasing cationic radius as shown in **figure 3**. As both apex oxygens of the same octahedral structure are not running parallel to the crystallographic *c* axis, the before described effect is noticeable in the lattice parameter *b* as well. Due to the difference of the bond lengths of M-O11 and M-O12, one octahedral chain forms a not pronounced zigzag chain which is also influenced by the rigidity of the trigonal planar BO_3 groups.

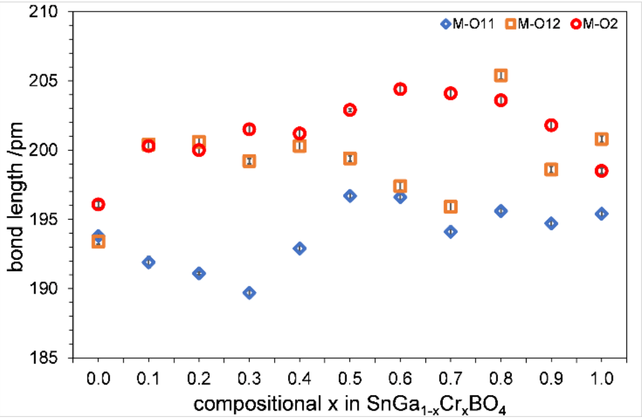

Figure 3: Representative plot of the M-O bond length of $Sn(Ga_{1-x}Cr_x)BO_4$ where each of the bonds is presented twice in the MO_6 octahedra. M-O2 is the bond to the apex oxygen atom and M-O11 and M-O12 are the two different equatorial oxygen atoms.

The distorted square pyramid of SnO_4 has three bonds to the same octahedron and one to an oxygen atom of another octahedral chain. Two of the three bonds are to apex oxygen atoms of two neighboring octahedra and the remaining one is to O11. These three bonds are quite similar in size which is shown in the representative plot of the Sn-O bond length in **figure 4** and in **figure S30** of the supplementary information. The last Sn-O11 bond to the other octahedral chain is longer due to steric effects in the structure.

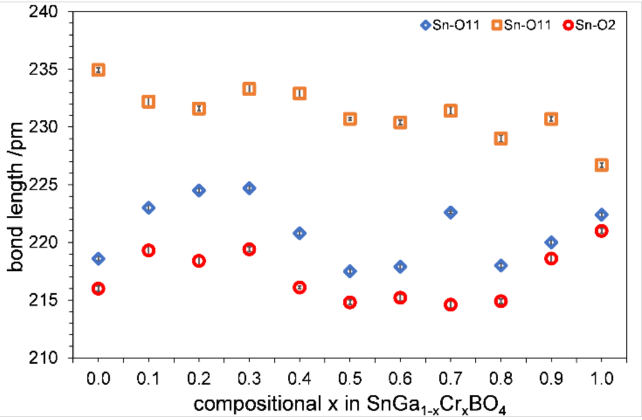

Figure 4: Representative plot of Sn-O bond length of $Sn(Ga_{1-x}Cr_x)BO_4$ with its three different bond types.

Another investigation which was done for these structures was the calculation of bond valence sum (BVS) of Sn^{2+}, M^{3+}, and B^{3+}. For Sn(II), the optimal value is two which is based on the results of the endmembers either slightly higher or slightly lower. The BVS values of the solid solutions are shown in **figure 5** where it can be observed that the values are between 1.75 and 2.20. Another trend is not obtained. A similar investigation can be done for both BVS parameters of M^{3+} and B^{3+}. Based on the BVS parameters the Wang Liebau eccentricity (WLE) parameter can be calculated which is shown in **figure 5** for all three solid solutions. For both solid solutions where aluminum is substituted by either gallium or chromium, the WLE increases with increasing cationic radius whereas for the remaining phases of $Sn(Ga_{1-x}Cr_x)BO_4$ the WLE decreases with increasing cationic radius. A likely reason might be the influence of the magnetic properties of chromium which is not considered if the difference of the two cationic radii is too large. In conclusion, a higher WLE value points to a more stereochemical active LEP which can influence the mullite-type structure and its bond lengths.

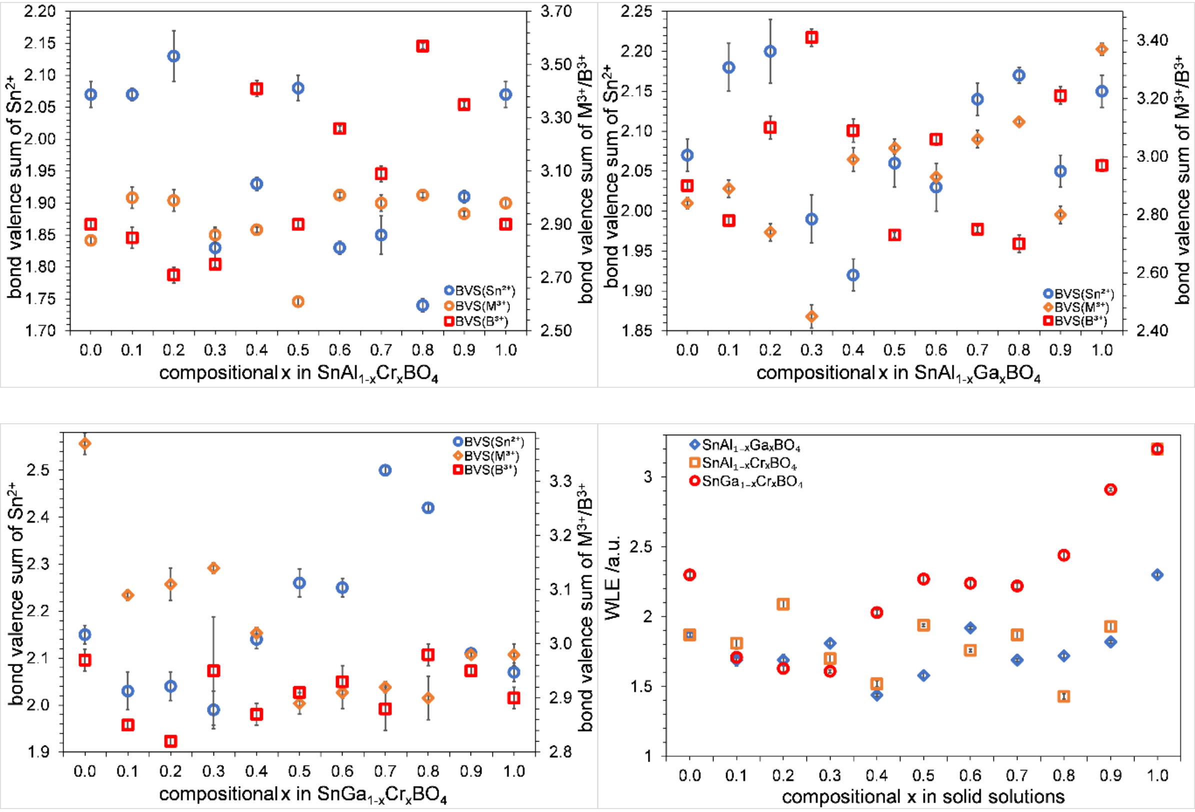

Figure 5: Bond valence sum (BVS) plots of Sn^{2+}, M^{3+}, and B^{3+} for the solid solutions and their Wang Liebau eccentricity parameters of the LEP of tin(II).

Vibrational spectroscopy

Factor group predicts 84 active modes are obtained where 36 are Raman active which is reduced due to technical limitations and low intensity of some bands. The earlier described three different ranges of obtained vibrational contributions is again observed in all solid solutions: (I) low-frequency range between 40 cm^{-1} and 300 cm^{-1}, (II) mid-range from 300 cm^{-1} to 600 cm^{-1} and (III) high-frequency range above 700 cm^{-1}, respectively, for the SnO_4, MO_6 and BO_3 groups. The Raman spectra of the three solid solutions are shown in **figure S31**. For all three solid solutions, a global red shift is observed which can be assigned to the quasi-harmonic nature of the increasing unit cells. In the mid-range region, signals are increasing for increasing metal content which is obtained e.g., in the stacked Raman plot for $SnAl_{1-x}Ga_xBO_4$ with a signal around 400 cm^{-1}. Another example is a signal around 550 cm^{-1} which is only obtained when the sample contains chromium. Hence, the influence of the different trivalent cations can be seen.

The band at around 84 cm^{-1} can be associated to the Sn-O stretching mode of the SnO_4 groups which is obtained for all newly synthesized compounds. For $Sn(Ga_{1-x}Cr_x)BO_4$, a nearly linear behavior is observed up to x = 0.2 and after x = 0.6, whereas between these two compositional x-values an increase of the Raman shift and therefore, a blue shift is observed. This also fits to the before made observation that with increasing cationic radius a red-shift is taken place which is true for $Sn(Al_{1-x}Cr_x)BO_4$. For $Sn(Al_{1-x}Ga_x)BO_4$, a nearly linear trend is obtained (**figure 6**).

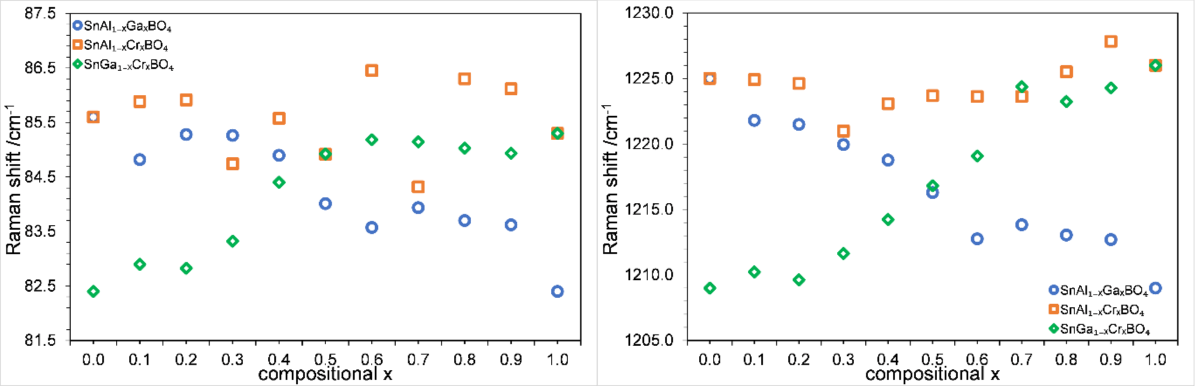

Figure 6: Trend of Raman shifts at around 85 cm^{-1} and 1220 cm^{-1} for Sn(Al$_{1-x}$Ga$_x$)BO$_4$ (circles), Sn(Al$_{1-x}$Cr$_x$)BO$_4$ (squares), and Sn(Ga$_{1-x}$Cr$_x$)BO$_4$ (diamonds).

For a band in the high-frequency region which is assigned to the BO$_3$ subgroups of the compositions, a red shift of the band is obtained with increasing cationic radius. Bands which can be associated with B-O symmetric stretching modes are decreasing for Sn(Al$_{1-x}$Ga$_x$)BO$_4$ as well as for Sn(Al$_{1-x}$Cr$_x$)BO$_4$ whereas the same band is nearly constant for Sn(Ga$_{1-x}$Cr$_x$)BO$_4$ (**figure S32**).

Another red shift can be observed for a band around 770 cm^{-1} which is associated with a O-M-O stretching mode [3]. The shift is more pronounced for the aluminum containing samples with increasing substitution of either gallium or chromium. This effect is again due to the influence of the cation with a larger cationic radius. Compared to the solid solution of Sn(Ga$_{1-x}$Cr$_x$)BO$_4$, where the red shift is obtained to larger chromium contents. This effect might be due to the magnetic property of chromium which influences the crystal structure in the way to obtain a slight red shift in Raman bands (**figure S33**).

Thermogravimetric analysis

The decomposition temperature obtained from the thermal analysis is shown in **figure 7**. Of the parental phases, the thermal stability (decomposition temperature) follows the order SnCrBO$_4$ > SnAlBO$_4$ > SnGaBO$_4$. In both Sn(Al$_{1-x}$Cr$_x$)BO$_4$ and Sn(Al$_{1-x}$Cr$_x$)BO$_4$ series the decomposition temperature follows a sigmoidal increase and Sn($Al_{1-x}Ga_x$)BO_4 a linear decrease with increasing x-value. Irrespective to the metric parameter, the high Cr-content samples (x = 0.8 & 0.9) exhibit similar thermal stability (**Figure 7**). High-temperature decomposition of $SnMBO_4$ results in SnO_2, $Al_{2-x}B_xO_9$ and B_2O_3.

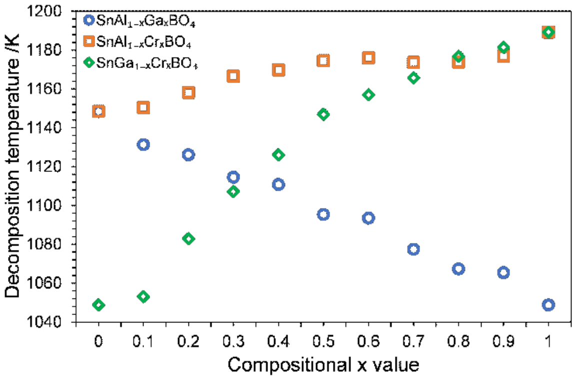

Figure 7: Decomposition temperatures for Sn($Al_{1-x}Ga_x$)BO_4 (circles), Sn($Al_{1-x}Cr_x$)BO_4 (squares), and Sn($Ga_{1-x}Cr_x$)BO_4 (diamonds).

4. Conclusion

Successful synthesis of Sn($Al_{1-x}Ga_x$)BO_4, Sn($Al_{1-x}Cr_x$)BO_4, and Sn($Ga_{1-x}Cr_x$)BO_4 with a chemical slice of x = 0.1 indicates complete miscibility between the respective parental phases. Comparative crystal chemical aspects in terms of metric parameter, bond length and stereochemical activity of the LEP of Sn^{2+} are discussed with respect to the compositional x-value. The stereochemical activity of LEP of Sn^{2+} is found to be stronger in Al-rich compounds than in Ga- and Cr-rich contents. The bulk structural features are complemented by Raman spectroscopy. The Cr-rich samples show higher thermal stability.

Acknowledgement

We gratefully thank the German science foundation (Deutsche Forschungsgemeinschaft, DFG) under grant number GE1981/14-1 for the financial support.

Reference

1. M. Curti, C.B. Mendive, T. Bredow, M. Mangir Murshed, T.M. Gesing, Structural, vibrational and electronic properties of $SnMBO_4$ (M = Al, Ga): a predictive hybrid DFT study, J Phys Condens Matter 31(34) (2019) 345701. DOI:10.1088/1361-648X/ab20a1
2. M. Curti, M.M. Murshed, T. Bredow, D.W. Bahnemann, T.M. Gesing, C.B. Mendive, Elastic, phononic, magnetic and electronic properties of quasi-one-dimensional $PbFeBO_4$, Journal of Materials Science 54(21) (2019) 13579-13593. DOI:10.1007/s10853-019-03866-1
3. T.M. Gesing, C.B. Mendive, M. Curti, D. Hansmann, G. Nénert, P.E. Kalita, K.E. Lipinska, A. Huq, A.L. Cornelius, M.M. Murshed, Structural properties of mullite-type $Pb(Al_{1-x}Mn_x)BO_4$, Zeitschrift für Kristallographie - Crystalline Materials 228(10) (2013). DOI:10.1524/zkri.2013.1640
4. M. Gogolin, M.M. Murshed, M. Ende, R. Miletich, T.M. Gesing, Uniaxial negative thermal expansion in the mullite- and borax-type $PbAlBO_4$ polymorphs, Journal of Materials Science 55(1) (2019) 177-190. DOI:10.1007/s10853-019-04013-6
5. H.-J. Koo, M.-H. Whangbo, Density functional investigation of the magnetic properties of $PbMBO_4$ (M=Cr, Mn, Fe), Solid State Communications 149(15-16) (2009) 602-604. DOI:10.1016/j.ssc.2009.01.030
6. T.M. Gesing, e. al., Crystal structure of mullite-type $PbMn_{0.5}Al_{0.5}BO_4$ determined by combined X-ray and neutron diffraction data, Zeitschrift für Kristallographie - New Crystal Structures 227(3) (2012) 285-286. DOI:10.1524/ncrs.2012.0181
7. S. Wittmann, M.M. Murshed, V. Bilovol, A. Koldemir, R. Pöttgen, U.G. Nielsen, T.M. Gesing, Mullite-type $EMBO_4$: synthesis, structural, optical, and vibrational properties of rare tin(II) borates with M = Al and Ga, Journal of the American Ceramic Society 107(2) (2023) 1302-1314. DOI:10.1111/jace.19476
8. M.M. Murshed, R.X. Fischer, T.M. Gesing, The role of the Pb^{2+}lone electron pair for bond valence sum analysis in mullite-type $PbMBO_4$(M = Al, Mn and Fe) compounds, Zeitschrift für Kristallographie - Crystalline Materials 227(8) (2012) 580-584. DOI:10.1524/zkri.2012.1483
9. R.D. Shannon, Revised effective ionic radii and systematic studies of interatomic distances, Acta Crystallographica A32 (1976) 751.
10. A.R. Denton, N.W. Ashcroft, Vegard's law, Physical Review A 43(6) (1991) 3161-3164. DOI:10.1103/PhysRevA.43.3161

Supporting information

Synthesis and characterization of mullite-type $Sn(M_{1-x}M'_x)BO_4$

(M = Al, Ga, Cr; M' = Al, Ga, Cr)

Sarah Wittmann[1], M. Mangir Murshed[1,2*], Thorsten M. Gesing[1,2]

[1]University of Bremen, Institute of Inorganic Chemistry and Crystallography, Leobener Straße 7, D-28359 Bremen, Germany

[2]University of Bremen, MAPEX Center for Materials and Processes, Bibliothekstraße 1, D-28359 Bremen, Germany

ORCID:

SW: 0000-0003-1404-3434
MMM: 0000-0002-9063-372X
TMG: 0000-0002-4119-2219

*Corresponding author: murshed@uni-bremen.de, phone: +49 (0)421 218 63144

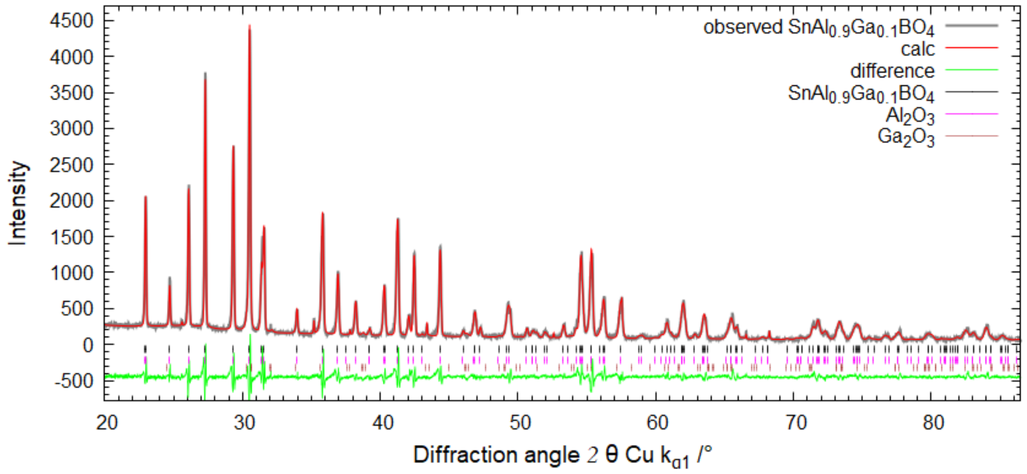

Figure S1: Rietveld refinement plot of $Sn(Al_{0.9}Ga_{0.1})BO_4$ with calculated (red) and observed (grey) patterns, difference curve (green), Bragg peaks of $Sn(Al_{0.9}Ga_{0.1})BO_4$ (black), impurities Al_2O_3 (pink) and Ga_2O_3 (orange).

Table S1: Crystal structure parameters of $Sn(Al_{0.9}Ga_{0.1})BO_4$.

Atom	*Pnam*	*x*	*y*	*z*	*Occupancy*	*B* /10^4 pm^2
Sn1	4*c*	0.0929(2)	0.3631(2)	¼	1	1.17(5)
Al1	4*a*	0	0	0	0.9	1.37(2)
Ga1	4*a*	0	0	0	0.1	1.37(6)
B1	4*c*	0.2800(3)	0.7680(3)	¼	1	0.95(6)
O11	4*c*	0.4054(2)	0.3737(2)	¼	1	0.90(3)
O12	4*c*	0.1546(2)	0.9072(2)	¼	1	1.80(4)
O2	8*d*	0.3367(1)	0.6922(1)	0.0382(2)	1	0.70(2)

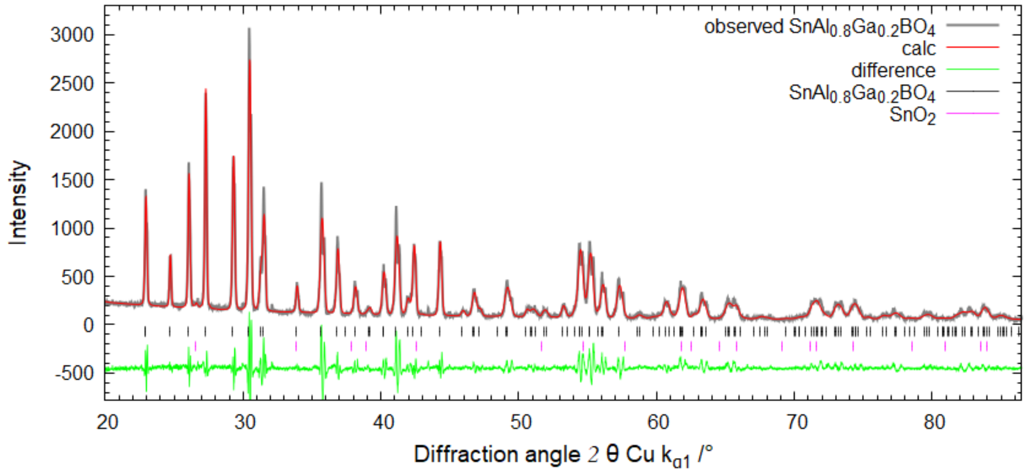

Figure S2: Rietveld refinement plot of $Sn(Al_{0.8}Ga_{0.2})BO_4$ with calculated (red) and observed (grey) patterns, difference curve (green), Bragg peaks of $Sn(Al_{0.8}Ga_{0.2})BO_4$ (black), impurity SnO_2 (pink).

Table S2: Crystal structure parameters of $Sn(Al_{0.8}Ga_{0.2})BO_4$.

Atom	*Pnam*	*x*	*y*	*z*	*Occupancy*	*B* /10^4 pm^2
Sn1	4*c*	0.0918(2)	0.3625(3)	¼	1	0.25(6)
Al1	4*a*	0	0	0	0.8	0.25(2)
Ga1	4*a*	0	0	0	0.2	0.25(1)
B1	4*c*	0.2230(7)	0.7270(8)	¼	1	0.30(2)
O11	4*c*	0.4072(2)	0.3210(2)	¼	1	0.30(5)
O12	4*c*	0.1606(2)	0.9082(2)	¼	1	0.30(3)
O2	8*d*	0.3330(2)	0.6938(2)	0.0546(2)	1	0.30(3)

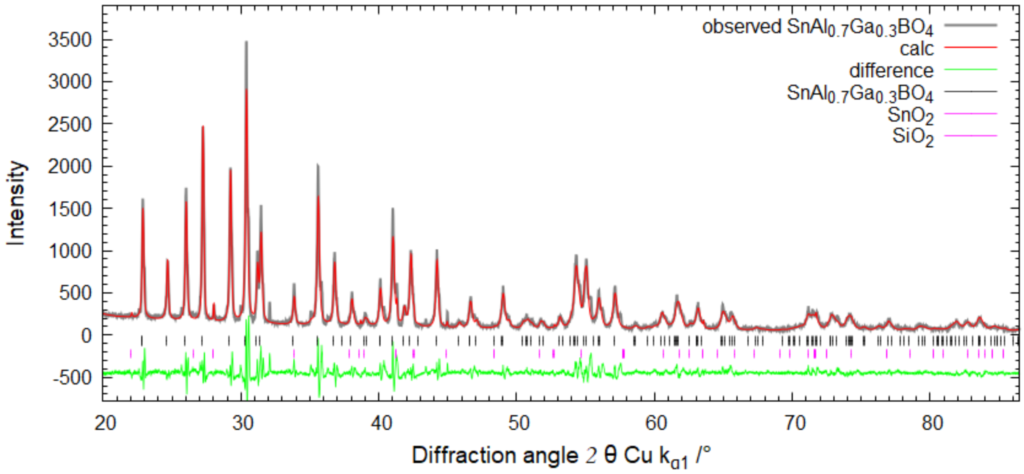

Figure S3: Rietveld refinement plot of $Sn(Al_{0.7}Ga_{0.3})BO_4$ with calculated (red) and observed (grey) patterns, difference curve (green), Bragg peaks of $Sn(Al_{0.7}Ga_{0.3})BO_4$ (black), impurities SnO_2 (pink) and SiO_2 (orange).

Table S3: Crystal structure parameters of $Sn(Al_{0.7}Ga_{0.3})BO_4$.

Atom	*Pnam*	*x*	*y*	*z*	*Occupancy*	*B* /10^4 pm^2
Sn1	4*c*	0.0918(3)	0.3620(3)	¼	1	0.25(7)
Al1	4*a*	0	0	0	0.7	0.25(2)
Ga1	4*a*	0	0	0	0.3	0.25(3)
B1	4*c*	0.2360(8)	0.7480(3)	¼	1	0.30(2)
O11	4*c*	0.3800(3)	0.3821(3)	¼	1	0.30(5)
O12	4*c*	0.1750(2)	0.8030(3)	¼	1	0.30(5)
O2	8*d*	0.3716(2)	0.6971(2)	0.0502(2)	1	0.30(3)

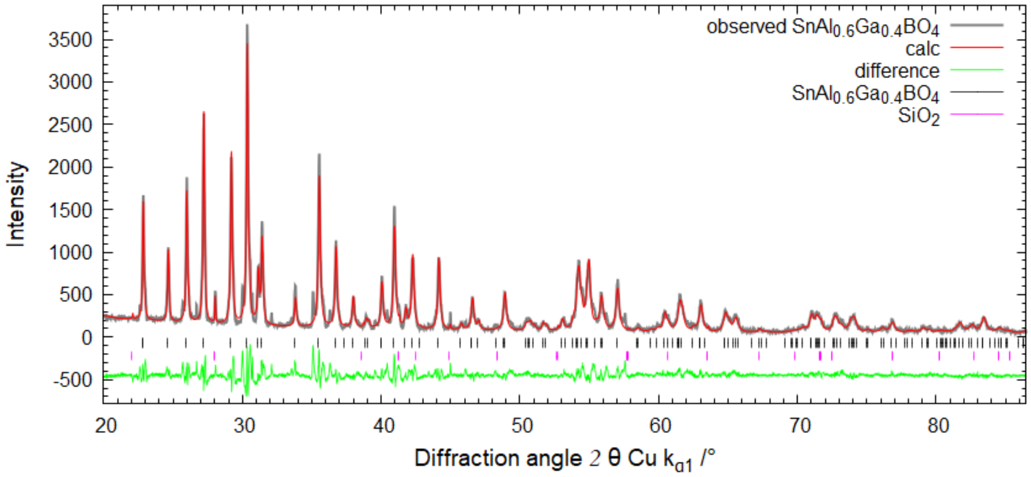

Figure S4: Rietveld refinement plot of Sn($Al_{0.6}Ga_{0.4}$)O_4 with calculated (red) and observed (grey) patterns, difference curve (green), Bragg peaks of Sn($Al_{0.6}Ga_{0.4}$)O_4 (black), impurity SiO_2 (pink).

Table S4: Crystal structure parameters of Sn($Al_{0.6}Ga_{0.4}$)BO_4.

Atom	*Pnam*	*x*	*y*	*z*	*Occupancy*	*B* /10^4 pm^2
Sn1	4*c*	0.0921(3)	0.3623(3)	¼	1	0.25(6)
Al1	4*a*	0	0	0	0.6	0.25(2)
Ga1	4*a*	0	0	0	0.4	0.25(2)
B1	4*c*	0.2430(8)	0.7330(8)	¼	1	0.30(5)
O11	4*c*	0.3948(2)	0.2360(2)	¼	1	0.30(3)
O12	4*c*	0.1610(2)	0.9040(2)	¼	1	0.30(3)
O2	8*d*	0.3230(2)	0.6040(2)	0.0492(6)	1	0.30(5)

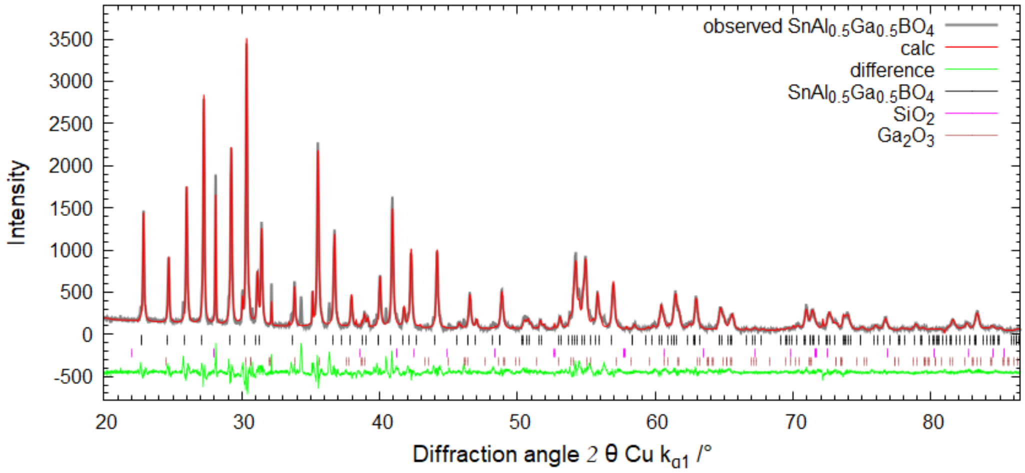

Figure S5: Rietveld refinement plot of Sn($Al_{0.5}Ga_{0.5}$)BO_4 with calculated (red) and observed (grey) patterns, difference curve (green), Bragg peaks of Sn($Al_{0.5}Ga_{0.5}$)BO_4 (black), impurities SiO_2 (pink) and Ga_2O_3 (orange).

Table S5: Crystal structure parameters of Sn($Al_{0.5}Ga_{0.5}$)BO_4.

Atom	*Pnam*	*x*	*y*	*z*	*Occupancy*	*B* /10^4 pm^2
Sn1	4*c*	0.0929(2)	0.3618(3)	¼	1	0.25(6)
Al1	4*a*	0	0	0	0.5	0.25(2)
Ga1	4*a*	0	0	0	0.5	0.25(8)
B1	4*c*	0.2660(4)	0.7710(4)	¼	1	0.30(7)
O11	4*c*	0.4039(2)	0.3762(2)	¼	1	0.30(3)
O12	4*c*	0.1613(2)	0.9126(2)	¼	1	0.30(4)
O2	8*d*	0.3383(2)	0.6966(2)	0.0408(2)	1	0.30(3)

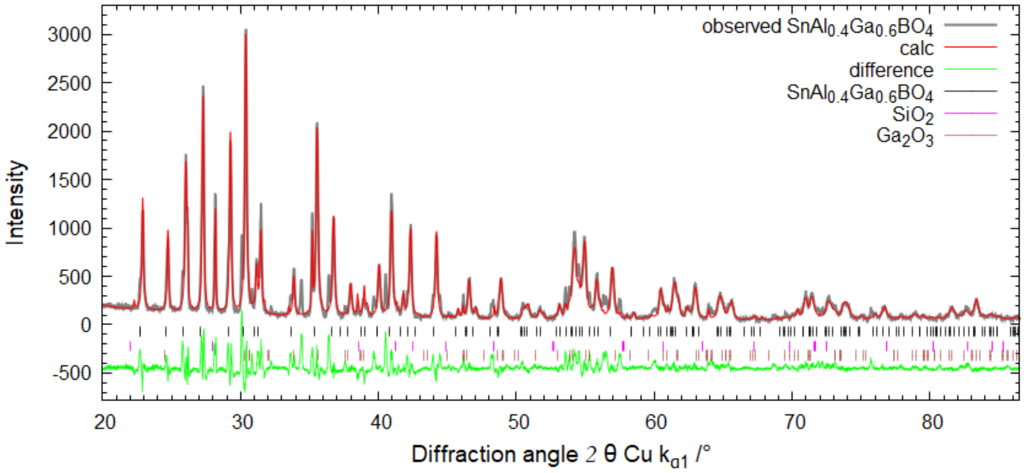

Figure S6: Rietveld refinement plot of Sn($Al_{0.4}Ga_{0.6}$)BO_4 with calculated (red) and observed (grey) patterns, difference curve (green), Bragg peaks of Sn($Al_{0.4}Ga_{0.6}$)BO_4 (black), impurities SiO_2 (pink) and Ga_2O_3 (orange).

Table S6: Crystal structure parameters of Sn($Al_{0.4}Ga_{0.6}$)BO_4.

Atom	*Pnam*	*x*	*y*	*z*	*Occupancy*	*B* /10^4 pm^2
Sn1	4*c*	0 0932(3)	0.3628(4)	¼	1	0.25(8)
Al1	4*a*	0	0	0	0.4	0.31(5)
Ga1	4*a*	0	0	0	0.6	0.31(2)
B1	4*c*	0.2370(2)	0.7230(3)	¼	1	0.67(7)
O11	4*c*	0.4060(2)	0.3500(3)	¼	1	0.30(4)
O12	4*c*	0.1600(3)	0.9120(3)	¼	1	0.30(4)
O2	8*d*	0.3218(2)	0.6950(2)	0.0500(2)	1	0.25(2)

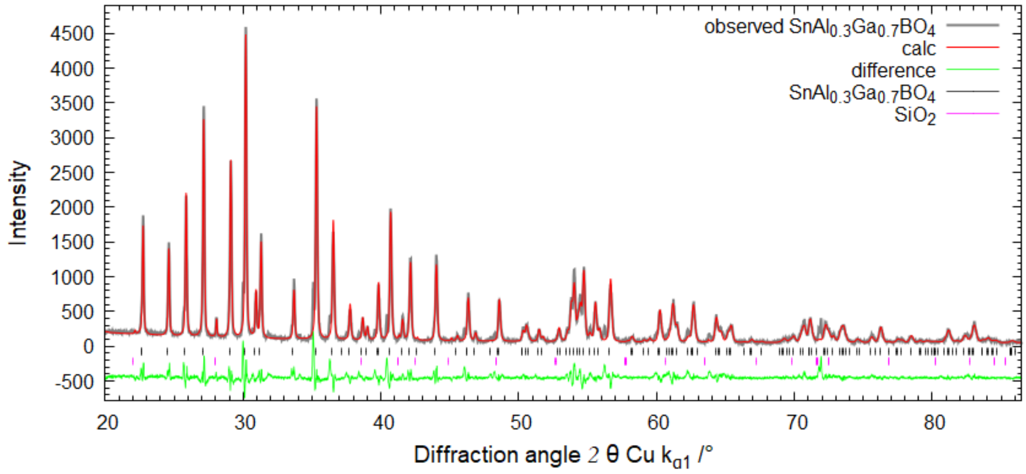

Figure S7: Rietveld refinement plot of Sn($Al_{0.3}Ga_{0.7}$)BO_4 with calculated (red) and observed (grey) patterns, difference curve (green), Bragg peaks of Sn($Al_{0.3}Ga_{0.7}$)BO_4 (black), impurity SiO_2 (pink).

Table S7: Crystal structure parameters of Sn($Al_{0.3}Ga_{0.7}$)BO_4.

Atom	*Pnam*	*x*	*y*	*z*	*Occupancy*	*B* /10^4 pm^2
Sn1	4*c*	0.0922(2)	0.3611(2)	¼	1	0.67(5)
Al1	4*a*	0	0	0	0.3	0.86(9)
Ga1	4*a*	0	0	0	0.7	0.86(2)
B1	4*c*	0.2730(3)	0.7630(3)	¼	1	0.70(7)
O11	4*c*	0.4004(2)	0.3725(2)	¼	1	0.30(3)
O12	4*c*	0.1583(2)	0.9074(2)	¼	1	0.30(4)
O2	8*d*	0.3424(1)	0.7004(1)	0.0414(2)	1	0.30(2)

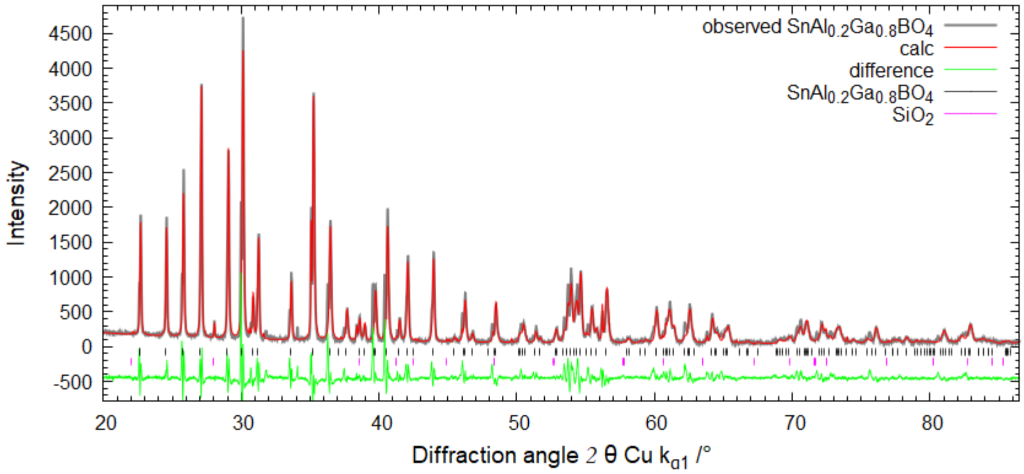

Figure S8: Rietveld refinement plot of Sn($Al_{0.2}Ga_{0.8}$)BO_4 with calculated (red) and observed (grey) patterns, difference curve (green), Bragg peaks of Sn($Al_{0.2}Ga_{0.8}$)BO_4 (black), impurity SiO_2 (pink).

Table S8: Crystal structure parameters of Sn($Al_{0.2}Ga_{0.8}$)BO_4.

Atom	*Pnam*	*x*	*y*	*z*	*Occupancy*	*B* /10^4 pm^2
Sn1	4*c*	0.0926(3)	0.3609(4)	¼	1	0.27(8)
Al1	4*a*	0	0	0	0.2	0.25(5)
Ga1	4*a*	0	0	0	0.8	0.25(5)
B1	4*c*	0.2670(5)	0.7640(5)	¼	1	0.30(9)
O11	4*c*	0.4030(2)	0.3750(2)	¼	1	0.30(4)
O12	4*c*	0.1550(2)	0.9130(2)	¼	1	0.30(6)
O2	8*d*	0.3424(2)	0.7068(2)	0.0421(2)	1	0.30(4)

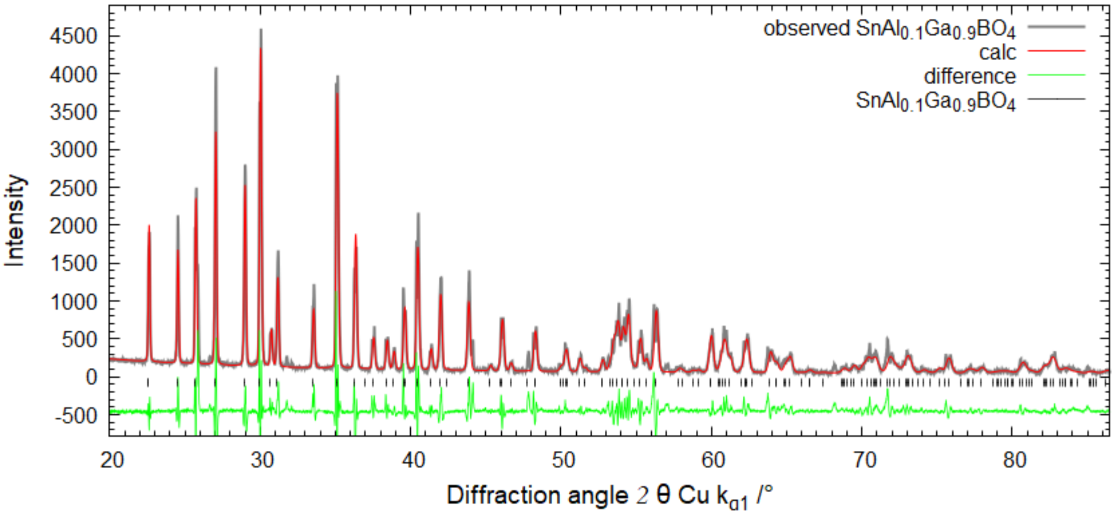

Figure S9: Rietveld refinement plot of Sn($Al_{0.1}Ga_{0.9}$)BO_4 with calculated (red) and observed (grey) patterns, difference curve (green), Bragg peaks of Sn($Al_{0.1}Ga_{0.9}$)BO_4 (black).

Table S9: Crystal structure parameters of Sn($Al_{0.1}Ga_{0.9}$)BO_4.

Atom	*Pnam*	*x*	*y*	*z*	*Occupancy*	*B* /10^4 pm^2
Sn1	4*c*	0.0933(3)	0.3610(4)	¼	1	0.56(8)
Al1	4*a*	0	0	0	0.1	0.39(3)
Ga1	4*a*	0	0	0	0.9	0.39(9)
B1	4*c*	0.2749(1)	0.7654(1)	¼	1	0.25(2)
O11	4*c*	0.3942(2)	0.3650(3)	¼	1	0.25(4)
O12	4*c*	0.1698(3)	0.9058(3)	¼	1	0.86(6)
O2	8*d*	0.3373(2)	0.7005(2)	0.0510(2)	1	0.30(4)

Table S10: X-ray powder data (Rietveld refined parameters) of $Sn(Al_{1-x}Ga_x)BO_4$.

Compositional x value	0.1	0.2	0.3	0.4	0.5	0.6	0.7	0.8	0.9
Temperature /K	296(2)	296(2)	296(2)	296(2)	296(2)	296(2)	296(2)	296(2)	296(2)
Instrument, radiation	D8 Advance, Bruker Cu $K_{\alpha 1}$								
Geometry	Bragg Brentano XRD sample holder								
Crystal system	orthorhombic								
Space group	*Pnam*								
a /pm	721.8(2)	722.7(3)	723.1(3)	724.0(3)	724.6(2)	725.3(4)	725.9(2)	726.7(3)	727.4(3)
b /pm	776.8(2)	778.3(4)	780.1(4)	781.4(3)	782.9(2)	784.5(4)	786.1(2)	788.2(3)	790.0(4)
c /pm	570.3(2)	571.9(3)	574.3(3)	575.5(3)	576.6(2)	577.9(3)	579.3(2)	580.8(2)	582.4(3)
V /10^6 pm^3	319.8(5)	321.7(9)	324.0(1)	325.6(9)	327.1(6)	328.8(2)	330.6(6)	332.7(8)	334.7(1)

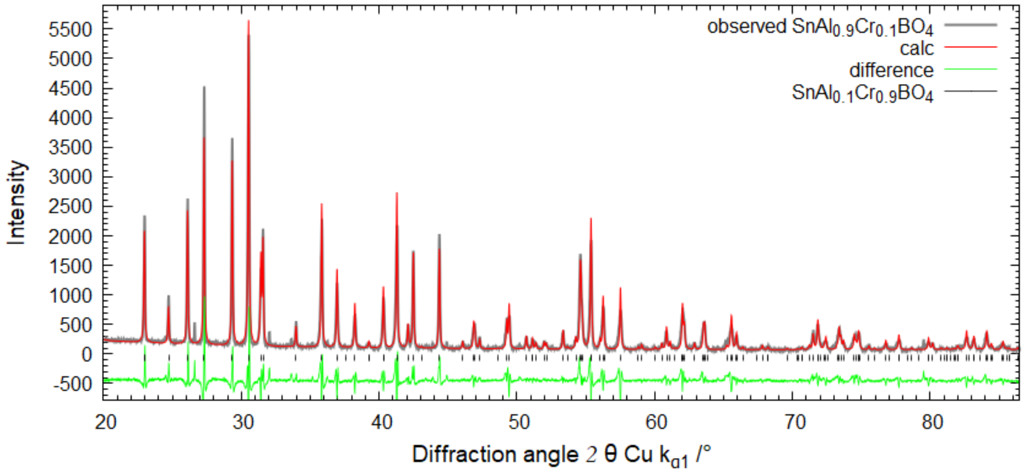

Figure S10: Rietveld refinement plot of $Sn(Al_{0.9}Cr_{0.1})BO_4$ with calculated (red) and observed (grey) patterns, difference curve (green), Bragg peaks of $Sn(Al_{0.9}Cr_{0.1})BO_4$ (black).

Table S11: Crystal structure parameters of $Sn(Al_{0.9}Cr_{0.1})BO_4$.

Atom	*Pnam*	*x*	*y*	*z*	*Occupancy*	*B* /10^4 pm^2
Sn1	4*c*	0.0914(2)	0.3625(2)	¼	1	0.85(5)
Al1	4*a*	0	0	0	0.9	0.70(9)
Cr1	4*a*	0	0	0	0.1	0.70(1)
B1	4*c*	0.2670(3)	0.7750(3)	¼	1	0.80(6)
O11	4*c*	0.4010(3)	0.3800(7)	¼	1	0.30(3)
O12	4*c*	0.1513(6)	0.9060(6)	¼	1	0.30(4)
O2	8*d*	0.3368(1)	0.6939(1)	0.0432(9)	1	0.30(2)

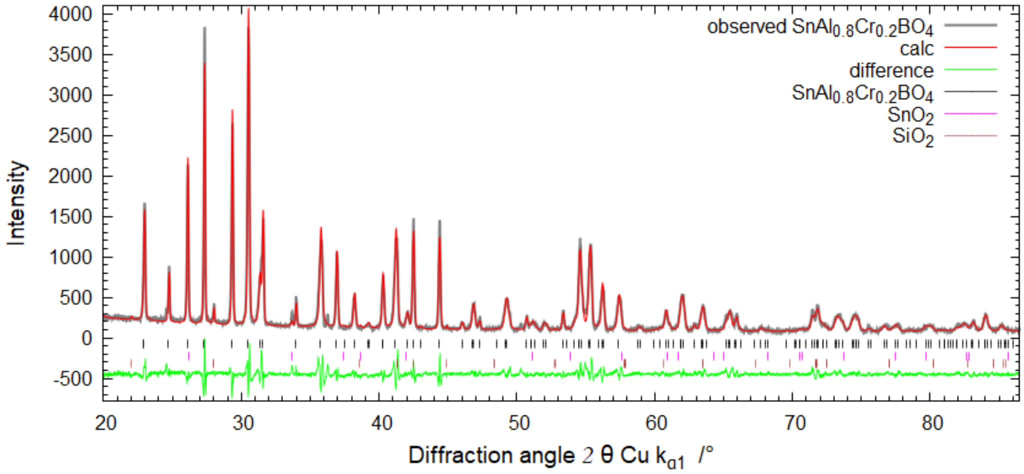

Figure S11: Rietveld refinement plot of $\mathrm{Sn(Al_{0.8}Cr_{0.2})BO_4}$ with calculated (red) and observed (grey) patterns, difference curve (green), Bragg peaks of $\mathrm{Sn(Al_{0.8}Cr_{0.2})BO_4}$ (black), impurities $\mathrm{SnO_2}$ (pink) and $\mathrm{SiO_2}$ (orange).

Table S12: Crystal structure parameters of $\mathrm{Sn(Al_{0.8}Cr_{0.2})BO_4}$

Atom	*Pnam*	*x*	*y*	*z*	*Occupancy*	*B* /10^4 pm^2
Sn1	4*c*	0.0920(2)	0.3630(3)	¼	1	0.25(6)
Al1	4*a*	0	0	0	0.8	052(7)
Cr1	4*a*	0	0	0	0.2	0.52(3)
B1	4*c*	0.2240(4)	0.7330(4)	¼	1	1.76(9)
O11	4*c*	0.4050(2)	0.3740(2)	¼	1	0.30(3)
O12	4*c*	0.1562(2)	0.9007(2)	¼	1	0.30(3)
O2	8*d*	0.3174(2)	0.6184(9)	0.0401(2)	1	0.80(5)

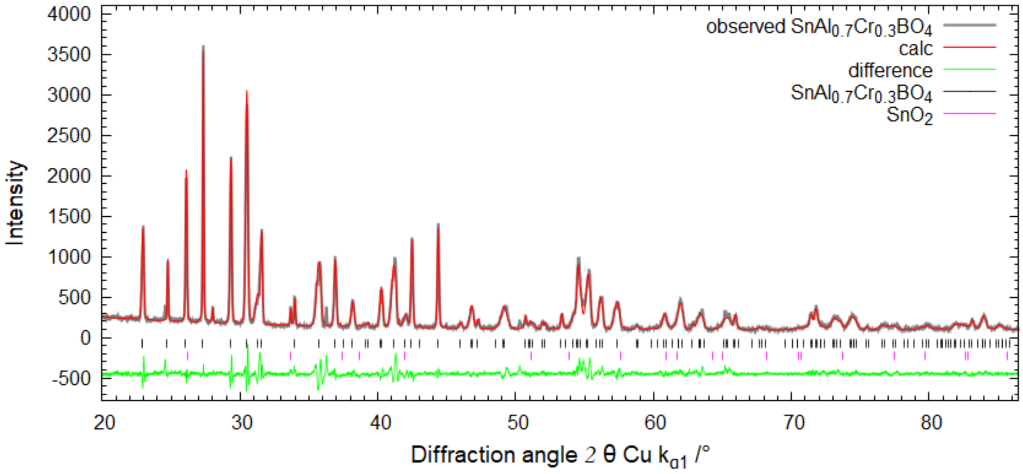

Figure S12: Rietveld refinement plot of $\mathrm{Sn(Al_{0.7}Cr_{0.3})BO_4}$ with calculated (red) and observed (grey) patterns, difference curve (green), Bragg peaks of $\mathrm{Sn(Al_{0.7}Cr_{0.3})BO_4}$ (black), impurity $\mathrm{SnO_2}$ (pink).

Table S13: Crystal structure parameters of $Sn(Al_{0.7}Cr_{0.3})BO_4$

Atom	*Pnam*	*x*	*y*	*z*	*Occupancy*	B /10^4 pm^2
Sn1	4*c*	0.0918(3)	0.3624(3)	¼	1	0.25(7)
Al1	4*a*	0	0	0	0.7	0.50(5)
Cr1	4*a*	0	0	0	0.3	0.50(4)
B1	4*c*	0.2390(8)	0.7120(9)	¼	1	0.30(9)
O11	4*c*	0.4099(2)	0.3810(2)	¼	1	0.30(4)
O12	4*c*	0.1600(2)	0.9004(2)	¼	1	0.30(3)
O2	8*d*	0.3346(9)	0.6050(9)	0.0526(8)	1	0.30(6)

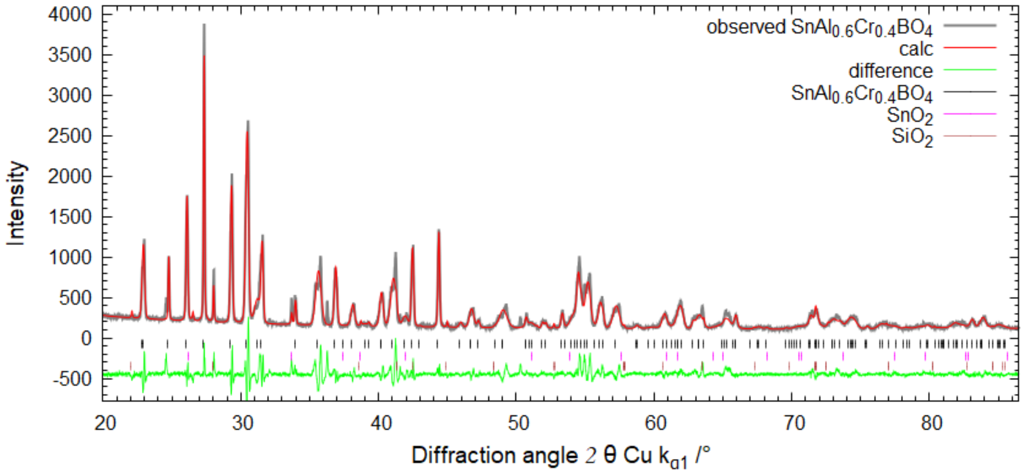

Figure S13: Rietveld refinement plot of $Sn(Al_{0.6}Cr_{0.4})BO_4$ with calculated (red) and observed (grey) patterns, difference curve (green), Bragg peaks of $Sn(Al_{0.6}Cr_{0.4})BO_4$ (black), impurities SnO_2 (pink) and SiO_2 (orange).

Table S14: Crystal structure parameters of $Sn(Al_{0.6}Cr_{0.4})BO_4$

Atom	*Pnam*	*x*	*y*	*z*	*Occupancy*	B /10^4 pm^2
Sn1	4*c*	0.0911(3)	0.3628(4)	¼	1	0.25(7)
Al1	4*a*	0	0	0	0.6	0.55(3)
Cr1	4*a*	0	0	0	0.4	0.55(4)
B1	4*c*	0.2222(9)	0.7220(9)	¼	1	0.25(2)
O11	4*c*	0.3999(2)	00.3221(2)	¼	1	0.30(4)
O12	4*c*	0.1612(2)	0.9007(3)	¼	1	0.30(4)
O2	8*d*	0.3426(4)	0.6901(9)	0.0560(9)	1	0.30(6)

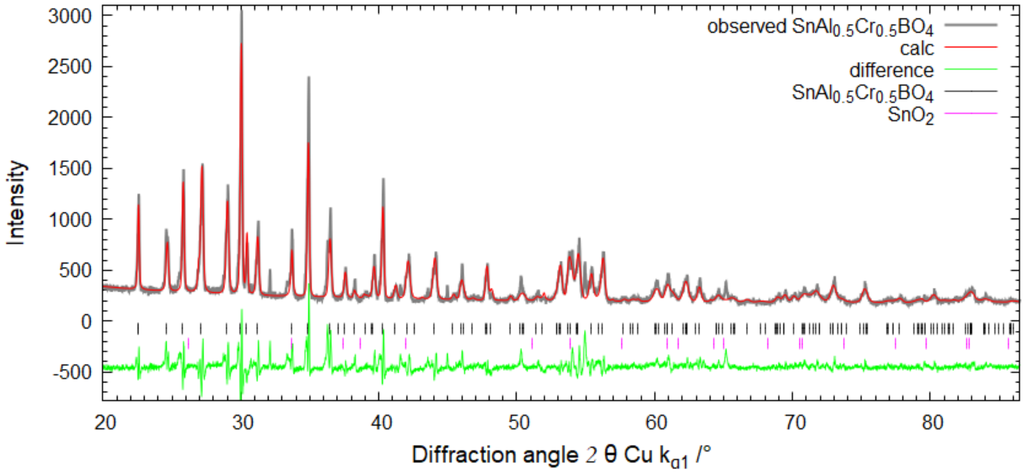

Figure S15: Rietveld refinement plot of $Sn(Al_{0.5}Cr_{0.5})BO_4$ with calculated (red) and observed (grey) patterns, difference curve (green), Bragg peaks of $Sn(Al_{0.5}Cr_{0.5})BO_4$ (black), impurity SnO_2 (pink).

Table S15: Crystal structure parameters of $Sn(Al_{0.5}Cr_{0.5})BO_4$

Atom	*Pnam*	*x*	*y*	*z*	*Occupancy*	*B* /10^4 pm^2
Sn1	4*c*	0.0876(5)	0.3627(5)	¼	1	0.42(9)
Al1	4*a*	0	0	0	0.5	0.25(9)
Cr1	4*a*	0	0	0	0.5	0.25(8)
B1	4*c*	0.1870(9)	0.7050(9)	¼	1	0.25(3)
O11	4*c*	0.4900(4)	0.3697(4)	¼	1	2.30(6)
O12	4*c*	0.1570(2)	0.9000(4)	¼	1	0.40(5)
O2	8*d*	0.3490(4)	0.6952(9)	0.5000(4)	1	1.90(9)

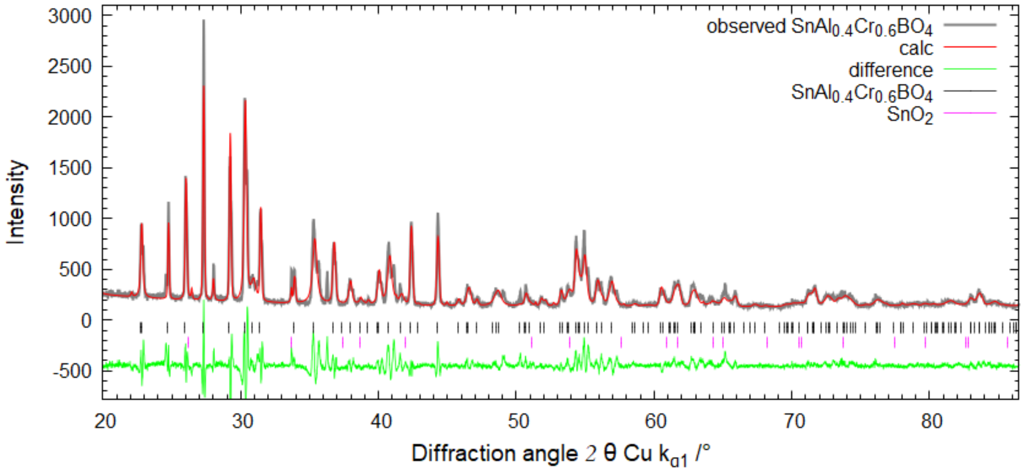

Figure S16: Rietveld refinement plot of $Sn(Al_{0.4}Cr_{0.6})BO_4$ with calculated (red) and observed (grey) patterns, difference curve (green), Bragg peaks of $Sn(Al_{0.4}Cr_{0.6})BO_4$ (black), impurity SnO_2 (pink).

Table S16: Crystal structure parameters of Sn($Al_{0.4}Cr_{0.6}$)BO_4

Atom	*Pnam*	*x*	*y*	*z*	*Occupancy*	*B* /10^4 pm^2
Sn1	4*c*	0.0902(3)	0.3636(5)	¼	1	0.25(9)
Al1	4*a*	0	0	0	0.4	0.25(8)
Cr1	4*a*	0	0	0	0.6	0.25(2)
B1	4*c*	0.2320(9)	0.721(9)	¼	1	0.25(2)
O11	4*c*	0.4050(2)	0.3791(3)	¼	1	0.30(5)
O12	4*c*	0.1621(2)	0.9006(3)	¼	1	0.30(4)
O2	8*d*	0.3158(2)	0.6062(6)		1	0.30(8)

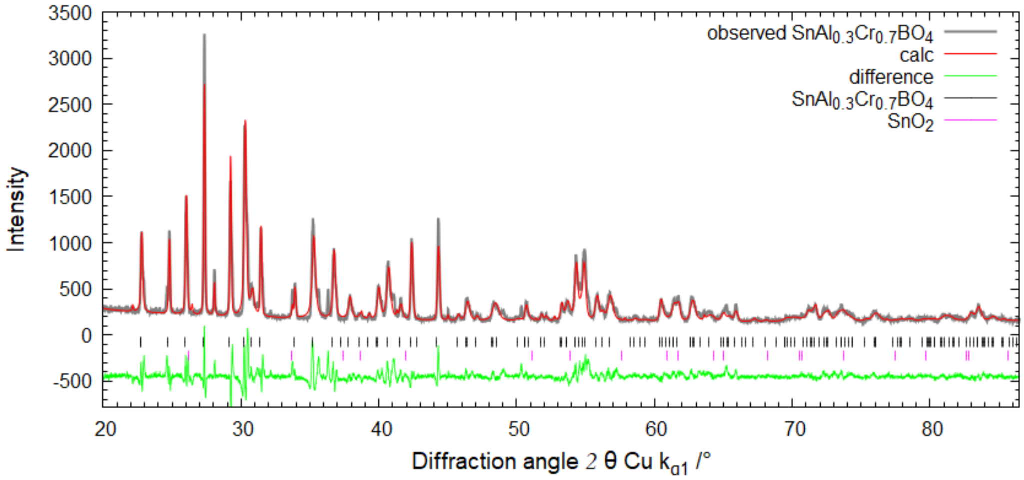

Figure S17: Rietveld refinement plot of Sn($Al_{0.3}Cr_{0.7}$)BO_4 with calculated (red) and observed (grey) patterns, difference curve (green), Bragg peaks of Sn($Al_{0.3}Cr_{0.7}$)BO_4 (black), impurity SnO_2 (pink).

Table S17: Crystal structure parameters of Sn($Al_{0.3}Cr_{0.7}$)BO_4

Atom	*Pnam*	*x*	*y*	*z*	*Occupancy*	*B* /10^4 pm^2
Sn1	4*c*	0.0895(3)	0.3627(5)	¼	1	0.25(9)
Al1	4*a*	0	0	0	0.3	0.25(7)
Cr1	4*a*	0	0	0	0.7	0.25(3)
B1	4*c*	0.2741(1)	0.7221(2)	¼	1	0.25(2)
O11	4*c*	0.4080(2)	0.3887(3)	¼	1	0.30(5)
O12	4*c*	0.1580(2)	0.9014(3)	¼	1	0.40(4)
O2	8*d*	0.3220(2)	0.6007(9)	0.0592(2)	1	0.30(7)

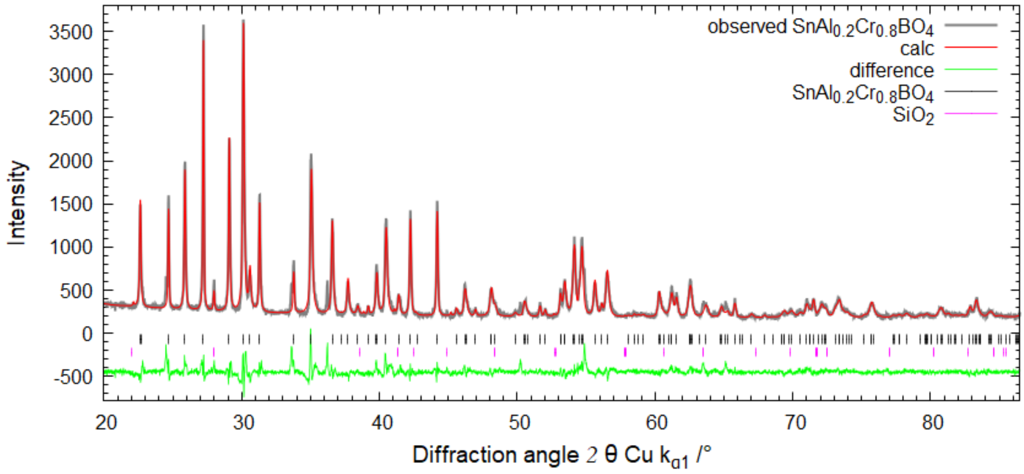

Figure S18: Rietveld refinement plot of $Sn(Al_{0.2}Cr_{0.8})BO_4$ with calculated (red) and observed (grey) patterns, difference curve (green), Bragg peaks of $Sn(Al_{0.2}Cr_{0.8})BO_4$ (black), impurity SiO_2 (orange).

Table S18: Crystal structure parameters of $Sn(Al_{0.2}Cr_{0.8})BO_4$

Atom	*Pnam*	*x*	*y*	*z*	*Occupancy*	*B* /10^4 pm^2
Sn1	4*c*	0.0889(3)	0.3635(4)	¼	1	0.25(8)
Al1	4*a*	0	0	0	0.2	0.25(5)
Cr1	4*a*	0	0	0	0.8	0.25(4)
B1	4*c*	0.2291(1)	0.7200(9)	¼	1	0.25(2)
O11	4*c*	0.4098(2)	0.3887(2)	¼	1	0.30(4)
O12	4*c*	0.1574(2)	0.9004(3)	¼	1	0.30(4)
O2	8*d*	0.3243(9)	0.7019(9)	0.629(8)	1	0.30(6)

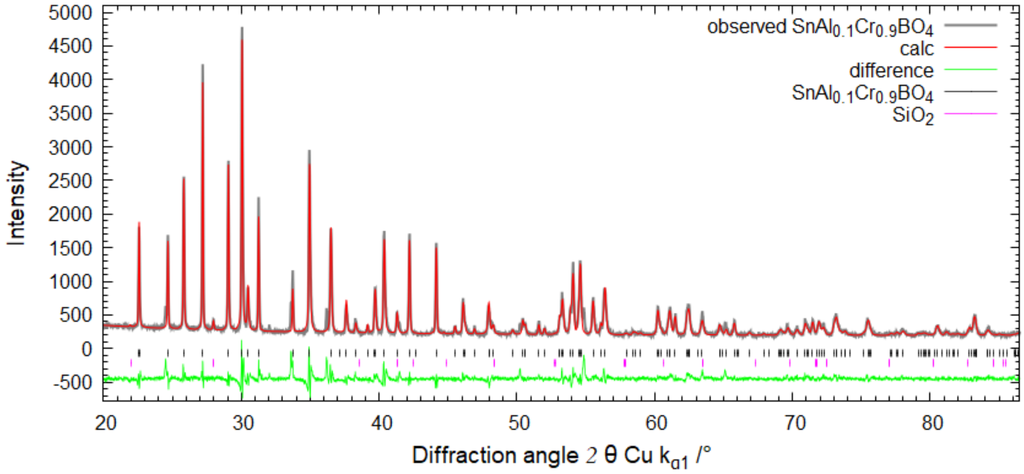

Figure S20: Rietveld refinement plot of $Sn(Al_{0.1}Cr_{0.9})BO_4$ with calculated (red) and observed (grey) patterns, difference curve (green), Bragg peaks of $Sn(Al_{0.1}Cr_{0.9})BO_4$ (black), impurity SiO_2 (orange).

Table S19: Crystal structure parameters of Sn($Al_{0.1}Cr_{0.9}$)BO_4

Atom	*Pnam*	*x*	*y*	*z*	*Occupancy*	*B* /10^4 pm^2
Sn1	4*c*	0.0890(3)	0.3617(4)	¼	1	0.25(7)
Al1	4*a*	0	0	0	0.1	0.25(5)
Cr1	4*a*	0	0	0	0.9	0.25(8)
B1	4*c*	0.2282(1)	0.7219(1)	¼	1	0.30(2)
O11	4*c*	0.4080(2)	0.3123(2)	¼	1	0.50(4)
O12	4*c*	03270(2)	0.9011(1)	¼	1	0.30(3)
O2	8*d*	0.3260(4)	0.6868(4)	0.0551(4)	1	0.30(6)

Table S20: X-ray powder data (Rietveld refined parameters) of Sn($Al_{1-x}Cr_x$)BO_4.

Compositional x value	0.1	0.2	0.3	0.4	0.5	0.6	0.7	0.8	0.9
Temperature /K	296(2)	296(2)	296(2)	296(2)	296(2)	296(2)	296(2)	296(2)	296(2)
Instrument, radiation	D8 Advance, Bruker Cu $K_{\alpha 1}$								
Geometry	Bragg Brentano XRD sample holder								
Crystal system	orthorhombic								
Space group	*Pnam*								
a /pm	720.9(1)	721.0(2)	721.0(2)	721.2(3)	721.2(5)	721.4(4)	721.4(3)	721.6(2)	721.6(2)
b /pm	776.0(1)	776.9(3)	778.1(3)	778.9(4)	780.3(5)	781.5(5)	782.3(5)	783.5(3)	784.6(2)
c /pm	570.9(8)	573.0(2)	574.4(3)	577.0(4)	578.1(3)	580.2(5)	581.9(4)	584.1(3)	586.0(2)
V /10^6 pm^3	319.3(1)	320.9(7)	322.2(8)	324.1(1)	325.3(1)	327.1(1)	328.4(1)	330.2(8)	331.8(6)

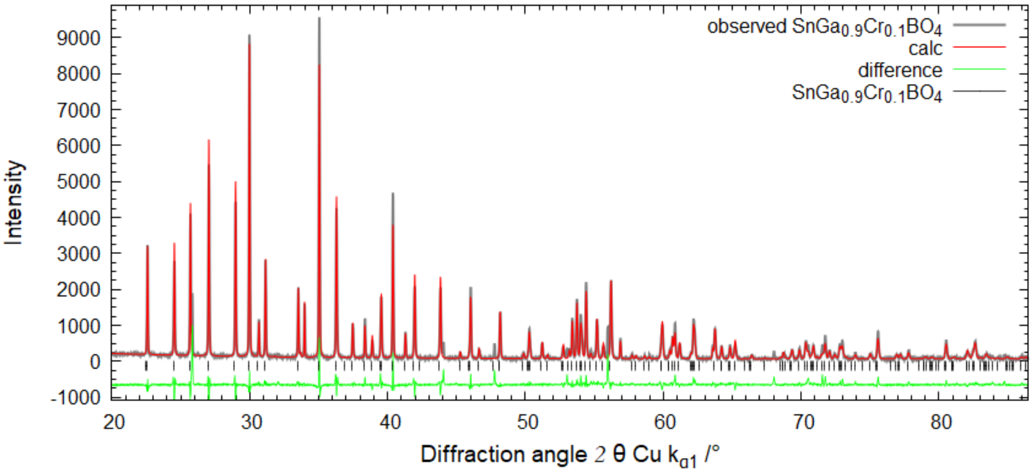

Figure S21: Rietveld refinement plot of Sn($Ga_{0.9}Cr_{0.1}$)BO_4 with calculated (red) and observed (grey) patterns, difference curve (green), Bragg peaks of Sn($Ga_{0.9}Cr_{0.1}$)BO_4 (black).

Table S21: Crystal structure parameters of $Sn(Ga_{0.9}Cr_{0.1})BO_4$

Atom	*Pnam*	*x*	*y*	*z*	*Occupancy*	*B* /10^4 pm^2
Sn1	4*c*	0.0926(2)	0.3601(5)	¼	1	0.67(7)
Ga1	4*a*	0	0	0	0.9	0.25(7)
Cr1	4*a*	0	0	0	0.1	0.25(6)
B1	4*c*	0.2798(2)	0.7800(6)	¼	1	0.57(2)
O11	4*c*	0.4015(1)	0.3761(3)	¼	1	0.58(9)
O12	4*c*	0.1633(9)	0.9083(3)	¼	1	0.29(1)
O2	8*d*	0.3347(4)	0.7042(8)	0.0558(9)	1	0.35(5)

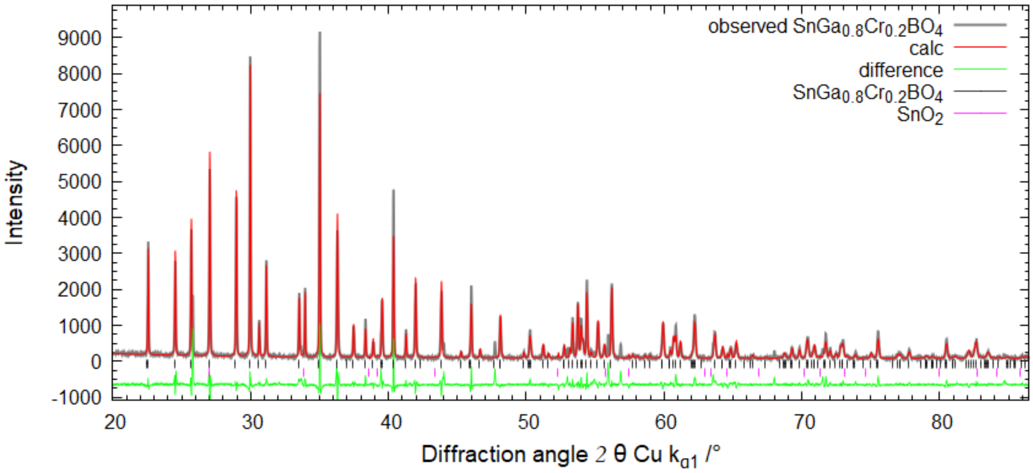

Figure S21: Rietveld refinement plot of $Sn(Ga_{0.8}Cr_{0.2})BO_4$ with calculated (red) and observed (grey) patterns, difference curve (green), Bragg peaks of $Sn(Ga_{0.8}Cr_{0.2})BO_4$ (black), impurity SnO_2 (pink).

Table S22: Crystal structure parameters of $Sn(Ga_{0.8}Cr_{0.2})BO_4$

Atom	*Pnam*	*x*	*y*	*z*	*Occupancy*	*B* /10^4 pm^2
Sn1	4*c*	0.0922(2)	0.3602(2)	¼	1	0.25(4)
Ga1	4*a*	0	0	0	0.8	0.25(2)
Cr1	4*a*	0	0	0	0.2	0.25(4)
B1	4*c*	0.2310(7)	0.7360(7)	¼	1	0.30(2)
O11	4*c*	0.4042(4)	0.3768(5)	¼	1	0.30(3)
O12	4*c*	0.1663(5)	0.9062(7)	¼	1	0.30(3)
O2	8*d*	0.3304(1)	0.6940(1)	0.0531	1	0.30(2)

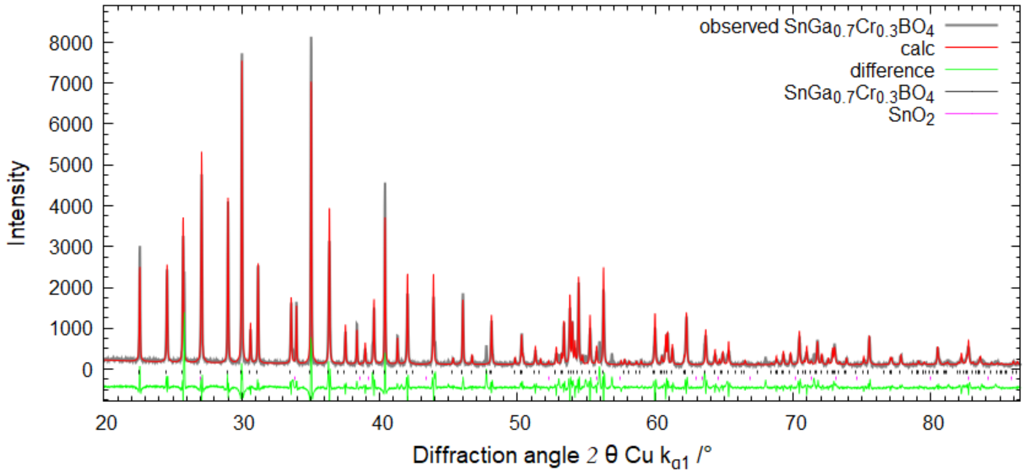

Figure S22: Rietveld refinement plot of Sn($Ga_{0.7}Cr_{0.3}$)BO_4 with calculated (red) and observed (grey) patterns, difference curve (green), Bragg peaks of Sn($Ga_{0.7}Cr_{0.3}$)BO_4 (black), impurity SnO_2 (pink).

Table S23: Crystal structure parameters of Sn($Ga_{0.7}Cr_{0.3}$)BO_4

Atom	*Pnam*	*x*	*y*	*z*	*Occupancy*	*B* /10^4 pm^2
Sn1	4*c*	0.0922(2)	0.3603(3)	¼	1	1.01(5)
Ga1	4*a*	0	0	0	0.7	0.25(5)
Cr1	4*a*	0	0	0	0.3	0.25(6)
B1	4*c*	0.2810(4)	0.7770(4)	¼	1	2.60(8)
O11	4*c*	0.4009(5)	0.3755(7)	¼	1	0.30(3)
O12	4*c*	0.1576(6)	0.9074(7)	¼	1	0.30(4)
O2	8*d*	0.3388(2)	0.7048(1)	0.0494(4)	1	0.90(3)

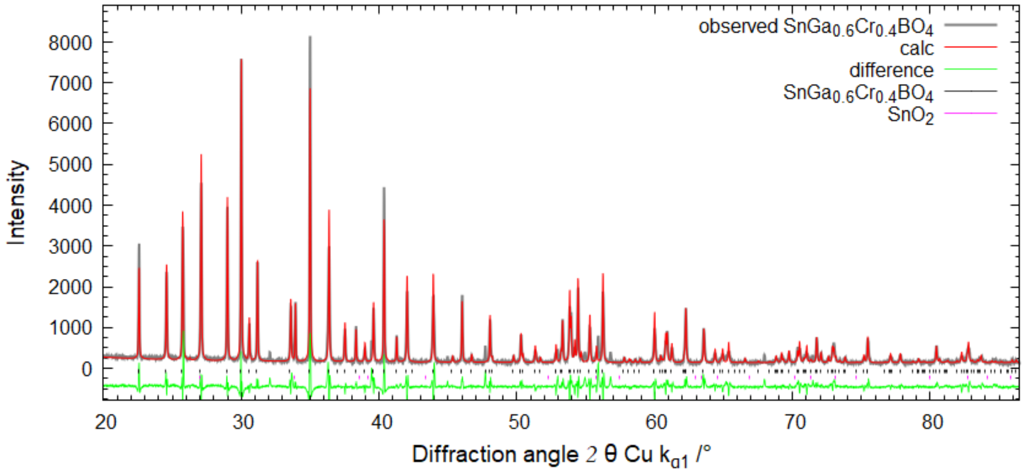

Figure S23: Rietveld refinement plot of Sn($Ga_{0.6}Cr_{0.4}$)BO_4 with calculated (red) and observed (grey) patterns, difference curve (green), Bragg peaks of Sn($Ga_{0.6}Cr_{0.4}$)BO_4 (black), impurity SnO_2 (pink).

Table S24: Crystal structure parameters of $\mathrm{Sn(Ga_{0.6}Cr_{0.4})BO_4}$

Atom	*Pnam*	*x*	*y*	*z*	*Occupancy*	B /10^4 pm^2
Sn1	4*c*	0.0917(2)	0.3602(3)	¼	1	1.22(6)
Ga1	4*a*	0	0	0	0.6	0.69(8)
Cr1	4*a*	0	0	0	0.4	0.69(6)
B1	4*c*	0.2850(4)	0.7810(4)	¼	1	0.70(7)
O11	4*c*	0.4000(6)	0.3738(7)	¼	1	0.30(3)
O12	4*c*	0.1551(6)	0.9056(8)	¼	1	0.30(4)
O2	8*d*	0.3384(2)	0.7066(2)	0.0480(4)	1	1.40(3)

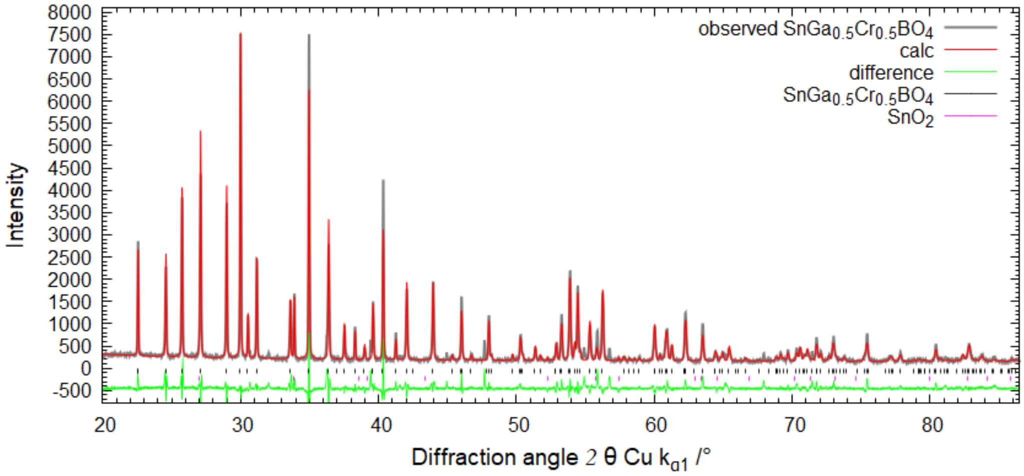

Figure S24: Rietveld refinement plot of $\mathrm{Sn(Ga_{0.5}Cr_{0.5})BO_4}$ with calculated (red) and observed (grey) patterns, difference curve (green), Bragg peaks of $\mathrm{Sn(Ga_{0.5}Cr_{0.5})BO_4}$ (black), impurity $\mathrm{SnO_2}$ (pink).

Table S25: Crystal structure parameters of $\mathrm{Sn(Ga_{0.5}Cr_{0.5})BO_4}$

Atom	*Pnam*	*x*	*y*	*z*	*Occupancy*	B /10^4 pm^2
Sn1	4*c*	0.0909(2)	0.3607(3)	¼	1	0.68(6)
Ga1	4*a*	0	0	0	0.5	0.25(8)
Cr1	4*a*	0	0	0	0.5	0.25(1)
B1	4*c*	0.2860(4)	0.7744(4)	¼	1	0.30(8)
O11	4*c*	0.3913(6)	0.3650(2)	¼	1	0.30(3)
O12	4*c*	0.1559(7)	0.9040(2)	¼	1	0.30(4)
O2	8*d*	0.3410(2)	0.7100(2)	0.0443(5)	1	0.60(3)

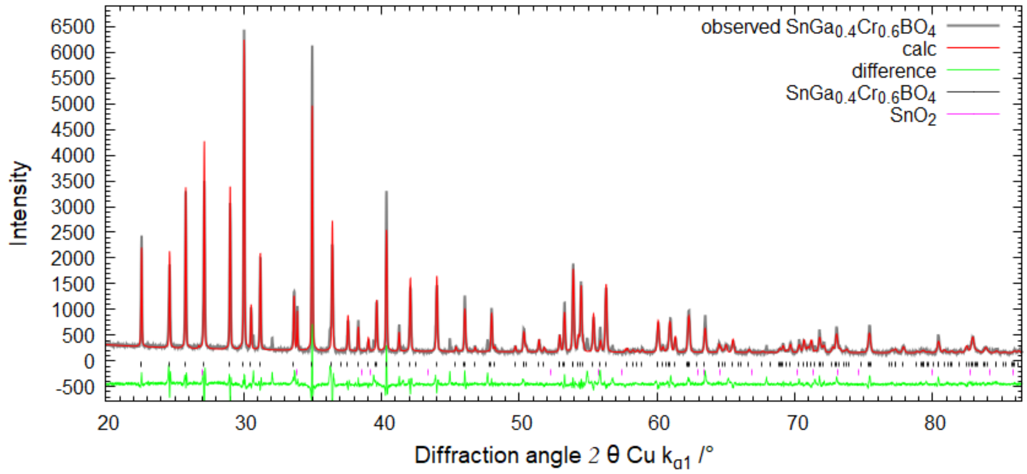

Figure S25: Rietveld refinement plot of Sn($Ga_{0.4}Cr_{0.6}$)BO_4 with calculated (red) and observed (grey) patterns, difference curve (green), Bragg peaks of Sn($Ga_{0.4}Cr_{0.6}$)BO_4 (black), impurity SnO_2 (pink).

Table S26: Crystal structure parameters of Sn($Ga_{0.4}Cr_{0.6}$)BO_4

Atom	*Pnam*	*x*	*y*	*z*	*Occupancy*	B /10^4 pm^2
Sn1	4*c*	0.0902(3)	0.3612(3)	¼	1	0.57(7)
Ga1	4*a*	0	0	0	0.4	0.25(2)
Cr1	4*a*	0	0	0	0.6	0.25(1)
B1	4*c*	0.2830(4)	0.7790(4)	¼	1	0.30(9)
O11	4*c*	0.3919(9)	0.3660(2)	¼	1	0.30(4)
O12	4*c*	0.1520(2)	0.9050(2)	¼	1	0.30(5)
O2	8*d*	0.3400(4)	0.7124(3)	0.0457(6)	1	0.30(3)

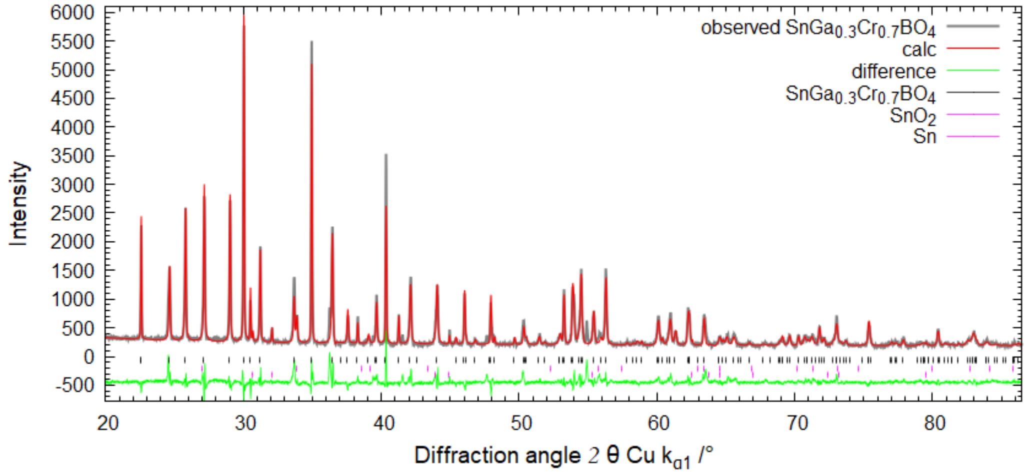

Figure S26: Rietveld refinement plot of Sn($Ga_{0.3}Cr_{0.7}$)BO_4 with calculated (red) and observed (grey) patterns, difference curve (green), Bragg peaks of Sn($Ga_{0.3}Cr_{0.7}$)BO_4 (black), impurities SnO_2 (pink) and Sn (orange).

Table S27: Crystal structure parameters of Sn($Ga_{0.3}Cr_{0.7}$)BO_4

Atom	*Pnam*	*x*	*y*	*z*	*Occupancy*	*B* /10^4 pm^2
Sn1	4*c*	0.0893(3)	0.3615(4)	¼	1	0.51(7)
Ga1	4*a*	0	0	0	0.3	0.25(1)
Cr1	4*a*	0	0	0	0.7	0.25(2)
B1	4*c*	0.2140(1)	0.715(1)	¼	1	0.25(2)
O11	4*c*	0.4090(2)	0.3210(2)	¼	1	0.30(4)
O12	4*c*	0.1570(2)	0.9006(3)	¼	1	0.30(6)
O2	8*d*	0.3422(6)	0.6289(7)	0.0512(7)	1	0.30(4)

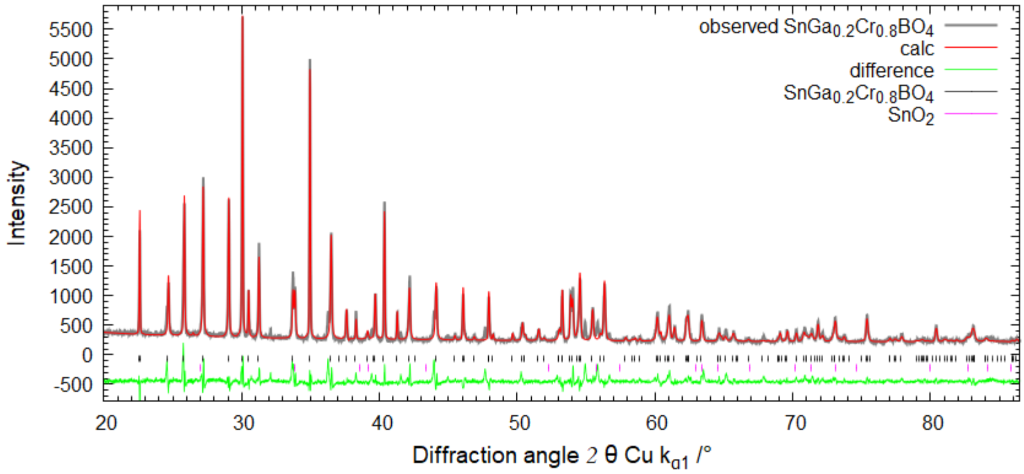

Figure S27: Rietveld refinement plot of Sn($Ga_{0.2}Cr_{0.8}$)BO_4 with calculated (red) and observed (grey) patterns, difference curve (green), Bragg peaks of Sn($Ga_{0.2}Cr_{0.8}$)BO_4 (black), impurity SnO_2 (pink).

Table S28: Crystal structure parameters of Sn($Ga_{0.2}Cr_{0.8}$)BO_4

Atom	*Pnam*	*x*	*y*	*z*	*Occupancy*	*B* /10^4 pm^2
Sn1	4*c*	0.0902(4)	0.3616(4)	¼	1	0.65(8)
Ga1	4*a*	0	0	0	0.2	0.25(9)
Cr1	4*a*	0	0	0	0.8	0.25(3)
B1	4*c*	0.2160(1)	0.7210(1)	¼	1	0.25(2)
O11	4*c*	0.4060(3)	0.3875(3)	¼	1	1.60(5)
O12	4*c*	0.3100(3)	0.9011(2)	¼	1	0.30(7)
O2	8*d*	0.3488(8)	0.6945(6)	0.0560(2)	1	0.60(4)

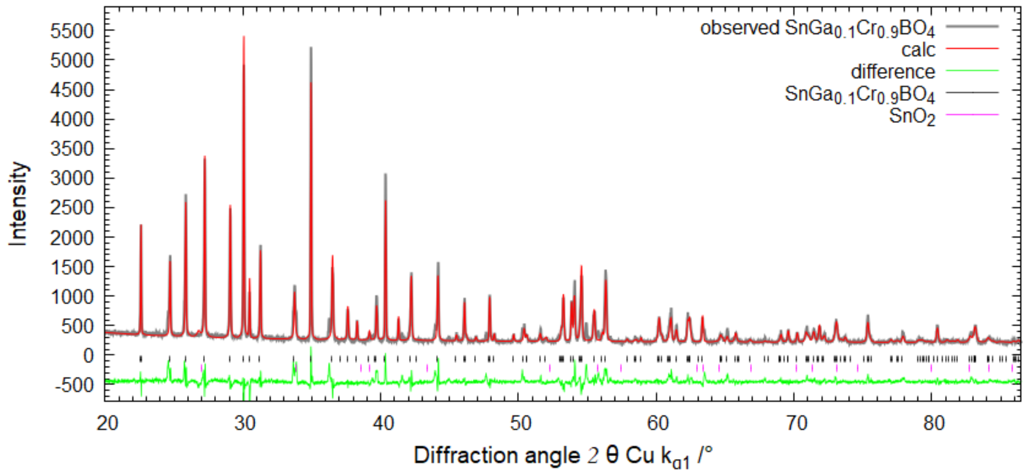

Figure S28: Rietveld refinement plot of $Sn(Ga_{0.1}Cr_{0.8})BO_4$ with calculated (red) and observed (grey) patterns, difference curve (green), Bragg peaks of $Sn(Ga_{0.1}Cr_{0.8})BO_4$ (black), impurity SnO_2 (pink).

Table S29: Crystal structure parameters of $Sn(Ga_{0.1}Cr_{0.9})BO_4$

Atom	*Pnam*	*x*	*y*	*z*	*Occupancy*	*B* /10^4 pm^2
Sn1	4*c*	0.0900(4)	0.3638(4)	¼	1	0.25(8)
Ga1	4*a*	0	0	0	0.1	0.25(7)
Cr1	4*a*	0	0	0	0.9	0.25(1)
B1	4*c*	0.2940(6)	0.7960(6)	¼	1	0.30(2)
O11	4*c*	0.4000(3)	0.3740(3)	¼	1	0.30(4)
O12	4*c*	0.1530(3)	0.9030(3)	¼	1	0.30(7)
O2	8*d*	0.3416(9)	0.7136(7)	0.0497(9)	1	0.30(4)

Table S30: X-ray powder data (Rietveld refined parameters) of $Sn(Ga_{1-x}Cr_x)BO_4$.

Compositional x value	0.1	0.2	0.3	0.4	0.5	0.6	0.7	0.8	0.9
Temperature /K	296(2)	296(2)	296(2)	296(2)	296(2)	296(2)	296(2)	296(2)	296(2)
Instrument, radiation	D8 Advance, Bruker Cu $K_{\alpha 1}$								
Geometry	Bragg Brentano XRD sample holder								
Crystal system	orthorhombic								
Space group	*Pnam*								
a /pm	727.4(1)	727.0(1)	726.5(1)	725.7(1)	725.0(1)	724.3(1)	723.6(1)	722.5(2)	721.7(1)
b /pm	790.8(1)	790.4(1)	789.8(1)	789.0(1)	788.2(1)	787.6(1)	787.2(2)	786.4(2)	786.2(2)
c /pm	584.1(1)	584.5(1)	584.9(1)	585.4(1)	585.8(1)	586.1(1)	586.5(1)	586.9(1)	587.2(1)
V /10^6 pm^3	336.1(3)	335.9(3)	335.6(3)	335.2(3)	334.7(3)	334.3(4)	334.1(4)	333.4(5)	333.1(4)

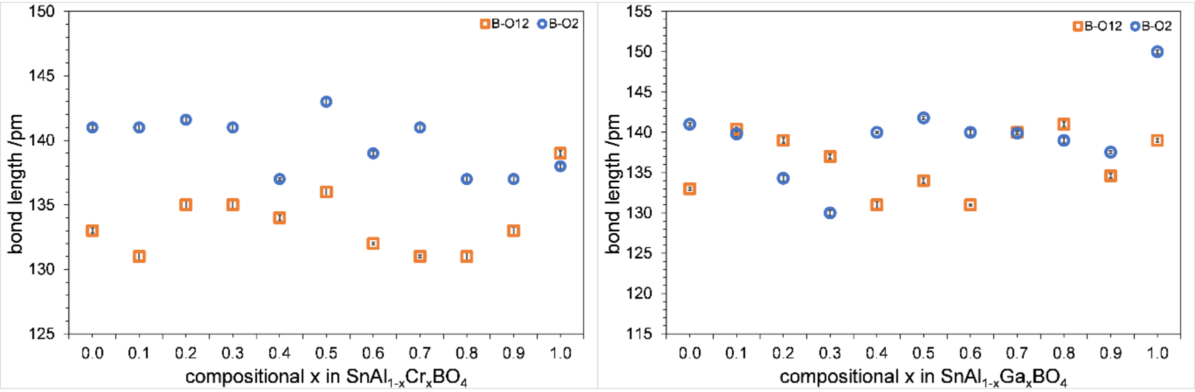

Figure S29: Development of the B-O bond length of $Sn(Al_{1-x}Cr_x)BO_4$ (left) and $Sn(Al_{1-x}Ga_x)BO_4$ (right).

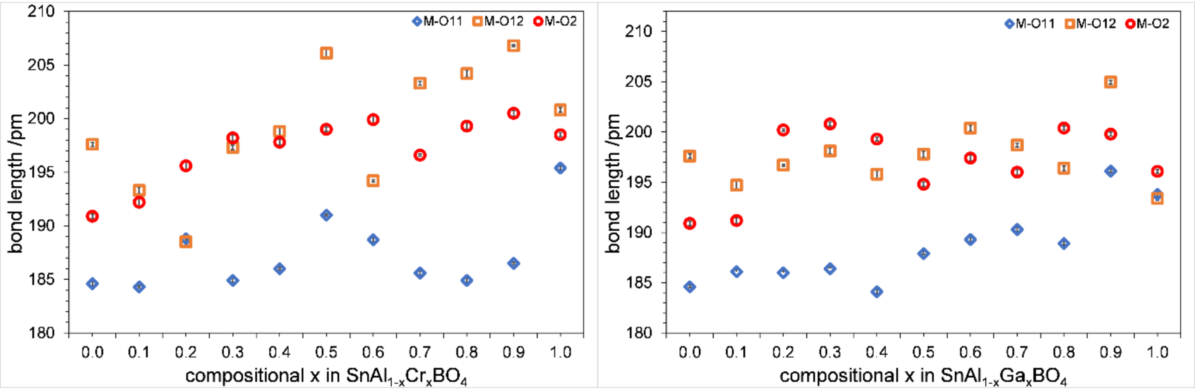

Figure S30: Development of the M-O bond length of $Sn(Al_{1-x}Cr_x)BO_4$ (left) and $Sn(Al_{1-x}Ga_x)BO_4$ (right).

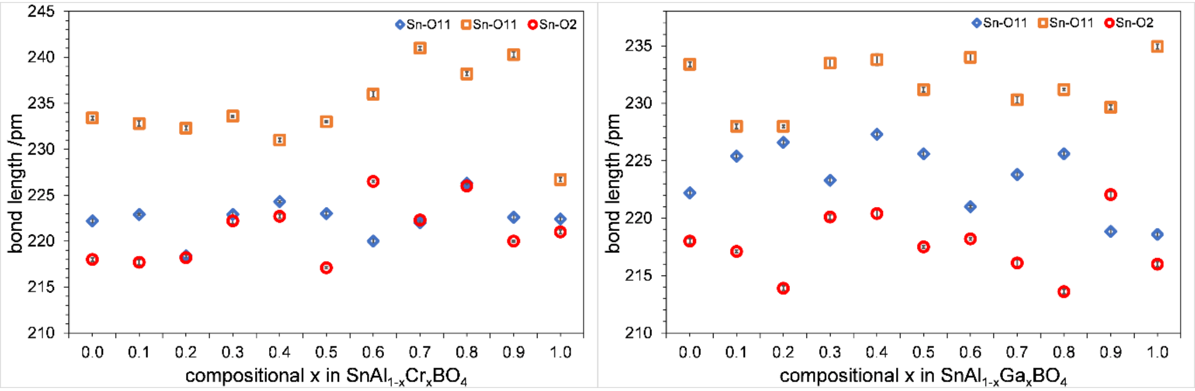

Figure S31: Development of the Sn-O bond length of $Sn(Al_{1-x}Cr_x)BO_4$ (left) and $Sn(Al_{1-x}Ga_x)BO_4$ (right).

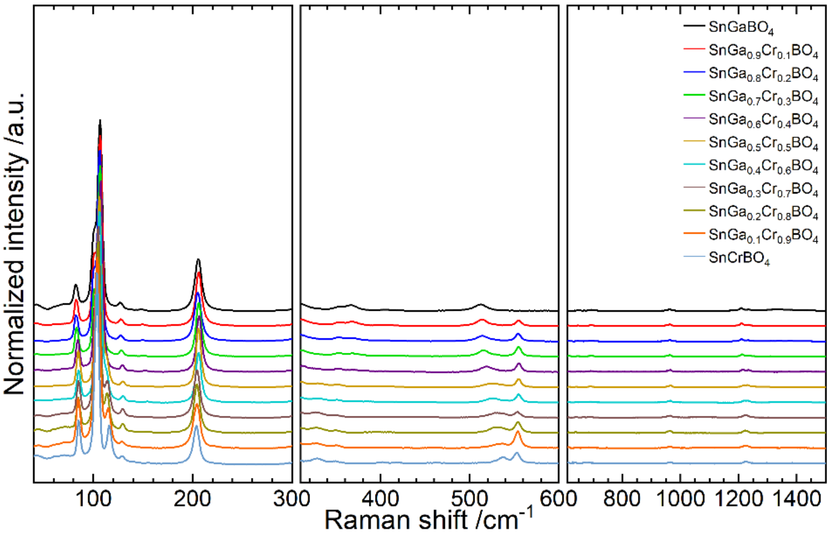

Figure S32: Stack plot of the Raman spectra of $Sn(Al_{1-x}Cr_x)BO_4$.

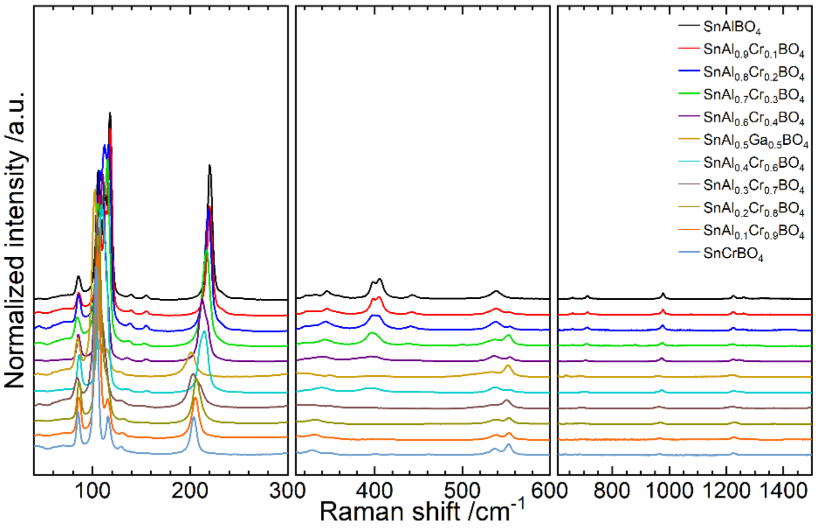

Figure S33: Stack plot of the Raman spectra of $Sn(Al_{1-x}Ga_x)BO_4$.

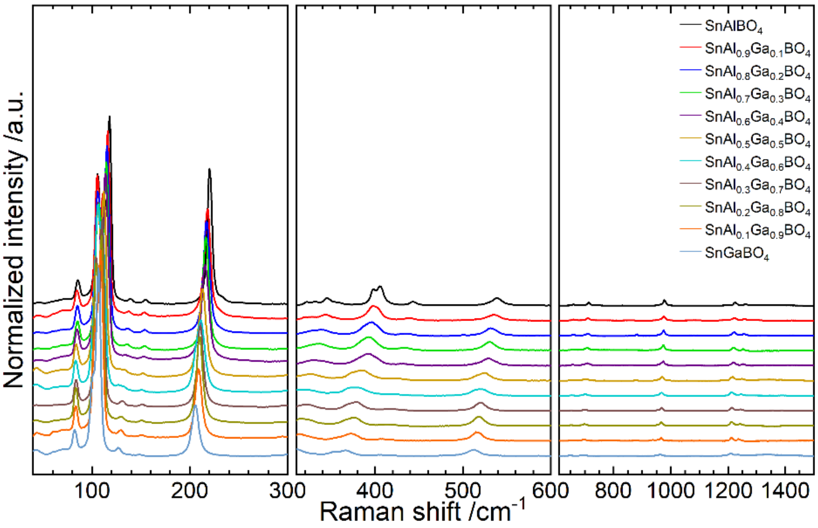

Figure S34: Stack plot of the Raman spectra of $Sn(Ga_{1-x}Cr_x)BO_4$.

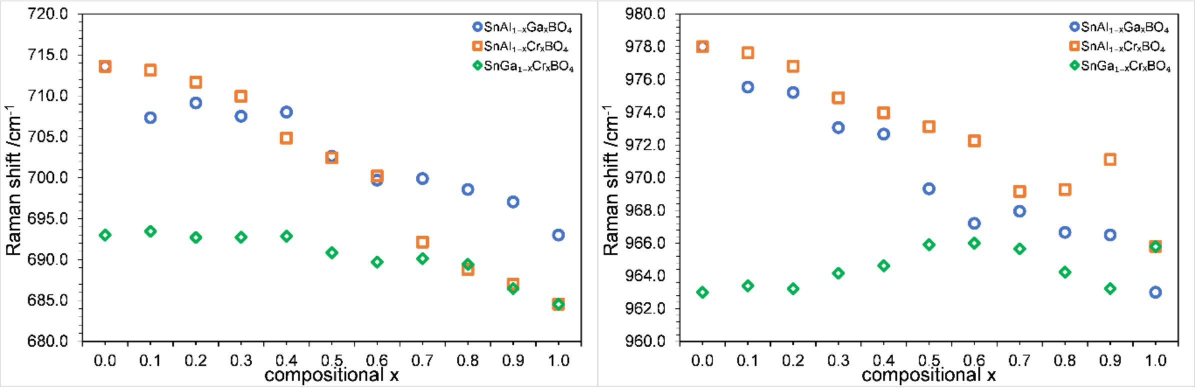

Figure S35: Development of Raman bands with respect to the solid solution $Sn(Al_{1-x}Ga_x)BO_4$ (circles), $Sn(Al_{1-x}Cr_x)BO_4$ (squares), and $Sn(Ga_{1-x}Cr_x)BO_4$ (diamond).

Chapter 7 – Synthesis of precursors as red SnO and MBO_3 (M = Cr, Al, Fe, Mn, Sc)

Different starting materials as well as different synthesis routes were tested for the synthesis of mullite-type target compounds. For instance, to avoid the oxidation of Sn^{2+} to Sn^{4+}, different tin oxides were tested. Commercial starting materials such as black bluish SnO, M_2O_3, and B_2O_3 were used for the synthesis of $SnMBO_4$. Tin(II)oxide has a second metastable polymorph which is supposed to be more reactive, and faster kinetics possibly prohibits further oxidation. Two-step solid state synthesis routes were also tested, where MBO_3 was synthesized first followed by adding tin(II) compound to get corresponding $SnMBO_4$ mullite-type compounds. The second part of this chapter is all about the synthesis and characterization of the starting MBO_3 compounds.

On red tin (II) oxide: temperature-dependent structural, spectroscopic, and thermogravimetric properties

Sarah Wittmann[1], M. Mangir Murshed[1,2*], Thorsten M. Gesing[1,2]

Reprinted with kind permission from Wiley and upon approval of the co-authors.

Published in: Z. Allg. Anorg. Chem. 648 (2022) e202200311 (1-11).

https://onlinelibrary.wiley.com/doi/10.1002/zaac.202200311

ORCID:

SW: 0000-0003-1404-3434
MMM: 0000-0002-9063-372X
TMG: 0000-0002-4119-2219

Journal of Inorganic and General Chemistry
ZAAC
Zeitschrift für anorganische und allgemeine Chemie
www.zaac.wiley-vch.de
RESEARCH ARTICLE

DOI: 10.1002/zaac.202200311

On red tin (II) oxide: temperature-dependent structural, spectroscopic, and thermogravimetric properties

Sarah Wittmann,[a] M. Mangir Murshed,*[a, b] and Thorsten M. Gesing[a, b]

This article is dedicated to the memory of Rudolf Hoppe and the everlasting question: What color is this compound?

Polycrystalline red tin(II)oxide (RSO) has been synthesized by a fast reflux method. X-ray powder diffraction (XRPD) data Rietveld refinement confirms the orthorhombic space group *Cmc*2_1 (Z=8). The presence of 5 s^2 lone electron pair (LEP) of the Sn^{2+} cation results in layers of highly distorted SnO_4 tetrahedra with an averaged Wang-Liebau eccentricity (WLE) parameter of 4.3(1) x10^{-5} as a measure of the stereochemical activity. The significantly different Sn–O bond distances demonstrate the under-bonding nature of both the tin and the oxygen atoms in the SnO_4 coordination. The band gap of red tin(II)oxide is found to be 1.75(1) eV which is compared with those of blue-black tin(II) (BSO) and white tin(IV) oxide (WSO) based on the UV-Vis diffuse reflectance spectral data. Temperature-dependent XRPD reveals the $RSO \xrightarrow{540(20)\ K} BSO \xrightarrow{700(20)\ K} WSO$ phase transitions, which is complemented by thermogravimetric and differential scanning calorimetry (TG/DSC) investigations. Moreover, in-situ Raman spectroscopy additionally hints to an intermediate phase either of Sn_2O_3 or Sn_3O_4 appears within a short temperature range before the RSO to BSO transition occurs. Due to axial negative thermal expansion for the *b*-lattice parameter RSO exhibits nearly a zero thermal expansion coefficient for a given temperature range above room temperature.

1. Introduction

Due to associated redox potential Sn^{2+} is more susceptible to oxidize into Sn^{4+}[1] that favors thermodynamically more stable[2] white SnO_2 (WSO). As such, the majority of the known tin minerals contain Sn^{4+} cations, and only six minerals are known to occur with Sn^{2+} cation, namely, Abhurite ($Sn_3O(OH)_2Cl_2$[3]), Foordite ($SnNb_2O_6$[4,5]), Thoreaulite ($SnTa_2O_6$[4]), Romarchite (SnO[3]), Hydroromarchite ($Sn_3O(OH)_2$[3]) and Stannomicrolite ($Sn_2Ta_2O_7$[6]). Whereas the direct oxidation ($SnO + {}^1\!/_2\ O_2 \rightarrow SnO_2$) occurs at 873 K without any intermediate phase,[7] the disproportionation of SnO into SnO_2 and Sn occurs at about 673 K.[7] Donaldson et al.[8] demonstrated that the true stability range of SnO is above the disproportionation temperature of 658 K. Of two modifications of Sn-(II)-oxides, the red SnO (RSO) is stable in air up to about 543 K, possibly owing to the presence of a thin protective coating of SnO_2.[8] The red SnO can be converted to blue-black SnO (BSO) using a non-oxidizing atmosphere at high-temperature.[8] The thermal modification of tin oxides is not limited to the two-fold valency of tin. Instead, the existence of Sn_xO_{x+1}[9–11] and SnO_{2-x}[12] phases clearly demonstrate the variation of oxidation state in tin-oxides. Such variability of oxidation state of a given cation in oxides can tailor the concentration of oxygen in the surface, leading to facilitate the Mars-van Krevelen mechanism based redox catalysis.[13] Both SnO and SnO_2 exhibit interesting physico-chemical properties as transparent conducting electrodes for flexible electronics,[14] opto-electronics[2] and semi-conductors.[7] WSO is an n-type semiconductor with a direct band gap of 3.6 eV,[7] which is widely used as transparent conducting oxide,[15] gas sensor[16] and catalyst.[17] RSO, on the other hand, is a p-type semiconductor with a narrower indirect band gap of 0.7 eV and an optical gap of 2.7 eV.[5]

The commercially available BSO crystallizes with the litharge structure type (*P*4/*nmm*)[18] and RSO crystallizes in the *Cmc*2_1 space group.[19] Figure 1 depicts the crystal structure of RSO, showing a schematic representation of different motifs and their connectivity. Starting from a regular MO_6 octahedra Brown[20] demonstrated how the stereo-chemically active lone electron pair (LEP) introduces distortion, leading to lower coordination for charge valence. The tin coordination both in RSO and BSO can be described as MO_4E coordination (E abbreviates to an active LEP), where the polyhedra can be seen as nido-trigonal bipyramid with the nido position occupied by one LEP. In the RSO structure both tin and oxygen are four-coordinated, forming a zeolite-like $4^6 6^2$ building unit with two 6-ring and six 4-ring windows. The 6-ring window conforms a cyclohexane chair-like structure with one shorter (<210 pm)

---

[a] S. Wittmann, M. M. Murshed, T. M. Gesing
University of Bremen, Institute of Inorganic Chemistry and Crystallography, Leobener Straße 7, D-28359 Bremen, Germany
E-mail address:
phone: +49 (0)421 218 63144
+49 421 218 63145
E-mail: murshed@uni-bremen.de
[b] M. M. Murshed, T. M. Gesing
University of Bremen, MAPEX Center for Materials and Processes, Bibliothekstraße 1, D-28359 Bremen, Germany

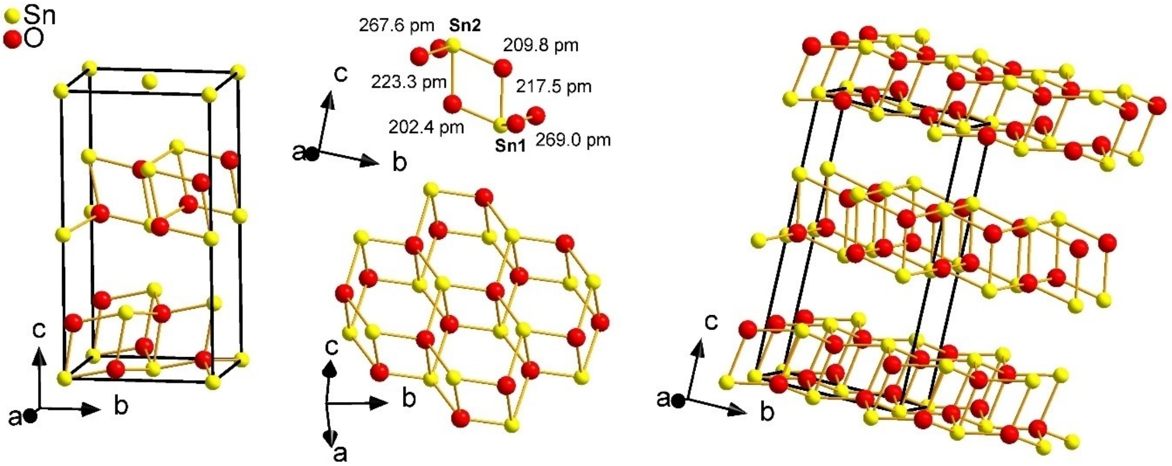

Figure 1. Crystal structure of red SnO (RSO), showing the unit cell (left), two linked SnO_4E units (E = stereo-chemical active lone electron pair) and their interatomic distances (middle) together with their inter-layer connectivity, forming $4^6 6^2$ units that serve as double layers and the orientation of these layers in the unit cell (right).

and two longer (~270 pm) Sn–O bond distances, and the intermediate Sn–O bond distance (~220 pm) bridges the 6-ring formed layers. The 6-rings are not entirely parallel to the **c**-axis. Instead, the Sn_3O- and O_3Sn-trigonal planes are parallel to the **c**-axis, and are separated by about 35 pm. The $4^6 6^2$ units are interconnecting by sharing the 4-rings, resulting in a double-layer of about 220 pm stacked along the crystallographic **c**-direction. The double layers are far away (ca. 300 pm) and hardly hold any electrostatic bindings. Instead, they are separated by strong stereo-chemical repulsion of the Sn^{2+} LEPs of the trigonal pyramidal SnO_3 units.[21] Due to presence of stereochemically active LEPs it is convenient to consider SnO_3E as distorted tetrahedra, where E refers to a stereo-chemically active LEP exposed perpendicular to the *ab* plane. Moreover, the 4-rings (square nets[19]) are also distorted, and the holes are filled by the LEPs. The crystal structure of RSO can be better compared to that of thallium iodide which, however, adopts more regular double-layers of cations and anions.[19] How LEPs influence the bond valence (BVS) of a LEP-containing cation in the centroid of a given coordination Wang and Liebau introduced a vector term.[22] The absolute value of the vector was later coined as Wang-Liebau eccentricity (WLE) parameter[23] that measures the deformation density of the LEP.

Since SnO is susceptible to oxidation into SnO_2, synthesis of pure RSO still remains a challenge using solid state synthesis method. Notably, hydrothermal synthesis using $SnCl_2$ releases hydrochloric acid that suppresses oxidation into SnO_2[7,24,25] at inert atmospheric conditions. Due to thermal stability, the crystal-physico-chemical properties of SnO_2 are experimentally well established while for SnO, the associated properties are mostly known from ab-initio calculations.[26] Moreover, since the intermediate thermal modification BSO is also a semiconductor, the RSO can serve as a thermochromic sensor via two phase transformations. The present investigation particularly emphasizes the synthesis of RSO via a different synthesis route followed by temperature-dependent structural, spectroscopic, and thermogravimetric investigations for the RSO→BSO→WSO transformations.

Experimental

Synthesis

To synthesize red SnO, $SnCl_2 \cdot 2H_2O$ was dissolved in 50 mL demineralized water. 5 M NH_3 was added to obtain a pH = 4.9. According to earlier reports,[19] the pH should be smaller than 5 to avoid formation of BSO. However, in our study, pH < 4.5 does not lead to formation of RSO. A small amount of H_3PO_3 was added before heating the solution to 371 K. At this temperature the appearance of RSO solid particles could be observed after two hours. After 3.5 h the mixture was cooled down to room temperature. The synthesized solid was washed with 2 M NH_3 to stabilize RSO. After washing, 50 mL of 2 M NH_3 was added to the mixture and heated to 358 K for another 2 h. The cooled mixture was washed with demineralized water and dried at 363 K in vacuum (very low-pressure) conditions. As the metastable RSO is sensitive to air, it is stored at vacuum conditions at room temperature.

X-ray diffraction

X-ray powder diffraction

Diffraction measurements were carried out at ambient conditions on a Stoe Stadi-MP diffractometer (Stoe & Cie. GmbH, Darmstadt, Germany) in Debye-Scherrer geometry using Ge(111) monochromatized $MoK_{\alpha 1}$ radiation. The samples were placed in a borosilicate glass capillary of 0.5 mm outer diameter and 0.01 mm wall thickness. Homogeneous irradiation and good diffraction statistics of the powders were achieved through a sample spinner. Data were collected in a range between 3° and 70.8° 2θ with a step size of 0.005° and a data collection time of 16560 s/data point. The fundamental parameter approach, where the fundamental parameters were fitted against a LaB6 standard material, was applied for the Rietveld refinement using the "Diffrac^{Plus} Topas 6" software (Bruker AXS GmbH, Karlsruhe, Germany). For the determination of the diffuse scattering contribution assumed to origin from quantum-crystalline or amorphous phase contents, 33.0(1) wt-% of NaCl were added to the sample as internal standard and carefully mixed.

High-temperature data were collected on a PANalytical MPD powder diffractometer in Bragg-Brentano geometry which was equipped with a secondary Ni filter, CuKα radiation, and an X'Celetator multi-strip detector using an Anton Paar HTK1200 N heating chamber. To prepare the sample in a flat corundum sample holder acetone was used and the small evaporation channels remaining served as additional space to compensate the samples thermal expansion. Measurements were carried out between 300 K and 1100 K with steps of 10 K. Each pattern was recorded from 10° to 85° 2θ with a step size of 0.0167° and a scan time of 0.95 s/step for red SnO and 0.45 s/step for BSO and WSO.

Low-temperature data were collected on a STOE Stadi-MP diffractometer configured in Bragg-Brentano geometry. They were recorded with a Dectris Mythen 1 K detector while limiting the angular coverage of the detector to 6.25° 2θ to avoid aberration effects. MoK$_{\alpha1}$ X-ray radiation was used with a Ge(111) monochromator. With a step width of 0.005° from 5° to 50° 2θ a total of 3007 data points were measured for 55 s/step using 428 channels of the detector. The samples were mixed into thick pastes with thermally conductive paint (Kemo Electronic L100 Conducting Silver) and fixed on a copper sample holder for improved thermal homogeneity. The temperature was controlled utilizing the Oxford Cryosystems PheniX cryostat and powder patterns were recorded from 293 K down to 13 K using 10 K increments. Additionally, data at 18 K were collected. For both instruments, the reflection profile was modeled using the fundamental parameter approach,[27] as implemented in TOPAS 6 (Bruker AXS GmbH, Karlsruhe, Germany). The structural starting model for the Rietveld refinements was taken from the published red SnO phase given by Köhler et al..[19] The resulting Rietveld plots are shown in Figure 2.

Spectroscopy

Raman

Raman spectra were recorded on a LabRam ARAMIS (Horiba Jobin Yvon) Micro-Raman Spectrometer equipped with a laser working at 633 nm and less than 20 mW. The use of a 50× objective (Olympus) with a numerical aperture of 0.55 provides a focus spot of about 2 μm diameter when closing the confocal hole to 200 μm. Raman spectra were collected in the range of 90 cm^{-1} to 800 cm^{-1} with a spectral resolution of approximately 1.2 cm^{-1} using a grating of 1800 grooves/mm and a thermoelectrically-cooled CCD detector (Synapse, 1024×256 pixels). The spectral position and the linearity of the spectrometer were calibrated against the Raman mode at 520.7 ± 0.1 cm^{-1} of a Si wafer and emission lines of a neon lamp, respectively. Temperature-dependent data sets were collected between 80 and 300 K using a Linkam THMS350 stage, and between 300 and 800 K using a Linkam TS1500 V stage with 10 K temperature increments. Peak positions, peak widths and profile shapes were deconvoluted into Gaussian and Lorentzian components using the LAMP software package.[28]

UV/Vis

The UV/Vis diffuse reflectance measurements were obtained on a Shimadzu UV/Vis spectrophotometer UV-2600 equipped with an ISR-2600 plus a two-detector integrating sphere. The sample holder was filled with barium sulfate as background. The reflection spectra were measured over a wavelength range of 190–800 nm in 1 nm steps. High-temperature UV/Vis data were collected using a heating Pike Technologies with a UV/Vis DiffuseIR heating chamber (Pike Technologies, USA) covered with a quartz-glass window. Spectra were measured between 295 K and 900 K with a constant heating rate of 2 K/min. Data were collected in the medium resolution mode with continuous scanning for 108 s.

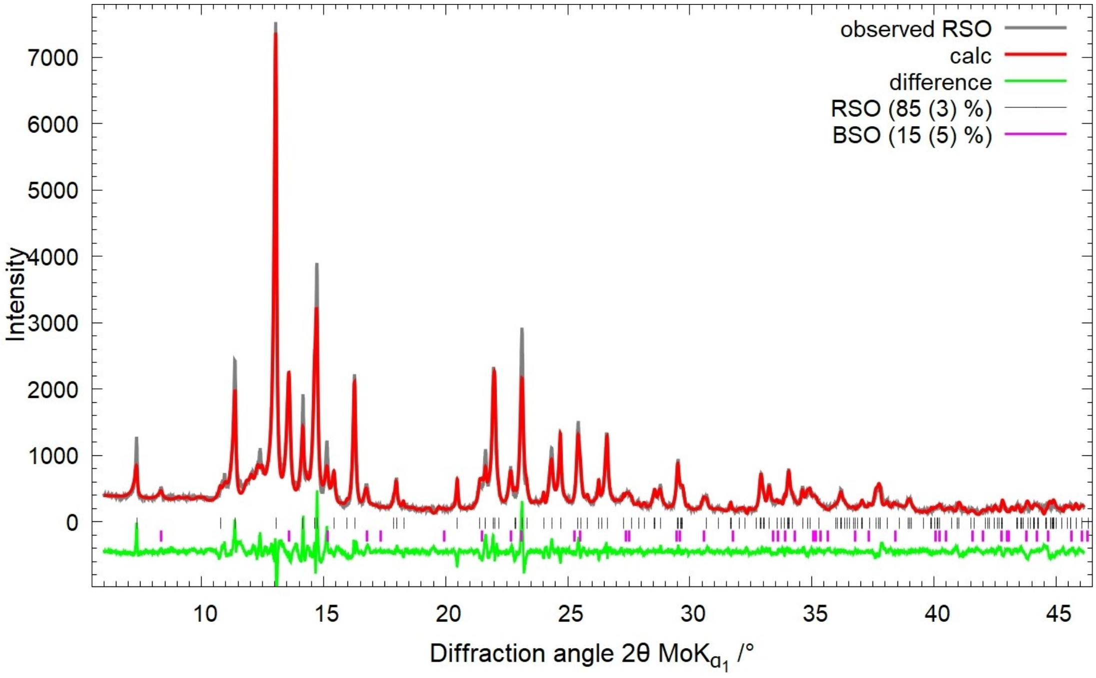

Figure 2. X-ray powder diffraction data Rietveld plot of red SnO (RSO), showing a small additional amount of black SnO (BSO).

SEM and EDX

Scanning electron microscopy (SEM) was carried out on a JSM-6510 (JEOL GmbH, Munich, Germany) equipped with energy dispersive X-ray (EDX) analysis facilities and an XFlash Detector 410-M (Bruker AXS GmbH, Karlsruhe, Germany). To obtain quality data, samples were sputtered with a thin film of gold having a thickness of approx. 10 nm. EDX spectra were collected using an excitation voltage of 20 kV.

Thermal analysis

Simultaneous thermal analyses of TG-DSC were carried out under a dry synthetic air atmosphere (80 vol% N2 and 20 vol% O2) and N_2 with a heating rate of 10 K/min from 303 K to 1473 K on a Mettler Toledo TGA/DSC 3^+ STARe System. 10.6(1) mg sample was measured relative to a corundum crucible with 10 mg Al_2O_3 as the reference. A drift correction to the data was applied using an empty corundum crucible measurement.

2. Results and discussion

2.1. Synthesis and SEM/EDX

RSO was synthesized based on the description of Köhler et al.[19] who dissolved metal tin into 5 M HCl followed by controlling the pH = 4.9. Instead, we used $SnCl_2 \cdot 2H_2O$ dissolved in demineralized water followed by the given procedure.[19] Alike of Köhler et al.,[19] $SnO \cdot xH_2O$ did not appear at any stage of the reaction but Sn_2O_3[12] which eventually reduced into RSO. While monitoring the reaction products using ex-situ XPRD, the amount of Sn_2O_3 gradually decreases, leading to RSO as the major phase. A small amount of Sn_2O_3 could be washed away during the last step using demineralized water.

A representative SEM image is given in Figure 3, showing RSO crystals/particles comprising of flake-like structure. The shapes and sizes are comparable to those seen in the reported images.[19] While the SEM image depicts the agglomerated size ranges from 10 to 30 μm, the average crystallize size is found to be 64.0(2) nm with the micro-strain of 0.121(3) % calculated from the XPRD data. The Sn/O atomic ratio obtained from the SEM/EDX (Sn: 54(4) At-%; O 45(4) At.%) unambiguously supports the chemical composition (SnO) of the sample.

2.2. X-ray diffraction

XRPD data Rietveld refinements confirm that RSO crystallizes in space group $Cmc2_1$. Details of the crystal structure of obtained RSO, BSO and WSO are listed in Table 1 and Table 2. The RSO unit-cell dimensions *a*, *b* and *c* are found to be 500.92(2) pm, 575.61(3) pm and 1107.32(5) pm, respectively, which lie close to the reported values.[19] A lattice parameter of 564.34(1) pm for the internal standard NaCl was additionally refined, corresponding to the NIST published value[29] for 298 K. The *a* and *c* metric parameters for BSO (*P4/nmm*) are observed as 380.14(1) pm and $c = 483.86(3)$ pm, respectively. Following Köhler et al.,[19] the transformation of the unit cells of RSO and BSO can be calculated for Z = 8 and Z = 2, respectively, from the following expression:

$$a\ (RSO) = \sqrt{2} \cdot a\ (BSO) = \sqrt{2} \cdot 380.14\ pm = 537.60\ pm$$

As for the tetragonal unit cell, $a = b$, the same equation can be used. That is, for the synthesized RSO, ***a*** (RSO) is about 7 % smaller and ***b*** (RSO) 7 % larger than those of the calculated values. Expression for the ***c*** lattice parameter:

$$c\ (RSO) = 2 \cdot c\ (BSO) = 2 \cdot 483.86\ pm = 967.72\ pm$$

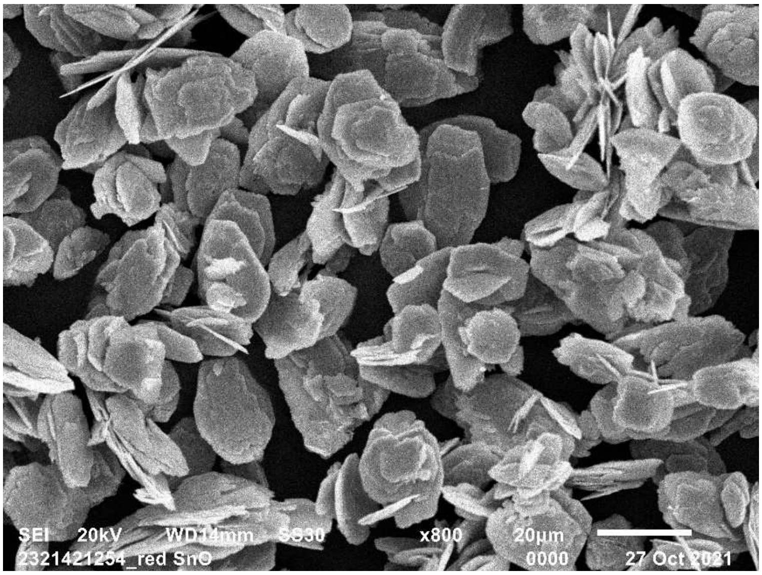

Figure 3. Scanning electron microscope image of red SnO (RSO).

Table 1. Rietveld refined parameters for red and black SnO and SnO_2.

Empirical formula	Red SnO (RSO)	Black SnO (BSO)	White SnO_2 (WSO)
Formula weight/(g/mol)	134.71(1)	134.71(1)	134.71(1)
Temperature/K	298(2)	300(1)	300(1)
Instrument, radiation	Stoe MP, Ag $K\alpha_1$	Stoe MP, Ag $K\alpha_1$	Stoe MP, Ag $K\alpha_1$
Geometry	DS, glass capillary	DS, glass capillary	DS, glass capillary
Crystal system	orthorhombic	tetragonal	tetragonal
Space group	$Cmc2_1$	*P4/nmm*	$P4_2/mnm$
a/pm	500.92(2)	380.20(2)	473.99(4)
b/pm	575.61(3)	$=a$	$=a$
c/pm	1107.32(5)	483.97(3)	318.82(3)
$V/10^6$ pm^3	319.28(3)	69.96(2)	71.63(3)
ACS $(L_{VOL}IB)$/nm	63(2)	42.8(6)	38.7(5)
R_B/%	7.3	5.3	6.1
R_{WP}/%	9.8	8.7	9.1
GOF	1.98	1.49	1.86
Density/(g/cm^3)	5.605(4)	6.394(1)	6.987(1)

Table 2. Crystal structural data of three tin oxides obtained from the X-ray powder diffraction data Rietveld refinement. The y and z position of Sn1 of RSO were fixed to 0 and their standard deviations calculated.

Site	Atom	Wyckoff	x	y	z	Occ.	$B_{iso}/10^{-4}$ pm^2
red SnO (RSO)							
Sn1	Sn^{+2}	4a	0	0.0000(2)	0.0000(2)	1	2.00(8)
Sn2	Sn^{+2}	4a	0	0.4177(4)	0.2344(5)	1	0.93(8)
O1	O^{-2}	4a	0	0.3446(4)	0.0364(3)	1	0.30(6)
O2	O^{-2}	4a	0	0.0617(4)	0.1938(3)	1	0.30(6)
blue-black SnO (BSO)							
Sn1	Sn^{+2}	2c	$^1/_4$	$^1/_4$	0.2379(2)	1	0.59(2)
O1	O^{-2}	2a	$^3/_4$	$^1/_4$	0	1	1.20(2)
white SnO_2 (WSO)							
Sn1	Sn^{+4}	2a	0	0	0	1	0.25(8)
O1	O^{-2}	4f	0.3071(1)	x	0	1	0.25(5)

also suggests that the synthesized ***c*** (RSO) is about 14% larger than that of the calculated one.

The obtained density (5.605(4) g/cm^3) of RSO is about 1% lower than that of the reported one, which is fine within the obtained standard deviations. Nevertheless, the density of RSO is much lower (13.4(1)%) than that of BSO (6.398(1) g/cm^3),[19] which is rather unusual. Such a density gradient possibly indicates a slow room-temperature open condition transformation into the more compact but higher symmetric BSO.[19] In contrast, the density of tetragonal low-temperature red PbO polymorph (litharge) and orthorhombic high-temperature yellow polymorph (massicot) are 9.12(1) g/cm^3[30] and 9.60(1) g/cm^3,[31] respectively. The former one is a stable and the latter one is a metastable polymorph (due to the very low transformation speed) at ambient condition.

The basal Sn–O bond distances of RSO spread between 202.4(3) and 269.0(1) pm which are comparable to the bond distance of BSO $d_{Sn-O}=222.25(6)$ pm. There are two different SnO_4E polyhedra (Figure 1) in RSO, where the smaller Sn–O bond distances of 202.4(3) pm (Sn1) and 217.5(4) pm lie more or less at the opposite side of the lone electron pairs (LEP) of Sn^{2+}. As the stereo-chemical influence the of the LEPs not only shorten these bond distances but also elongate the other two bond distances (Sn1–O1 = 269.0(1) pm and Sn2–O2 = 267.6(1) pm). Further bond distances within the polyhedra, such as Sn1–O2 (217.5(4) pm) and Sn2–O1 (223.3(3) pm) are additionally influenced by the linkage of the SnO_4E polyhedra, forming the single double layers separated from each in the **c**-direction of the unit cell (Figure 1) by the associated LEPs therein. From these findings the SnO_4E polyhedra can be better described as a distorted nido-like trigonal bipyramid where the nido direction ("missing" oxygen atom) is replaced by the active LEP. As such, the highly asymmetric shape of SnO_4E polyhedra in RSO can be explained in terms of sole influence of the LEPs which, however, is not the case for the tetragonal BSO. Due to slightly a different geometry, Sn1 is more distorted (WLE = $4.96(1)\cdot10^{-5}$) than Sn2 (WLE = $3.54(1)\cdot10^{-5}$) in the SnO_4E polyhedra. The highly distorted two types of SnO_4 polyhedra comprising of significantly different bond distances result in a strong under-bonded nature of the Sn-atoms (Table 3). The averaged BVS of Sn-atom is however excellently satisfying the valence of the oxygen atoms.

Table 3. Bond distances and bond valence sum (BVS) of red SnO (RSO), black SnO (BSO) and white SnO_2 (WSO).

	bond distance/pm			BVS/v.u.		
Sample	Sn–O	Sn–Sn	Sn	average	O	average
RSO Sn1	202.4(3) 1× 217.5(4) 1× 269.0(1) 2×	363.8(2)	1.79(2)	1.67(1)	−1.70(1)	−1.67(1)
RSO Sn2	209.8(3) 1× 223.3(3) 1× 267.6(1) 2×		1.55(1)		-1.64(1)	
BSO	222.25(6) 4x	369.64(14)	1.86(1)	1.86(1)	−1.86(1)	−1.86(1)
WSO	205.81(1) 4× 205.21(1) 2×	318.73(2)	4.01(1)	4.01(1)	−2.01(1)	−2.01(1)

2.3. Temperature-dependent properties

Results of the thermogravimetric combined with differential scanning calorimetry (TG/DSC) are shown in Figure 4. At lower-temperatures the sample slightly losses weight up to 666(2) K in a weak endothermic process. This might be due to removal of the remaining humidity of the sample. Above this temperature the steepness of the endothermic signal slightly increases along with almost a constant sample weight till a strong exothermic signal appears at 738(2) K (onset temperature). Afterward, a broader exothermic peak is seen with an onset temperature of 763(2) K followed by a third even broader exothermic event between 908(5) k and 1057(5) K. Comparing these findings with those obtained from TD-XRPD data the thermal events could be correlated to a stable appearance of RSO up to 580(10) K, where the phase transition RSO→BSO starts with a week endothermic process. The strong exothermic event can be understood in terms of phase-transformation of BSO to the structurally unknown tin-sesquioxide (SSO) Sn_2O_3. The following broader exothermic event is associated with the transformation of WSO. The broader exothermic signal at higher-temperature can interpreted as concomitant crystallization, Ostwald ripening and defect healing of the WSO phase. Of notes, slightly different event temperatures are observed by TD-XRPD than those in TG/DSC, and a correlation of $T_{TG/DSC} = 1.11(2)\ T_{TD-XRPD}$ could be derived. This also hints to a rather slow phase-transition and phase-transformation processes. It is of particularly interest that the formation of Sn_2O_3 starts at slightly a higher temperature when micro-crystalline BSO is initially used (Figure 4). Indeed, it further hints to a strong influence of crystallite size and defect concentration on the transformation temperature.

Comparing the TD-XRPD measurements of RSO, BSO and WSO, as shown in Figure 5, it is clear that at least one additional phase appears between 500 K and 600 K while heating the RSO, and between 650 K and 850 K while heating the BSO. It is assumed that it is SSO that forms either from RSO via BSO or directly from BSO. Nonetheless, in all three heating events the

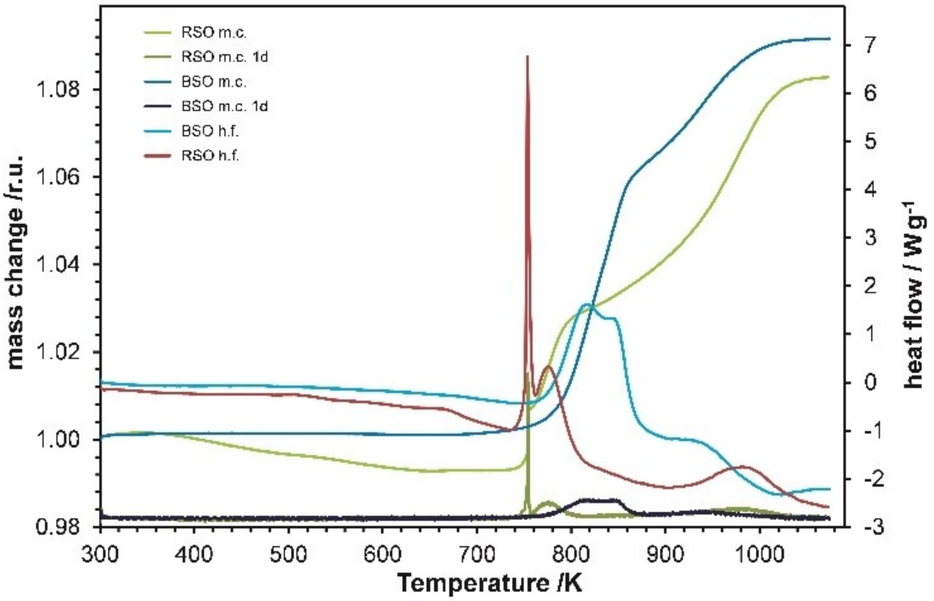

Figure 4. Thermogravimetric analysis of red (RSO) and black (BSO) SnO with its mass change (m.c.) and heat flow (h.f.) as well as the first derivative of the mass change (m.c. 1d).

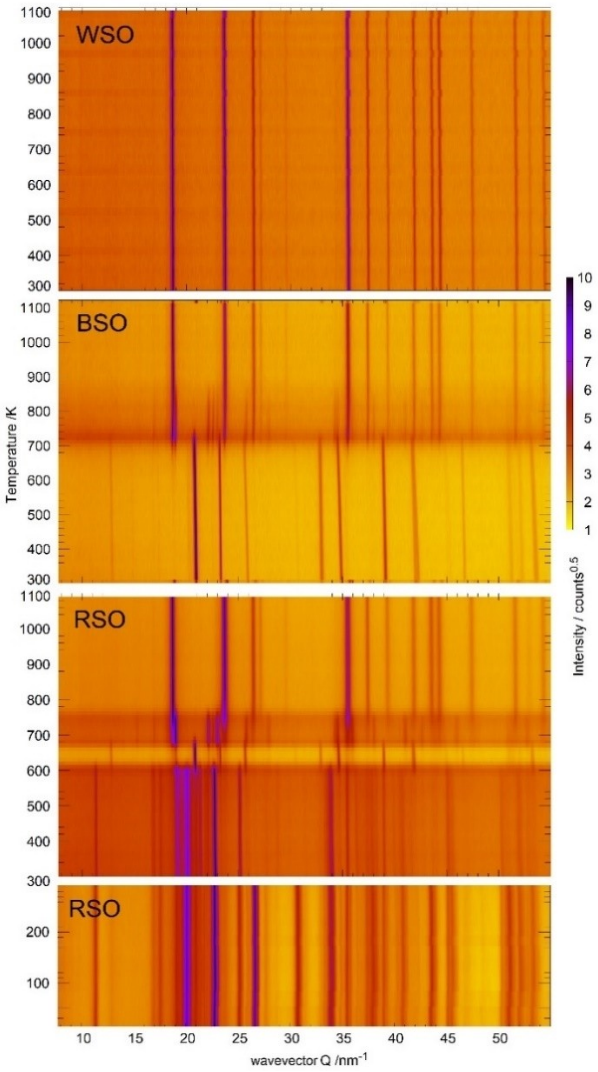

Figure 5. 3D plots of the temperature-dependent XRPD data of red tin oxide (RSO), black tin oxide (BSO) and white tin dioxide (WSO). The low-temperature pattern of RSO depicts additional reflections of the silver glue. Difference in intensity of some RSO reflections should be considered due to different preferred orientations in two separate measurements.

SSO transforms into WSO, which is not observed during the heating of WSO. The structure of SSO is of long debates.[32] Materials Project[33] recently suggests some crystal structural features based on theoretical calculations. Their given space group and metric parameters, however, cannot index the observed reflections. Nevertheless, based on the given suggestions the observed data could well be fitted with a unit cell of $a = 370.69(9)$ pm, $b = 1009.57(38)$ pm, $c = 2455.06(78)$ pm in the space group *P*222.

Although the average crystallite size (L_{Vol}-*IB*) of nanocrystalline RSO is only 63(2) nm, temperature-dependent evolution of the metric parameters can be followed. The lattice thermal expansion behavior was modeled using the Debye-Einstein-Anharmonicity (DEA)[34–38] approach. The metric parameters of RSO together with the DEA model lines are given in Figure 6, and the fit parameters are given in Table 4. Of interests, the ***b***-lattice parameter only slightly decreases from 576.39(51) pm to 575.80(65) pm for a temperature range between 10 K and 550 K. In the same temperature range the ***a***-lattice parameter increases from 498.17(25) pm to 500.50(51) pm and the ***c***-lattice parameter from 1099.17(54) pm to 1106.60(66) pm. The temperature change of 540 K corresponds to a change of 0.47(1) %, −0.10(1) % and 0.68(1) % for the ***a***-, ***b***- and ***c***-lattice parameters, respectively. All metric parameters require two Debye terms for the investigated range of temperature. Of them, the first one shows a positive thermoelastic parameter[39–42] for ***a***, ***c*** and ***V*** whereas the second one is found to be negative. Such a negative term apparently refers to negative Grüneisen parameter for the respective Debye spectrum. However, an opposite behavior is obtained for the ***b***-lattice parameter. In any case, the thermal expansion coefficient (TEC) in the whole temperature range is small for all metric parameters with values between −5 to 20 μK^{-1}. At around 500 K all TECs remain close to zero in all three lattice directions. The corresponding temperature-dependent anisotropy of the metric parameters is given in Figure 7. A maximum TEC anisotropy could be observed at around 140 K which decreases with increasing temperature. At around 500 K no anisotropy is observed and the RSO exhibits a pseudo-cubic expansion behavior, followed by increasing deviation with further increasing temperature. Above 540 K it drops again in hand with strong deviations from the DEA fittings. From this, the transformation of RSO into BSO is assumed to intrinsically start around 500 K and becomes obvious around 540 K, although an XRD based visible effect is seen at even higher temperatures.

Table 4. Debye-Einstein-Anharmonicity (DEA) fit parameters of red SnO (RSO).

Fit-parameter	Cell volume ***V***	lattice parameters ***a***	***b***	***c***
$V_0/10^{-6}$ pm^3	315.60(43)	498.17(25)	576.39(51)	1099.17(54)
$k_{D1}/10^{-12}$ GPa	16.1(1)	13.3(1)	−5.2(1)	41.1(1)
θ_{D1}/K	106(38)	180(18)	493(71)	180(24)
$k_{D2}/10^{-12}$ GPa	−33.7(1)	−37.2(1)	25.5(1)	−76.3(1)
θ_{D2}/K	2040(728)	2593(263)	3600(520)	1896(255)

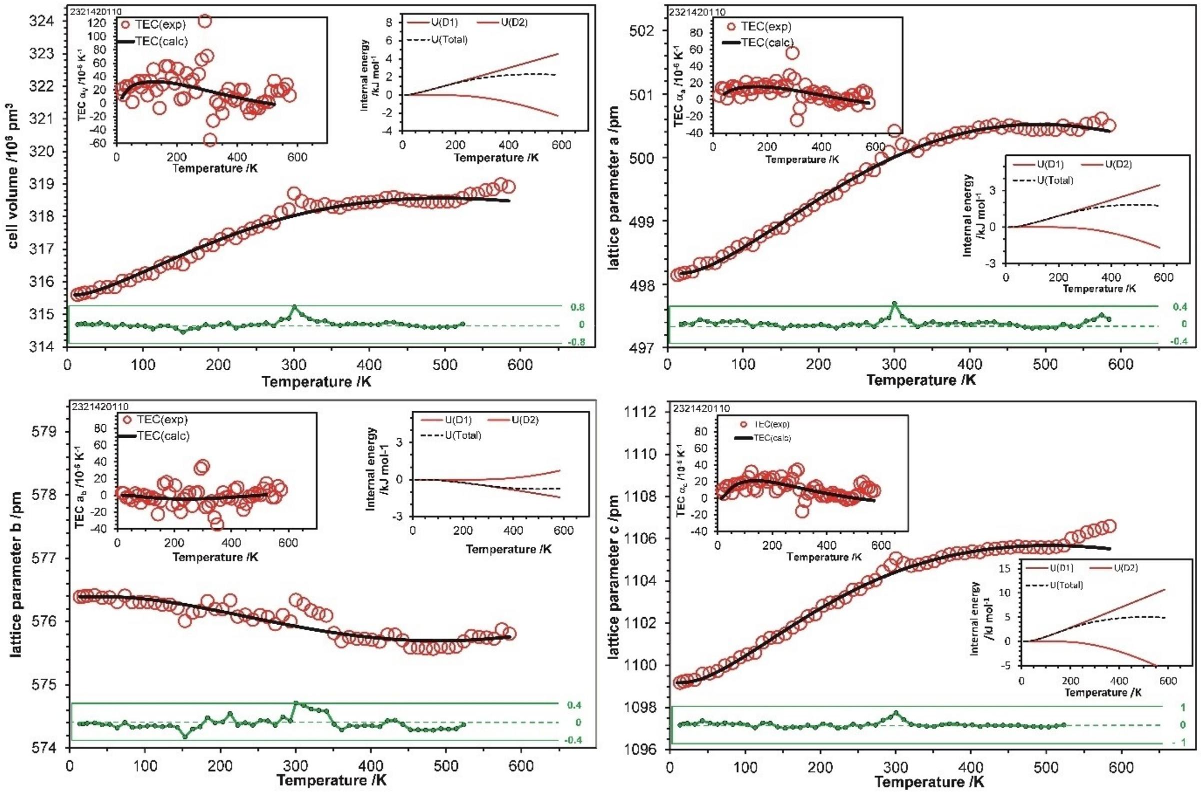

Figure 6. Debye-Einstein-Anharmonicity (DEA) fits of the metric parameters of red SnO (RSO). The respective thermal expansion coefficients (TECs) and the Debye energy terms are seen as insets.

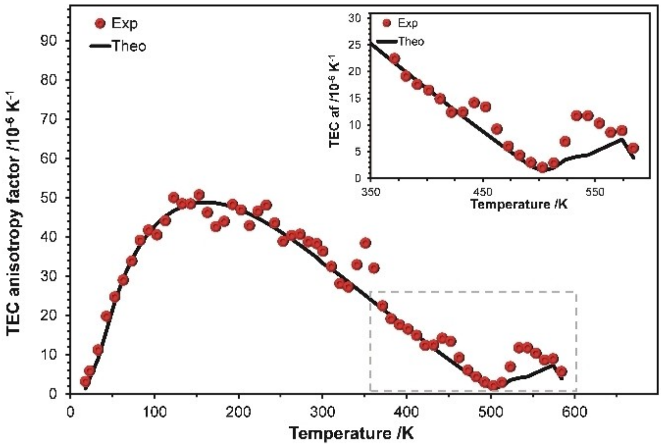

Figure 7. Temperature-dependent thermal expansion coefficient (TEC) anisotropy parameter of RSO.

2.4. Vibrational spectroscopy

Stack-plots of the temperature-dependent Raman spectra are shown in Figure 8. Factor group analysis suggests 24 vibrational modes at the zone center ($8\,A_1+4\,A_2+4B_1+8B_2$). Three of them are acoustic ($A_1+B_1+B_2$), four are IR ($2\,A_1+1B_1+2B_2$) and six are Raman active ($2\,A_1+1\,A_2+1B_1+2B_2$) modes. The Raman spectrum collected at ambient condition requires twelve pseudo-Voigt peaks as given in Table 5. Of them, four peaks at 265.1, 425.5, 491.3, 642.3 are found to be low-intense. The characteristic vibrational features of BSO and WSO are observed in the range between 107 cm^{-1} and 500 cm^{-1}, and 120 cm^{-1} and 780 cm^{-1}, respectively.[43] In analogy, the Raman shift of RSO is expected to be in the similar region. The peak maxima at lower-frequency at about 100.3 cm^{-1}, 114.1(1) cm^{-1} and 211.7(1) cm^{-1} can be assigned to lattice vibration, and the others are to normal vibrations of the SnO_4 polyhedra. With increasing temperature most of the peak frequencies show slightly a red-shift due to quasi-harmonic nature of the respective vibrations till around 300 K. Afterward, the peak positions remain almost unchanged. At 500 K a new band appears at about 165 cm^{-1} along with significant changes of both intensity and frequency of the other vibrational features (Figure 8). From the normalized spectra (to 215 cm^{-1}) the highest intensity of this band is observed at 550 K, which shows a random decrease with increasing temperature may be due to local kinetics. This band frequency can be correlated to the appearance of either Sn_2O_3 or Sn_3O_4.[44] Indeed, this observation supports the TD-XRPD results for an intermediate transformation of RSO into either Sn_2O_3 or Sn_3O_4 within the investigated range up to 600 K.

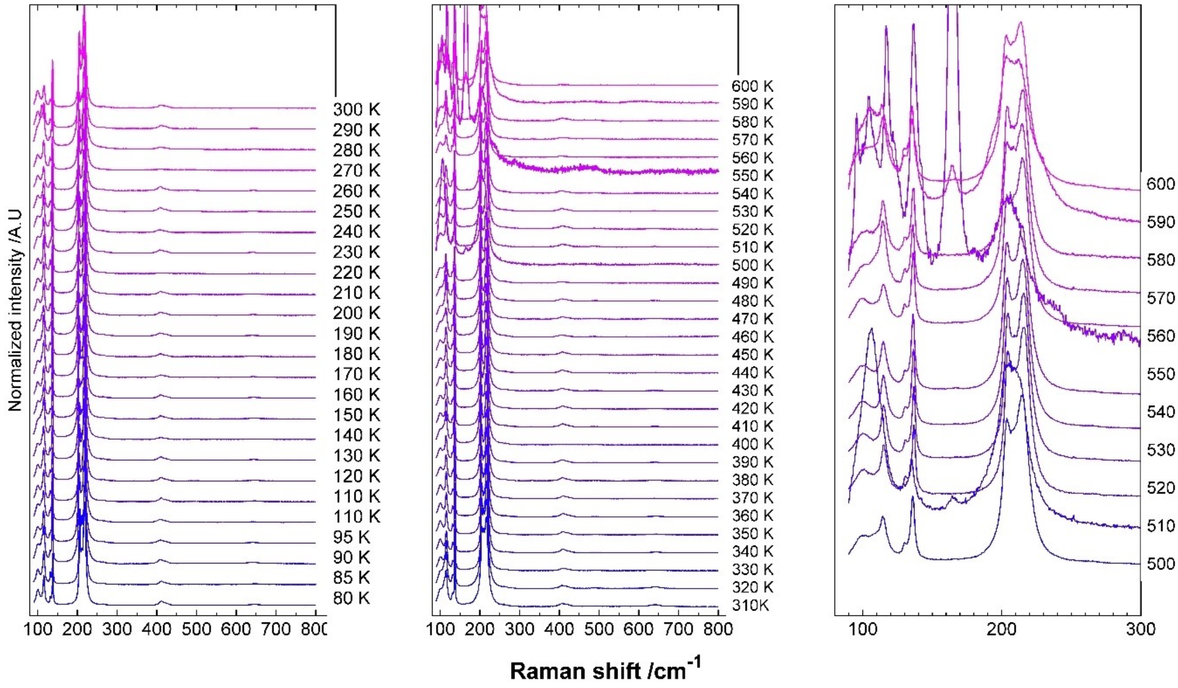

Figure 8. Temperature-dependent Raman spectra of red tin-(II) oxide (RSO), The appearance of a peak at around 165 cm^{-1} at ≥ 500 K is shown with magnification (right panel).

Table 5. Fitted ambient condition Raman data peak maxima (± 0.1 cm^{-1}) of red tin(II)oxide (RSO), blue-black tin(II)oxide (BSO) and white tin(IV)oxide (WSO).

RSO	BSO	WSO
100.3	114.1	474.9
115.9	211.7	633.4
131.1	226.8	694.5
137.5	–	760.7
204.9	–	775.2
209.7	–	–
217.3	–	–
265.1	–	–
413.2	–	–
425.5	–	–
491.3	–	–
642.9	–	–

2.5. UV/Vis spectroscopy

For the determination of the optical band gap, the derivation of absorption spectrum fitting (DASF) method is used.[45] The DASF method hardly provides any new value, which however, can be compared with those obtained from the Tauc's direct or indirect bandgap value, leading to understand the type of band gap.[46] Using the Tauc method the band gap is obtained from the intercept of the abscissa from the expression: $a\ (h\nu) \approx B\left(h\nu - E_g\right)^n$ where a is the extinction coefficient, h the Planck constant, ν the frequency of light, E_g the band-gap energy in eV and n the nature of transition;[46] $n = 2$ for an indirect bandgap and $n = {}^{1}/_{2}$ for a direct band gap.[46] Indeed, the Tauc method is limited by the selection of n-value and the nature of transition as well. Taking the extinction coefficient as approximation of the Kubelka-Munk function F(R) the relation between band-gap energy, transition type and absorption is given by the equation: $F(R) = B\left(h\nu - E_g\right)^n$ which could be transformed to $ln\ F(R) = ln\ B + \ n\ln\left(h\nu - E_g\right)$. From the first-derivative expression,[46,47] the band-gap value can be calculated from the peak-shape of the UV/Vis data. The DASF results are compared with those obtained from the Tauc method, and the nature of transition can be figured out from the combined approach known as RATD method (reflection, absorption, Tauc and DASF).[48]

A representative RATD analysis is shown in Figure 9, where RSO is found to possess an indirect and direct Tauc transition energy of $E_i = 1.87(3)$ eV and $E_d = 4.18(3)$ eV, respectively, at ambient temperature. BSO, on the other hand, exhibits a direct and indirect transition energy of $E_i = 2.35(3)$ eV and $E_d = 3.90(3)$ eV, respectively. If the DASF band-gap energy of $E_g = 1.75(1)$ eV, calculated from the maximum of the distribution function E_V minus the full-width at half maximum F_V, is compared to the obtained indirect and direct transition energies of RSO, as given in Table 6 it is noticed that the indirect values lie close to each other. Compared to the literature value of 1 eV calculated for RSO[19] the experimental band-gap energy of $E_g = 1.75(1)$ eV shows a significant difference of 0.75 eV. This indicates that the early calculations most probably underestimated the optical band gap of RSO.

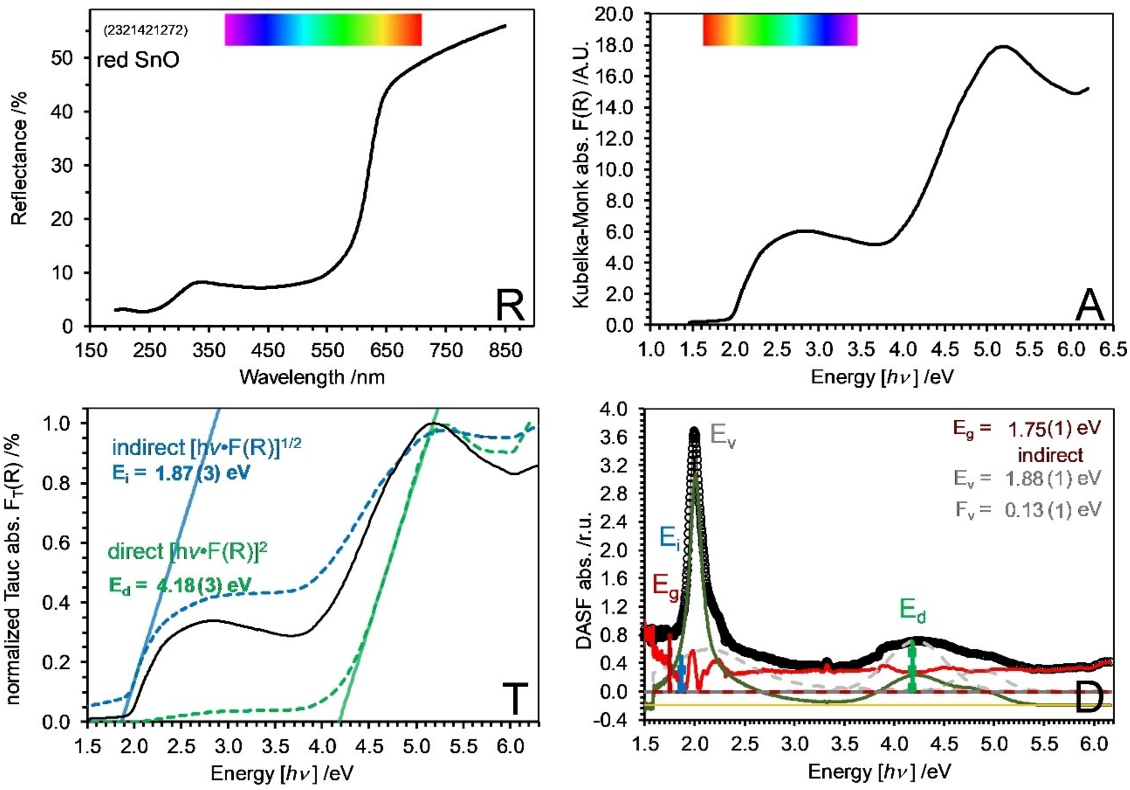

Figure 9. RATD plot of red tin(II)oxide with reflection spectrum (R), the absorption spectrum (A), the Tauc plot (T)and the DASF plot (D).

Table 6. Experimental and-gap energy (E_g) and transition type, DASF peak energy maximum (E_v), band-gap flatness parameter (F_v), and transition energies for the indirect (E_i) and direct (E_d) Tauc transition for red SnO (RSO), black tin(II) oxide (BSO) and white tin(IV) oxide (WSO).

Sample	Eg/eV	type	Ev/eV	Fv/eV	Ei/eV	Ed/eV
RSO	1.75(1)	indirect	1.88(1)	0.13(1)	1.87(3)	4.18(3)
BSO	2.85(7)	indirect	3.08(11)	0.23(3)	1.35(3)	3.90(3)
WSO	3.41(5)	indirect	3.57(7)	0.16(3)	3.72(3)	4.03(3)

3. Conclusion

Red tin(II) oxide (RSO) was synthesized using slightly a modified reflux method within three to four hours than that of Köhler et al.[19] reported to take as long as five days. A careful pH adjustment is of critical importance to synthesize the RSO using the method explained. It was repeatedly tested that the pH could only be adjusted within a narrow range below 5.3. The crystal structural data of RSO obtained from Rietveld refinements are in excellent agreement with those of Köhler et al..[19] Multi-tool temperature-dependent investigations unanimously support the phase transformation into blue-black tin(II) oxide (BSO) followed by the oxidation to white SnO_2 (WSO). The axial negative thermal expansion in the ***b***-direction leads to an overall zero thermal expansion coefficients at a given temperature range above room temperature. Temperature-dependent Raman spectroscopy supports the XRPD results for possible formation of either Sn_2O_3 or Sn_3O_4, which, however, requires thorough in situ investigations.

Acknowledgements

We gratefully thank the German science foundation (Deutsche Forschungsgemeinschaft, DFG) under grant number GE1981/14-1 for the financial support. The University of Bremen is cordially acknowledged for the technical and administrative supports. Open Access funding enabled and organized by Projekt DEAL.

Conflict of Interest

The authors declare no conflict of interest.

Data Availability Statement

The data that support the findings of this study are available from the corresponding author upon reasonable request.

Keywords: red tin(II) oxide · crystal structure · lone electron pair · thermal property · band gap

[1] H. Giefers, F. Porsch, G. Wortmann, *Solid State Ionics* **2005**, *176*, 199–207.
[2] Y. Hu, X. Yao, D. G. Schlom, S. Datta, K. Cho, *Chem. Mater.* **2021**, *33*, 212–225.
[3] S. E. Dunkle, J. R. Craig, J. D. Rimstidt, W. R. Lusardi, *The Canadian Mineralogist* **2003**, *41*, 659–669.
[4] P. Cerny, A.-M. Fransolet, T. S. Ercit, R. Chapman, *The Canadian Mineralogist* **1988**, *26*, 889–898.
[5] T. S. Ercit, P. Cerny, *The Canadian Mineralogist* **1988**, *26*, 899–903.
[6] T. S. Ercit, P. Cerny, J. Siivola, *N. Jb. Mineral. Mh.* **1987**, *6*, 249–252.
[7] A. Huda, C. T. Handoko, M. D. Bustan, B. Yudono, F. Gulo, *Mater. Lett.* **2018**, *211*, 293–295.
[8] J. D. Donaldson, W. Moser, W. B. Simpson, *Journal of the Chemical Society (Resumed)* **1961**, 839–841.
[9] E. L. Peltzer y Blancá, A. Svane, N. E. Christensen, C. O. Rodríguez, O. M. Cappannini, M. S. Moreno, *Phys. Rev. B* **1993**, *48*, 15712–15718.
[10] A. Seko, A. Togo, F. Oba, I. Tanaka, *Phys. Rev. Lett.* **2008**, *100*, 045702.
[11] G. Murken, M. Trömel, *Z. Anorg. Allg. Chem.* **1973**, *397*, 117–126.
[12] M. Becker, A. Polity, P. J. Klar, B. K. Meyer†, *physica status solidi (RRL) – Rapid Research Letters* **2015**, *9*, 326–330.
[13] C. Doornkamp, V. Ponec, *J. Mol. Catal. A* **2000**, *162*, 19–32.
[14] J.-H. Lee, Y.-J. You, M. A. Saeed, S. H. Kim, S.-H. Choi, S. Kim, S. Y. Lee, J.-S. Park, J. W. Shim, *NPG Asia Mater.* **2021**, *13*.
[15] S. Yu, L. Li, D. Xu, H. Dong, Y. Jin, *Thin Solid Films* **2014**, *562*, 501–505.
[16] I. Kocemba, S. Szafran, J. Rynkowski, T. Paryjczak, *Adsorpt. Sci. Technol.* **2002**, *20*, 897–905.
[17] M. Batzill, U. Diebold, *Prog. Surf. Sci.* **2005**, *79*, 47–154.
[18] G. R. Levi, *Il Nuovo Cimento (1924-1942)* **1924**, *1*, 335–344.
[19] J. Köhler, J. Tong, R. Dinnebier, A. Simon, *Z. Anorg. Allg. Chem.* **2012**, *638*, 1970–1975.
[20] I. D. Brown, *J. Solid State Chem.* **1974**, *11*, 214–233.
[21] J. S. Knyrim, F. M. Schappacher, R. Pöttgen, J. Schmedt auf der Günne, D. Johrendt, H. Huppertz, *Chem. Mater.* **2007**, *19*, 254–262.
[22] X. Wang, F. Liebau, **1996**, *211*, 437–439.
[23] M. Curti, T. M. Gesing, M. M. Murshed, T. Bredow, C. B. Mendive, *Z.Krist. – Cryst.Mat.* **2013**, *228*.
[24] J. R. Partington, W. Moser, *Nature* **1944**, *3916*, 643.
[25] F. W. Bury, J. R. Partington, *J. Chem. Soc. Trans.* **1922**, *121*, 1998–2004.
[26] L. A. Errico, *Physica B: Condensed Matter* **2007**, *389*, 140–144.
[27] R. W. Cheary, A. Coelho, *J. Appl. Crystallogr.* **1992**, *25*, 109–121.
[28] D. Richard, M. Ferrand, G. J. Kearley, *J. Neutron Res.* **1996**, *4*, 33–39.
[29] H. E. Swanson, R. K. Fuyat, *Standard X-ray Diffraction Powder Patterns, Vol. 539*, National Bureau of Standards Circular 539, U. S. Government Printing Office, Washington DC, **1953**.
[30] P. Boher, P. Garnier, J. R. Gavarri, A. W. Hewat, *J. Solid State Chem.* **1985**, *57*, 343–350.
[31] M. I. Kay, *Acta Crystallogr.* **1961**, *14*, 80–81.
[32] M. A. Mäki-Jaskari, T. T. Rantala, *Modell. Simul. Mater. Sci. Eng.* **2004**, *12*, 33–41.
[33] M. Project, *Vol. mvc-427*, Materials Project, materialsproject.org/materials/mvc-427/.
[34] M. Ali, P. Nagels, *physica status solidi b* **1967**, *21*, 113–116.
[35] H. R. Glyde, *J. Phys. Chem. Solids* **1967**, *28*, 2061–2065.
[36] P. Mishra, B. K. Pandey, *AIP Conference Proceedings 2220* **2020**, 020061(020061-020065).
[37] D. Schroeer, *Phys. Lett.* **1966**, *21*, 123–124.
[38] M. Wolpmann, L. Robben, T. M. Gesing, *Z. Krist.-Cryst. Mater.* **2022**, *237*, 39–50.
[39] A. K. Wong, R. Jones, J. G. Sparrow, *J. Phys. Chem. Solids* **1987**, *48*, 749–753.
[40] M. M. Murshed, C. B. Mendive, M. Curti, M. Šehović, A. Friedrich, M. Fischer, T. M. Gesing, *J. Solid State Chem.* **2015**, *229*, 87–96.
[41] M. M. Murshed, T. M. Gesing, *Mater. Res. Bull.* **2013**, *48*, 3284–3291.
[42] M. M. Murshed, C. B. Mendive, M. Curti, G. Nenert, P. E. Kalita, K. Lipinska, A. L. Cornelius, A. Huq, T. M. Gesing, *Mater. Res. Bull.* **2014**, *59*, 170–178.
[43] H. Hellwig, A. F. Goncharov, E. Gregoryanz, H.-k. Mao, R. J. Hemley, *Phys. Rev. B* **2003**, *67*, 174110.
[44] B. Eifert, M. Becker, C. T. Reindl, M. Giar, L. Zheng, A. Polity, Y. He, C. Heiliger, P. J. Klar, *Physical Review Materials* **2017**, *1*, 014602.
[45] D. Souri, Z. E. Tahan, *Applied Physics B* **2015**, *119*, 273–279.
[46] A. Kirsch, M. M. Murshed, M. Schowalter, A. Rosenauer, T. M. Gesing, *J. Phys. Chem. C* **2016**, *120*, 18831–18840.
[47] K. Ghosh, M. M. Murshed, M. Fischer, T. M. Gesing, *J. Am. Ceram. Soc.* **2021**, *105*, 728–741.
[48] T. M. Gesing, M. M. Murshed, S. Schuh, O. Thüringer, K. Krämer, T. Neudecker, C. B. Mendive, L. Robben, *J. Mater. Sci.* **2022**,*57*, 19280–19299.

Manuscript received: September 15, 2022
Revised manuscript received: November 18, 2022
Accepted manuscript online: November 27, 2022

Synthesis of MBO_3 (M = Al, Cr, Fe, In, Sc, Mn) compounds

Synthesis of MBO_3 phases was more difficult as it was discussed in the literature [1]. During this work, two types of syntheses were done. The first one was carried out in a corundum crucible whereas the other one was in platinum crucibles (**figure A7.1**). The hydrothermal synthesis routes left only the starting materials without any chemical reactions. Hence, two solid-state synthesis methods were prioritized and optimized, leading to, however, different results. Syntheses of $AlBO_3$, in both cases, resulted in colorless solid lumps at the bottom of the reaction container, which were too hard to grind (**figure A7.1**), and they were not used for further synthesis for mullite-type compounds.

For a target compound of $CrBO_3$, the hard green product was identified as starting Cr_2O_3 by X-ray diffraction Rietveld refinement (**figure A7.2**). The second synthesis route in a platinum crucible, however, yielded 40 % $CrBO_3$ and 60 % Cr_2O_3 (**figure A7.3**). The crystal structure of $CrBO_3$ is shown in **figure 7.1**, the sample color is shown in the Appendix in **figure A7.1** which crystallizes in space group $R\bar{3}c$ [2].

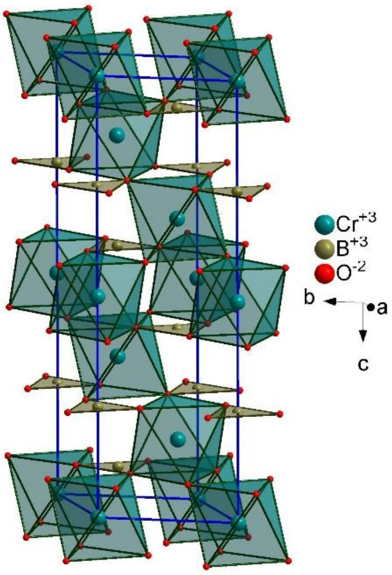

Figure 7.1: Crystal structure of $CrBO_3$ with CrO_6 octahedra and trigonal planar BO_3 groups [2].

The CrO_6 octahedral and trigonal planar BO_3 building blocks are interconnected, forming layers in the cell. As Cr_2O_3 seems to be more stable, the target $CrBO_3$ compound could not be found as phase single phase, and they could not be used as starting materials for mullite-type compounds.

Trial for the synthesis of $MnBO_3$ in an alumina crucible resulted in manganese dioxide only, which was found to be reacted with the crucible (**figure A7.1**). Hence, the choice of the crucible is important for this synthesis. The second synthesis was done with a platinum crucible, where a blackish MnB_4O_7 was obtained identified by the XRPD data Rietveld refinements (**figure A7.4**). Again, this investigation was not further continued. The Rietveld refinement of the mixture of Fe_2O_3 and H_3BO_3 in an alumina crucible results in a crystalline Fe_2O_3 (**figure A7.5**) and an amorphous boron-containing phase which could not be analyzed by XRPD. Compared to the synthesis in platinum crucibles where the product is bordeaux red, the observed phases were Fe_3BO_6 and Fe_2O_3 (**figure A7.6**) Both the synthesized products did not contain the expected $FeBO_3$ phase instead of the starting material Fe_2O_3. The second synthesized product was another iron borate which was not also further used. The procedure for colorless $ScBO_3$ was more promising as the result was for both routes 50 - 70 % $ScBO_3$ and the remaining material was Sc_2O_3 which did not react (**figure A7.7** and **figure A7.8**). Hence, in future work, this synthesis should be optimized to get a pure compound for the synthesis of mullite-type $SnScBO_4$ phase, which might be difficult as discussed in **chapter 2**. Colorless $InBO_3$ was synthesized in alumina crucibles with a purity of 100(2) % (**figure A7.9**), which crystallized in the same space group $R\overline{3}c$ as mentioned for $CrBO_3$ [3]. As In^{3+} has a larger cationic radius (80.0 pm) compared to Cr^{3+} (61.5 pm) [4] the cell volume as well as the lattice parameter were found to be larger for $InBO_3$ compared to $CrBO_3$. As this was the only synthesis that resulted in a pure metal borate, the second step was tried afterward.

A synthesis with $InBO_3$ and SnO either the commercial form or the beforehand explained red polymorph was tried in an open solid-state synthesis resulted in $InBO_3$ and SnO_2 with small amounts of In_2O_3 (**figure A7.10**). As such, the synthesis route was not used, where oxidation of Sn^{2+} to Sn^{4+} occurred along with formation of starting In_2O_3. These trails and the associated reaction products might be due to several reasons. Firstly, $InBO_3$ is quite stable whereas the oxidation from SnO (Sn^{2+}) to SnO_2 (Sn^{4+}) is at lower temperatures of about 830 K which was described elsewhere [5] about red SnO. This temperature is lower compared to the synthesis temperature and secondly, the system was chosen to be at ambient condition. Hence, the oxidation of tin was more likely instead of forming mullite-type structure. Another factor might be the size of the cationic radius which is discussed in **chapter 2**.

Reference

1. J.C. Joubert, T. Shirk, W.B. White, R. Roy, Stability, infrared spectrum and magnetic properties of $FeBO_3$, Materials Research Bulletin 3(8) (1968) 671-676. DOI:10.1016/0025-5408(68)90116-5
2. H. Schmidt, X-ray evidence for $CrCO_3$, VBO_3 and $TiBO_2$ with calcite structure, Acta Cryst. 17 (1964) 1080-1081.
3. J.R. Cox, D.A. Keszler, $InBO_3$, Acta Cryst. C50 (1994) 1857-1859. DOI:10.1107/S0108270194003999
4. R.D. Shannon, Revised effective ionic radii and systematic studies of interatomic distances, Acta Crystallographica A32 (1976) 751.
5. S. Wittmann, M.M. Murshed, T.M. Gesing, On red tin (II) oxide: temperature-dependent structural, spectroscopic, and thermogravimetric properties, Zeitschrift für anorganische und allgemeine Chemie 648(24) (2022) e202200311. DOI:10.1002/zaac.202200311

Chapter 8 – Synthesis of dolomite-type $MSn(BO_3)_2$ (M = Mn, Fe, Co, Ni)

As already mentioned earlier, the synthesis of mullite-type $SnMBO_4$ compounds is challenging due to a susceptible oxidation state of Sn(II) [1] at the reaction condition. If the M = Fe^{3+} or Mn^{3+} as in isostructural $PbFeBO_4$ and $PbMnBO_4$ phases [2-6], the yield is not the mullite-type compound but dolomite-compound $MSn(BO_3)_2$. Since the main goal was synthesis and characterization of mullite-type EMBO phases, several different synthesis routes were tried. Firstly, the sealed quartz tube method with reduced pressure for the synthesis to avoid the oxidation of Sn(II) results in the dolomite-type structures. Another idea was to use more reactive red SnO which should accelerate the formation of the mullite-type structures. However, these trails resulted in dolomite-type structures. In these syntheses, Sn^{2+} played the roles of a reducing agent to reduce M^{3+} to M^{2+} at the cost of itself oxidized into Sn^{4+}. A possible reason for this result is respective redox potentials of the reacting cations as mentioned in **chapter 1**. A detailed investigations of these dolomite-type materials are described in this chapter as a published work.

Synthesis, structural and spectroscopic investigations of dolomite-type $MSn(BO_3)_2$ with M = Mn, Fe, Co and Ni

Sarah Wittmann[1], M. Mangir Murshed[1,2*], Vitaliy Bilovol[3,4], Thorsten M. Gesing[1,2]

Reprinted with kind permission from DeGruyter and upon approval of the co-authors.

Published in: Z. Kristallogr. 238(5-6) (2023) 167-175.

https://www.degruyter.com/document/doi/10.1515/zkri-2023-0002/html

ORCID:

SW:	0000-0003-1404-3434
MMM:	0000-0002-9063-372X
VB:	0000-0002-3363-1840
TMG:	0000-0002-4119-2219

Sarah Wittmann, M. Mangir Murshed*, Vitaliy Bilovol and Thorsten M. Gesing

Synthesis, structural and spectroscopic investigations of dolomite-type $MSn(BO_3)_2$ with M = Mn, Fe, Co and Ni

https://doi.org/10.1515/zkri-2023-0002
Received January 6, 2023; accepted March 8, 2023;

Abstract: Dolomite-type $MSn(BO_3)_2$ phases for M = Mn, Fe, Co and Ni have been synthesized using solid-state synthesis carried out in sealed quartz tubes. X-ray powder diffraction data Rietveld refinements confirm the rhombohedral space group $R\bar{3}$ for all compositions. The change in unit-cell parameters follows the increasing nature of the radius of the M-cations. Both the MO_6 and SnO_6 octahedra are found to be quite regular. ^{119}Sn Mössbauer spectroscopy investigations complement the almost undistorted nature of the SnO_6 octahedra and the tetra-valent charge of the tin-atoms. Detailed vibrational features are described from the Raman and the FTIR spectral data collected at ambient conditions. The frequency shifts of some selective Raman and IR bands are explained in terms of the change of cationic sizes and the respective M–O bond distances. The UV/Vis diffuse reflectance data are analyzed using the RATD method, leading to direct bandgaps for all the investigated samples. The wide bandgap semiconductors (3 – 4 eV) show increasing transition energies with increasing cation sizes of the high-spin M-cations in the dolomite types.

Keywords: bandgap; crystal structure; dolomite; ^{119}Sn Mössbauer; vibrational property.

1 Introduction

Compounds showing the general chemical composition $M^{2+}M^{4+}(BO_3)_2$ crystallize in the structure type of anhydrous dolomite $CaMg(CO_3)_2$ which is known to widely occur in many natural deposits such as Dolomite Alps [1, 2] and in some Rocky Mountain regions [3, 4]. The dolomite-type nordenskiöldine $CaSn(BO_3)_2$ has been known as early as 1934 [5, 6], which is isostructural to calcite structure [7]. Members of nordenskiöldine were extended by producing their synthetic analogues such as $FeSn(BO_3)_2$, $MgSn(BO_3)_2$, $SrSn(BO_3)_2$, $BaSn(BO_3)_2$, $MnSn(BO_3)_2$, $CoSn(BO_3)_2$, $NiSn(BO_3)_2$ and $CdSn(BO_3)_2$ [8–10]. Of notes, the Mn-containing synthetic analogue was known to exist [11] more or less 20 years earlier than the mineral Tusionite $(Mn,Fe)Sn(BO_3)_2$ was discovered [3]. Till today most reports on $M^{2+}M^{4+}(BO_3)_2$ compounds are based on mineralogical aspects of either carbonate (CO_3^{2-}) or borate (BO_3^{3-}) subgroups [6, 12–14]. These compounds draw diverse attentions due to their thermal stability [12], magnetism [14], luminescence [7, 15] and crystal-chemical properties [8, 14]. Alkaline-earth metal stannic borates are known to serve as host lattice for efficient luminescent centers for Pb^{2+} [7] and Ti^{4+} [16–18] cations. For instance, $MZr(BO_3)_2$ (M = Ca, Sr and Ba) with low concentrated Pb^{2+} was demonstrated showing blue emission [7]. Moreover, $M^{2+}Sn^{4+}(BO_3)_2$ could be interesting model compounds to understand the structural response when larger CO_3^{2-} be replaced by smaller BO_3^{3-} groups along with cationic size and/or charge valence on the M^{2+} and Sn^{4+} sites. For example, in $MSn(BO_3)_2$, it is shown that the deviation between the MO_6 and SnO_6 octahedral size increases with increasing radius of the M-cations. As such, with relatively similar M–O and Sn–O bond distances it is not surprising that an enhanced distortion of the MnO_6 and CaO_6 octahedra enables a complete miscibility between the respective octahedral sites [19]. Representative member of the alkaline earth metal stannic borates such as $MnSn(BO_3)_2$ crystallizes in space group $R\bar{3}$ [10], as seen in Figure 1, where the $M^{2+}O_6$ and $Sn^{4+}O_6$ octahedra form layers in the *ab*-plane separated by the

---

Current address: Vitaliy Bilovol, Academic Centre for Materials and Nanotechnology, AGH University of Science and Technology, Al. Mickiewicza 30, 30-059 Krakow, Poland

---

***Corresponding author: M. Mangir Murshed**, Institute of Inorganic Chemistry and Crystallography, University of Bremen, Leobener Straße 7, D-28359 Bremen, Germany; and MAPEX Center for Materials and Processes, University of Bremen, Bibliothekstraße 1, D-28359 Bremen, Germany, E-mail: murshed@uni-bremen.de. https://orcid.org/0000-0002-9063-372X
Sarah Wittmann, Institute of Inorganic Chemistry and Crystallography, University of Bremen, Leobener Straße 7, D-28359 Bremen, Germany. https://orcid.org/0000-0003-1404-3434
Vitaliy Bilovol, Laboratorio de Sólidos Amorfos – INTECIN, University of Buenos Aires, Av. Paseo Colón 850-C1063ACV, Buenos Aires, Argentina. https://orcid.org/0000-0002-3363-1840
Thorsten M. Gesing, Institute of Inorganic Chemistry and Crystallography, University of Bremen, Leobener Straße 7, D-28359 Bremen, Germany; and MAPEX Center for Materials and Processes, University of Bremen, Bibliothekstraße 1, D-28359 Bremen, Germany. https://orcid.org/0000-0002-4119-2219

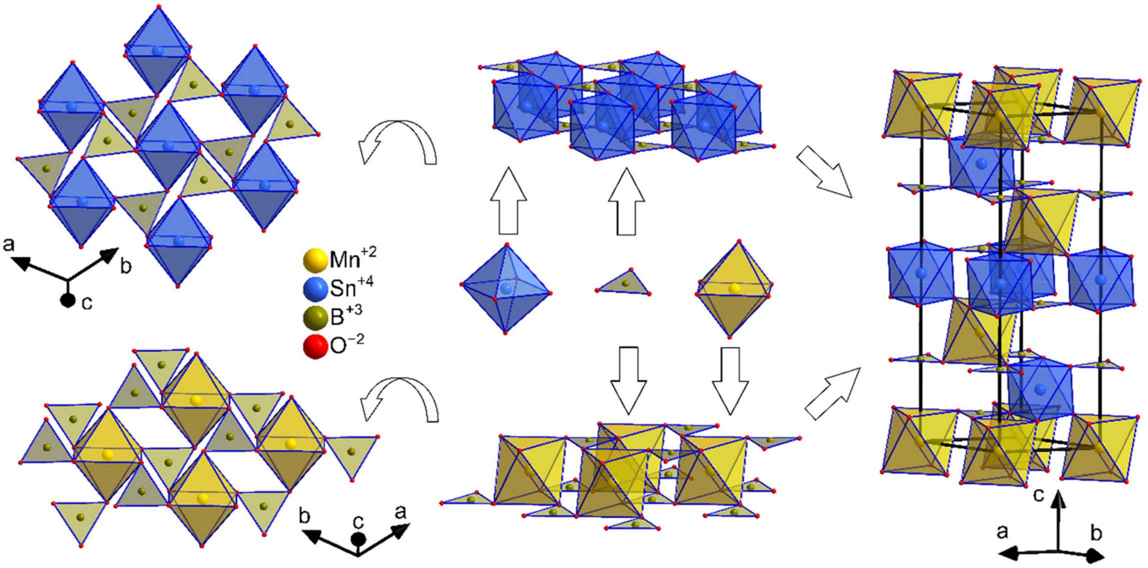

Figure 1: Representative crystal structure of $MnSn(BO_3)_2$, showing MnO_6 and SnO_6 octahedra and trigonal planar BO_3 building units, their orientations within a unit cell and the layers formed out of the primary building units.

trigonal planar BO_3 groups [20]. Due to rather a long Mn–Mn distance, the magnetic couplings via either Mn–Mn direct exchange or Mn–O–Mn super exchange seems to be weak. However, for a given disordering between the M^{2+} and M^{4+} sites the M–O–M distance may reduce to 380 pm for direct as well as super exchange, leading to spin-ordering in these phases. For $MnSn(BO_3)_2$, $FeSn(BO_3)_2$, $CoSn(BO_3)_2$ and $NiSn(BO_3)_2$ till now only the lattice parameters are reported [10]. Whereas these compounds were produced by conventional solid-state methods, and the oxidation state of tin (Sn^{2+}) is susceptible to disproportionation, each of their phase purity might be an issue and their structural information as well. The crystal structure of $MnSn(BO_3)_2$ was reported from a single crystal of the mineral (Mn, Fe, Ca, W)$Sn(BO_3)_2$ along with trace amounts of other cations [4]. From this point of view, this report bears particular importance in producing phase-pure samples followed by their structural characterizations using X-ray powder diffraction (XRPD) and spectroscopic details using Raman, FTIR, UV/Vis and ^{119}Sn Mössbauer spectroscopies.

2 Experimental

2.1 Synthesis

Due to susceptible oxidation of SnO to SnO_2 and the simultaneous reduction of M_2O_3 (M = Mn, Fe) at reaction temperature in open condition, we used a closed solid state synthesis route. Due to higher thermal stability of SnO_2, each synthesis was carried out using tin(II) oxide that oxidized into required Sn^{4+} in the phase. Stoichiometric amounts of Sn (powder), SnO, either M_2O_3 (M = Mn, Fe) or M′O (M′ = Co, Ni) and B_2O_3 were dried at 473 K overnight, mixed and put into a quartz tube which was also preheated at 1073 K for about 15 h. The mixture was further heated at 473 K for 2 h to remove the absorbed moisture. The internal pressure of the quartz tube was then reduced to 10^{-7} MPa. During the dynamic vacuum process, the tube was sealed. The sample containing tubes were placed into an oven and heated at 1023 K for three days with a heating and cooling rate of 200 K/h each to obtain the microcrystalline powder.

2.2 X-ray diffraction

Diffraction measurements were carried out on a Stoe Stadi-MP diffractometer (Stoe & Cie. GmbH, Darmstadt, Germany) in Debye-Scherrer geometry. The samples were placed in a borosilicate glass capillary of 0.5 mm outer diameter and 0.01 mm wall thickness. Homogeneous irradiation of the powders was further achieved through sample spinning. Ge(111) monochromatized MoKα_1 radiation was used in combination with a Mythen-1K detector. Data were collected at ambient conditions between 7.00° and 80.98° 2θ with a step size of 0.005° and a data collection time of 40 s/step. The fundamental parameter approach, where the fundamental parameters were fitted against a LaB6 standard material, was applied for the Rietveld refinements using "Diffrac^{Plus} Topas 6" software (Bruker AXS GmbH, Karlsruhe, Germany). For this purpose, the starting atomic coordinates were taken from the single crystal structural data [5] available with the ICSD reference code 28266. During the Rietveld refinements, the background, unit-cell parameters, atomic coordinates, and isotropic displacement parameters were optimized. Parameters associated with the average crystallite-size and micro-strain were concomitantly refined for the description of the reflection profiles of each phase.

2.3 Spectroscopy

2.3.1 Fourier transform infrared (FTIR): FTIR data were collected on a Bruker VERTEX 80v spectrometer using the standard KBr method (2 mg sample in 200 mg KBr) in the mid-infrared range between 370 and 4000 cm^{-1}. All IR spectra are plotted in absorption units (A.U.) according to $-\ln(I/I_O)$, where I and I_O refer to transmitted intensity of the sample plus KBr and pure KBr disc, respectively.

2.3.2 Raman: Raman spectra were recorded on a LabRam ARAMIS (Horiba Jobin Yvon) micro-Raman spectrometer equipped with laser working at 633 nm and less than 20 mW. The use of a 50× objective (Olympus) with a numerical aperture of 0.55 provided a focus spot of about 2 μm diameter when closing the confocal hole to 200 μm. Raman spectra were collected in the range of 100–1500 cm^{-1} with a spectral resolution of approximately 1.2 cm^{-1} using a grating of 1800 grooves/mm and a thermoelectrically cooled CCD detector (Synapse, 1024 × 256 pixels). The spectral position of the spectrometer was calibrated against the peak maximum at 520.7 ± 0.1 cm^{-1} of a Si wafer. The linearity of the spectrometer was adjusted against the emission lines of a neon lamp. Raman peak maxima were obtained from fitted Pseudo-Voigt profiles.

2.3.3 UV/Vis: UV/Vis diffuse reflectance spectra were collected on a Shimadzu UV/Vis spectrophotometer UV-2600 equipped with an ISR-2600 plus two-detector integrating sphere. Barium sulfate was used for the background measurements. The reflection spectrum was measured over the photon wavelength range of 190–850 nm in 1 nm steps. The bandgap energies and the transition types were determined using the RATD method [21].

2.3.4 ^{119}Sn Mössbauer: Samples were analyzed by Mössbauer spectroscopy using data collected at room temperature where the γ-radiation of 23.875 keV from a $Ca^{119m}SnO_3$ source in transition geometry was used. The isomer shifts are reported relative to $CaSnO_3$ at room temperature. Mössbauer spectra were recorded by a standard conventional acceleration spectrometer with a radioactive source of 5 mCi of nominal activity. The calibration was carried out employing the ^{57}Fe 14.4 keV γ-radiation from a ^{57}Co(Rh) source with sodium nitroprusside as absorber. The experimental data were fitted to Lorentzian profiles by least-squares method using the NORMOS 90 program [22].

2.4 Scanning electron microscopy (SEM)

SEM was carried out on a JSM-6510 (JEOL GmbH, Munich, Germany). To obtain quality data, samples were sputtered with a thin film of gold having a thickness of approx. 10 nm. Micrographs were taken using an acceleration energy of 20 KV and a working distance of 15 mm.

3 Results and discussion

The polycrystalline samples of violet $CoSn(BO_3)_2$, grey $FeSn(BO_3)_2$ and $NiSn(BO_3)_2$, and colorless $MnSn(BO_3)_2$ are shown in Figure S1 (Supplementary Material). The degree of crystallinity was obtained to be 80% and 95% for $CoSn(BO_3)_2$ and $MnSn(BO_3)_2$, respectively. $MnSn(BO_3)_2$ was found to be phase pure based on the Rietveld refinements, whereas the other three samples contain minor phases such as Ni_3Sn_2 (20 wt%) and SnO_2 (9 wt%) for $NiSn(BO_3)_2$, CoSn (2 wt%) and Sn (3 wt%) for $CoSn(BO_3)_2$ and elemental Sn (2 wt%) for $FeSn(BO_3)_2$. While the appearance of starting elemental Sn may not be surprising, the intermetallic CoSn and Ni_3Sn_2 might form as the respective formation temperature of ca. 473 and 1073 K could be easily reached within the sealed tube synthesis condition. Moreover, the redox potentials of Ni(II) to Ni(0) and Co(II) to Co(0) support the formation of the Sn-containing intermetallics via oxidation of SnO to Sn(IV). The SEM micrographs, as shown in Figure 2, depict plate like morphology of each sample with an average dimension of about 1–2 μm. This appearance well correlates the shorter *a*- and longer *c*-lattice parameters, where the **c**-dimension lies perpendicular to the plate plane. Indeed, the hexagonal shape of the crystals supports this assumption.

XRPD data Rietveld refinements confirm that all the investigated $MSn(BO_3)_2$ compounds crystallize in the dolomite-type structure with space group $R\overline{3}$. A representative Rietveld plot of $MnSn(BO_3)_2$ is shown in Figure 3, and those of the other phases in Figures S2–S4. Details of the crystal structural information are given in Tables 1 and S1. A comparative view of the metric parameters of the compounds is listed in Table 2. The trend of each metric parameter of the compounds can be explained in terms of their respective cationic sizes (Mn^{2+} = 97 pm (hs), Ni^{2+} = 83 pm [23]) as the geometry of the SnO_6 and BO_3 polyhedra do not significantly change, as can be compared in Table 3. Indeed, both the B–O and Sn–O distances remain close to an averaged value of 136.0(4) and 206.3(5) pm, respectively.

The larger M-cation leads to larger MO_6 octahedral volume, resulting in increasing the metric parameters. The trend of the *a*-lattice parameters is found to be linear for both low-spin and high-spin configuration of the M-cations, as shown in Figure S5. On the other hand, the *c*-lattice parameter lies close to the linear trend of the high-spin cationic size, but abruptly departs from the low-spin trendline. Since all the metric parameters (Figure S5) show a linear trend with the respect high-spin cationic size, we therefore presume that the Mn^{2+}, Fe^{2+} and the Co^{2+} cations in the respective MO_6 octahedra keep high-spin configurations [24].

With increasing the size of the M-cation the deviation between the M–O and Sn–O distances increases whereas the geometric distortions of the respective MO_6 and SnO_6 octahedra are insignificant. Due to symmetry reasons both the SnO_6 and MO_6 octahedra comprise of respective Sn–O and the M–O distances identical within the estimated uncertainty, leading to negligible bond distortion. However, a

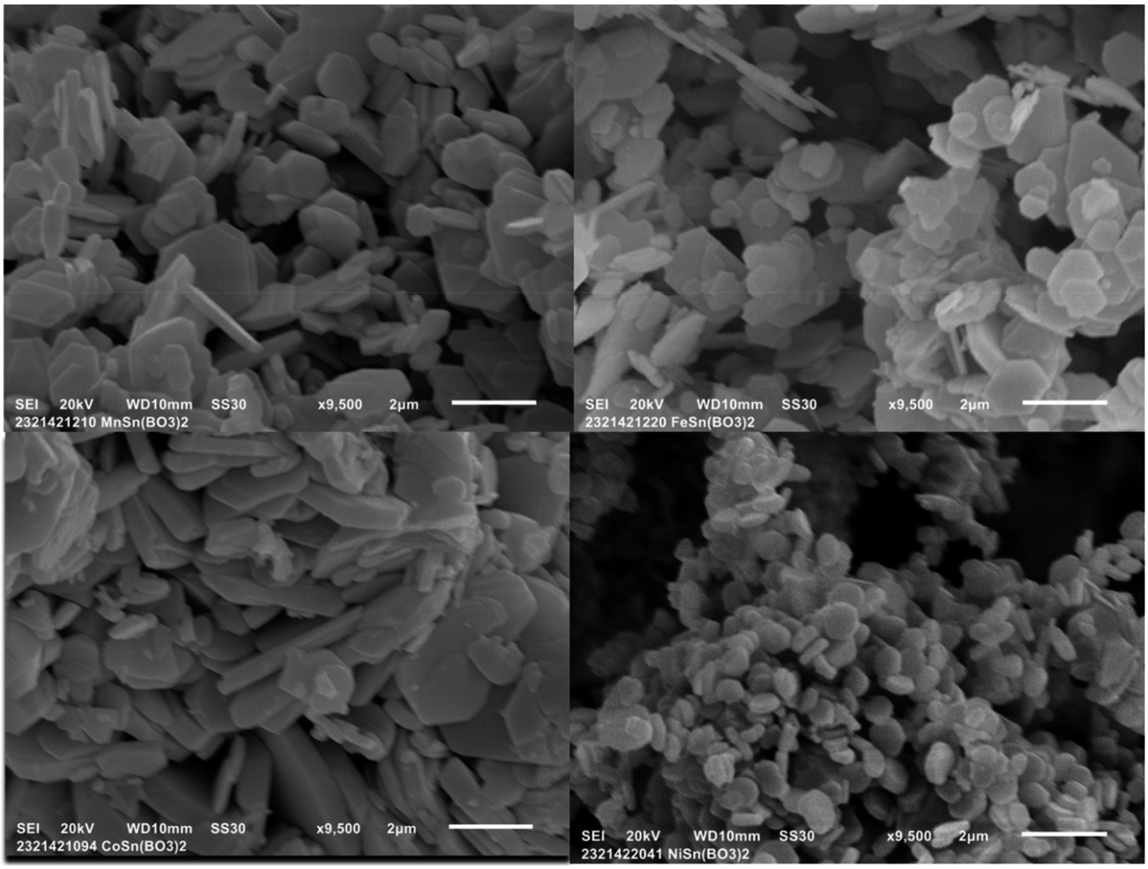

Figure 2: SEM images of $MSn(BO_3)_2$ (M = Mn, Fe, Ni and Co) polycrystalline powders.

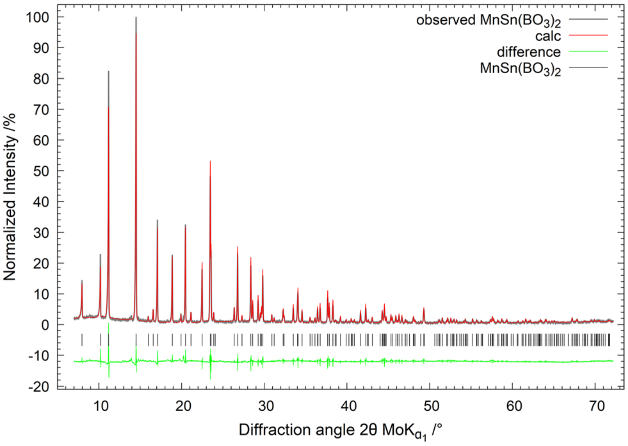

Figure 3: Representative Rietveld plot of $MnSn(BO_3)_2$, where the vertical bars show the respective Bragg peak position (*hkl*-tics).

Table 1: XRPD Rietveld refined structural parameters of $MnSn(BO_3)_2$ in the hexagonal settings of the space group $R\overline{3}$.

Atom	Occ.	Site	*x*	*y*	*z*	$B_{iso}/10^{-4}$ pm^2
Mn	1	3*a*	0	0	0	0.47(2)
Sn	1	3*b*	0	0	½	0.41(1)
B	1	6*c*	0	0	0.245(1)	0.30(9)
O	1	18*f*	0.0137(7)	0.2890(6)	0.2457(2)	0.68(5)

slight angle variance can be seen, which is higher in the SnO_6 octahedra than that in the MO_6 octahedra (Table S2). The planar BO_3 groups show usual rigidity, keeping an averaged B–O distance of 139.1(3) pm. The bond-valence calculations suggest that the cations keep their oxidation state close to the respective formal values (Table 3). Of notes, the Ni-containing compound exhibits over-bonding and under-bonding natures of tin and nickel, respectively. Since tin and nickel have similar cationic radii of 69 pm in a given octahedral coordination [23], an inversion between SnO_6 and NiO_6 octahedra would not be surprising, as known from spinel-type compounds [25, 26]. Based on this assumption, Rietveld refinements result in an exchange between Ni^{2+} and Sn^{4+} sites of approximately 1%, which is only slightly higher than the respective estimated uncertainty. It is known from the spinel phase such as $ZnFe_2O_4$ that the degree of inversion (x in $(Zn_{1-x}Fe_x)(Fe_{1-1/2x}Zn_{1/2x})_2O_4$) is temperature dependent,

Table 2: Powder X-ray data Rietveld refined parameters of $MSn(BO_3)_2$ along with average crystallite size (ACS), microstrain (MS) and the radius (r_M) of the M^{2+} cations in MO_6 octahedra.

Compound	$MnSn(BO_3)_2$	$FeSn(BO_3)_2$	$CoSn(BO_3)_2$	$NiSn(BO_3)_2$
Formula weight/g mol^{-1}	291.264	292.171	295.259	295.019
Temperature/ K	296(2)	296(2)	296(2)	296(2)
Instrument, radiation	Stoe MP, $MoK_{\alpha1}$	Stoe MP, $MoK_{\alpha1}$	Stoe MP, $MoK_{\alpha1}$	Stoe MP, $MoK_{\alpha1}$
Geometry	DS, glass capillary	DS, glass capillary	DS, glass capillary	DS, glass capillary
Space group	$R\bar{3}$	$R\bar{3}$	$R\bar{3}$	$R\bar{3}$
a/pm	477.37(2)	473.52(4)	472.24(2)	469.03(3)
c/pm	1530.48(2)	1512.62(2)	1490.79(5)	1478.12(3)
$V/10^6$ pm^3	302.05(4)	293.72(3)	287.92(2)	282.33(2)
r_M/pm [23]	97	92	89	83
ACS/ nm	210.05(3)	222.82(2)	298.22(7)	271.40(2)
MS/ %	0.2013(2)	0.1071(4)	0.1615(3)	0.2121(1)
D_{calc} (g/ cm^3)	4.58(4)	4.96(2)	4.87(4)	4.97(5)
R_{wp}/ %	9.63	7.45	9.98	10.42
GOF on F^2	6.31	4.78	2.43	4.41

Table 3: Selective bond distances, octahedral volume (V_{oct}) and bond-valence sum (BVS) of the cations calculated from the crystal structure data of the $MSn(BO_3)_2$ compounds.

Compound	Bond distance/pm				
	Sn–O	M–O	<B–O>	Sn–M	M–M
$MnSn(BO_3)_2$	207.1(4)	222.2(3)	134.8(2)	375.5(1)	477.4(2)
$FeSn(BO_3)_2$	207.1(6)	211.9(8)	138.5(4)	371.8(3)	473.5(4)
$CoSn(BO_3)_2$	206.0(4)	214.3(6)	135.5(5)	368.9(3)	472.2(3)
$NiSn(BO_3)_2$	205.1(6)	212.0(9)	135.2(8)	366.3(4)	469.6(5)

Compound	$V_{Oct}/10^6$ pm^3		BVS/v.u.		
	MO_6	SnO_6	B	Sn	M
$MnSn(BO_3)_2$	14.59(1)	11.85(1)	2.87(1)	4.08(1)	1.93(1)
$FeSn(BO_3)_2$	12.58(2)	11.84(1)	2.88(1)	3.88(1)	2.00(1)
$CoSn(BO_3)_2$	13.09(3)	11.65(2)	2.82(1)	3.93(1)	1.97(1)
$NiSn(BO_3)_2$	12.69(3)	11.49(2)	2.81(1)	4.25(1)	1.80(1)

which starts at 700 K ($x > 0$) and increases to $x = 0.35$ up to 1400 K. As such, temperature-dependent diffraction up to the decomposition/melting temperatures can better understand the possible inversion between these two sites. Although the synthesis temperature of $NiSn(BO_3)_2$ dolomite phases was 1023 K, an inversion of only 1% may not explain the respective under-bonding and the over-bonding nature of tin and nickel, respectively. However, the vibrational spectroscopic analysis sheds light on the issue (see below).

Factor group analysis for the dolomite-type $MSn(BO_3)_2$ structures results in 30 vibrational modes ($4A_g + 6A_u + 4^1E_g + 6^1E_u + 4^2E_g + 6^2E_u$). Of them, 12 modes are Raman active ($4A_g + 4^1E_g + 4^2E_g$), 15 are IR active ($5A_u + 5^1E_u + 5^2E_u$) and three ($A_u + {}^1E_u + {}^2E_u$) belong to acoustic modes. Figure 4 depicts the stack plots of Raman and FTIR spectra of the samples, and the respective fitted component peak maxima are given in Table 4.

Raman bands with frequencies between 240 and 400 cm^{-1} belong to lattice modes [27]. Each mode shows a linear trend with respect to the high-spin cationic size of the M-cation, as shown in Figure S6. Bands in the region of 400–470 cm^{-1} can be assigned to M–O stretching vibrations. From the analogy of cassiterite (SnO_2) [28] Raman band resolved at 474.4(4) cm^{-1} in $MnSn(BO_3)_2$ can be assigned to the A_g mode of the SnO_6 octahedra, which also shifts to higher wavenumber values (Table 4) with decreasing the cationic radius (Figure S6). Data departed from the trendline may be due to substantial change of the M–O force constants (ionicity/covalency) of the respective bonds. The lower value of the slope can be explained in terms of the modicum change of the ionicity between the M–O bonds. The planar BO_3 group possesses D_{3h} symmetry; thus can be characterized by nonplanar nondegenerate (ν_2), antisymmetric degenerate (ν_3), and deformational degenerate (ν_4) vibrations and the corresponding observed frequencies at 1235–1280 cm^{-1} and 665 cm^{-1} are assigned, respectively, for $MnSn(BO_3)_2$. The mode observed at about 946.1(2) cm^{-1} can be assigned to the B–O symmetric stretching (ν_1) which slightly shifts to lower wavenumber of 942.9(1), 941.0(4) and 944.3(1) cm^{-1}, respectively, for the Fe-, Co- and Ni-containing phases. An additional shoulder can be resolved at 971.7(5) cm^{-1} for the Mn-containing sample, indicating more than one types of B–O bond distances. Splitting of the ν_3 modes either to sharp components or to broadening of the spectral intensity can be seen between 1200 and 1500 cm^{-1} both for the Raman and FTIR spectra. The sharp intense Raman feature observed at

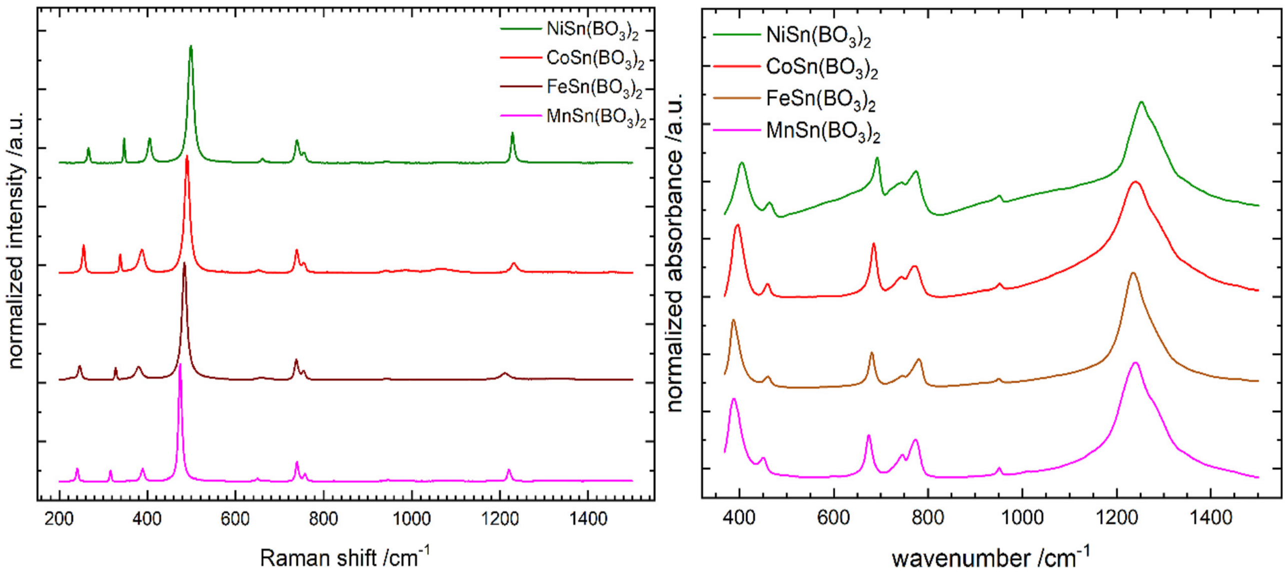

Figure 4: Stack plots of Raman and FTIR spectra of $MSn(BO_3)_2$ dolomite-type compounds.

Table 4: Raman and FTIR spectra fit peak maxima/cm^{-1} of $MSn(BO_3)_2$.

Raman				FTIR			
Mn	**Fe**	**Co**	**Ni**	**Mn**	**Fe**	**Co**	**Ni**
240.9(7)	246.3(4)	255.2(2)	266.3(7)	–	–	–	–
316.4(1)	328.1(7)	338.4(9)	347.3(8)	–	–	–	–
389.1(6)	380.3(5)	387.5(1)	397.8(9)	389.5(1)	389.6(2)	395.9(2)	405.0(3)
474.4(4)	484.1(3)	490.1(7)	498.5(1)	449.7(1)	459.4(1)	458.6(3)	462.4(2)
649.8(9)	661.1(5)	652.8(8)	661.6(2)	674.6(2)	680.6(1)	685.0(1)	691.7(2)
739.4(2)	737.8(3)	738.9(8)	739.4(1)	745.3(1)	745.1(2)	740.9(1)	740.1(3)
757.3(9)	754.0(5)	754.5(3)	754.9(3)	772.4(2)	779.7(2)	772.8(2)	774.2(3)
946.1(2)	942.9(1)	941.0(4)	944.3(1)	950.7(2)	949.7(1)	951.4(1)	949.6(4)
971.7(5)	–	–	–	–	–	–	–
994.8(1)	–	*984.3(3)*	–	–	–	–	–
1084(1)	–	*1069(1)*	–	*1009(2)*	–	–	–
1221(1)	1212(1)	1232(2)	1229(2)	1234(3)	1233(4)	1237(2)	1247(2)
1324(3)	*1329(5)*	*1324(3)*	–	1383(4)	1285(5)	1382(6)	1386(3)
1446(5)	*1454(4)*	*1456(5)*	*1452(5)*	–	–	–	–

Values in italic numbers refer to either overtone, combinations, or from glass/impurities.

1221(1) cm^{-1} for $MnSn(BO_3)_2$ shifts to 1212(1), 1232(2) and 1229(2) cm^{-1}, respectively, for the Fe-, Co- and Ni-containing phases. Two FTIR bands can be resolved in this high-frequency region (Table 4). Relatively two broad Raman peaks are observed at around 1330(5) and 1445(5) cm^{-1}, which can be assigned to either shorter B–O distances in the possible glasses formed with the quartz [29] or highly distorted BO_3 groups which could not be identified from the averaged structure obtained from the XRPD data. For instance, for the out-of-plane vibration, both the types of B–O bond lengths and how far the averaged B-position sits play roles. As such, B locates at about 4, 5, 3 and 2 pm above the O3 plane for the Mn-, Fe-, Co- and Ni-phases, respectively. Moreover, the distribution of ^{11}B and ^{10}B should also be considered for the additional spectral intensity in the high-frequency region.

For a purely symmetric BO_3 group the symmetric B–O stretching must be infrared inactive due lack of dipole moment. However, it's presence at around 950 cm^{-1} along with a broad feature between 910 and 955 cm^{-1} in the FTIR spectra (Figure 4) confirms that the D_{3h} symmetry of BO_3 reduces to C_s driven by the local distortion. Indeed, we observed a slight deviation (3.7(2) pm) between two types of B–O bond lengths in the O3-scalene triangle, where the

B-atom locates slightly above the O3 plane. Although factor group allows for 12 infrared modes, each spectrum requires only 10 bands within the measured region (Table 4) due to strong overlapping between the absorbed regions. Again, the splitting of each of the ν_1 and ν_3 modes in the infrared spectra can be explained due to ^{10}B and ^{11}B isotopic substitution and the integrated intensity at 1234 and 1277 cm^{-1} results in 25(3) and 75(3)% ^{11}B and ^{10}B, respectively, which remains close to the natural abundance of boron.

With the knowledge of the RATD analysis method [21] for the UV/Vis data the nature of transition can be figured out as shown in Figure 5 and Figures S7–S9. All the investigated samples possess a direct bandgap. $MnSn(BO_3)_2$ requires a bandgap transition energy of 3.97(4) eV, $FeSn(BO_3)_2$ of 3.93(4) eV, $CoSn(BO_3)_2$ of 3.86(2) eV, and $NiSn(BO_3)_2$ of 3.67(5) eV. That is, the observed bandgaps lie between 3 and 4 eV, which is in the range of wide bandgap semiconductors. For nickel containing compound, the bandgap deviation might be an effect of the likely high-spin configurations of the other three metal cations. Since the crystal structure of all samples is similar, and the geometry of SnO_6 and the BO_3 does not significantly change, the associated bandgaps are the characteristic crystal-chemical features of the M-cations. Due to high reflectance in the visible range for $MnSn(BO_3)_2$, the sample is colorless. Alike, the grey color of the samples $NiSn(BO_3)_2$ and $FeSn(BO_3)_2$ can be explained. However, the violet color of $CoSn(BO_3)_2$ is due to absorption between the green and blue range, leading to complemental color as the sample-color.

The ^{119}Sn Mössbauer spectroscopy technique is well known to better understand the local environment of Sn-atom in the Sn-containing solid samples. The local environment is usually expressed by means of the hyperfine interactions of tin atoms in a given solid matrix. The ^{119}Sn Mössbauer spectra of $FeSn(BO_3)_2$ and $MnSn(BO_3)_2$ samples are shown in Figure 6, and the fitted values are listed in Table 5. Both these spectra are qualitatively similar consisting of two singlets: a dominating one centered at almost 0 mm/s, and the other close to 2 mm/s with moderate intensity. A single peak is associated with a ^{119}Sn nucleus located in high-symmetry environments in the samples. In other words, there is no electric field gradient around the Sn

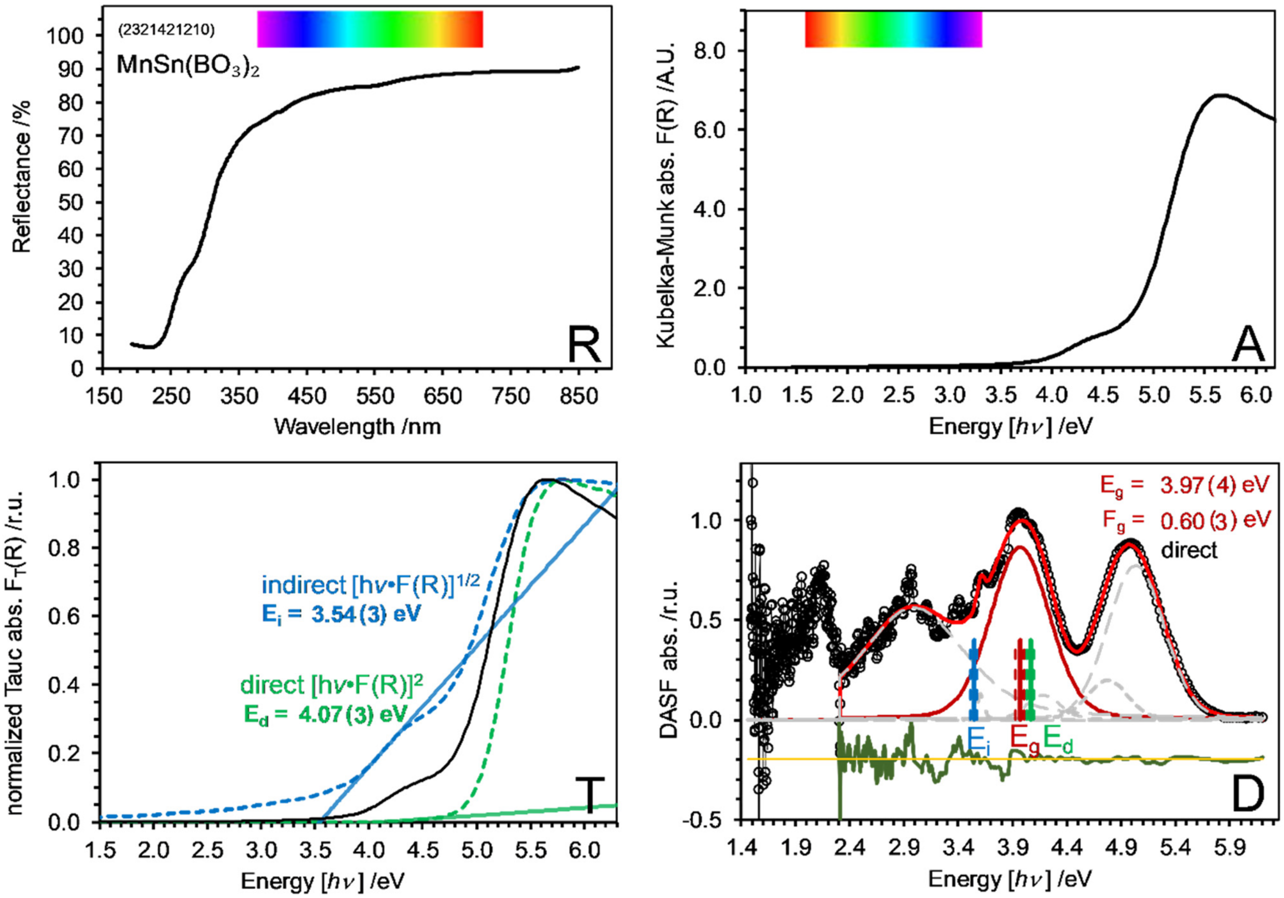

Figure 5: Representative RATD plot for $MnSn(BO_3)_2$.

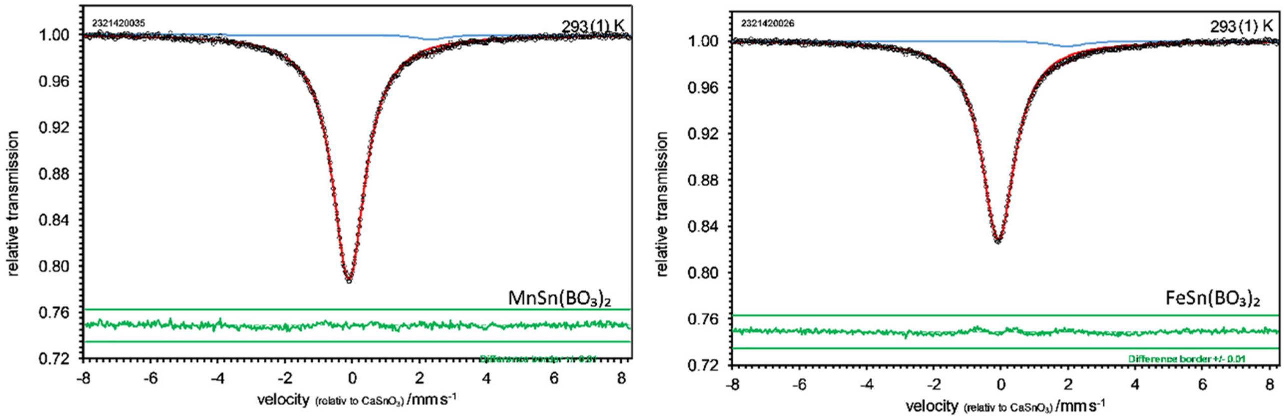

Figure 6: ^{119}Sn Mössbauer spectra of $MnSn(BO_3)_2$ and $FeSn(BO_3)_2$, showing both the observed (filled cycles) and the fit data (solid lines).

Table 5: Hyperfine fitted parameters of the ^{119}Sn Mössbauer spectra of $MnSn(BO_3)_2$ and $FeSn(BO_3)_2$ samples; δ: isomer shift; Δ: quadrupole splitting; Γ: absorber linewidth.

	$MnSn(BO_3)_2$		$FeSn(BO_3)_2$	
δ/(mm/s)	−0.10(1)	2.34(5)	−0.08(1)	1.96(4)
Δ/(mm/s)	0		0	
Γ/(mm/s)		1.20(2)		1.20(2)

nucleus that justifies the absence of quadrupole splitting (Δ = 0 mm/s) for nearly a symmetrical local environment. The isomer shift (δ), which is proportional to the electron charge density at a Sn nucleus, giving information about the oxidation state of Sn in the sample. The δ-values close to 0 mm/s relative to the source unambiguously support the 4+ oxidation state of tin [30]. Since δ-value depends on bond lengths (Sn–O), the almost equal δ-values (within the estimated uncertainties) of the dominant components of the $FeSn(BO_3)_2$ and $MnSn(BO_3)_2$ compounds indicate the similar Sn–O bond lengths. This is in an excellent agreement with the Sn–O bond distances calculated for from the XRPD data (Table 3). The small interaction (absorption area of about 3%) with an isomer shift of 1.96 mm/s for $FeSn(BO_3)_2$ may be consistent with the presence of elemental Sn [30] detected by the XRPD (Figure S3). In case of $MnSn(BO_3)_2$, for the small interaction (absorption area of about 2%) with an isomer shift of 2.36 mm/s can also be attributed to a trace amount of $MnSn_2$ [31].

4 Conclusions

Dolomite-type compounds were successfully synthesized with a solid-state method and a sintering time of three days. For all four materials of $MSn(BO_3)_2$ (M = Mn, Fe, Co and Ni), the suggested starting materials such as tin(II)oxide and tin are of critical importance to succeed in the synthesis, where Sn^{2+} oxidizes into Sn^{4+} and M^{3+} reduces to M^{2+} in the case of Mn- and Fe-containing samples. The structural features obtained from the X-ray powder diffraction are complemented by the Raman, FTIR and the ^{119}Sn Mössbauer spectroscopic data. All four synthesized compounds are isostructural with slightly different lattice parameters which is predominantly determined by the larger M^{2+}-cation. The cationic sizes influence the Raman and IR spectral frequencies of some modes. The liner trends of the metric parameters and the Raman shifts suggest for the high-spin configuration of the M^{2+} cations (M = Mn, Fe and Co). An inversion of nickel and tin on their octahedral positions could neither be excluded nor be confirmed from the investigated structural and spectroscopic data. The RATD [21] has been shown to be an effective analysis method for a deeper understating of the indirect transitions and the bandgap energies of the dolomite-type compounds using the UV/Vis diffuse reflectance spectroscopy.

Acknowledgements: We gratefully thank the German Science Foundation (Deutsche Forschungsgemeinschaft, DFG) under grant number GE1981/14-1 for the financial support and for large instrument support within grant INST144/435-1FUGG and INST144/458-1FUGG. The University of Bremen is cordially acknowledged for the technical and administrative supports. V.B. is highly thankful to INTECIN (CONICET) for the partial financial supports. The Universidad de Buenos Aires (UBACyT 20020190200037BA) is also acknowledged.

Author contributions: All the authors have accepted responsibility for the entire content of this submitted manuscript and approved submission.

Research funding: This work was funded by the German Science Foundation (Deutsche Forschungsgemeinschaft, DFG) under grant number GE1981/14-1 for the financial support and for large instrument support within grant INST144/435-1FUGG and INST144/458-1FUGG.

Conflict of interest statement: The authors declare no conflicts of interest regarding this article.

References

1. Hermann J., Troitzsch U., Scott D. Experimental subsolidus phase relations in the system $CaCO_3$–$CaMg(CO_3)_2$ up to 6.5 GPa and implications for subducted marbles. *Contrib. Mineral. Petrol.* 2016, *171*, 84.
2. Bickle M. J., Powell R. Calcite-dolomite geothermometry for iron-bearing carbonates. *Contrib. Mineral. Petrol.* 1977, *59*, 281–292.
3. Konovalenko S. I., Voloshin A. V., Pakhomovskiy Y. A., Anen'yev S. S., Perlina G. A., Rogachev D. L., Kuznetsov V. Y. Tusionite, $MnSn(BO_3)_2$, a new borate from granite pegmatite of southwestern pamir. *Int. Geol. Rev.* 1984, *26*, 481–485.
4. Cooper M., Hawthorne F. C., Novak M. The crystal structure of tusionite, $Mn^{2+}Sn^{4+}(BO_3)_2$, a dolomite-structure borate. *Can. Mineral.* 1994, *32*, 903–907.
5. Vicat J., Aléonard S. Etude de borates $MeMe'(BO_3)_2$ de structure dolomite. *Mater. Res. Bull.* 1968, *3*, 611–620.
6. Mirakov M. A., Pautov L. A., Shodibekov M. A., Plechov P. Y., Karpenko V. Y. A new scandium-bearing variety of tusionite from the Eastern Pamirs (Tajikistan). *Geol. Ore Deposits* 2020, *61*, 809–817.
7. Blasse G., Sas S. J. M., Smit W. M. A., Konijnendijk W. L. Luminescent materials with dolomite structure. *Mater. Chem. Phys.* 1986, *14*, 253–258.
8. Suknev V. S., Diman E. N. The infrared spectra of norde nskiöldine and its analogs. *J. Appl. Spectrosc.* 1969, *10*, 234–236.
9. Pottier M.-J. Spectre vibrationnel des orthoborates de type dolomite – l'influence des couplage vibrationnels sur la vibration de déformation v_2 des groupments isotopiques $^{10}BO_3$ et $^{11}BO_3$. *Spectrochim. Acta* 1976, *33*, 625–630.
10. Aléonard S., Vicat J. Borates de structure dolomie. *Bull. Soc. Fr. Minéral. Cristallogr.* 1966, *89*, 271–272.
11. Suknev V. S., Diman E. N. The infrared spectra of nordenskiöldine and its analogs. *Zh. Prikl. Spektrosk.* 1969, *10*, 326–328.
12. Bayer G. Thermal expansion anisotropy of dolomite-type borates $Me^{2+}Me^{4+}B_2O_6$. *Z. Kristallogr.* 1971, *133*, 85–90.
13. Gunasekaran S., Anbalagan G. Thermal decomposition of natural dolomite. *Bull. Soc. Fr. Minéral. Cristallogr.* 2007, *30*, 339–344.
14. Doi Y., Satou T., Hinatsu Y. Crystal structures and magnetic properties of lanthanide containing borates $LnM(BO_3)_2$ (Ln = Y, Ho–Lu; M = Sc, Cr). *J. Solid State Chem.* 2013, *206*, 151–157.
15. Zhao S., Zhang G., Zhang X., Wang L., Hao W., Wu Y. Growth and optical properties of $Na_3Gd_2(BO_3)_3$ crystal. *Opt. Mater.* 2012, *34*, 1464–1467.
16. Kawano T., Yamane H. Synthesis, crystal structure and luminescent properties of titanium(IV)-doped calcium borostannates, $CaSn_{1-x}Ti_x(BO_3)_2$. *J. Alloys Compd.* 2010, *490*, 443–447.
17. Macke A. J. H. Investigations on the luminescence of titanium-activated stannates and zirconates. *J. Solid State Chem.* 1976, *18*, 337–346.
18. Blasse G., Dalhoeven G. A. M., Choisnet J., Studer F. On the luminescence of titanium-activated stannates. *J. Solid State Chem.* 1981, *39*, 195–198.
19. Peacor D. R., Essene E. J., Gaines A. M. Petrologic and crystal-chemical implications of cation order-discorder in kutnahorite $[CaMn(CO_3)_2]^*$. *Am. Mineral.* 1987, *72*, 319–328.
20. Hornebecq V., Gravereau P., Chaminade J. P., Lebraud E. $BaZr(BO_3)_2$: a non-centrosymmetric dolomite-type superstructure. *Mater. Res. Bull.* 2002, *37*, 2165–2178.
21. Gesing T. M., Murshed M. M., Schuh S., Thüringer O., Krämer K., Neudecker T., Mendive C. B., Robben L. Nano-crystalline precursor formation, stability, and transformation to mullite-type visible-light photocatalysts. *J. Mater. Sci.* 2022, *57*, 19280–19299.
22. Brand R. A. *Normos Programs (SITE-DIST) (Ed.: Duisburg University)*; Angew. Phys., 1991.
23. Shannon R. D. Revised effective ionic radii and systematic studies of interatomic distances. *Acta Crystallogr.* 1976, *A32*, 751.
24. Housecroft S., Sharpe A. G. *Inorganic Chemistry*, 4th ed.; Pearson: Harlow, England, 2012; pp. 639–777.
25. Granone L. I., Ulpe A. C., Robben L., Klimke S., Jahns M., Renz F., Gesing T. M., Bredow T., Dillert R., Bahnemann D. W. Effect of the degree of inversion on optical properties of spinel $ZnFe_2O_4$. *Phys. Chem. Chem. Phys.* 2018, *20*, 28267–28278.
26. Hiremath V., Kwon H. J., Jung I.-S., Kwon S., Kwon S. H., Lee S. G., Lee H. C., Seo J. G. Mg-ion inversion in MgO@MgO–Al_2O_3 oxides: the origin of basic sites. *ChemSusChem* 2019, *12*, 2810–2818.
27. Li D., Peng N., Bancroft G. M. The vibrational spectra and structure of Nordenskiödine. *Can. Mineral.* 1994, *32*, 81–86.
28. Peercy P. S., Morosin B. Pressure and temperature dependences of the Raman-active phonons in SnO_2. *Phys. Rev. B* 1973, *7*, 2779–2786.
29. Manghnani M., Hushur A., Wu J., Stebbins J., Williams Q. Brillouin, and nuclear magnetic resonance spectroscopic studies on shocked borosilicate glass. *J. Appl. Phys.* 2011, *109*, 113509.
30. Lippens P. E. Interpretation of the ^{119}Sn Mössbauer isomer shifts in complex tin chalcogenides. *Phys. Rev. B* 1999, *60*, 4576–4586.
31. Mahmoud A., Chamas M., Jumas J.-C., Philippe B., Dedryvère R., Gonbeau D., Saadoune I., Lippens P.-E. Electrochemical performances and mechanisms of $MnSn_2$ as anode material for Li-ion batteries. *J. Power Sources* 2013, *244*, 246–251.

Supplementary Material: This article contains supplementary material (https://doi.org/10.1515/zkri-2023-0002).

Supplementary Information

Synthesis, structural and spectroscopic investigations of dolomite-type $MSn(BO_3)_2$ with M = Mn, Fe, Co and Ni

Sarah Wittmann[1], M. Mangir Murshed[1,2*], Vitaliy Bilovol[3,4], Thorsten M. Gesing[1,2]

[1]University of Bremen, Institute of Inorganic Chemistry and Crystallography, Leobener Straße 7, D-28359 Bremen, Germany

[2]University of Bremen, MAPEX Center for Materials and Processes, Bibliothekstraße 1, D-28359 Bremen, Germany

[3]University of Buenos Aires, Laboratorio de Sólidos Amorfos – INTECIN, Av. Paseo Colón 850- C1063ACV – Buenos Aires, Argentina

[4]Current address: Academic Centre for Materials and Nanotechnology, AGH University of Science and Technology, Al. Mickiewicza 30, 30-059 Krakow, Poland

*Corresponding author: e-mail address: murshed@uni-bremen.de, phone: +49 (0)421 218 63144, fax: +49 421 218 63145

ORCID:

SW: 0000-0003-1404-3434
MMM: 0000-0002-9063-372X
VB: 0000-0002-3363-1840
TMG: 0000-0002-4119-2219

Table S1: Powder X-ray diffraction data Rietveld refined structural parameters of $MSn(BO_3)_2$ dolomite type compounds in the hexagonal settings of space group $R\overline{3}$.

$CoSn(BO_3)_2$: a = 472.24(2) pm, c = 1490.79(5) pm

Atom	Occ.	Site	*x*	*y*	*z*	U_{iso} /10^{-4} pm^2
Co	1	3*a*	0	0	0	0.340(3)
Sn	1	3*b*	0	0	½	0.299(18)
B	1	6*c*	0	0	0.2503(8)	0.250(11)
O	1	18*f*	0.0079(8)	0.2908(8)	0.2477(3)	0.530(7)
$FeSn(BO_3)_2$: a = 473.52(4) pm, c = 1512.62(2) pm						
Fe	1	3*a*	0	0	0	0.470(4)
Sn	1	3*b*	0	0	½	0.550(2)
B	1	6*c*	0	0	0.2460(10)	0.600(16)
O	1	18*f*	0.0082(6)	0.2994(9)	0.2473(3)	0.630(8)
$NiSn(BO_3)_2$: a = 469.03(3) pm, c = 1478.12(3) pm						
Ni	1	3*a*	0	0	0	0.300(5)
Sn	1	3*b*	0	0	½	0.280(3)
B	1	6*c*	0	0	0.2527(15)	0.250(19)
O	1	18*f*	0.0082(18)	0.2918(13)	0.2482(5)	0.520(11)

Table S2: Angles and angle variances (BAV) calculated from the respective crystal data of $MSn(BO_3)_2$ compounds.

Compound	**Angle/ deg.**			**BAV /deg.^{2}**	
	O-M-O	O-Sn-O	Sn-O-M	MO_6	SnO_6
$MnSn(BO_3)_2$	86.9(1) 93.1(1)	88.8(1) 91.2(1)	123.7(16)°	10.6(1)	1.6(2)
$FeSn(BO_3)_2$	87.3(3) 92.7(3)	88.3(3) 91.7(3)	124.2(3)°	7.9(1)	3.1(4)
$NiSn(BO_3)_2$	87.8(3)4 92.2(3)	88.4(4) 91.6(4)	124.9(4)°	5.3(4)	2.7(1)
$CoSn(BO_3)_2$	87.8(2) 92.2(2)	88.4(3) 91.6(3)	124.6(3)°	5.3(1)	2.9(1)

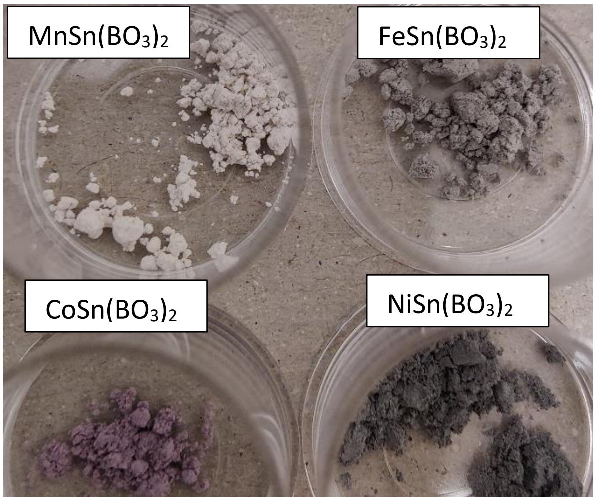

Figure S1: Photograph of samples in plastic containers.

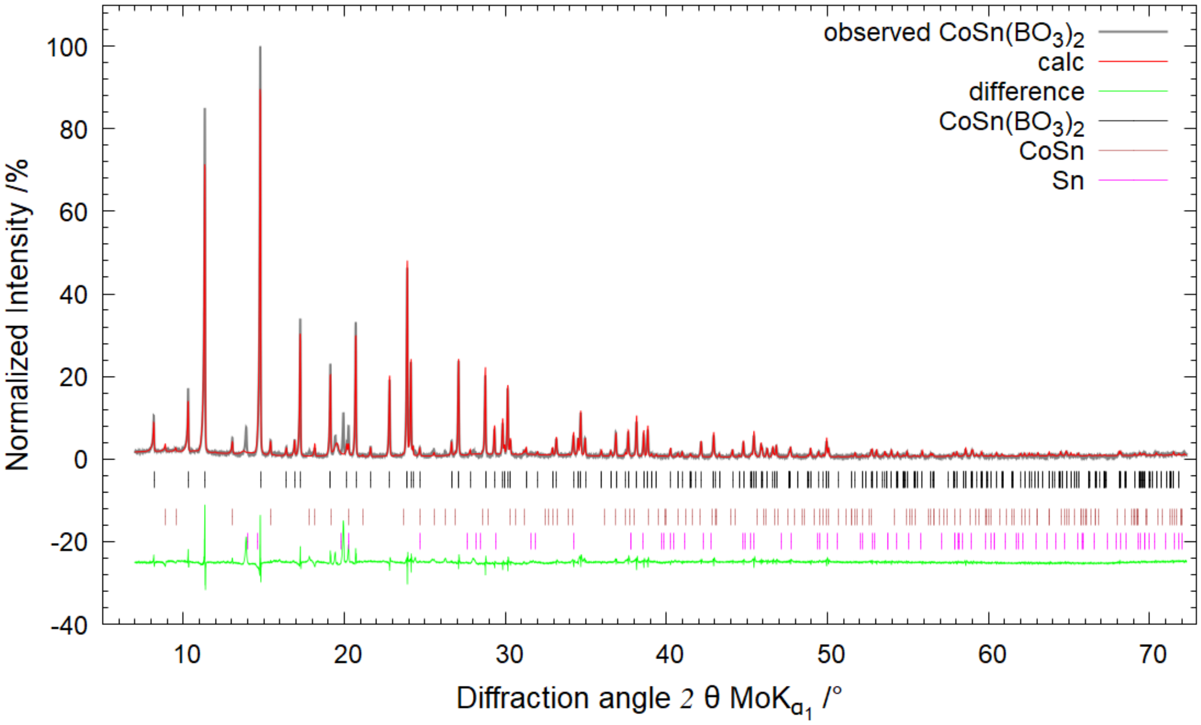

Figure S2: Powder X-ray diffraction data Rietveld plot of $CoSn(BO_3)_2$.

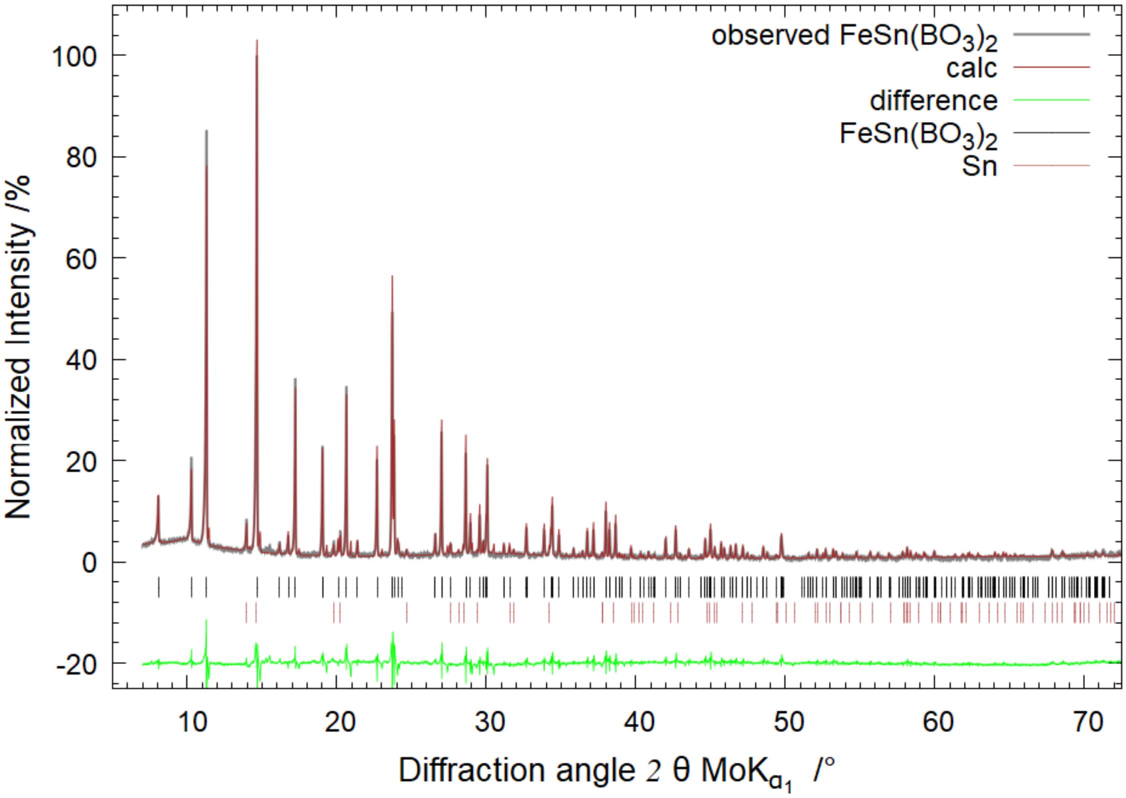

Figure S3: Powder X-ray diffraction data Rietveld plot of $FeSn(BO_3)_2$.

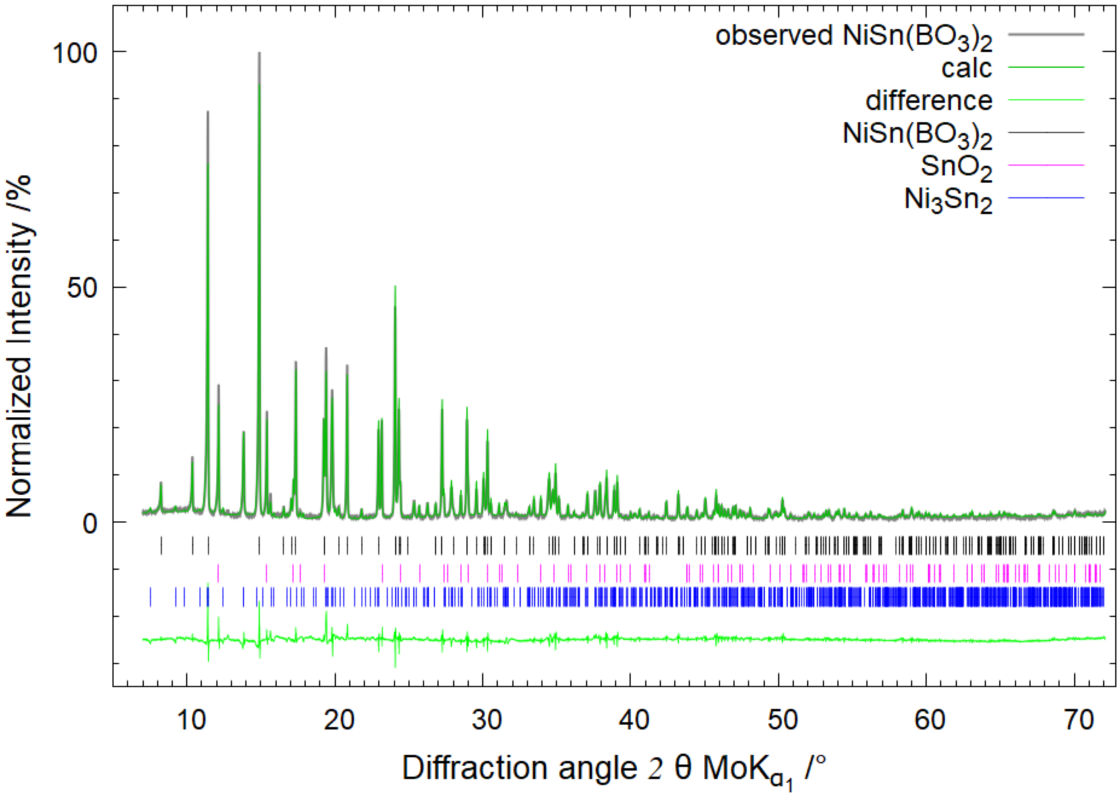

Figure S4: Powder X-ray diffraction data Rietveld plot of $NiSn(BO_3)_2$.

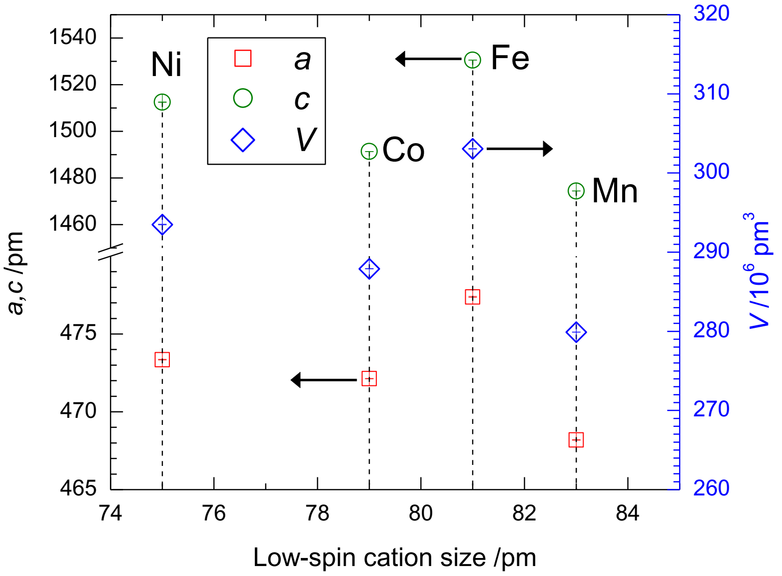

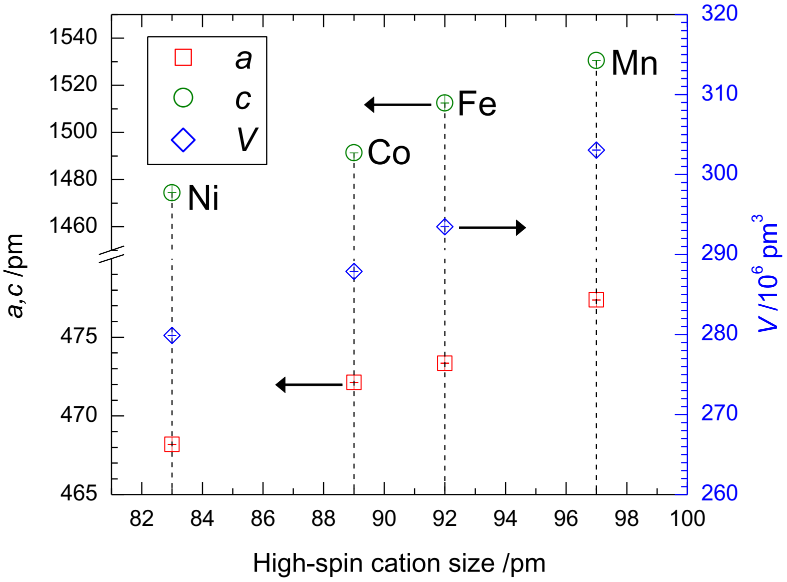

Figure S5: Metric parameters of $MnSn(BO_3)_2$ in the R-3H space group against low-spin and high-spin cationic radii in $FeSn(BO_3)_2$, $CoSn(BO_3)_2$, $MnSn(BO_3)_2$ and $NiSn(BO_3)_2$.

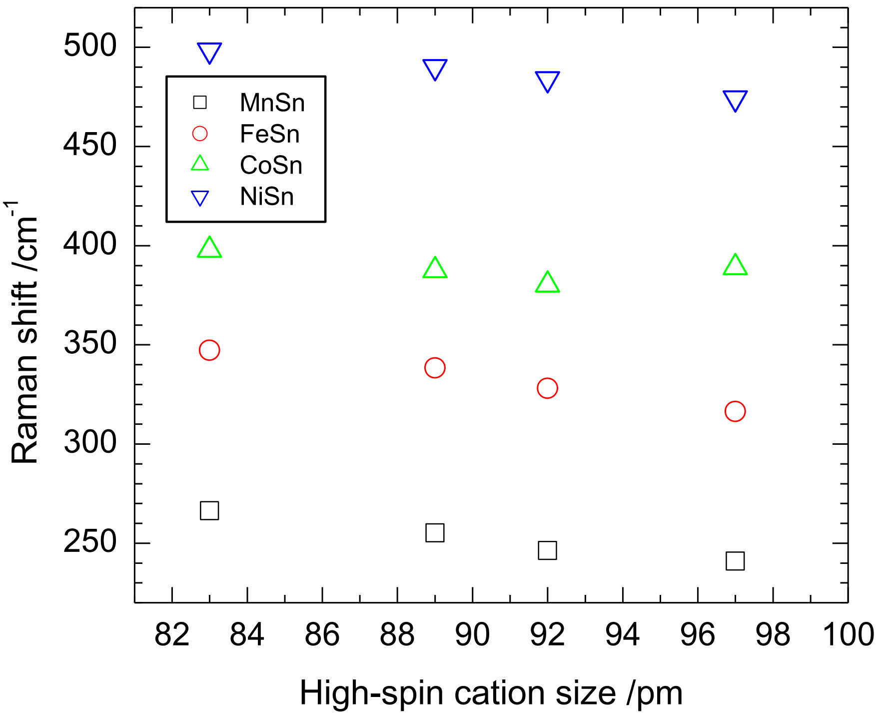

Figure S6: Raman shift against the cationic high-spin radii of the compounds $FeSn(BO_3)_2$, $CoSn(BO_3)_2$, $MnSn(BO_3)_2$ and $NiSn(BO_3)_2$, showing a linear trend.

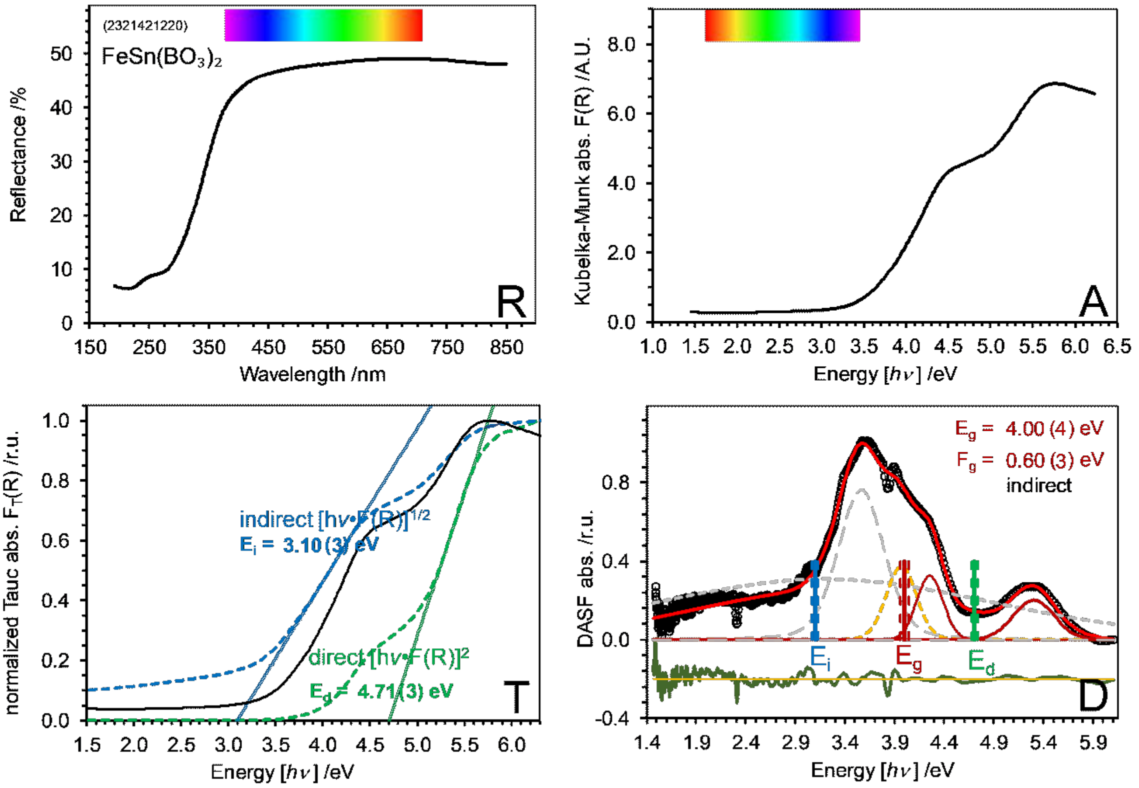

Figure S7: RATD plot of $FeSn(BO_3)_2$.

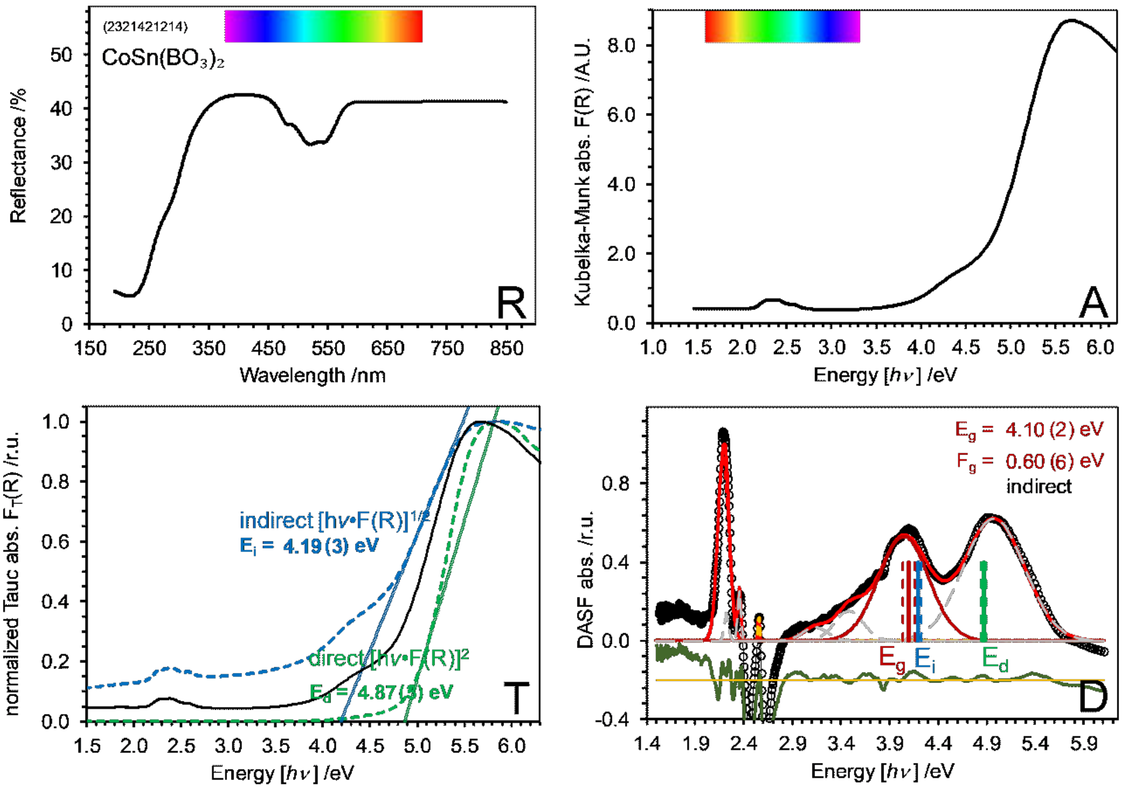

Figure S8: RATD plot of $CoSn(BO_3)_2$.

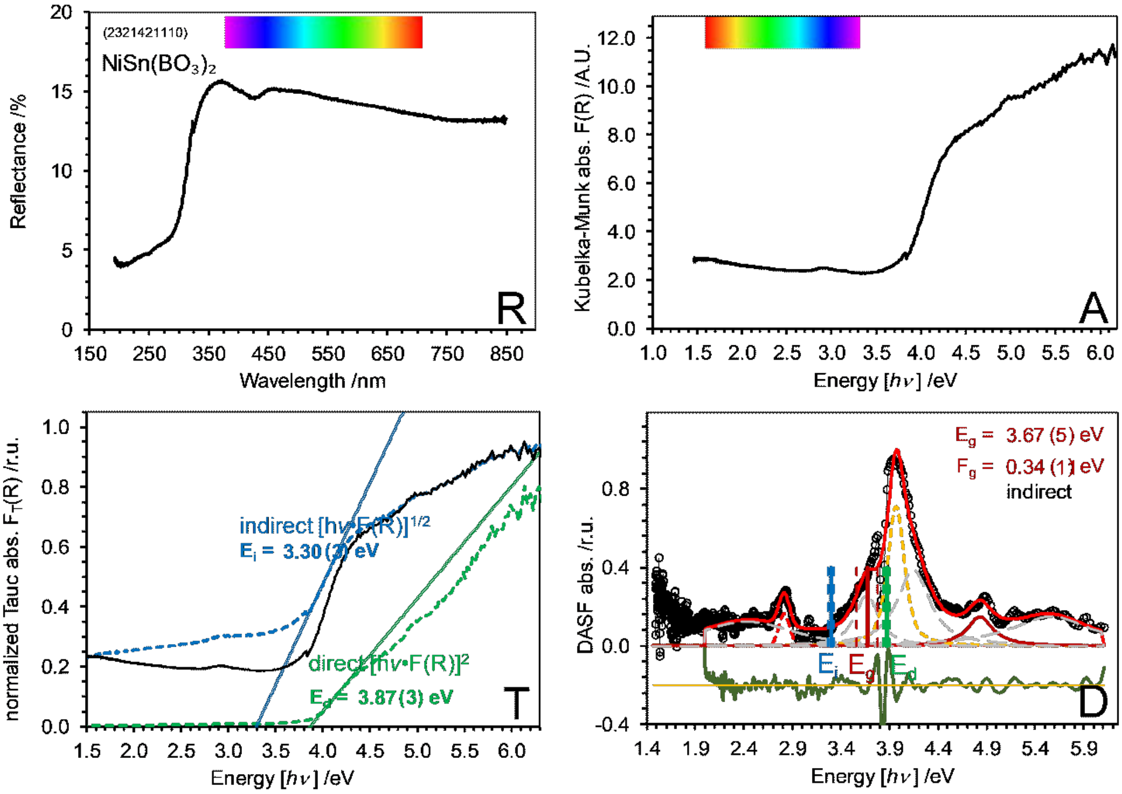

Figure S9: RATD plot of $NiSn(BO_3)_2$.

Most of the studies until now where on minerals of the dolomite-type structure whereas the here mentioned study was for synthesized materials. For a future work, different other materials can be tried on the M-position for $MSn(BO_3)_2$ which are for examples manganese or copper. Another possibility to continue this study is to exchange the tin by another metal cation which could be Ti^{4+}, Mn^{4+}, or Pb^{4+} with different M. With all these different types of materials the properties and applications can be tested. Possible applications are for example photocatalysis or luminescent materials which was done for some minerals before [7]. Another investigation which can be done in the future, is a solid solution at the M-position in the known dolomite-type phases as for example $Mn_{1-x}Fe_xSn(BO_3)_2$ to get an idea of the change of the properties of the materials as for example a change in the magnetic behavior.

Reference

1. J.D. Donaldson, The chemistry of bivalent tin, Inorganic Chemsitry 8 (1967).
2. S.N. Martynov, Ground state of the orbitally ordered $PbMnBO_4$ ferromagnet, JETP Letters 115(11) (2022) 679-684. DOI:10.1134/S0021364022600860
3. A. Pankrats, M. Kolkov, S. Martynov, S. Popkov, A. Krasikov, A. Balaev, M. Gorev, Peculiarities of a magnetic transition in a quasi-one-dimensional ferromagnet $PbMnBO_4$, Journal of Magnetism and Magnetic Materials 471 (2019) 416-422. DOI:10.1016/j.jmmm.2018.09.098
4. M. Curti, M.M. Murshed, T. Bredow, D.W. Bahnemann, T.M. Gesing, C.B. Mendive, Elastic, phononic, magnetic and electronic properties of quasi-one-dimensional $PbFeBO_4$, Journal of Materials Science 54(21) (2019) 13579-13593. DOI:10.1007/s10853-019-03866-1
5. M.M. Murshed, C.B. Mendive, M. Curti, G. Nénert, P.E. Kalita, K. Lipinska, A.L. Cornelius, A. Huq, T.M. Gesing, Anisotropic lattice thermal expansion of $PbFeBO_4$: A study by X-ray and neutron diffraction, Raman spectroscopy and DFT calculations, Materials Research Bulletin 59 (2014) 170-178. DOI:10.1016/j.materresbull.2014.07.005
6. A.I. Pankrats, K.A. Sablina, D.A. Velikanov, O.A. Bayukov, A.M. Vorotynov, A.D. Balaev, M.S. Molokeev, M.I. Kolkov, Magnetic and dielectric properties of $PbFeBO_4$ and $PbMnBO_4$ single crystals, Solid State Phenomena 215 (2014) 372-377. DOI:10.4028/www.scientific.net/SSP.215.372
7. G. Blasse, S.J.M. Sas, W.M.A. Smit, W.L. Konijnendijk, Luminescent materials with dolomite Structure, Materials Chemistry and Physics 14 (1986) 253-258.

Chapter 9 – General discussion and unsuccessful synthesis of mullite-type solid solutions

Several different trivalent cations should be tried to add to the mullite-type $SnMBO_4$ phase. M = Al, Ga, and Cr are working fine as already discussed, which is comparable to the isostructural $PbMBO_4$ (M= Al, Ga, Cr) O8-phases [1-3]. Additionally, vanadium could be introduced to the structure, which was also explained for the room temperature data before in the paper about $SnCrBO_4$ and $SnVBO_4$. As mentioned in **chapter 2**, other trivalent metal cations should be introduced to the system which are scandium, indium, arsenic, and antimony. In this chapter, the results of the syntheses with these metals are described. Additionally, different solid solutions with two or more trivalent metal cations are described and compared to some isostructural $PbMBO_4$ phases with more than one metal cation.

For the materials $SnScBO_4$ and $SnInBO_4$, the synthesis with M_2O_3, B_2O_3 and SnO resulted in MBO_3 and SnO_2. Hence, the oxidation of Sn^{2+} to Sn^{4+} is faster than the synthesis of the mullite-type compound and the MBO_3 phase might be more stable [4] and therefore, preferred. The result for the synthesis of $SnInBO_4$ explains maybe also the result if SnO and $InBO_3$ are mixed and heated which was explained in **chapter 7**. Another reason for the unsuccessful synthesis could be the larger cationic radius with 80 pm [5] which is too large for the octahedra in the mullite type compound.

For the synthesis for $SnAsBO_4$, the result was SnO_2 and a molten compound with the quartz tube walls. An explanation might be that As_2O_3 has a melting point of around 738 K which is lower than the reaction temperature of 1023 K. A lower synthesis temperature cannot be chosen if the pressure is similar as the calculations for $SnAlBO_4$ and $SnGaBO_4$ suggested [6]. Hence, the oxidation of Sn^{2+} to Sn^{4+} is preferred. Another reason for an unsuccessful synthesis if that the redox potential is higher for As^{3+} to As^{5+} [7] as shown in **figure 2.1**.

For $SnSbBO_4$, the result is the oxidation of tin to SnO_2, a reduction of antimony to elementary Sb and an amorphous phase based on the XRPD data which might be some boron oxides. A similar reason for the failure of the synthesis might be a conflict with the redox potential of antimony compared to tin (**figure 2.1**). Another reason might be cationic size with 76 pm for Sb^{3+} which is quite large [5]. Additionally, As^{3+} as well as Sb^{3+} have an LEP which might influence the synthesis [8, 9] and lead to a product which is not the expected mullite-type O8 phase. Hence, for all four newly introduced metal cations a synthesis to get mullite-type O8 compound with its chemical formular $SnMBO_4$ is not possible and therefore not further tried during this work.

As of now, the parental phases of the mullite-type compounds $SnMBO_4$ are defined with M = Al, Ga, Cr, and V. Some of their solid solutions were done which were described in **chapter 4** and **chapter 6** of this work. If the before described solid solutions (**chapter 6**) of $Sn(Al_{1-x}Cr_x)BO_4$ and $Sn(Ga_{1-x}Cr_x)BO_4$ are compared to the isostructural Pb(II) mullite-type compounds, a similar trend of the metric parameters is observed (**figure 9.1**). A linear line can be drawn from one parental phase of a solid solution to another one which follows the rule of Vegard's law [10]. Hence, an increase of the lattice parameters with the smaller averaged cationic radius to the larger ones is obtained for lattice parameters *a* and *b* as well as the cell volume. For lattice parameter *c*, an increase is obtained for both solid solutions with an alumina content, whereas the lattice parameter of the $PbCrBO_4$ parental phase is larger compared to the one of $PbGaBO_4$, even if the radii are vice versa. The same observation was done for the isostructural tin compounds and therefore, the lattice parameter *c* decreases with increasing averaged cationic radius of the structure. This effect can be explained by the magnetic influence of Cr^{3+} and a larger elongation of the octahedral chain along the crystallographic *c* axis. As the difference of the lattice parameter *a* of $PbAlBO_4$ and $PbCrBO_4$ is only 0.8 pm, the mismatches of the same lattice parameter of the solid solution of $Pb(Al_{1-x}Cr_x)BO_4$ can be explained due to uncertainties during the Rietveld refinements. Hence, the trend does not look like the rule of Vegard’s law.

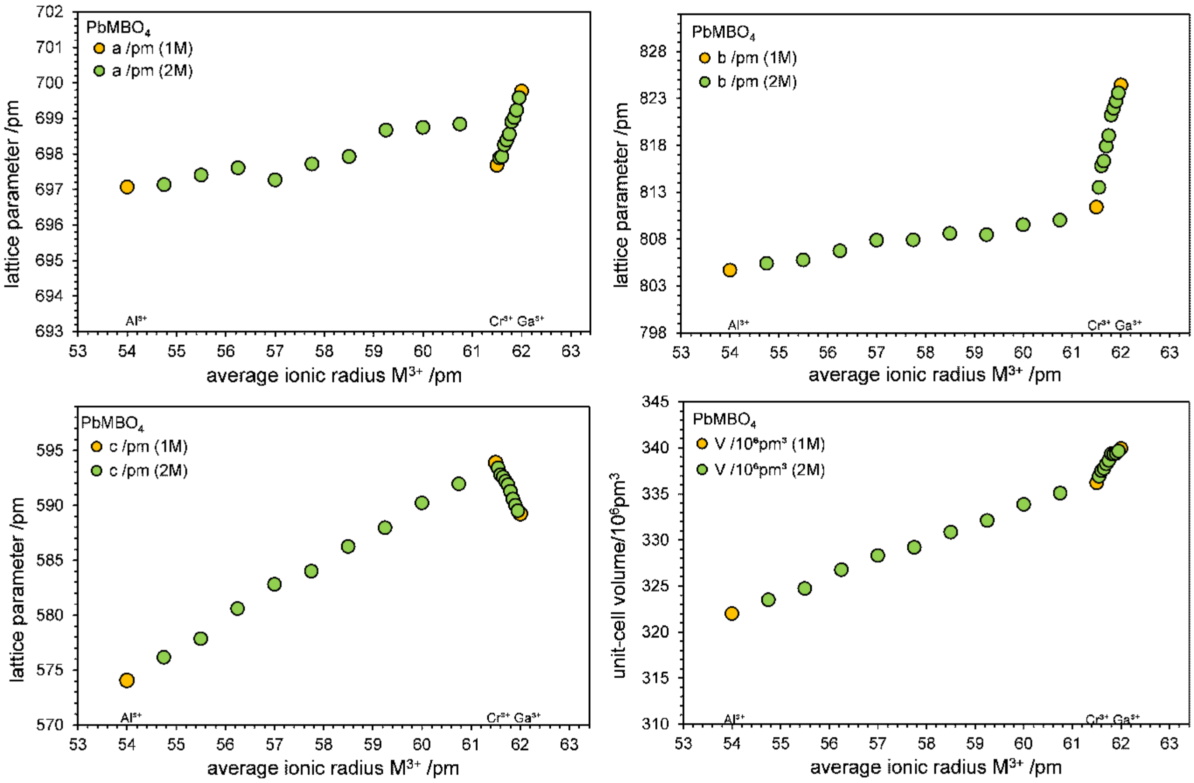

Figure 9.1: Trend of the metric parameters of the solid solutions $Pb(Al_{1-x}Cr_x)BO_4$ and $Pb(Ga_{1-x}Cr_x)BO_4$ for x = 0.0 – 1.0.

As Pb^{2+} has a larger cationic radius compared to Sn^{2+} [5], the lattice parameter *b* is larger due to needed space of lead. Lattice parameter *c* is mostly dependent on the octahedral chain and its central metal cation and therefore, the values are comparable in the two isostructural systems. Due to the rigidity of the BO_3 group the elongation along the crystallographic *a* axis is restricted, which is slightly smaller for $PbMBO_4$ compounds and its solid solutions compared to the tin containing mullite-type compounds. Interestingly, the solid solution $Pb(Al_{1-x}Ga_x)BO_4$ is the hardest one to synthesize compared to the other two already described ones which is like the isostructural tin containing solid solutions. As the substitution of aluminum by gallium is not 100 % pure where the synthesis needed to be optimized, this row is not part of this work. For some future work, it would be interesting to synthesize a pure phase of $Pb(Al_{1-x}Ga_x)BO_4$ to investigate different properties as the thermal stability or conductivity of them.

Beside the three already discussed solid solutions, which contained tin, other ones with the last beforehand discussed end member $SnVBO_4$ are possible, which are $Sn(Al_{1-x}V_x)BO_4$, $Sn(Ga_{1-x}V_x)BO_4$, and $Sn(Cr_{1-x}V_x)BO_4$ (**chapter** 4). During the syntheses, it was noticed that the substitution of gallium by vanadium was easier to get a pure phase compared to the other two solid solutions which is due to a smaller distance of the cationic radii of Ga^{3+} (62.0 pm) and V^{3+} (64.0 pm) compared to Al^{3+} (53.5 pm) and Cr^{3+} (61.5 pm). As $Sn(Cr_{1-x}V_x)BO_4$ is already discussed in **chapter 4** the focus of the following discussion is about the other two solid solutions and their characteristics. If the lattice parameters as well as the cell volumes of both solid solutions are plotted against the averaged cationic radii, a linear trend which follows again the before discussed Vegards law is obtained (**figure 9.2**) [10].

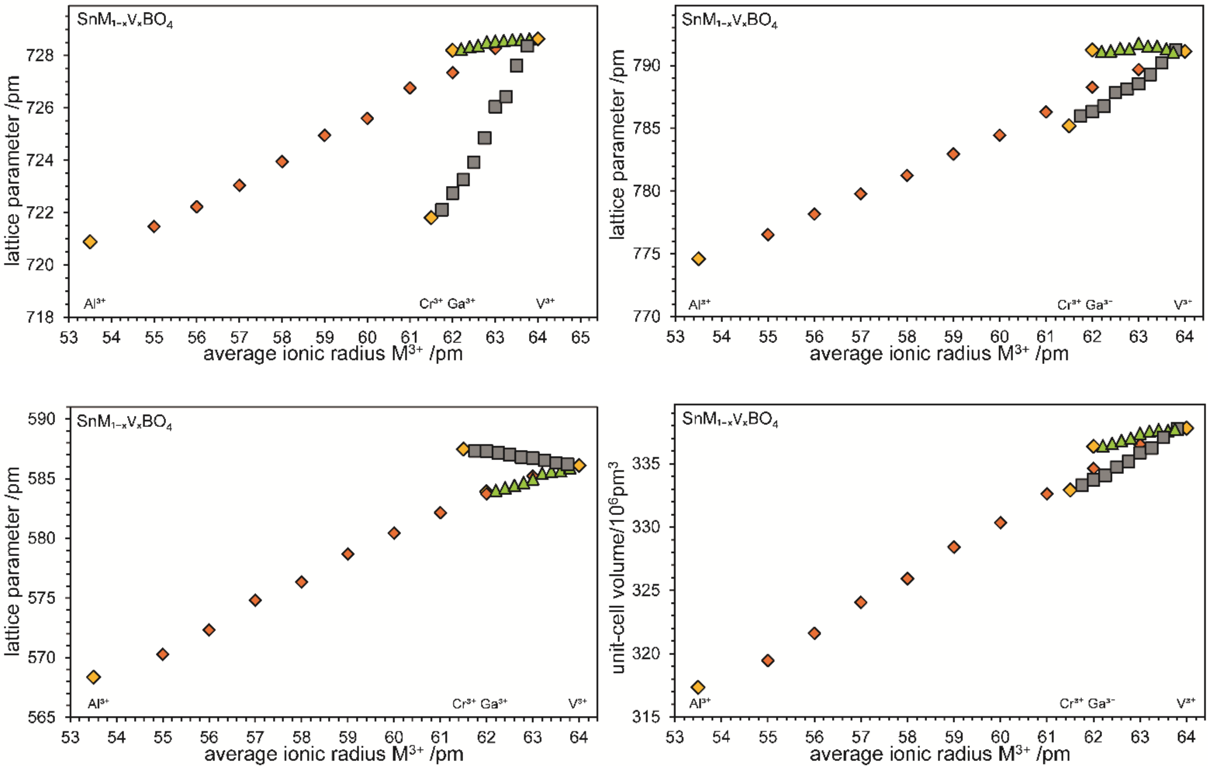

Figure 9.2: Trend of the metric parameters of the solid solutions $Sn(M_{1-x}V_x)BO_4$ with M = Al (orange diamonds), Ga (green triangular), and Cr (grey squares) for x = 0 – 1.0.

For Sn($Al_{1-x}V_x$)BO_4, the lattice parameters as well as the cell volume is increasing with increasing vanadium content, which can be seen in an increasing averaged cationic radius of the metal ion. The same is true for the cell volume and lattice parameters *a* and *c* of Sn($Ga_{1-x}V_x$)BO_4. As the value of lattice parameter *b* is nearly constant of the two endmembers, the influence of the increasing cationic side is again nearly constant.

As mentioned in **chapter 8**, another goal was to synthesize $SnMBO_4$ where M = Fe and Mn which did not result in a mullite-type compound but in a so-called dolomite-compound. Another interesting goal of this work was to synthesize solid solutions with two different trivalent metal cations where one should be either Fe^{3+} or Mn^{3+} and the other one is one of the known parental phases of $SnMBO_4$ (M = Al, Ga, Cr, and V). The results of these syntheses are interesting as the substitution of M by either Fe^{3+} or Mn^{3+} works for small x values up to 0.3 if M = Al^{3+} and Cr^{3+}, up to 0.4 for M = Ga^{3+} and only up to 0.1 for M = V^{3+}. Afterwards the synthesized product also contains an increasing amount of the respective dolomite-type phase. In these syntheses the occupancy factor of the solid solution is not the expected one, which have a lower value for Mn^{3+} or Fe^{3+} as these starting materials are used to get the dolomite-type phase. Hence, two phases are built during the solid-state synthesis where one is the mullite-type compound with M = Al, Ga, Cr, or V whereas the other one is the dolomite-type compound M'Sn(BO_3)$_2$ (M' = Fe or Mn). As a successful synthesis of $PbFeBO_4$ as well as $PbMnBO_4$ is possible, it is not surprising that the solid solutions of Pb($Al_{1-x}Fe_x$)BO_4 and Pb($Al_{1-x}Mn_x$)BO_4 are successful which is for example published for Pb($Al_{1-x}Mn_x$)BO_4 [1]. As done for the already described solid solutions, the lattice parameters are plotted against the averaged cationic radius of the M position which is shown in **figure 9.3**.

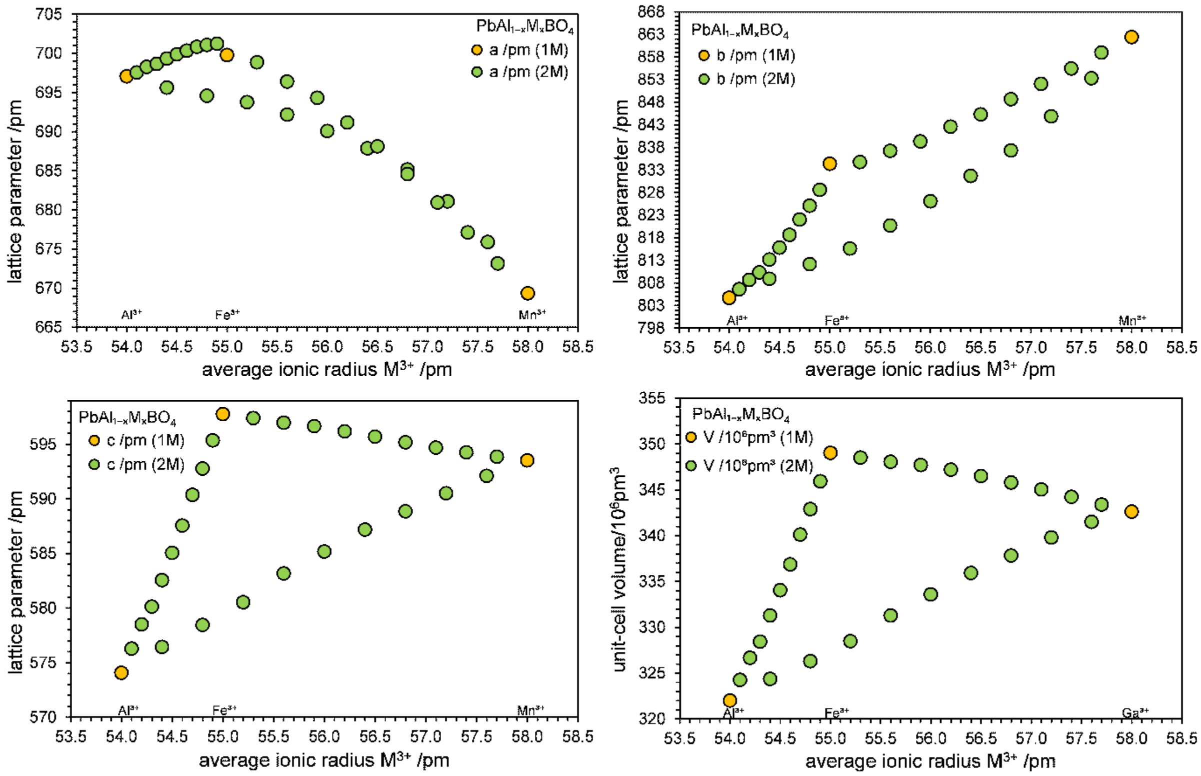

Figure 9.3: Trend of the metric parameters of the solid solutions $Pb(Al_{1-x}M_x)BO_4$ with M = Fe and Mn as well as $Pb(Fe_{1-x}Mn_x)BO_4$ for x = 0.0 – 1.0.

The trend for $Pb(Al_{1-x}Fe_x)BO_4$ is again with increasing averaged cationic radii the lattice parameter of the solid solution increases which is the same for $Pb(Al_{1-x}Mn_x)BO_4$ for the lattice parameters *b* and *c*. As lattice parameter *a* of $Pb(Al_{1-x}Mn_x)BO_4$ with x = 1.0 is smaller compared to x = 0.0, the trend is vice versa as Mn^{3+} (58 pm) has a larger cationic radius compared to Al^{3+} (54 pm) [5]. The influence of the Jahn-Teller effect as well as the influence of the LEP of Pb^{2+} leads to a smaller lattice parameter *a* for $PbMnBO_4$ [1] even if the cationic size of Mn^{3+} is larger than the one of Al^{3+} [5]. For $Pb(Mn_{1-x}Fe_x)BO_4$, the trend is a bit more complex. With increasing averaged cationic radius at the M-position, lattice parameter *b* increases whereas lattice parameters *a* and *c* and the cell volume decrease. This might be due to several effects in the structure. Firstly, $PbMnBO_4$ has an antiferromagnetic magnetism whereas $PbFeBO_4$ is ferromagnetic [11, 12]. Hence, the influence of the change in the magnetic field influences the values of the lattice parameters. Another reason could be the possibility of the Jahn-Teller distortion for manganese which is not possible for iron [13]. The last reason could be that Fe^{3+}

has one electron more compared to Mn^{3+} which influences the size of the octahedra and therefore also the size of the crystal structure of the mullite-type compound. Hence, more investigations on this structure should be done for future work to get an idea of the influence of the trivalent metal cation to the structure. Moreover, a study of the solid solutions for $Pb(M_{1-x}Fe_x)BO_4$ and $Pb(M_{1-x}Mn_x)BO_4$ with M = Ga, Cr is necessary to compare the influence of the trivalent metal cations to the mullite-type crystal structure.

For the synthesis of the multi-element mullite-type compounds, stoichiometric mixtures of the metal oxides were used for three ($x_M = 1/3$), four ($x_M = 0.25$) and five ($x_M = 0.2$) different metal ions. The result of the synthesis of $Sn(Fe_{0.33}Mn_{0.33}M_{0.33})BO_4$ (M = Al, Ga, Cr, and V), is always a dolomite-type phase with a smaller amount of a mullite-type phase which has, based on the Rietveld refinements, not or only to small amounts of Fe^{3+} and/or Mn^{3+}. As these syntheses with a larger amount of Fe^{3+} and Mn^{3+} are not promising, they were not done for the other triple trivalent cation element compounds. As already mentioned before, solid solutions with Cr^{3+} and V^{3+} are complicated as the synthesis temperature for $SnCrBO_4$ is higher and the synthesis time is longer compared to $SnVBO_4$. Hence, the synthesis with both trivalent metal cations with Mn^{3+} or Fe^{3+} are not successful for a mullite-type compound whereas the result of $x_M = 1/3$ is both a part of the mullite-type compound as well as partly a dolomite-type compound. For the samples with either Mn^{3+} or Fe^{3+} combined with two out of Al^{3+}, Ga^{3+}, Cr^{3+}, or V^{3+} the result is a mullite-type compound with three different metal cations (**figure A9.21**). If an imaginary triangular is drawn between the lattice parameter of three parental phases, the lattice parameter of the respective solid solution is within this triangular which was expected. For example, a smaller value of lattice parameters as well as the cell volume of $Sn(Al_{0.33}Ga_{0.33}Cr_{0.33})BO_4$ is obtained compared to $Sn(Al_{0.33}Ga_{0.33}V_{0.33})BO_4$ as well as $Sn(Ga_{0.33}Cr_{0.33}V_{0.33})BO_4$.

The trend is similar to the obtained values with all three known parental phases. This result was expected as the lattice parameters of $SnMnBO_4$ and $SnFeBO_4$ are somewhere in the middle between the one of $SnAlBO_4$ and the other three $SnMBO_4$ parental phases (M = Cr, Ga, V). This expectation is based on the different cationic radii which are for Mn^{3+} and Fe^{3+} in the middle between Al^{3+} and either Ga^{3+}, Cr^{3+} or V^{3+} [5].

For $PbMBO_4$, combinations of Al^{3+}, Ga^{3+}, Cr^{3+}, Mn^{3+}, and Fe^{3+} metal cations are possible. As the overlap to the $SnMBO_4$ phases are Al^{3+}, Ga^{3+}, and Cr^{3+}, these three materials are tested for the isostructural lead containing mullite-type compounds. The lattice parameter *a* is smaller compared to the parental phases $PbAlBO_4$, $PbGaBO_4$, and $PbCrBO_4$ where the other two lattice parameter as well as the cell volume is larger for the solid solution. The combination of three different metal cations seems to have a larger impact to the structure than the isostructural tin containing compound. This might be due to the larger Pb^{2+} cation which stretches the structure more compared to Sn^{2+} and therefore, the values differ more compared to their parental phases for Pb(II) containing compounds than their tin containing compounds.

As mentioned in the discussion about solid solutions with two different M-cations of tin containing mullite-type compounds, a combination of Cr^{3+} and V^{3+} is quite difficult to get the pure phase. With additional Mn^{3+} or Fe^{3+}, the synthesis might be even more difficult as the oxidation of Sn^{2+} to Sn^{4+} is more likely than a mullite-type compound as a product. Syntheses with four metal cations where only stable and possible to synthesis for either a combination of Al^{3+}, Ga^{3+}, Cr^{3+}, and V^{3+} or with only one of Cr^{3+} and V^{3+} and one of Mn^{3+} and Fe^{3+}. For the syntheses with five different trivalent metal cations, only combinations with three out of Cr^{3+}, V^{3+},Mn^{3+}, or Fe^{3+} are possible with the already synthesized products before. Hence, the result was not successful with a pure phase and therefore, different further investigations as the analysis of the metric parameters or the influences of the different cations could not be done. The synthesis of these combinations should be done in a future work to obtain high entropy materials which can be compared to the isostructural lead mullite-type compounds.

As both, $SnMBO_4$ as well as $PbMBO_4$, are known, another idea during this work was to synthesize solid solutions of them with several different M as Al^{3+}, Ga^{3+}, Cr^{3+}, and Mn^{3+}. The main goal was to get an idea of the influence of the LEPs of Sn^{2+} and Pb^{2+} and how it will change during the substitution of one by the other. As for $SnMBO_4$ the easiest mullite-type compound to synthesis was $SnAlBO_4$. The first trivalent metal cation which was used in the synthesis of solid solutions between tin(II) and lead(II) was Al^{3+} where the substitution was started from the Sn(II) parental phase. Another starting point is the Pb(II) parental phase for which Mn^{3+} was chosen to be the M^{3+} cation. If the starting point is the Sn(II) parental phase, the synthesis was done in a quartz tube to avoid the oxidation of Sn^{2+} to Sn^{4+}. On the other hand, if the starting point was the Pb(II) parental phase, the solid-state synthesis was done via the glycerin method [2]. The glycerin method and the sealed-quartz-tube method were chosen as the two parental phases $PbMBO_4$ and $SnMBO_4$ were successfully synthesized, respectively. If the compositional x-value in $(Sn_{1-x}Pb_x)AlBO_4$ is 0.1 or 0.2, the synthesis resulted in the expected mullite-type compound which had either no impurities or a small amount of Al_2O_3 based on the Rietveld refinements.

The lattice parameters for this solid solution are a = 720.1(3) pm, b = 774.6(3) pm, c = 568.8(5) pm, and $V = 317.3(2) \cdot 10^6$ pm^3 which are all quite close to $SnAlBO_4$. This result gives a hint that the synthesized composition is not the expected one for x = 0.2. For increasing compositional x-values the result is an oxidation of Sn^{2+} to Sn^{4+} with SnO_2 whereas Pb^{2+} is reduced to elementary Pb(0) as well as $Al_4B_2O_9$ which is a before described (**chapter 1**) mullite-type compound. For $(Sn_{1-x}Pb_x)MnBO_4$, if the synthesis is done with the glycerin method, the result is similar with elementary Pb(0), SnO_2 and Mn_2O_3. Hence, the substitution of tin(II) by lead(II) and vice versa seems is not promising. As mullite-type structures of the $EMBO_4$ family have MO_6 octahedra as well as rigid BO_3 groups which mainly do not change in both parental phases the influence of the LEP as well as the easily oxidation of tin must be the reason that the substitution does not work.

Reference

1. T.M. Gesing, C.B. Mendive, M. Curti, D. Hansmann, G. Nénert, P.E. Kalita, K.E. Lipinska, A. Huq, A.L. Cornelius, M.M. Murshed, Structural properties of mullite-type $Pb(Al_{1-x}Mn_x)BO_4$, Zeitschrift für Kristallographie - Crystalline Materials 228(10) (2013). DOI:10.1524/zkri.2013.1640
2. M. Gogolin, M.M. Murshed, M. Ende, R. Miletich, T.M. Gesing, Uniaxial negative thermal expansion in the mullite- and borax-type $PbAlBO_4$ polymorphs, Journal of Materials Science 55(1) (2019) 177-190. DOI:10.1007/s10853-019-04013-6
3. H. Park, R. Lam, J.E. Greedan, J. Barbier, Synthesis, crystal structure, crystal chemistry, and magnetic properties of $PbMBO_4$ (M = Cr, Mn, Fe): A new structure type exhibiting one-dimensional magnetism, Chemistry of Materials 15(8) (2003) 1703-1712. DOI:10.1021/cm0217452
4. O. Gomis, H.M. Ortiz, J.A. Sans, F.J. Manjón, D. Santamaría-Pérez, P. Rodríguez-Hernández, A. Muñoz, $InBO_3$ and $ScBO_3$ at high pressures: An ab initio study of elastic and thermodynamic properties, Journal of Physics and Chemistry of Solids 98 (2016) 198-208. DOI:10.1016/j.jpcs.2016.07.002
5. R.D. Shannon, Revised effective ionic radii and systematic studies of interatomic distances, Acta Crystallographica A32 (1976) 751.
6. M. Curti, C.B. Mendive, T. Bredow, M. Mangir Murshed, T.M. Gesing, Structural, vibrational and electronic properties of $SnMBO_4$ (M = Al, Ga): a predictive hybrid DFT study, J Phys Condens Matter 31(34) (2019) 345701. DOI:10.1088/1361-648X/ab20a1
7. P. Vanýsek, Electrochemical series.
8. P.A. O'Day, Chemistry and mineralogy of arsenic, Elements 2 (2006) 77-83.
9. K. Tolborg, C. Gatti, B.B. Iversen, Expression and interactions of stereochemically active lone pairs and their relation to structural distortions and thermal conductivity, IUCrJ 7(Pt 3) (2020) 480-489. DOI:10.1107/S2052252520003619
10. A.R. Denton, N.W. Ashcroft, Vegard's law, Physical Review A 43(6) (1991) 3161-3164. DOI:10.1103/PhysRevA.43.3161
11. M. Curti, M.M. Murshed, T. Bredow, D.W. Bahnemann, T.M. Gesing, C.B. Mendive, Elastic, phononic, magnetic and electronic properties of quasi-one-dimensional $PbFeBO_4$, Journal of Materials Science 54(21) (2019) 13579-13593. DOI:10.1007/s10853-019-03866-1
12. H.-J. Koo, M.-H. Whangbo, Density functional investigation of the magnetic properties of $PbMBO_4$ (M=Cr, Mn, Fe), Solid State Communications 149(15-16) (2009) 602-604. DOI:10.1016/j.ssc.2009.01.030
13. S. Housecroft, Inorganic Chemistry.

Chapter 10 – Summary and outlook

Within the scope of this thesis several new members of the mullite-type O8-phases, namely, $SnAlBO_4$, $SnGaBO_4$, $SnVBO_4$, $SnCrBO_4$ and, their solid solutions $Sn(Al_{1-x}Ga_x)BO_4$, $Sn(Al_{1-x}V_x)BO_4$, $Sn(Al_{1-x}Cr_x)BO_4$, $Sn(Ga_{1-x}V_x)BO_4$, $Sn(Ga_{1-x}Cr_x)BO_4$ and $Sn(Cr_{1-x}V_x)BO_4$ are synthesized using solid state method. Each sample is characterized using X-ray powder diffraction Rietveld refinement, Raman-, FTIR-, UV/Vis- and Mössbauer spectroscopy. Their thermal stabilities are suggested based on the decomposition temperatures.

The crystal structure features are less influenced by the respective LEPs than that of the trivalent metal cations Al^{3+}, Ga^{3+}, Cr^{3+}, and V^{3+}. Nevertheless, the influence of the LEP is strongest in the $SnAlBO_4$ mullite-type compound compared to the other three parental phases. The electronic band gaps are obtained from the UV/Vis diffuse reflectance, which suggests that all four compounds are high band gap semiconductors. Based on the Mössbauer spectroscopy, a Sn^{2+} cation is proven. This can be also observed in the MAS NMR spectroscopy of $SnAlBO_4$ and $SnGaBO_4$. For the temperature dependent measurements of the parental phases, it can be observed that the Sn^{2+} cation splits at lower temperatures in the ^{119}Sn Mössbauer measurements to two different Sn^{2+} environments. This splitting is based on a symmetry change of the crystal structure of the mullite-type phase which could not be obtained in the in-house TD-XRPD measurements. The decomposition temperature of the four different phases is in the range of 960 K to 1074 K, which is proven by thermal investigations and TD-XRPD measurements. $SnAlBO_4$ shows the highest stability of the four compounds whereas $SnVBO_4$ is the weakest ceramic. Repeated trials to synthesize isostructural $SnScBO_4$, $SnInBO_4$, $SnAsBO_4$ and $SnSbBO_4$ are not successful within the given methods, yielding corresponding metal borate (MBO_3) and SnO_2 (see **chapter 7**). These findings are explained in terms of redox potential between Sn^{2+}, Sn^{4+} and M^{3+}, the susceptible oxidation of Sn^{2+} to Sn^{4+} and larger cationic (M) radius fitting to the structures. For $SnAsBO_4$ and $SnSbBO_4$ both the lower melting points of As_2O_3 and Sb_2O_3 and the stereochemical activity of the $4s^2$ and $5s^2$ lone electron pairs, respectively.

The four mentioned solid solutions $Sn(Al_{1-x}Ga_x)BO_4$, $Sn(Al_{1-x}Cr_x)BO_4$, $Sn(Ga_{1-x}Cr_x)BO_4$, and $Sn(Cr_{1-x}V_x)BO_4$ are successfully synthesized where the trend of the metric parameters follows Vegard's law. If the cationic radius of the trivalent metal cation of one parental phase is closer to the cationic radius of the other parental phase, the synthesis of the solid solutions is easier compared to a higher difference of the radii. Thermal investigations of these solid solutions show that a higher stability and therefore, a higher decomposition temperature is given for ceramics which contain Cr^{3+} as $SnCrBO_4$. They have the highest decomposition temperature at 1074 K. During the work, the last two remaining solid solutions $Sn(Al_{1-x}V_x)BO_4$ and $Sn(Ga_{1-x}V_x)BO_4$ were synthesized, where the substitution of Ga^{3+} by V^{3+} was easier compared to Al^{3+} by V^{3+} where in the future, investigations of the bands in vibrational spectroscopy, magnetic properties and thermal analysis are interesting for the comparison to the already explained solid solutions. As mentioned in **chapter 2**, different trivalent metal cations as Fe^{3+} and Mn^{3+} are possible to synthesize in the isostructural $PbMBO_4$ phases. The parental phases are not possible to synthesize which was discussed in **chapter 8**, solid solutions with a partial substitution of the four successful parental phases were tried to synthesize. The results of these syntheses are quite interesting as the substitution of M by either Fe^{3+} or Mn^{3+} works for small $x_M = 0.1$, 0.3, or 0.4 if $M = V^{3+}$, Al^{3+} and Cr^{3+}, or Ga^{3+}, respectively. Afterwards the synthesized product also contains an increasing amount of the respective dolomite-type phase. As solid solutions can be done with more than two trivalent metal cations, different multi-element solid solutions were tried where the ratios are either $x_M = 1/3$, $x_M = 0.25$, or $x_M = 0.2$. Synthesis with three different metal cations is possible to obtain a pure phase especially if the three trivalent metal cations are one of the successful parental phases. Syntheses with four metal cations where only stable and possible to synthesis for either a combination of aluminum, gallium, chromium, and vanadium or with only one of chromium and vanadium and one of manganese and iron. For the syntheses with five different trivalent metal cations, only combinations with three out of chromium, vanadium, manganese, or iron are possible with the already synthesized products before. Hence, the result was not successful with a pure phase and therefore, different further investigations as the analysis of the metric parameters or the influences of the different cations could not be done. Anyways, the synthesis of these combinations should be done in a future work to obtain high entropy materials which can be compared to the isostructural lead mullite-type compounds.

As mentioned in the introduction of this work, one goal was to replace Pb^{2+} by Sn^{2+} due to environmental issues. One important investigation of the $SnMBO_4$ phases was the influence of the LEP to the structures. Hence, another idea during the work was to synthesize solid solutions of Pb^{2+} and Sn^{2+} to obtain the different influence of the LEPs of these two divalent metal cations. For these investigations two different starting points were chosen where either Sn^{2+} was substituted by Pb^{2+} or vice versa. The result was that these solid solutions are not possible to synthesize as probably the stereochemical activity of the LEPs are too different to stabilize the mullite-type ceramics.

Another idea to investigate the influence of the LEPs to the structure is the comparison of isostructural solid solutions where $Pb(Al_{1-x}Cr_x)BO_4$, and $Pb(Ga_{1-x}Cr_x)BO_4$ are used where the resulted metric parameters follow again the Vegard's law. As Pb^{2+} has a larger cationic radius compared to Sn^{2+} [1] the lattice parameter *b* is larger due to needed space of lead. Anyways, for the influence of the strength of the LEPs several different investigations should be done in a future work.

Another study which was done during this PhD work was to synthesize different starting materials than the commercial ones which was described in **chapter 7**. Red SnO is supposed to be more reactive and therefore, the idea was to avoid impurities as SnO_2 as the synthesis of the mullite-type ceramic is faster compared to the synthesis with the commercial SnO. As the synthesis of red SnO was described in the literature [2], the first route was similar to the described one which was optimized to a shorter synthesis time. Investigations of the thermal properties of red SnO were done where the phase transition to commercial black blueish SnO and afterward to SnO_2 was obtained. Another starting material was MBO_3 which should be synthesized to easier produce $SnMBO_4$. Hence, different trivalent metal cations were tried with Cr^{3+}, In^{3+}, and Sc^{3+} were the most promising ones. These three borate structures were too stable to continue the synthesis to the mullite-type ceramics. Hence, this synthesis was not further continued during this work.

As mentioned before, $SnMBO_4$ phases do not appear when M = Fe or Mn. They result in the so-called dolomite-type phases with the chemical formular $MSn(BO_3)_2$. Investigations of these structures were done during the work of this PhD thesis and discussed in **chapter 8**. The crystal structure is rhombohedral and the unit cell parameters increase with the increasing nature of the radius of the M-cations which are Mn^{2+}, Fe^{2+}, Co^{2+}, and Ni^{2+}. The crystal structure is a combination of one layer of MO_6 octahedra which are interconnected by trigonal planar BO_3 group to one layer of SnO_6 octahedra. These observations were proven by vibrational and Mössbauer spectroscopy. The direct band gaps analyzed by UV/Vis diffuse reflectance data are in the range of semiconductors. These structures help the study of mullite-type compounds as they have a trigonal planar BO_3 group and contain tin which was a main focus of the work. Hence, different oxidation states of tin were investigated during this work.

Reference

1. R.D. Shannon, Revised effective ionic radii and systematic studies of interatomic distances, Acta Crystallographica A32 (1976) 751.
2. J. Köhler, J. Tong, R. Dinnebier, A. Simon, Crystal structure and electronic structure of red SnO, Zeitschrift für anorganische und allgemeine Chemie 638(12-13) (2012) 1970-1975. DOI:10.1002/zaac.201200263

Appendix

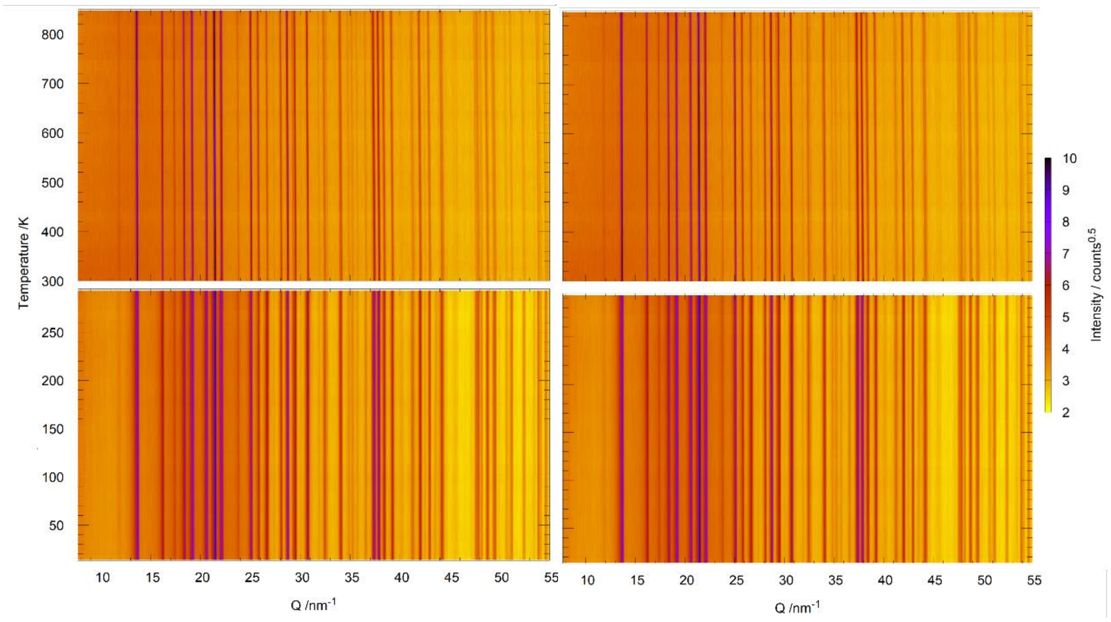

Figure A5.1: 2D plot of temperature-dependent X-ray powder diffraction patter of SnCrBO$_4$ (left) and SnVBO$_4$ (right).

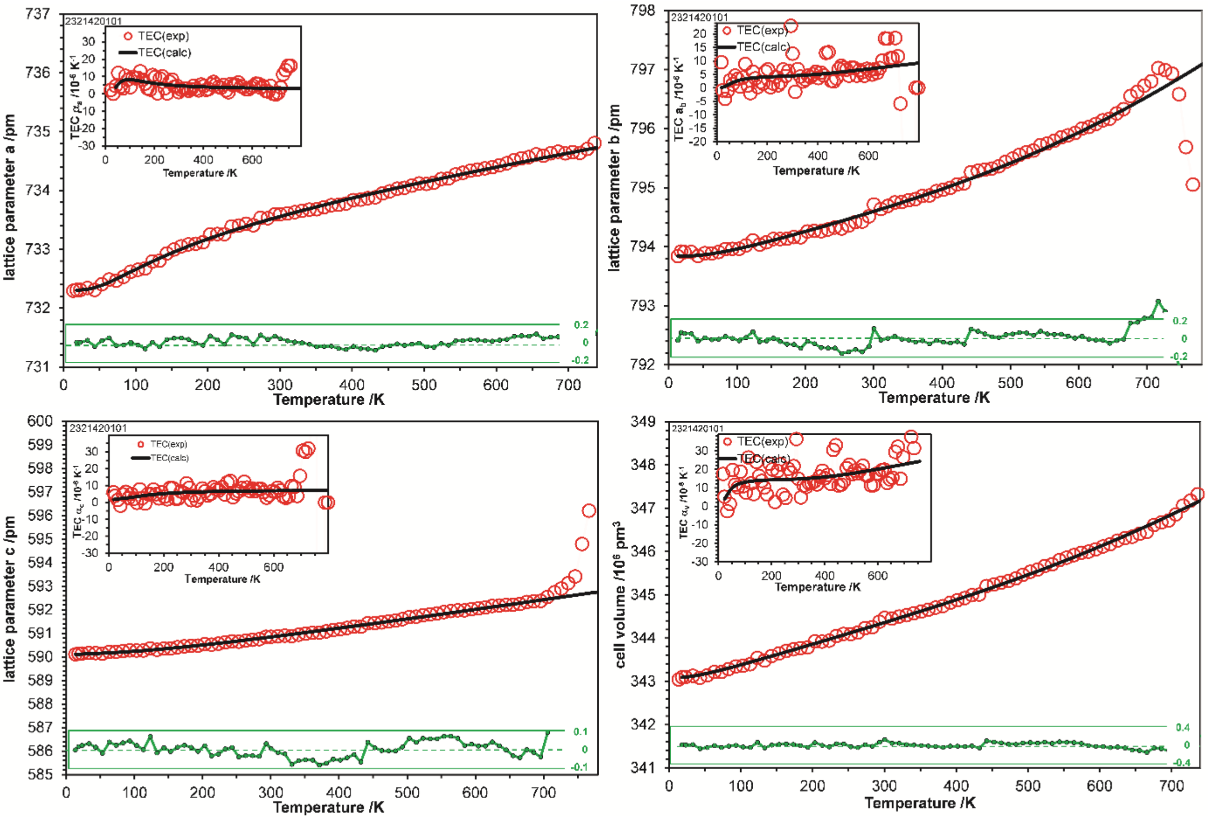

Figure A5.2: Debye-Einstein-Anharmonicity (DEA) fits of the metric parameters of SnVBO$_4$. The respective thermal expansion coefficients (TECs) and the Debye energy terms are seen as insets.

Table A5.1: Debye-Einstein-Anharmonicity (DEA) fit parameters of $SnVBO_4$

	Cell volume	lattice parameters		
Fit-parameter	***V***	***a***	***b***	***c***
M_0 /10^{-6} pm^3	343.10(3)	732.19(9)	793.88(10)	590.11(7)
k_{D1} /10^{-12} GPa	2.56(1)	2.72(1)	4.16(1)	2.85(1)
θ_{D1} /K	348(3)	944(5)	969(3)	1090(4)
k_E /10^{-12} GPa	2.48(1)	4.66(1)	0.87(1)	1.48(1)
θ_E /K	104(10)	11(1)	16(1)	27(1)

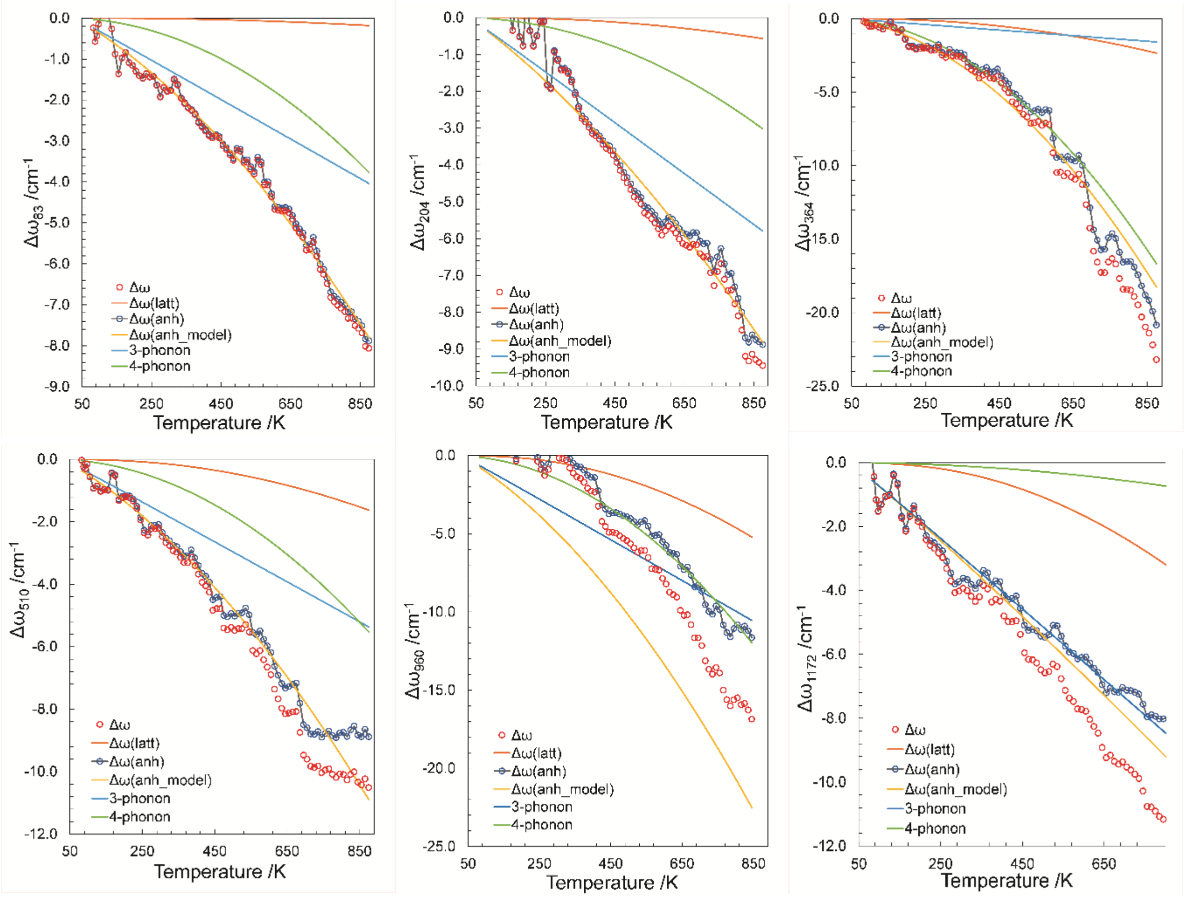

Figure A5.3: Temperature dependent change of phonon frequencies of some representative Raman bands of $SnVBO_4$. The red circles, the blue circles combined with the grey solid line, and the orange solid line refer to observed frequency shift, frequency shift due to volume and anharmonic contributions, respectively. The solid lines in blue and green represent the model calculation based on the phonon-phonon interactions.

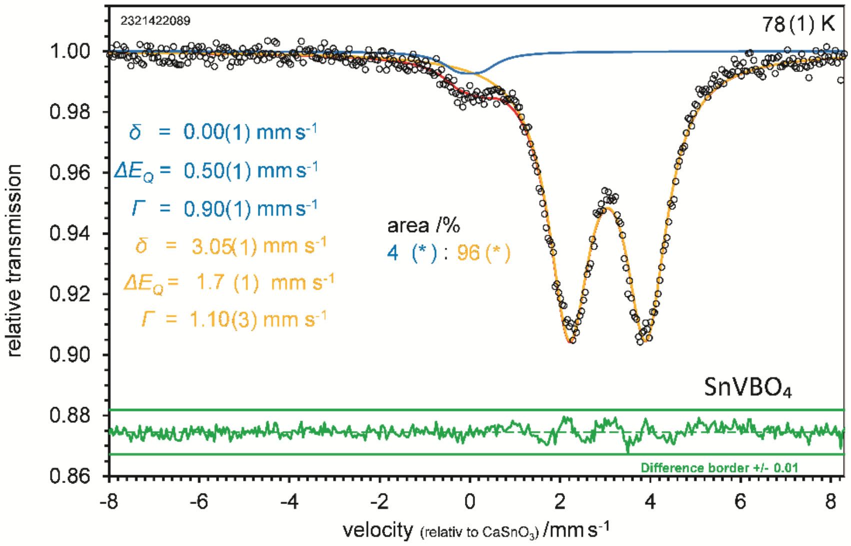

Figure A5.4: ^{119}Sn Mössbauer spectrum of $SnVBO_4$, open circle and solid line refer to observed and fit data.

Table A5.2: Fitting parameters of ^{119}Sn Mössbauer spectroscopic measurements of $SnVBO_4$ at room temperature and 78 K (with two different fittings). δ = isomer shift; ΔE_Q = electric quadrupole splitting; Γ = experimental line width.

Parameter	**$SnVBO_4$ (293 K)**	**$SnVBO_4$ (78 K)**
δ /(mm/s)	2.98(1)	3.05(1)
ΔE_Q /(mm/s)	1.50(1)	1.70(1)
Γ /(mm/s)	0.99(3)	1.10(3)
n_s	1.20(6)	1.29(1)
n_p	0.78(3)	0.71(3)
(n_x+n_y)	0.27(2)	0.38(1)
n_z	0.47(2)	0.52(1)

Figure A7.1: Syntheses in corundum crucible with burned-in $MnBO_3$ (left), platinum crucible with colorless $AlBO_3$ (middle), and colors of samples (right) with $FeBO_3$ (red-brownish), $MnBO_3$ (greyish), $CrBO_3$ (green), and $ScBO_3$ (colorless)

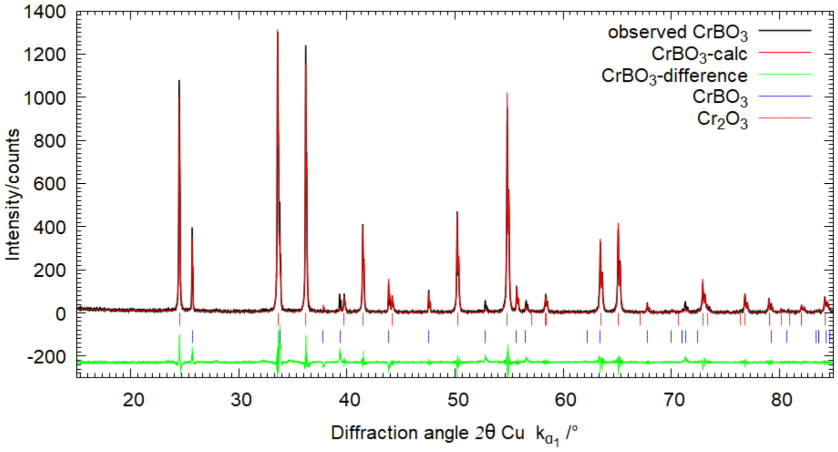

Figure A7.2: Rietveld refinement plot of the synthesis of $CrBO_3$ (2321419067) of corundum crucible with calculated (red) and observed (grey) patterns, difference curve (green), Bragg peaks of $CrBO_3$ (blue) and impurity Cr_2O_3 (red).

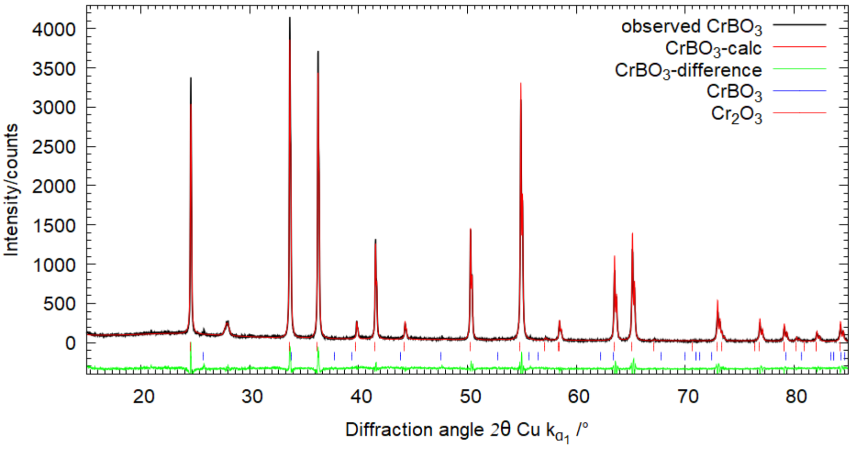

Figure A7.3: Rietveld refinement plot of the synthesis of $CrBO_3$ (2321423369) of platinum crucible with calculated (red) and observed (grey) patterns, difference curve (green), Bragg peaks of $CrBO_3$ (blue) and impurity Cr_2O_3 (red).

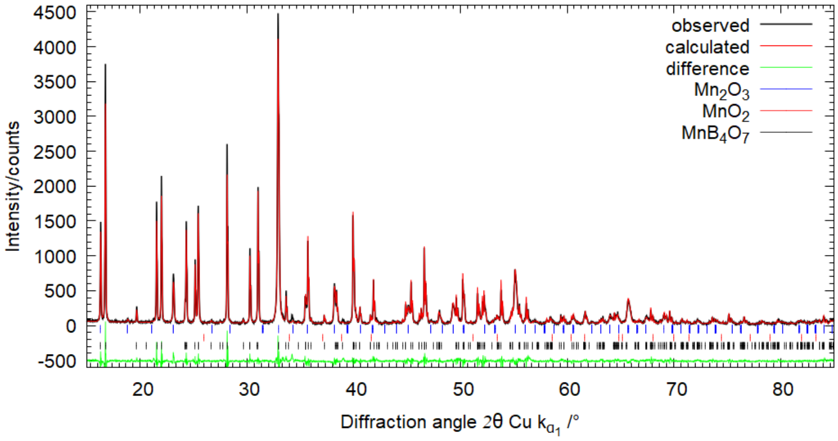

Figure A7.4: Rietveld refinement plot of the synthesis of $MnBO_3$ (2321423370) of platinum crucible with calculated (red) and observed (grey) patterns, difference curve (green), Bragg peaks of MnO_2 (pink), MnB_4O_7 (black), and Mn_2O_3 (blue).

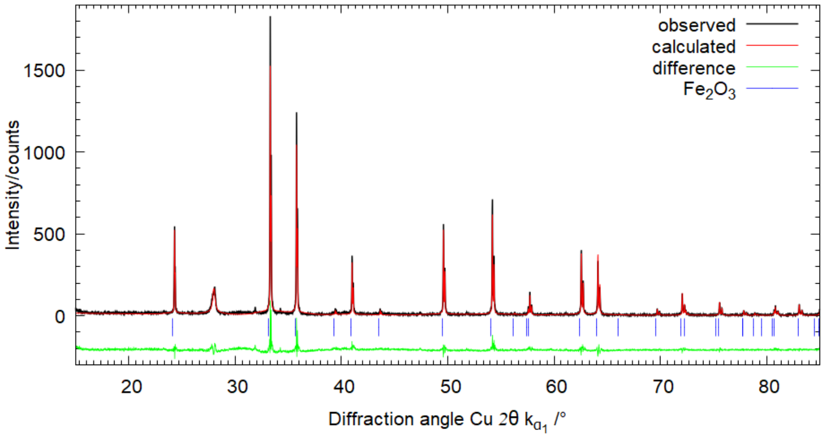

Figure A7.5: Rietveld refinement plot of the synthesis of $FeBO_3$ (2321422014) of corundum crucible with calculated (red) and observed (grey) patterns, difference curve (green), Bragg peaks of Fe_2O_3 (blue).

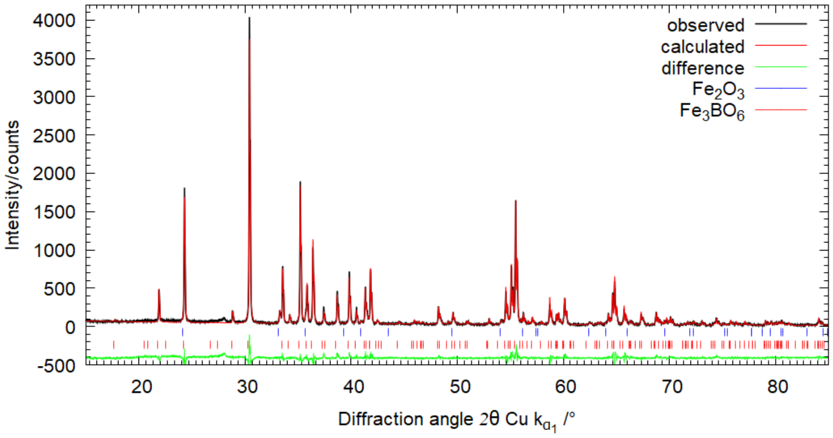

Figure A7.6: Rietveld refinement plot of the synthesis of $FeBO_3$ (2321423368) of platinum crucible with calculated (red) and observed (grey) patterns, difference curve (green), Bragg peaks of Fe_2O_3 (blue) and Fe_3BO_6 (pink).

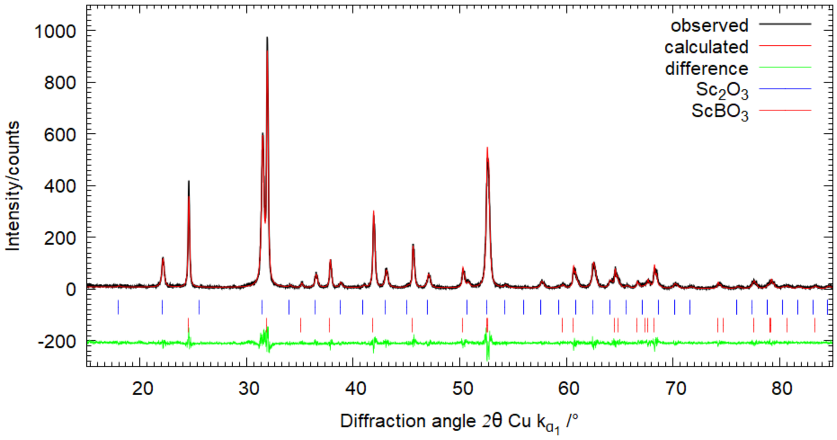

Figure A7.7: Rietveld refinement plot of the synthesis of ScBO$_3$ (2321420107) of corundum crucible with calculated (red) and observed (grey) patterns, difference curve (green), Bragg peaks of Sc$_2$O$_3$ (blue) and ScBO$_3$ (pink).

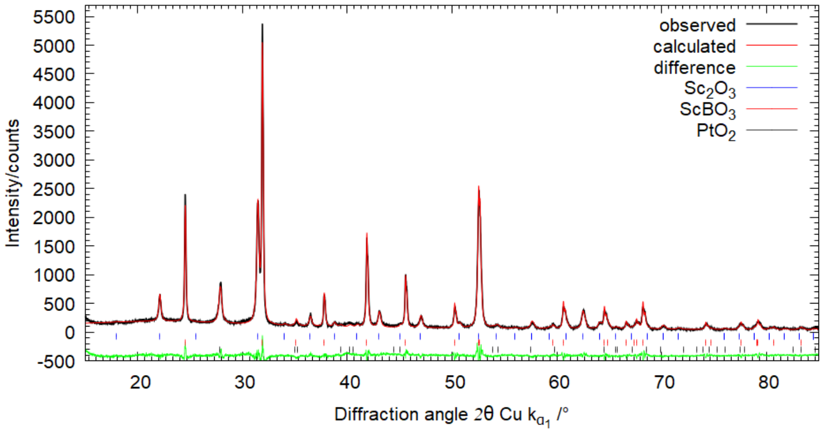

Figure A7.8: Rietveld refinement plot of the synthesis of ScBO$_3$ (2321423371) of platinum crucible with calculated (red) and observed (grey) patterns, difference curve (green), Bragg peaks of Sc$_2$O$_3$ (blue) and ScBO$_3$ (pink) as well as a PtO$_2$ impurity (black).

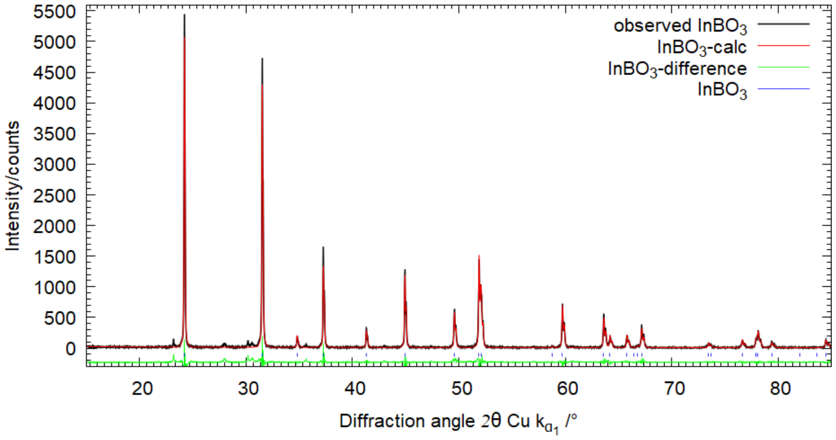

Figure A7.9: Rietveld refinement plot of the synthesis of InBO$_3$ (2321421377) of corundum crucible with calculated (red) and observed (grey) patterns, difference curve (green), Bragg peaks of InBO$_3$ (blue).

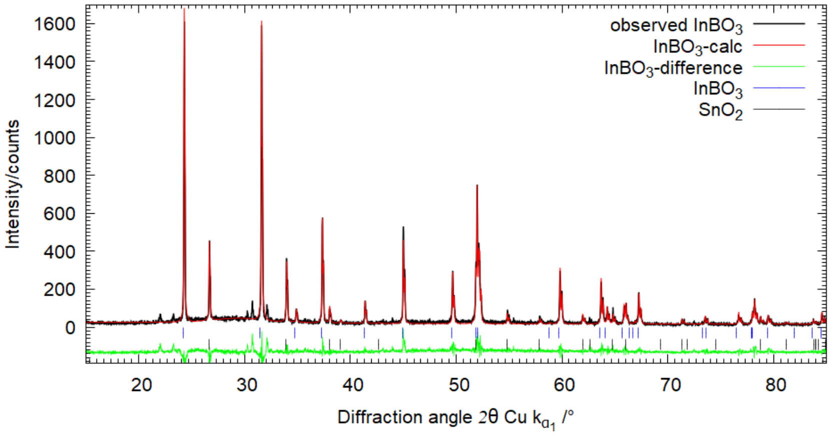

Figure A7.10: Rietveld refinement plot of the synthesis of $InBO_3$ with SnO (2321422016) of corundum crucible with calculated (red) and observed (grey) patterns, difference curve (green), Bragg peaks of SnO_2 (black) and $InBO_3$ (blue).

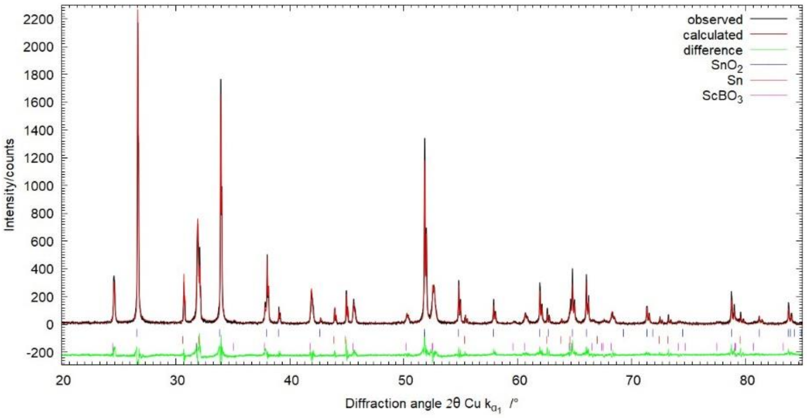

Figure A9.1: Rietveld refinement plot of the synthesis of $SnScBO_4$ (2321419084) with calculated (red) and observed (grey) patterns, difference curve (green), Bragg peaks of SnO_2 (black), Sn (orange) and $ScBO_3$ (pink).

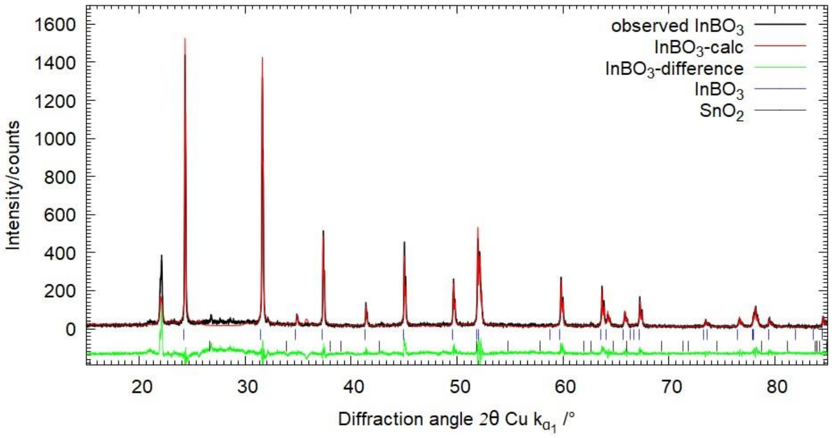

Figure A9.2: Rietveld refinement plot of the synthesis of $SnInBO_4$ (2321420042) with calculated (red) and observed (grey) patterns, difference curve (green), Bragg peaks of SnO_2 (black) and $ScBO_3$ (blue).

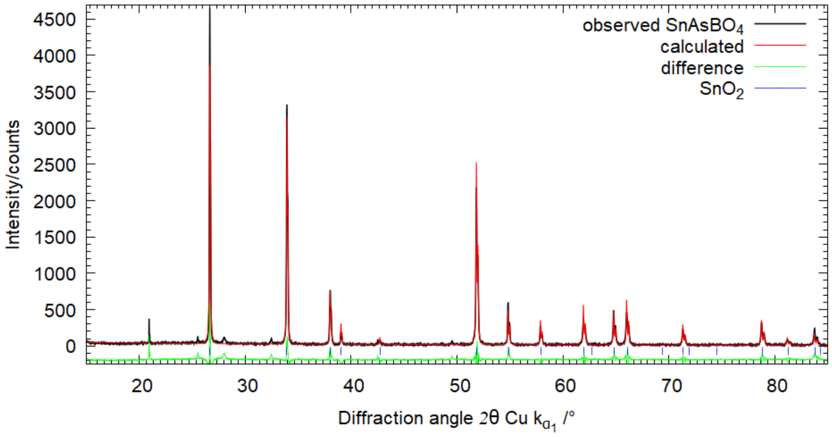

Figure A9.3: Rietveld refinement plot of the synthesis of $SnAsBO_4$ (2321421253) with calculated (red) and observed (grey) patterns, difference curve (green), Bragg peaks of SnO_2 (blue).

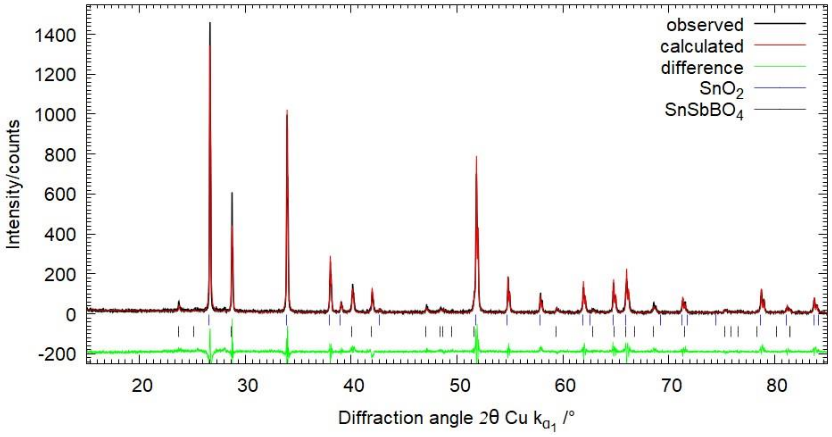

Figure A9.4: Rietveld refinement plot of $SnSbBO_4$ (2321420030) with calculated (red), observed (grey) patterns, difference curve (green), Bragg peaks of SnO_2 (blue) and $SnSbBO_4$ (black).

Table A9.1: Syntheses of $PbAl_{1-x}Cr_xBO_4$ which can be found with the following USI number.

x - value	USI number	Who did it?
0.1	2113121021	Master thesis of Louis
0.2	2113121020	Master thesis of Louis
0.3	2113121019	Master thesis of Louis
0.4	2113121018	Master thesis of Louis
0.5	2113121017	Master thesis of Louis
0.6	2113121016	Master thesis of Louis
0.7	2113121015	Master thesis of Louis
0.8	2113121059	Master thesis of Louis
0.9	2113121058	Master thesis of Louis

Table A9.2: Syntheses of $PbGa_{1-x}Cr_xBO_4$ which can be found with the following USI number.

x - value	USI number	Who did it?
0.1	2113121044	Master thesis of Louis
0.2	2113121043	Master thesis of Louis
0.3	2113121057	Master thesis of Louis
0.4	2113121041	Master thesis of Louis
0.5	2113121056	Master thesis of Louis
0.6	2113121039	Master thesis of Louis
0.7	2113121048	Master thesis of Louis
0.8	2113121069	Master thesis of Louis
0.9	2113121068	Master thesis of Louis

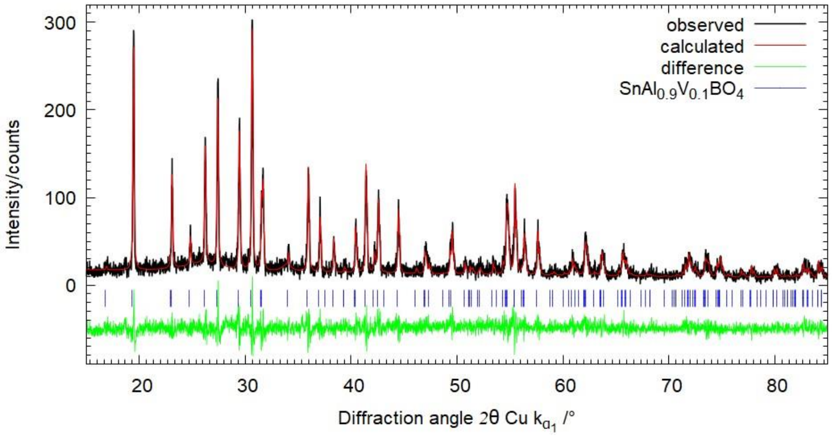

Figure A9.5: Rietveld refinement plot of $SnAl_{0.9}V_{0.1}BO_4$ (2321422268) with calculated (red), observed (grey) patterns, difference curve (green), Bragg peaks of $SnAl_{0.9}V_{0.1}BO_4$ (blue).

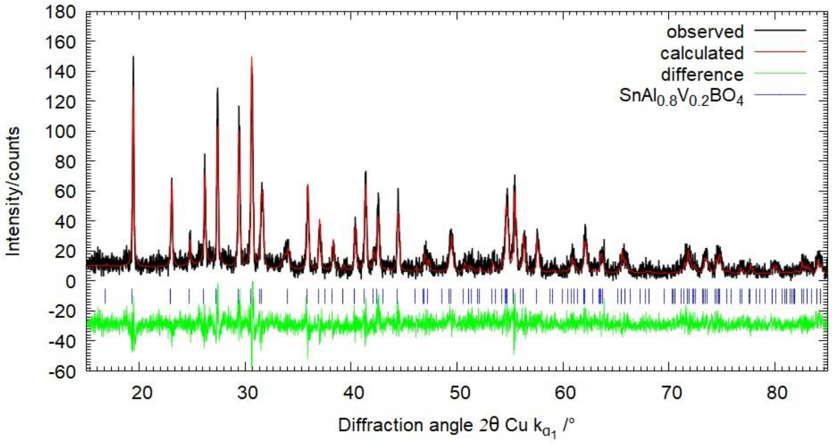

Figure A9.6: Rietveld refinement plot of $SnAl_{0.8}V_{0.2}BO_4$ (2321422263) with calculated (red), observed (grey) patterns, difference curve (green), Bragg peaks of $SnAl_{0.8}V_{0.2}BO_4$ (blue).

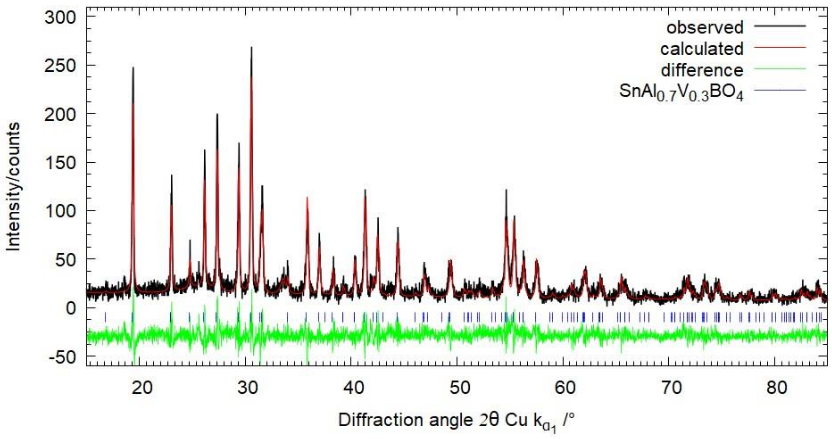

Figure A9.7: Rietveld refinement plot of $SnAl_{0.7}V_{0.3}BO_4$ (2321422260) with calculated (red), observed (grey) patterns, difference curve (green), Bragg peaks of $SnAl_{0.7}V_{0.3}BO_4$ (blue).

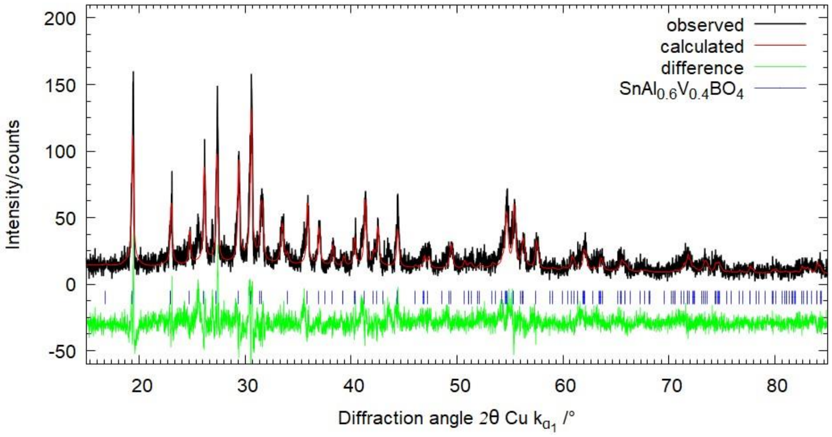

Figure A9.8: Rietveld refinement plot of $SnAl_{0.6}V_{0.4}BO_4$ (2321422257) with calculated (red), observed (grey) patterns, difference curve (green), Bragg peaks of $SnAl_{0.6}V_{0.4}BO_4$ (blue).

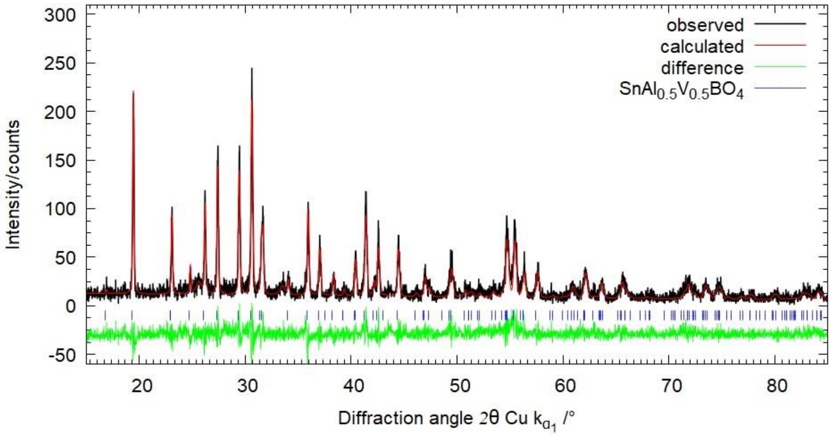

Figure A9.9: Rietveld refinement plot of $SnAl_{0.5}V_{0.5}BO_4$ (2321422254) with calculated (red), observed (grey) patterns, difference curve (green), Bragg peaks of $SnAl_{0.5}V_{0.5}BO_4$ (blue).

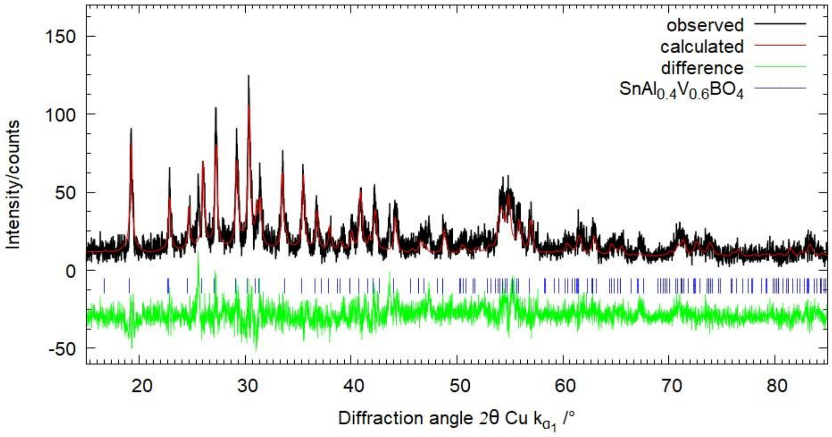

Figure A9.10: Rietveld refinement plot of $SnAl_{0.4}V_{0.6}BO_4$ (2321422253) with calculated (red), observed (grey) patterns, difference curve (green), Bragg peaks of $SnAl_{0.4}V_{0.6}BO_4$ (blue).

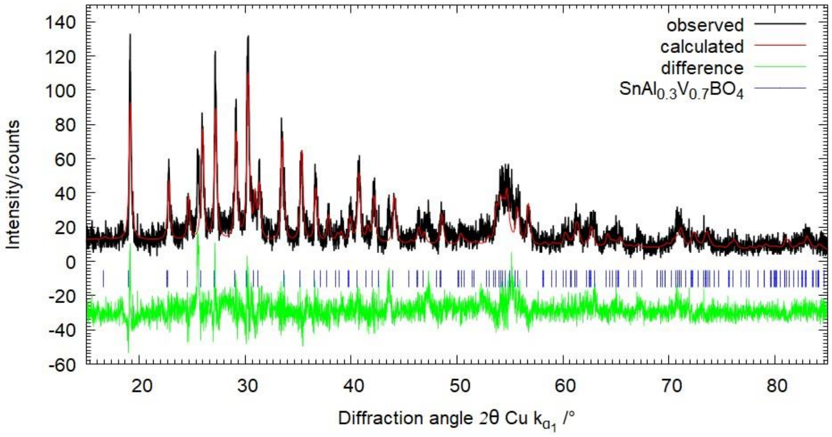

FigureA9.11: Rietveld refinement plot of $SnAl_{0.3}V_{0.7}BO_4$ (2321422249) with calculated (red), observed (grey) patterns, difference curve (green), Bragg peaks of $SnAl_{0.3}V_{0.7}BO_4$ (blue).

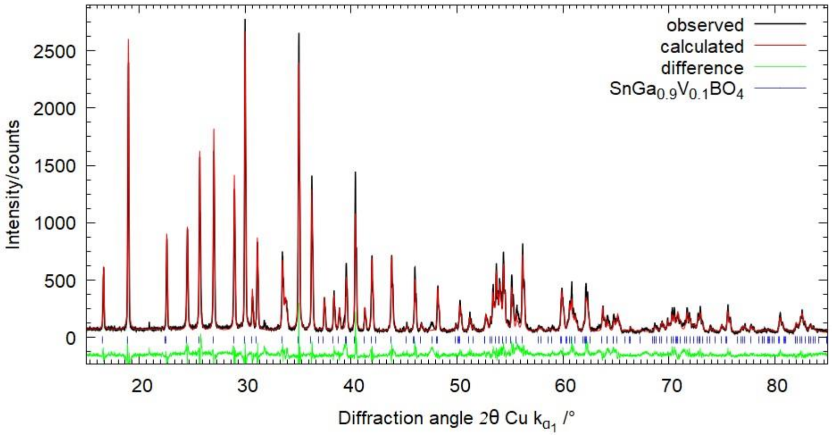

Figure A9.12: Rietveld refinement plot of $SnGa_{0.9}V_{0.1}BO_4$ (2321423103) with calculated (red), observed (grey) patterns, difference curve (green), Bragg peaks of $SnGa_{0.9}V_{0.1}BO_4$ (blue).

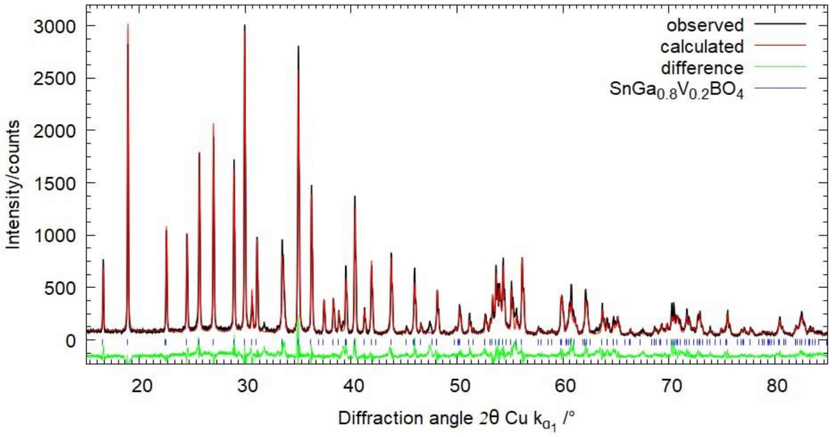

Figure A9.13: Rietveld refinement plot of $SnGa_{0.8}V_{0.2}BO_4$ (2321423102) with calculated (red), observed (grey) patterns, difference curve (green), Bragg peaks of $SnGa_{0.8}V_{0.2}BO_4$ (blue).

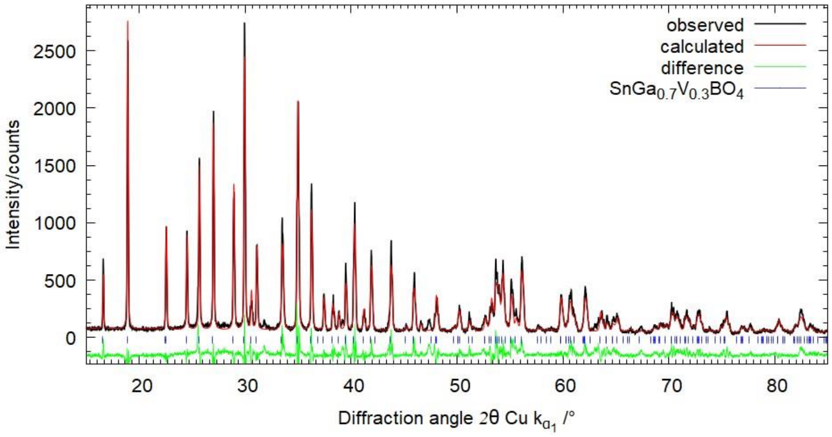

Figure A9.14: Rietveld refinement plot of $SnGa_{0.7}V_{0.3}BO_4$ (2321423101) with calculated (red), observed (grey) patterns, difference curve (green), Bragg peaks of $SnGa_{0.7}V_{0.3}BO_4$ (blue).

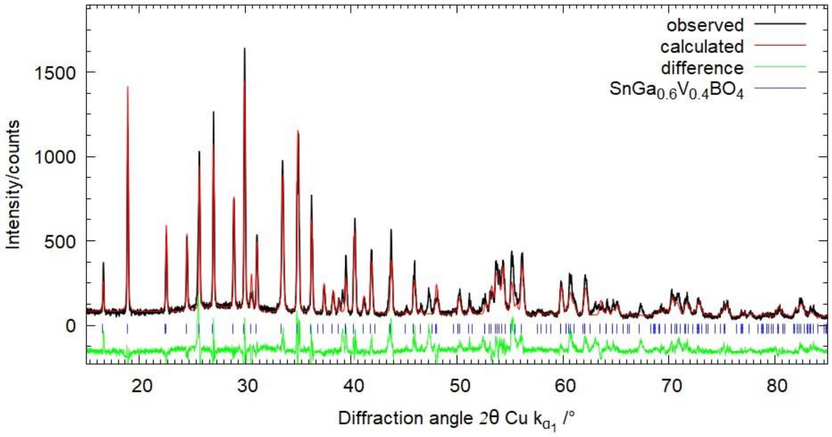

Figure A9.15: Rietveld refinement plot of $SnGa_{0.6}V_{0.4}BO_4$ (2321423100) with calculated (red), observed (grey) patterns, difference curve (green), Bragg peaks of $SnGa_{0.6}V_{0.4}BO_4$ (blue).

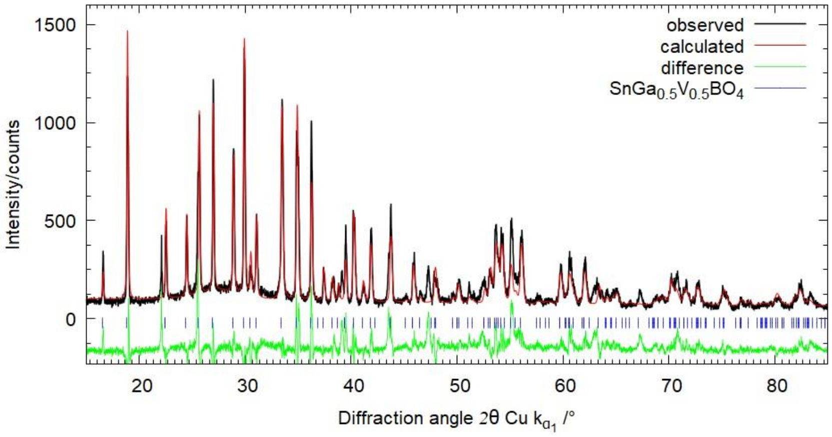

Figure A9.16: Rietveld refinement plot of $SnGa_{0.5}V_{0.5}BO_4$ (2321423099) with calculated (red), observed (grey) patterns, difference curve (green), Bragg peaks of $SnGa_{0.5}V_{0.5}BO_4$ (blue).

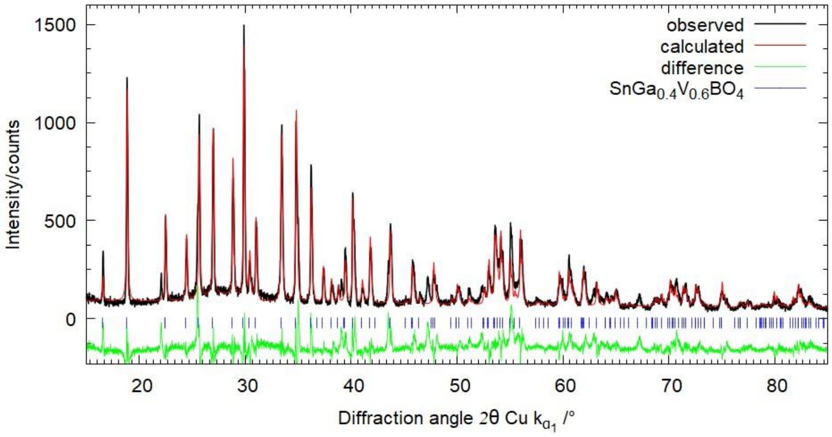

Figure A9.17: Rietveld refinement plot of $SnGa_{0.4}V_{0.6}BO_4$ (2321423098) with calculated (red), observed (grey) patterns, difference curve (green), Bragg peaks of $SnGa_{0.4}V_{0.6}BO_4$ (blue).

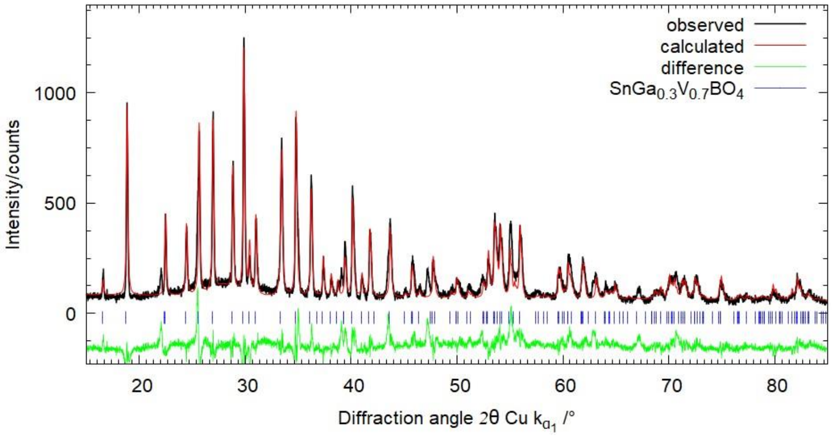

Figure A9.18: Rietveld refinement plot of $SnGa_{0.3}V_{0.7}BO_4$ (2321423097) with calculated (red), observed (grey) patterns, difference curve (green), Bragg peaks of $SnGa_{0.3}V_{0.7}BO_4$ (blue).

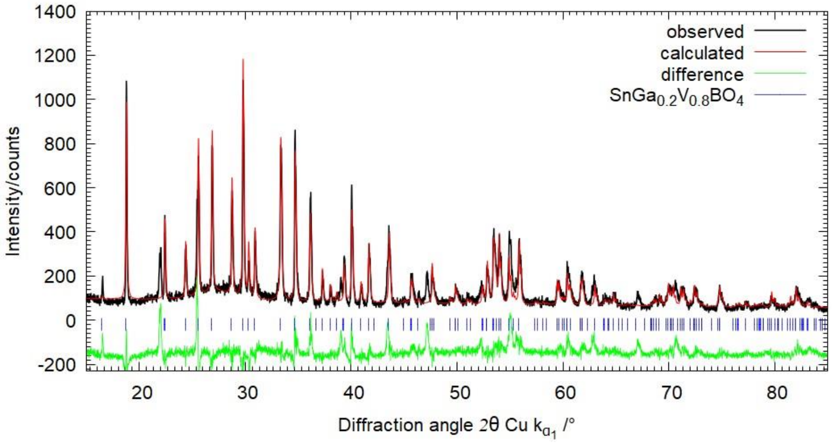

Figure A9.19: Rietveld refinement plot of $SnGa_{0.2}V_{0.8}BO_4$ (2321423096) with calculated (red), observed (grey) patterns, difference curve (green), Bragg peaks of $SnGa_{0.2}V_{0.8}BO_4$ (blue).

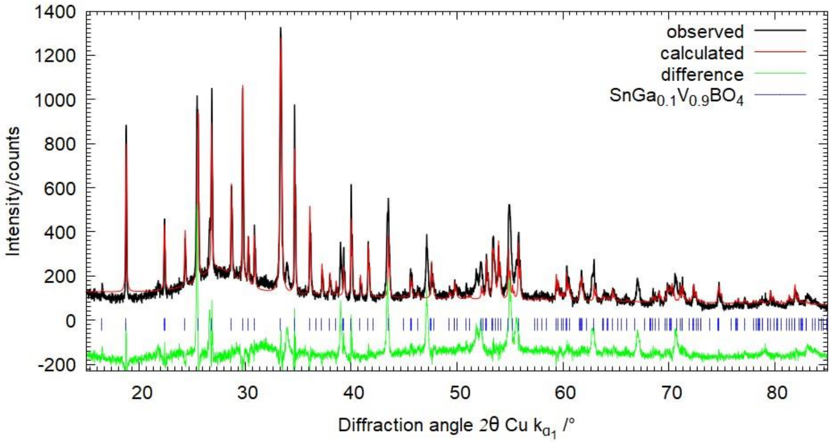

Figure A9.20: Rietveld refinement plot of $SnGa_{0.1}V_{0.9}BO_4$ (2321423095) with calculated (red), observed (grey) patterns, difference curve (green), Bragg peaks of $SnGa_{0.1}V_{0.9}BO_4$ (blue).

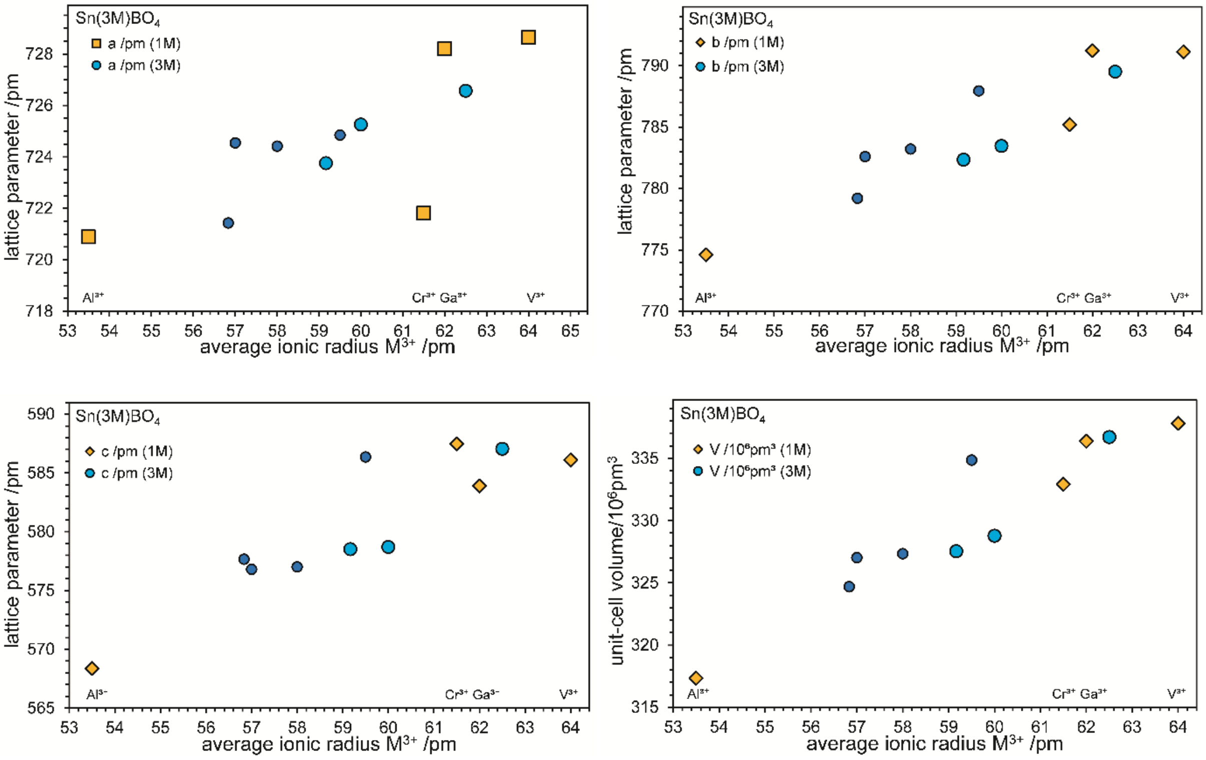

Figure A9.21: Trend of the metric parameters of the solid solutions with three trivalent metal cations with M = Al (orange diamonds), Ga (green triangular), and Cr (grey squares) for x = 0 – 1.0.

Appendix

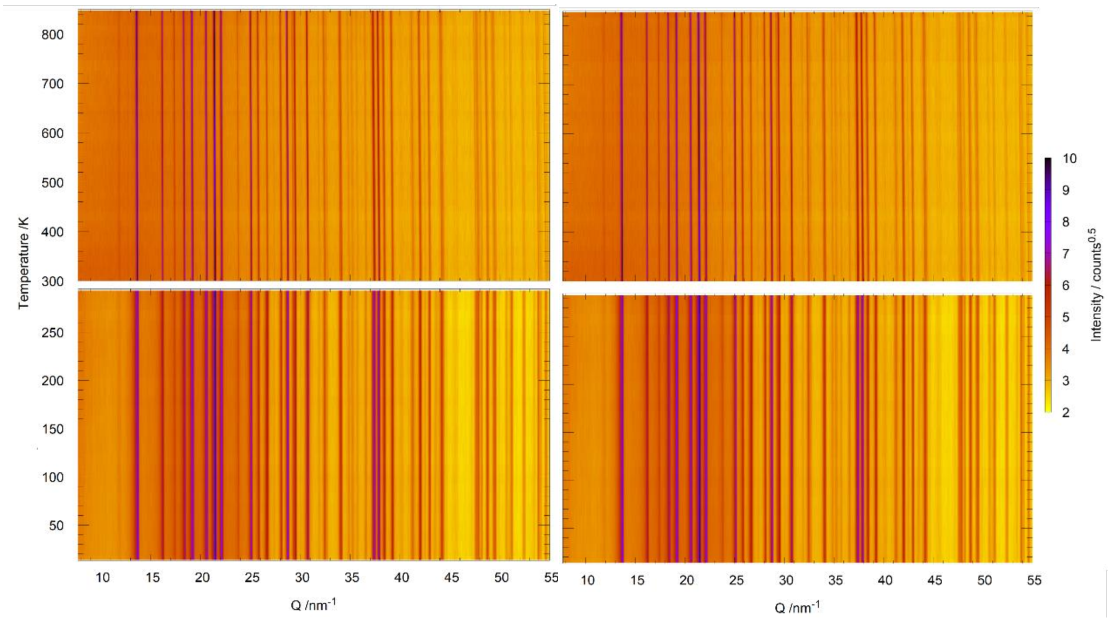

Figure A5.1: 2D plot of temperature-dependent X-ray powder diffraction patter of $SnCrBO_4$ (left) and $SnVBO_4$ (right).

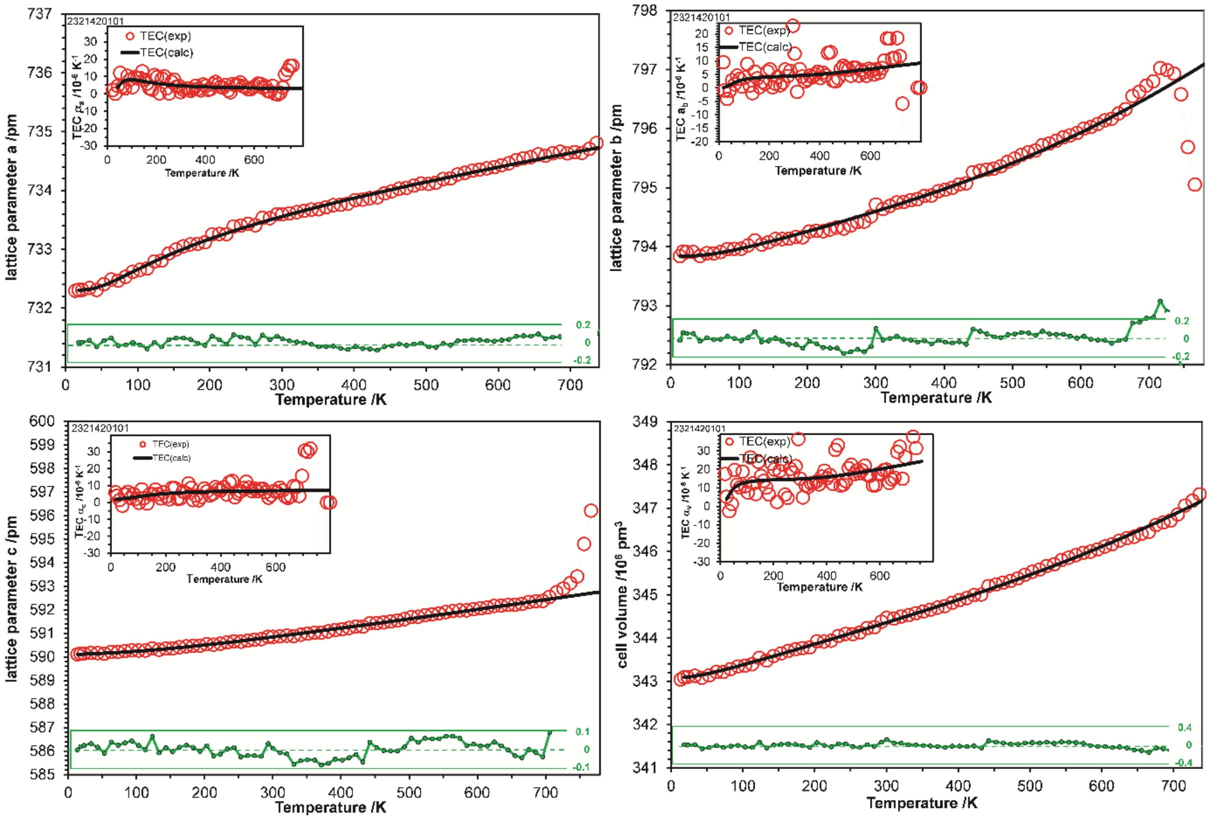

Figure A5.2: Debye-Einstein-Anharmonicity (DEA) fits of the metric parameters of $SnVBO_4$. The respective thermal expansion coefficients (TECs) and the Debye energy terms are seen as insets.

Table A5.1: Debye-Einstein-Anharmonicity (DEA) fit parameters of SnVBO$_4$

	Cell volume	lattice parameters		
Fit-parameter	***V***	***a***	***b***	***c***
M_0 /10^{-6} pm^3	343.10(3)	732.19(9)	793.88(10)	590.11(7)
k_{D1} /10^{-12} GPa	2.56(1)	2.72(1)	4.16(1)	2.85(1)
θ_{D1} /K	348(3)	944(5)	969(3)	1090(4)
k_E /10^{-12} GPa	2.48(1)	4.66(1)	0.87(1)	1.48(1)
θ_E /K	104(10)	11(1)	16(1)	27(1)

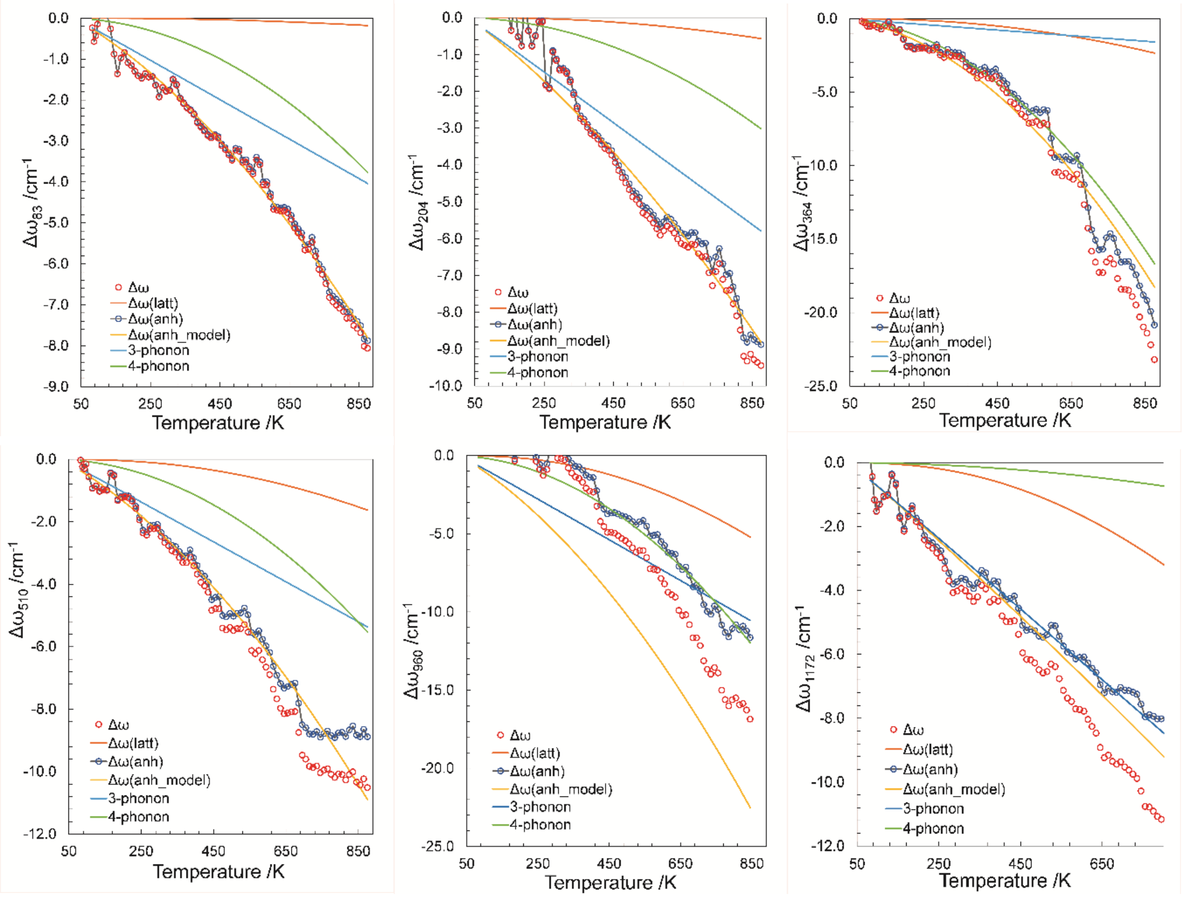

Figure A5.3: Temperature dependent change of phonon frequencies of some representative Raman bands of SnVBO$_4$. The red circles, the blue circles combined with the grey solid line, and the orange solid line refer to observed frequency shift, frequency shift due to volume and anharmonic contributions, respectively. The solid lines in blue and green represent the model calculation based on the phonon-phonon interactions.

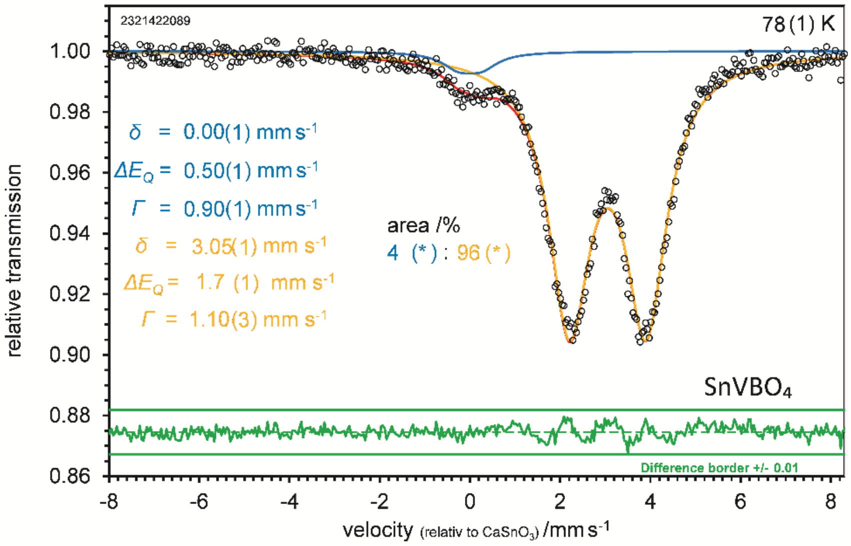

Figure A5.4: ^{119}Sn Mössbauer spectrum of $SnVBO_4$, open circle and solid line refer to observed and fit data.

Table A5.2: Fitting parameters of ^{119}Sn Mössbauer spectroscopic measurements of $SnVBO_4$ at room temperature and 78 K (with two different fittings). δ = isomer shift; ΔE_Q = electric quadrupole splitting; Γ = experimental line width.

Parameter	**$SnVBO_4$ (293 K)**	**$SnVBO_4$ (78 K)**
δ /(mm/s)	2.98(1)	3.05(1)
ΔE_Q /(mm/s)	1.50(1)	1.70(1)
Γ /(mm/s)	0.99(3)	1.10(3)
n_s	1.20(6)	1.29(1)
n_p	0.78(3)	0.71(3)
(n_x+n_y)	0.27(2)	0.38(1)
n_z	0.47(2)	0.52(1)

Figure A7.1: Syntheses in corundum crucible with burned-in $MnBO_3$ (left), platinum crucible with colorless $AlBO_3$ (middle), and colors of samples (right) with $FeBO_3$ (red-brownish), $MnBO_3$ (greyish), $CrBO_3$ (green), and $ScBO_3$ (colorless)

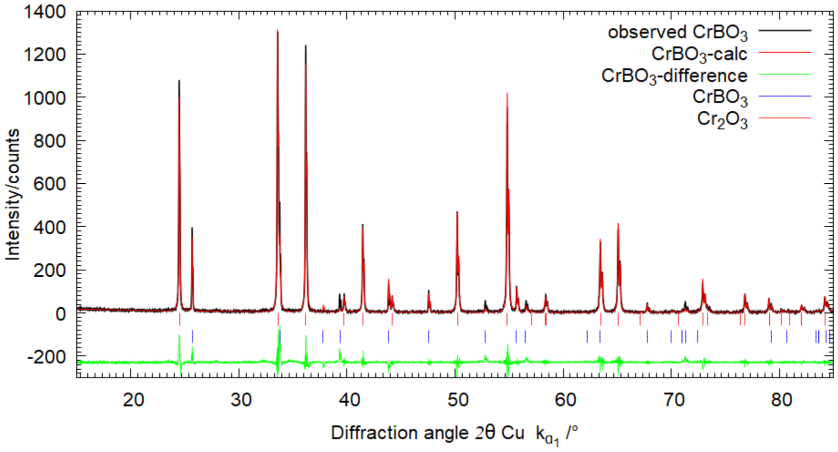

Figure A7.2: Rietveld refinement plot of the synthesis of $CrBO_3$ (2321419067) of corundum crucible with calculated (red) and observed (grey) patterns, difference curve (green), Bragg peaks of $CrBO_3$ (blue) and impurity Cr_2O_3 (red).

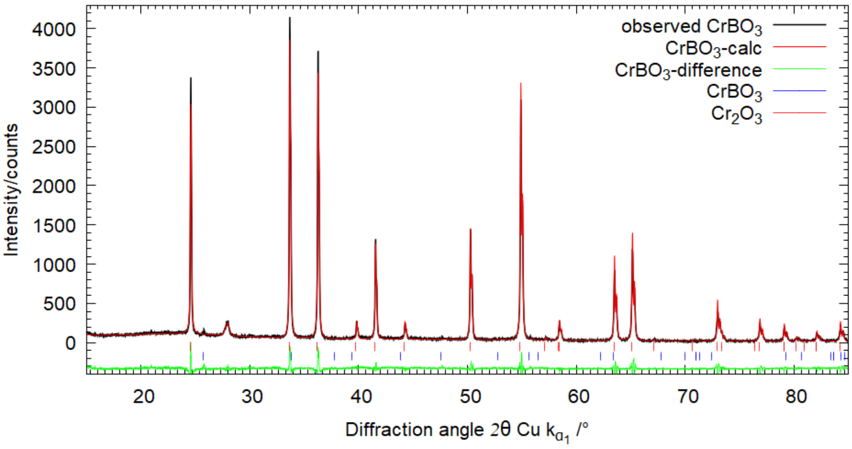

Figure A7.3: Rietveld refinement plot of the synthesis of $CrBO_3$ (2321423369) of platinum crucible with calculated (red) and observed (grey) patterns, difference curve (green), Bragg peaks of $CrBO_3$ (blue) and impurity Cr_2O_3 (red).

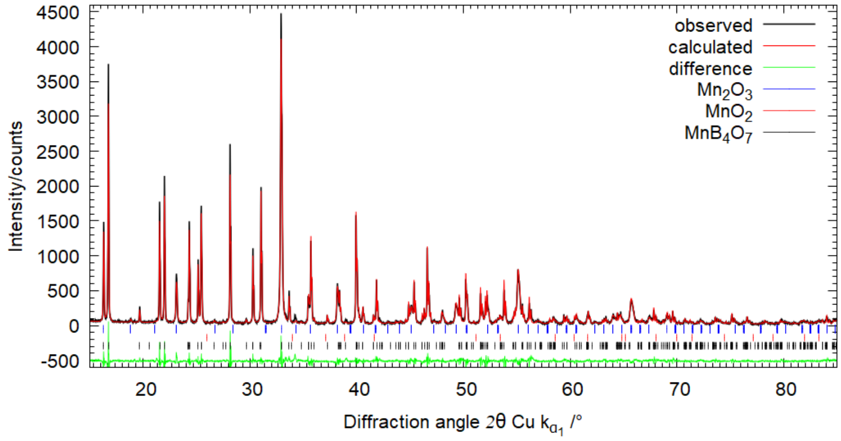

Figure A7.4: Rietveld refinement plot of the synthesis of $MnBO_3$ (2321423370) of platinum crucible with calculated (red) and observed (grey) patterns, difference curve (green), Bragg peaks of MnO_2 (pink), MnB_4O_7 (black), and Mn_2O_3 (blue).

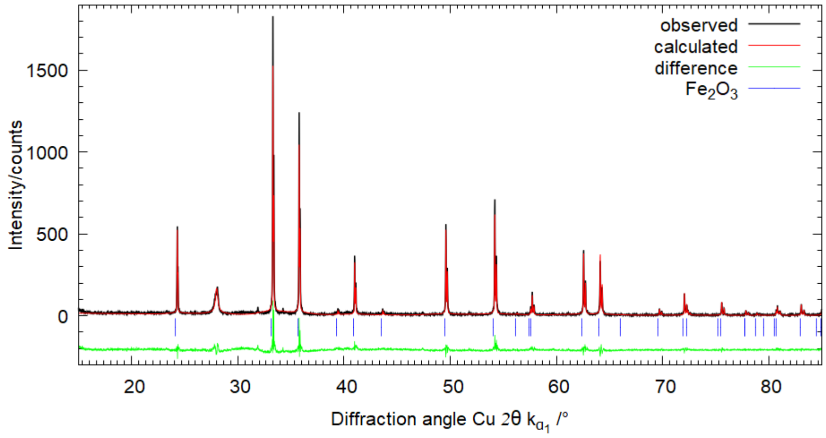

Figure A7.5: Rietveld refinement plot of the synthesis of $FeBO_3$ (2321422014) of corundum crucible with calculated (red) and observed (grey) patterns, difference curve (green), Bragg peaks of Fe_2O_3 (blue).

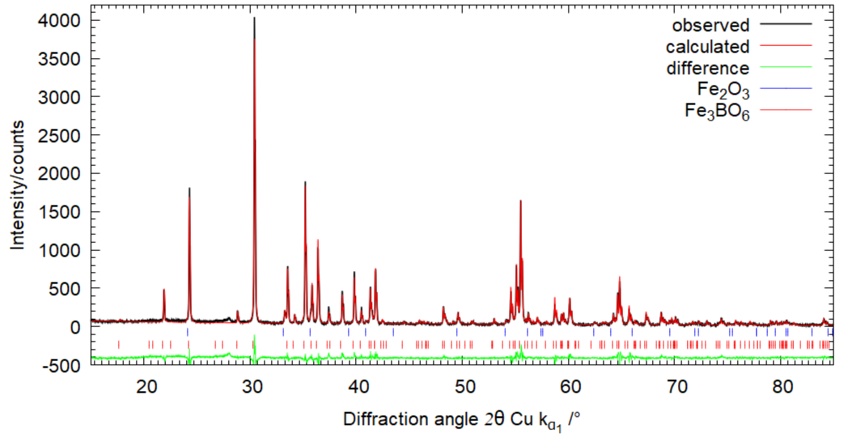

Figure A7.6: Rietveld refinement plot of the synthesis of $FeBO_3$ (2321423368) of platinum crucible with calculated (red) and observed (grey) patterns, difference curve (green), Bragg peaks of Fe_2O_3 (blue) and Fe_3BO_6 (pink).

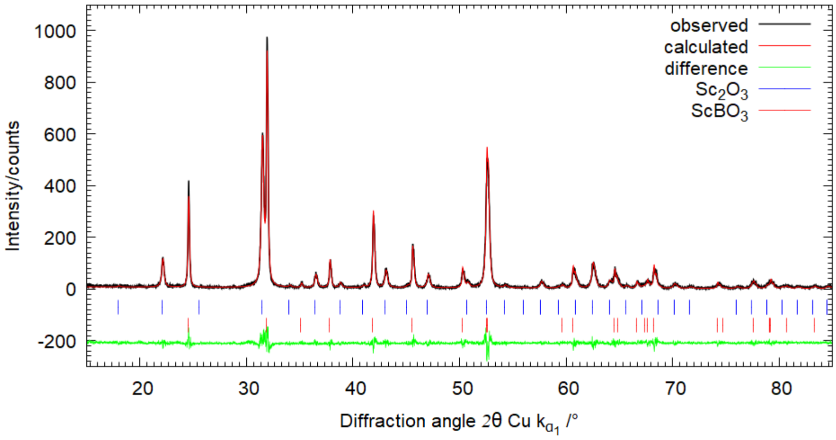

Figure A7.7: Rietveld refinement plot of the synthesis of $ScBO_3$ (2321420107) of corundum crucible with calculated (red) and observed (grey) patterns, difference curve (green), Bragg peaks of Sc_2O_3 (blue) and $ScBO_3$ (pink).

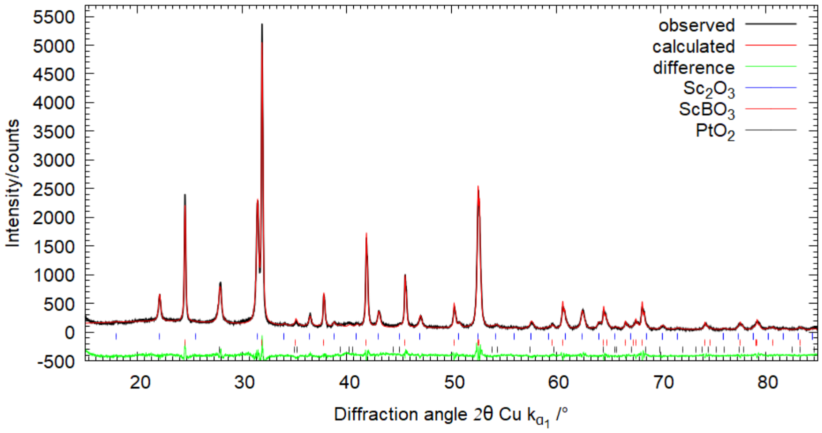

Figure A7.8: Rietveld refinement plot of the synthesis of $ScBO_3$ (2321423371) of platinum crucible with calculated (red) and observed (grey) patterns, difference curve (green), Bragg peaks of Sc_2O_3 (blue) and $ScBO_3$ (pink) as well as a PtO_2 impurity (black).

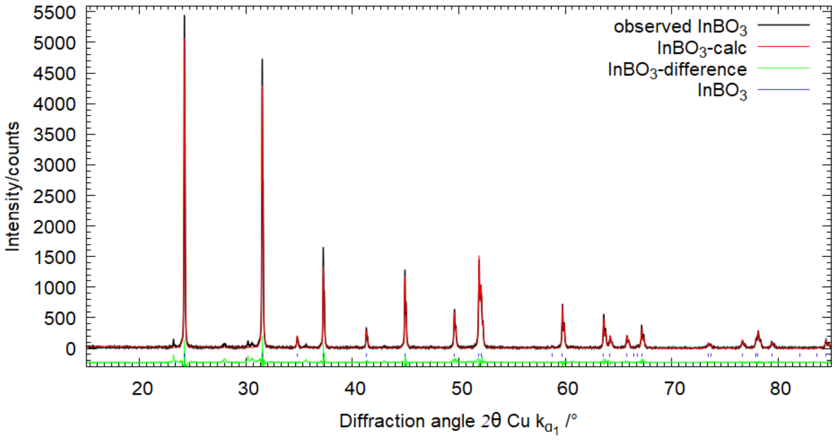

Figure A7.9: Rietveld refinement plot of the synthesis of $InBO_3$ (2321421377) of corundum crucible with calculated (red) and observed (grey) patterns, difference curve (green), Bragg peaks of $InBO_3$ (blue).

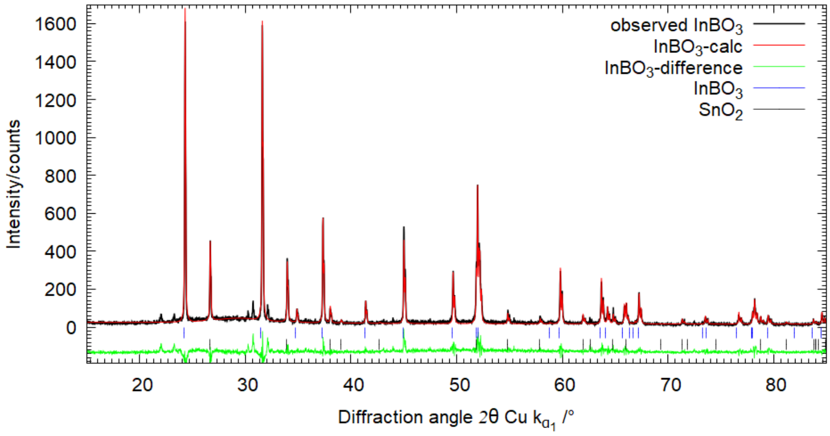

Figure A7.10: Rietveld refinement plot of the synthesis of $InBO_3$ with SnO (2321422016) of corundum crucible with calculated (red) and observed (grey) patterns, difference curve (green), Bragg peaks of SnO_2 (black) and $InBO_3$ (blue).

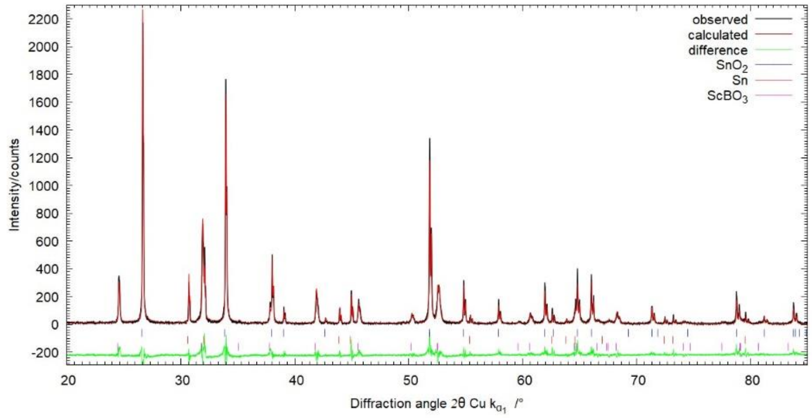

Figure A9.1: Rietveld refinement plot of the synthesis of $SnScBO_4$ (2321419084) with calculated (red) and observed (grey) patterns, difference curve (green), Bragg peaks of SnO_2 (black), Sn (orange) and $ScBO_3$ (pink).

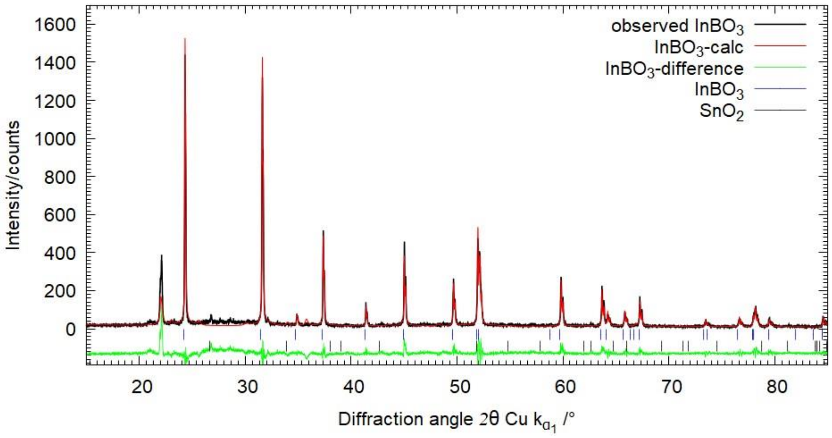

Figure A9.2: Rietveld refinement plot of the synthesis of $SnInBO_4$ (2321420042) with calculated (red) and observed (grey) patterns, difference curve (green), Bragg peaks of SnO_2 (black) and $ScBO_3$ (blue).

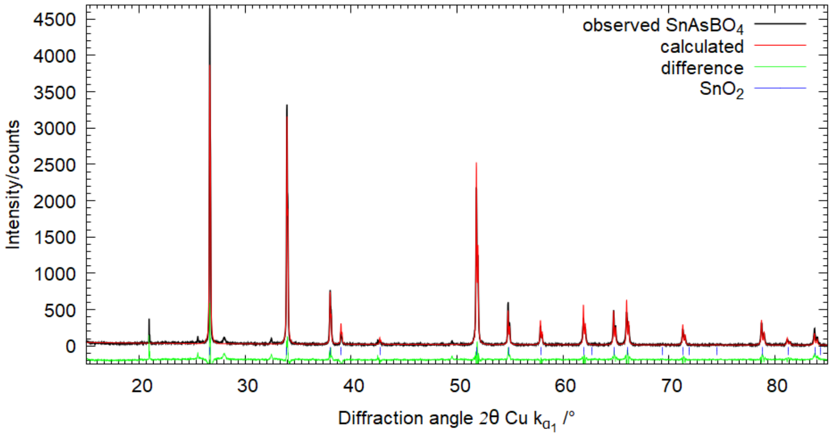

Figure A9.3: Rietveld refinement plot of the synthesis of $SnAsBO_4$ (2321421253) with calculated (red) and observed (grey) patterns, difference curve (green), Bragg peaks of SnO_2 (blue).

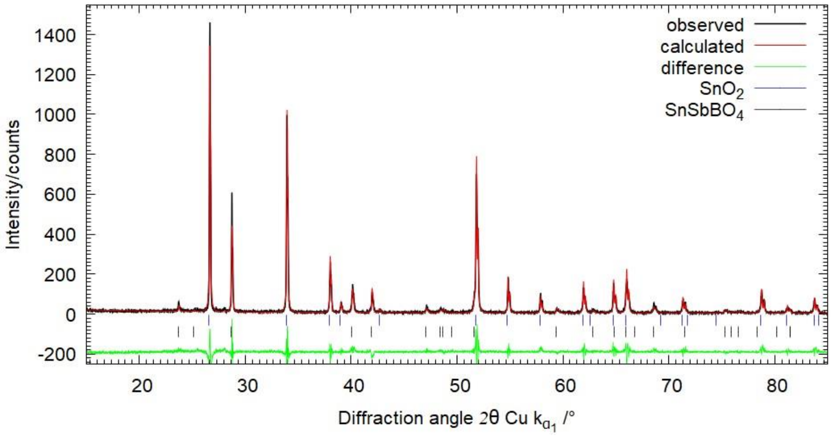

Figure A9.4: Rietveld refinement plot of SnSbBO$_4$ (2321420030) with calculated (red), observed (grey) patterns, difference curve (green), Bragg peaks of SnO$_2$ (blue) and SnSbBO$_4$ (black).

Table A9.1: Syntheses of PbAl$_{1-x}$Cr$_x$BO$_4$ which can be found with the following USI number.

x - value	USI number	Who did it?
0.1	2113121021	Master thesis of Louis
0.2	2113121020	Master thesis of Louis
0.3	2113121019	Master thesis of Louis
0.4	2113121018	Master thesis of Louis
0.5	2113121017	Master thesis of Louis
0.6	2113121016	Master thesis of Louis
0.7	2113121015	Master thesis of Louis
0.8	2113121059	Master thesis of Louis
0.9	2113121058	Master thesis of Louis

Table A9.2: Syntheses of PbGa$_{1-x}$Cr$_x$BO$_4$ which can be found with the following USI number.

x - value	USI number	Who did it?
0.1	2113121044	Master thesis of Louis
0.2	2113121043	Master thesis of Louis
0.3	2113121057	Master thesis of Louis
0.4	2113121041	Master thesis of Louis
0.5	2113121056	Master thesis of Louis
0.6	2113121039	Master thesis of Louis
0.7	2113121048	Master thesis of Louis
0.8	2113121069	Master thesis of Louis
0.9	2113121068	Master thesis of Louis

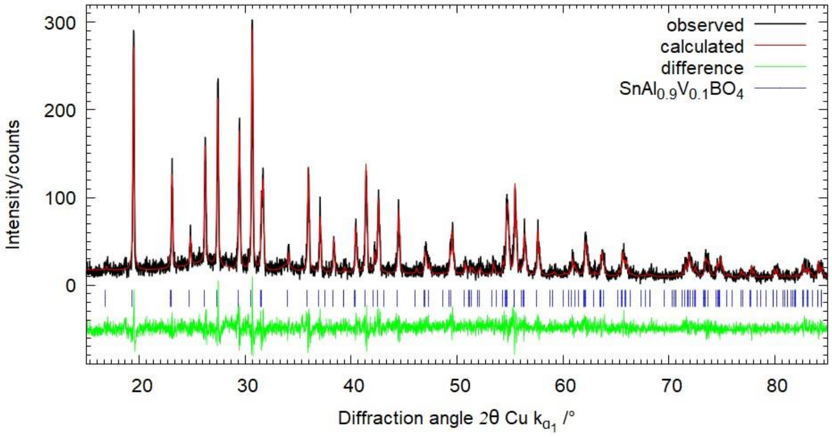

Figure A9.5: Rietveld refinement plot of $SnAl_{0.9}V_{0.1}BO_4$ (2321422268) with calculated (red), observed (grey) patterns, difference curve (green), Bragg peaks of $SnAl_{0.9}V_{0.1}BO_4$ (blue).

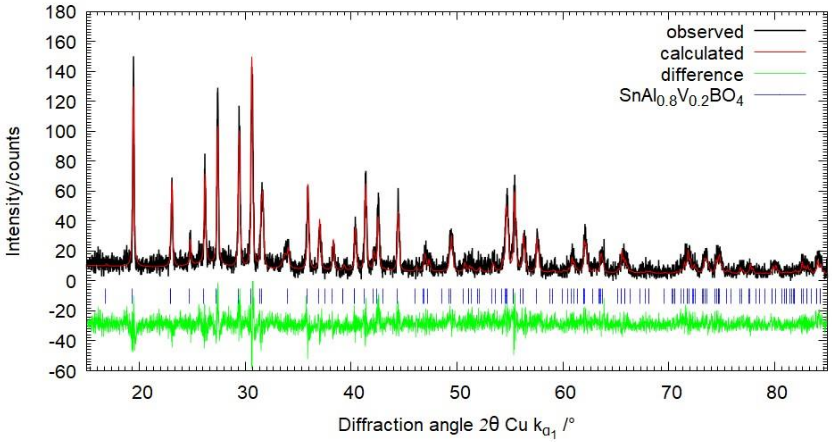

Figure A9.6: Rietveld refinement plot of $SnAl_{0.8}V_{0.2}BO_4$ (2321422263) with calculated (red), observed (grey) patterns, difference curve (green), Bragg peaks of $SnAl_{0.8}V_{0.2}BO_4$ (blue).

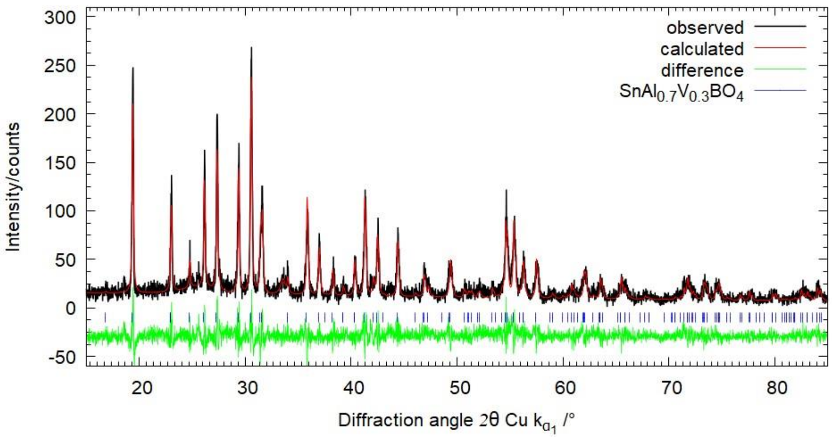

Figure A9.7: Rietveld refinement plot of $SnAl_{0.7}V_{0.3}BO_4$ (2321422260) with calculated (red), observed (grey) patterns, difference curve (green), Bragg peaks of $SnAl_{0.7}V_{0.3}BO_4$ (blue).

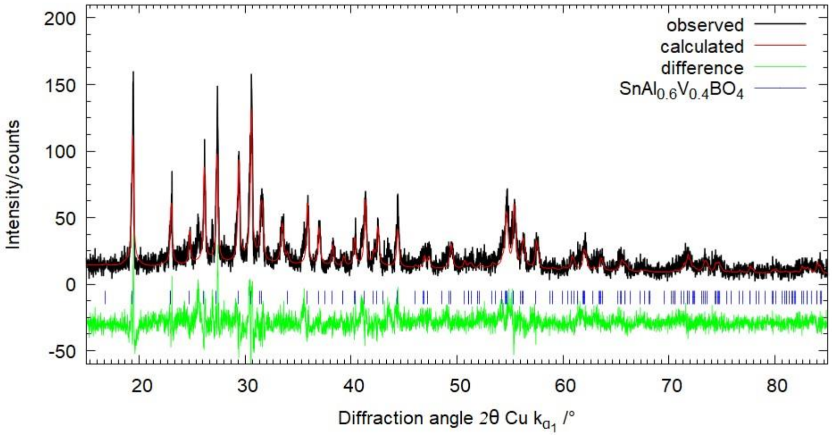

Figure A9.8: Rietveld refinement plot of $SnAl_{0.6}V_{0.4}BO_4$ (2321422257) with calculated (red), observed (grey) patterns, difference curve (green), Bragg peaks of $SnAl_{0.6}V_{0.4}BO_4$ (blue).

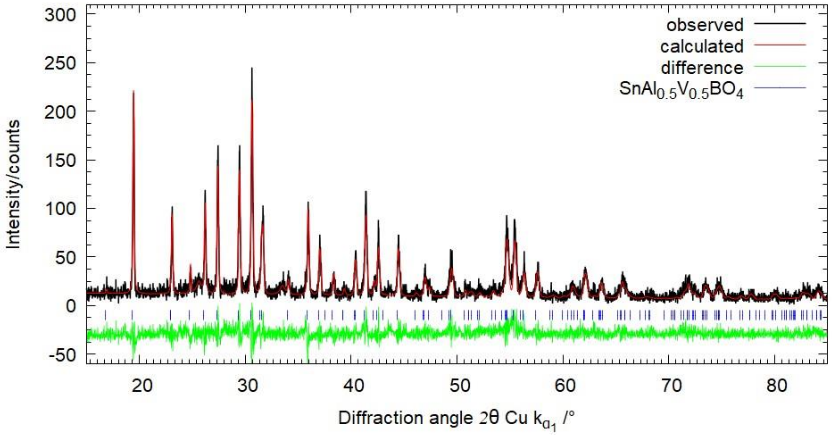

Figure A9.9: Rietveld refinement plot of $SnAl_{0.5}V_{0.5}BO_4$ (2321422254) with calculated (red), observed (grey) patterns, difference curve (green), Bragg peaks of $SnAl_{0.5}V_{0.5}BO_4$ (blue).

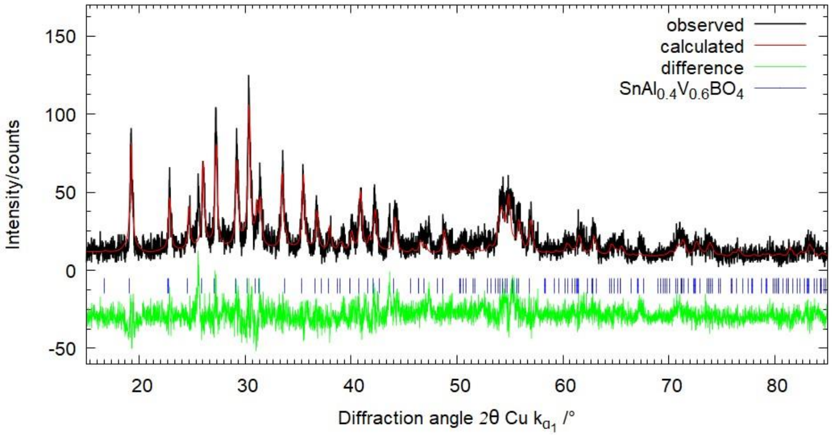

Figure A9.10: Rietveld refinement plot of $SnAl_{0.4}V_{0.6}BO_4$ (2321422253) with calculated (red), observed (grey) patterns, difference curve (green), Bragg peaks of $SnAl_{0.4}V_{0.6}BO_4$ (blue).

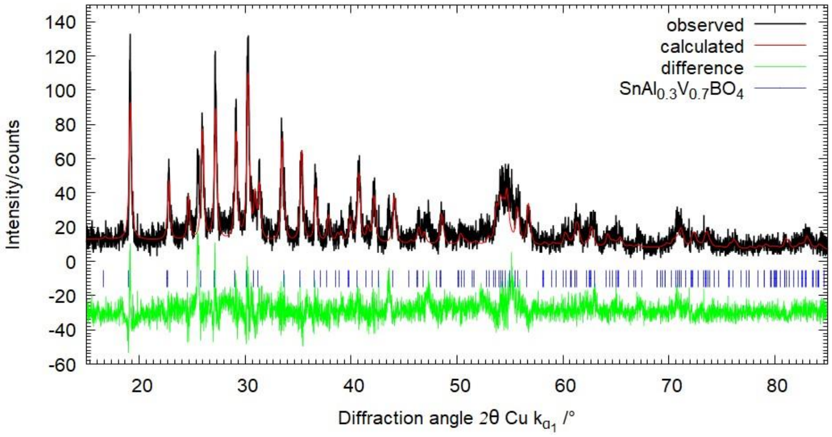

FigureA9.11: Rietveld refinement plot of $SnAl_{0.3}V_{0.7}BO_4$ (2321422249) with calculated (red), observed (grey) patterns, difference curve (green), Bragg peaks of $SnAl_{0.3}V_{0.7}BO_4$ (blue).

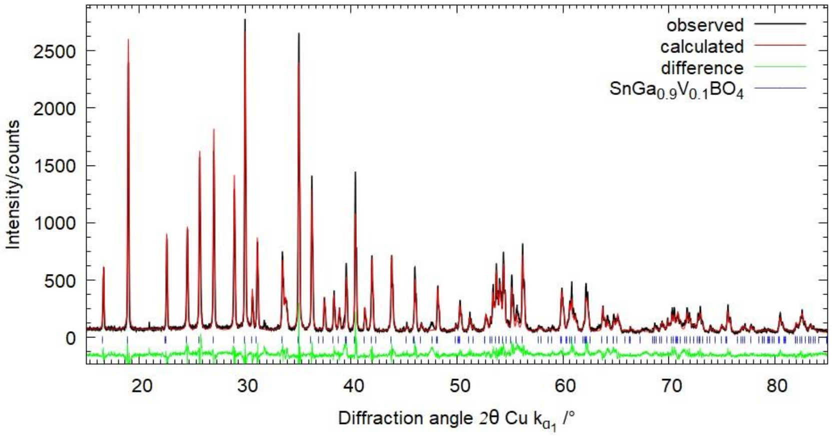

Figure A9.12: Rietveld refinement plot of $SnGa_{0.9}V_{0.1}BO_4$ (2321423103) with calculated (red), observed (grey) patterns, difference curve (green), Bragg peaks of $SnGa_{0.9}V_{0.1}BO_4$ (blue).

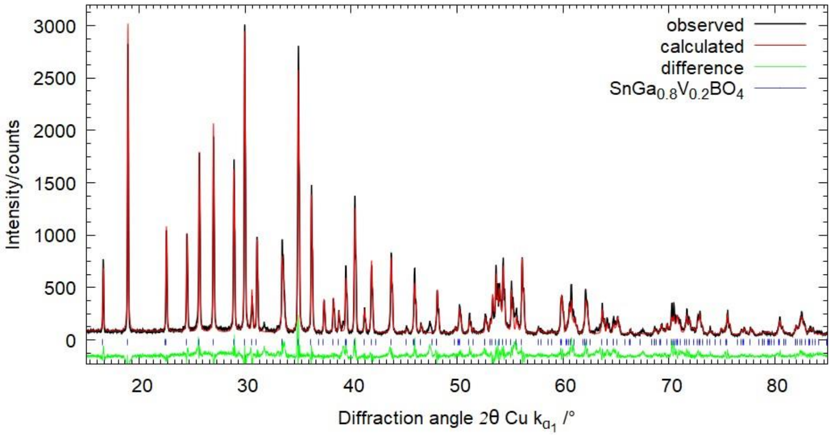

Figure A9.13: Rietveld refinement plot of $SnGa_{0.8}V_{0.2}BO_4$ (2321423102) with calculated (red), observed (grey) patterns, difference curve (green), Bragg peaks of $SnGa_{0.8}V_{0.2}BO_4$ (blue).

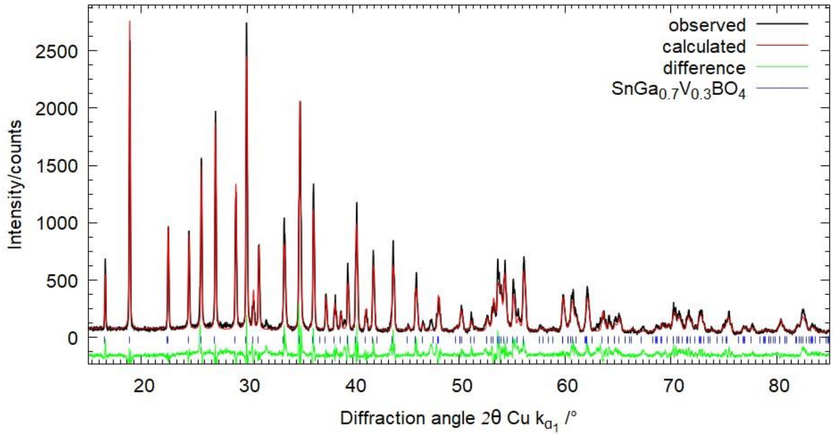

Figure A9.14: Rietveld refinement plot of $SnGa_{0.7}V_{0.3}BO_4$ (2321423101) with calculated (red), observed (grey) patterns, difference curve (green), Bragg peaks of $SnGa_{0.7}V_{0.3}BO_4$ (blue).

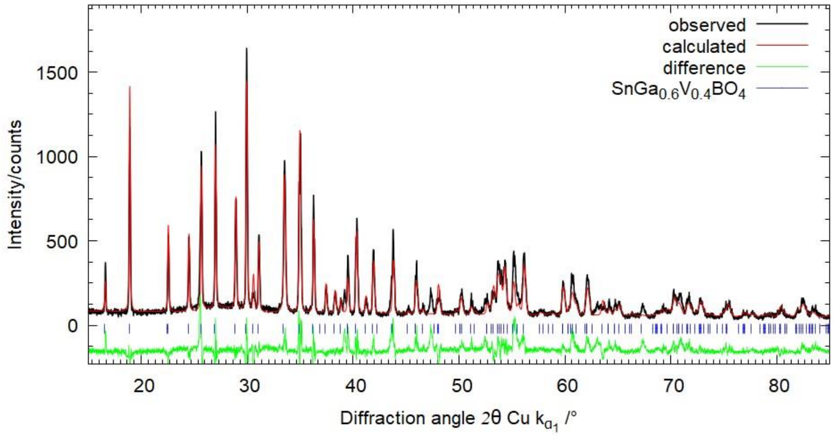

Figure A9.15: Rietveld refinement plot of $SnGa_{0.6}V_{0.4}BO_4$ (2321423100) with calculated (red), observed (grey) patterns, difference curve (green), Bragg peaks of $SnGa_{0.6}V_{0.4}BO_4$ (blue).

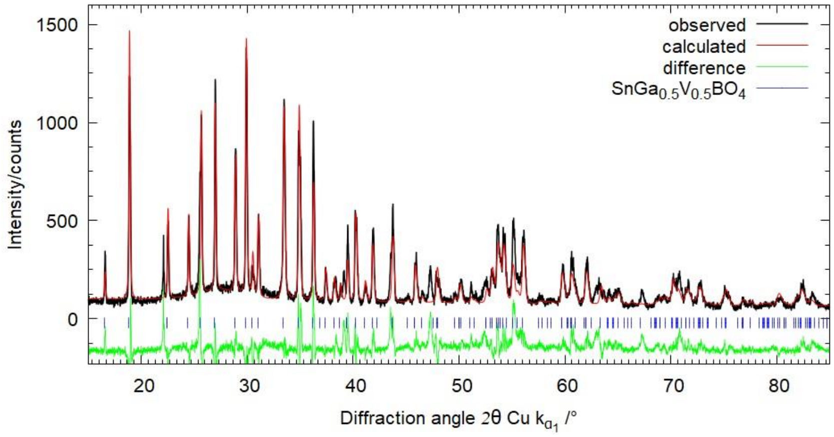

Figure A9.16: Rietveld refinement plot of $SnGa_{0.5}V_{0.5}BO_4$ (2321423099) with calculated (red), observed (grey) patterns, difference curve (green), Bragg peaks of $SnGa_{0.5}V_{0.5}BO_4$ (blue).

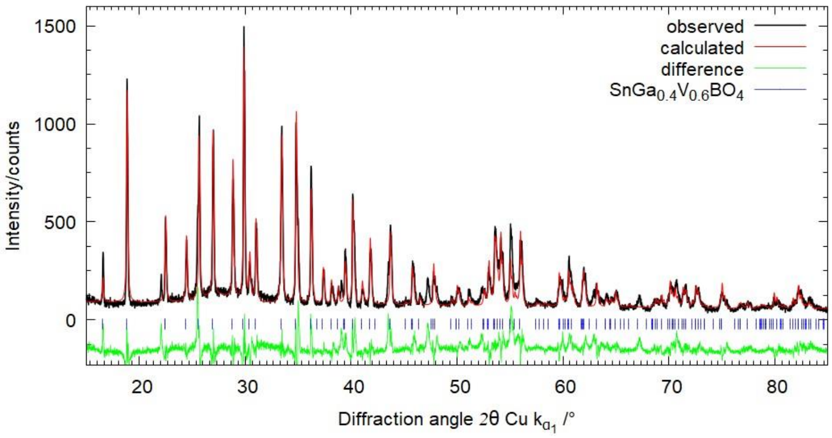

Figure A9.17: Rietveld refinement plot of $SnGa_{0.4}V_{0.6}BO_4$ (2321423098) with calculated (red), observed (grey) patterns, difference curve (green), Bragg peaks of $SnGa_{0.4}V_{0.6}BO_4$ (blue).

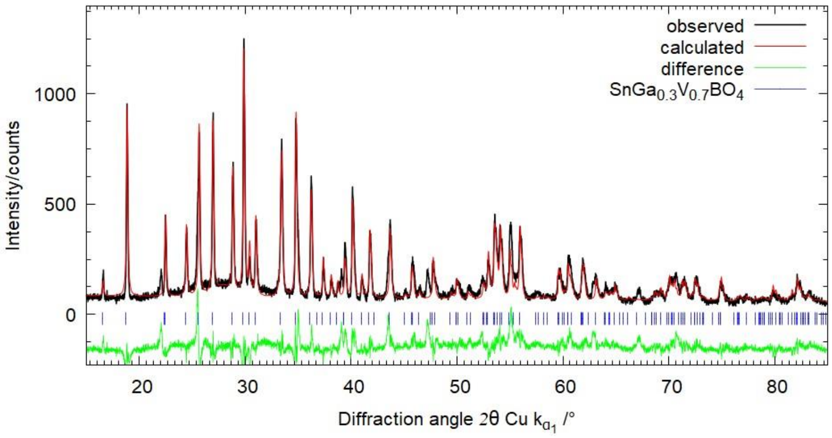

Figure A9.18: Rietveld refinement plot of $SnGa_{0.3}V_{0.7}BO_4$ (2321423097) with calculated (red), observed (grey) patterns, difference curve (green), Bragg peaks of $SnGa_{0.3}V_{0.7}BO_4$ (blue).

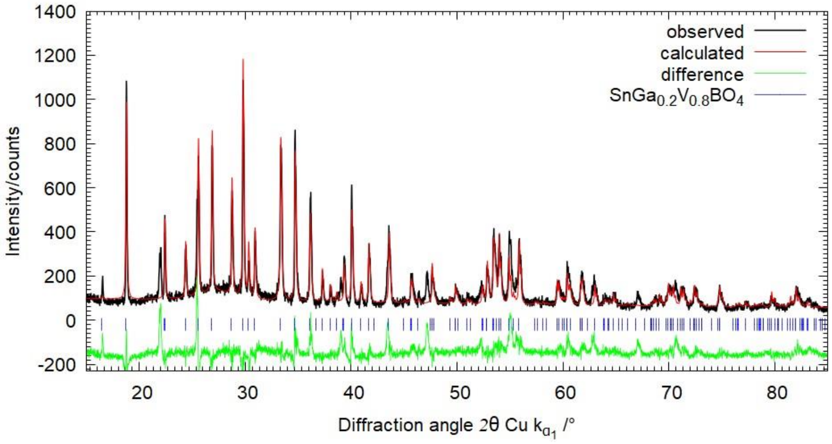

Figure A9.19: Rietveld refinement plot of $SnGa_{0.2}V_{0.8}BO_4$ (2321423096) with calculated (red), observed (grey) patterns, difference curve (green), Bragg peaks of $SnGa_{0.2}V_{0.8}BO_4$ (blue).

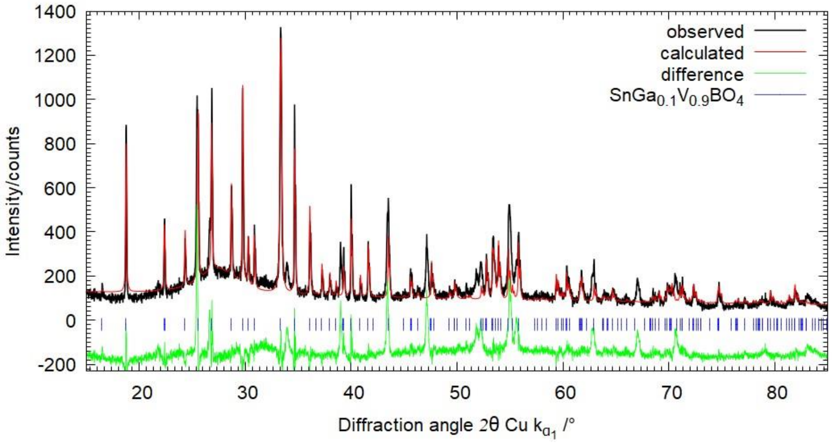

Figure A9.20: Rietveld refinement plot of $SnGa_{0.1}V_{0.9}BO_4$ (2321423095) with calculated (red), observed (grey) patterns, difference curve (green), Bragg peaks of $SnGa_{0.1}V_{0.9}BO_4$ (blue).

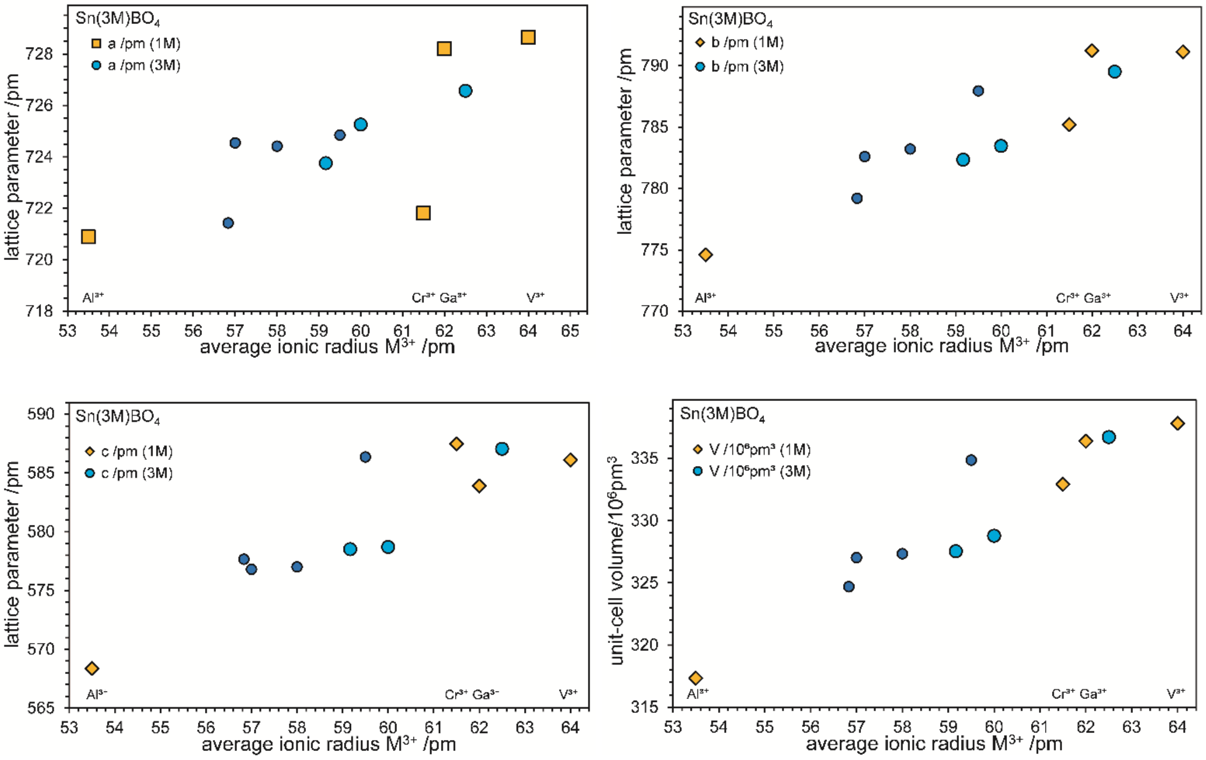

Figure A9.21: Trend of the metric parameters of the solid solutions with three trivalent metal cations with M = Al (orange diamonds), Ga (green triangular), and Cr (grey squares) for x = 0 – 1.0.